Blind Quantum Computing with Trapped Ions and Single Photons

Peter Drmota

Linacre College

University of Oxford

A thesis submitted for the degree of

Doctor of Philosophy

Trinity 2023

Acknowledgements

I am extremely grateful to Prof. David Lucas for giving me the opportunity to work on this project and believing in me. As my supervisor, he made sure that I could focus almost exclusively on the exciting scientific and technical challenges, and as little as possible on administrative and financial matters. Thank you David, for injecting optimism and sage advice when problems came up in the lab, for fine-tuning innumerous drafts, and for keeping the group running smoothly.

This work was enabled by the joint effort of an amazing group of people. Chris Ballance, David Nadlinger, Laurent Stephenson, Bethan Nichol, Joseph Goodwin and Shuoming An had built a large fraction of the apparatus and control system before I joined. Dougal Main transformed our qubit coherence times and installed the Raman laser system. Gabriel Araneda and Raghavendra Srinivas have become an instrumental part of the team; their support ranged from plumbing water chiller pipes to fixing lasers. Ayush Agrawal contributed to simulations of our mixed-species gate error budget and Ellis Ainley built the Raman AOM breadboard. Elham Kashefi and Dominik Leichtle developed the theory behind our experiments and Atul Mantri guided me through the relevant literature.

Thanks to David Nadlinger for numerous brain-storming sessions, late nights in the lab, for keeping our software up to date, for maintaining the 674-nm laser, co-designing electronics, merging pull requests, and solving many interesting problems together. Thanks to Dougal for making every minute of this journey fun and enjoyable, all your hard work, and for sharing the excitement that taught us not to judge a scan by its first three points. Many thanks to Beth for repeatedly assembling our vacuum systems, aligning the high-NA lenses, and for spreading the positivity that carried me through many difficult days. Thanks to Gabriel for always looking out for me, getting things done in the lab, and for bringing the group closer together. Thank you Raghu, for helping me debug gate sequences and for reliably providing constructive feedback on abstracts and paper drafts. Thank you Chris for teaching me the fundamentals of ion trapping, sharing your enthusiasm for quantum technologies with me, and providing perspective, directions, and career advice whenever needed. Thanks to blade runners Oana and Sebastian for being such amazing fellow lab-one inmates and looking after our shared equipment. I highly appreciate everyone who kindly agreed to proof-read versions of various abstracts, manuscripts, and chapters of this thesis.

I am grateful for the stimulating lunch discussions, cinema evenings, cake clubs, birthday celebrations, pub trips, and group retreats, together with my family with a ph. Thanks to Marius Weber for developing SURF, but also for introducing me to a wonderful group of people who became our housemates. I had a lot of fun together with the B0tley B0yz, Andy, Andrew, Marius and John, and Covid refugees Margie and Rand. Thanks to the best travel companions, Kathi, Viki, Moritz, Veronika, Dom, and Emma, for managing to distract me for prolonged periods from this work and recharging me.

Danke an alle Freunde, die mich über die Jahre in Oxford besucht haben und mich trotz der Distanz nicht aus den Augen verloren haben. Danke, Kathi, für deine Geduld mit deinem Langzeitstudenten, deine unermüdliche Unterstützung und Verständnis für meine Leidenschaft, und für die wunderschöne gemeinsame Zeit in Oxford, London, und Wien. Danke an meine Eltern, Gabi und Michael, die mein Interesse für Technik früh entdeckt und gefördert haben, und mir das Physikstudium ermöglicht haben. Danke an Hanni, Heidi, Michi, Willi, Opa Peter, Oma Lisl, Opa Poldi, Maria, Felix, Luki, Xandi, und Danny, die beste Großfamilie, die man sich wünschen kann, auf die ich immer zählen kann. Meine Familie hat mir viel Arbeit abgenommen, damit ich mich auf meine akademischen Projekte fokussieren kann, wofür ich ihnen unendlich dankbar bin – durch ihren Einsatz und ihre Unterstützung haben sie großteilig zu diesem Erfolg beigetragen.

Abstract

Verifiable blind quantum computing enables a client to delegate computations while hiding their data and even the underlying algorithm from the cloud server. Because quantum information cannot be copied and measurements irreversibly change the quantum state, information stored in these systems can be protected with unconditional security, and incorrect operation of the server or attempted attacks can be detected. In this thesis, we report the first hybrid matter-photon implementation of verifiable blind quantum computing.

Our experimental platform consists of a trapped-ion quantum server and a client-side photonic detection system networked via a fibre-optic quantum link. We integrate a long-lived memory qubit into a trapped-ion quantum network node to enable simultaneous storage and manipulation of multiple entangled states across a network of quantum processors. We perform laser-based quantum gates between a $^{88}Sr^+$ and a $^{43}Ca^+$ ion with 0.961(2) fidelity, and between two $^{43}Ca^+$ ions with 0.985(5) fidelity. Ion-photon entanglement generated with a network qubit in $^{88}Sr^+$ is transferred to $^{43}Ca^+$ with 0.977(7) fidelity using error detection. We show that the fidelity of ion-photon entanglement decays ~ 70 times slower on a memory qubit in $^{43}Ca^+$ than on the network qubit. Using dynamical decoupling, ion transport and sympathetic cooling, we further extend the storage duration; we measure an ion-photon entanglement fidelity of 0.81(4) after 10 s. We demonstrate that subsequent ion-photon entanglement generation with $^{88}Sr^+$ has no effect on the fidelity of ion-photon entanglement previously transferred to the memory. Our apparatus enables deterministic feedforward control (as required for measurement-based blind quantum computing), supporting fast switching of polarisation measurement basis by the client and deterministic logic gates between the network and the memory qubit in the server. We perform blind computations on linear cluster states and measure error rates surpassing a recently-discovered threshold for secure and robust verification. We quantify the privacy of this system at $\lesssim 0.03$ leaked classical bits per qubit in the cluster state. These results show a clear path to scalable and verified universal quantum computing in the cloud, which has wide-ranging applications in areas where confidentiality and verifiability are paramount, such as healthcare, finance, and defence.

Contents

List of Figures

1 Introduction

Contents

The topic of this thesis falls into the wider category of experimental quantum physics. We trap individual atomic ions inside of an ultra-high vacuum (UHV) chamber using electric fields, we cool them and manipulate their electronic and motional state using lasers. We generate single photons that are entangled with the spin of an ion to demonstrate world-first proof-of-principle quantum technologies. The methods, devices, and the mathematical framework that enable these applications today are a result of quantum physics research conducted over a century-long period, which I briefly summarise here. I then introduce the concept of secure cloud computing in both the classical and the quantum case before motivating the use of trapped ions for this purpose.

In 1874, Max Planck was advised by his teacher against a career in physics, as "almost everything is already discovered, and all that remains is to fill a few holes" [Pla44]. Little did they know about the wealth of discoveries that followed from

there. Among the remaining "little holes" were explanations for the absence of ether winds [MM87] and for the avoided ultraviolet catastrophe [Ehr11]. Answering these two questions turned out to be a much more involved undertaking – the theories of relativity and quantum mechanics have been revolutionising physics since.

Incidentally, it was Planck himself who discovered in 1900 that the problem of the ultraviolet catastrophe could be solved by quantising electromagnetic energy into units (quanta) of $\hbar\omega$ each, where $2\pi\hbar \approx 6.626 \times 10^{-34}\,\mathrm{J\,Hz^{-1}}$ is the Planck constant and ω the angular frequency of the radiation [Pla00]. The quantisation of this energy into photons flew in the face of the prevailing notion that light was a wave; the wave-particle duality we take for granted now was much more revolutionary then. Three years later, Albert Einstein used a similar notion to explain the photoelectric effect [Ein05], for which he received the Nobel Prize in Physics.

Around the same time, new experimental evidence was found by Geiger and Marsden, who measured the reflection of α particles from a gold foil [GMR09]. They discovered that the positive charge of an atom and almost their entire mass is concentrated in a small volume, the nucleus. After this observation, Niels Bohr devised an atomic theory that reproduced the gross structure of absorption and emission spectra of atoms [Boh13].

The years of 1924 and 1925 saw a period of exceptional productivity in the area of quantum physics: de Broglie consolidated the matter-wave duality, and Heisenberg, Pascal, Jordan and Schrödinger developed the foundation of quantum mechanics in its current form. Dirac combined these ideas with relativity in 1928, predicting the existence of the electron spin from quantum electrodynamics. With major contributions by von Neumann, Pauli, Hartree and Fock, the quantum theory of atoms and photons matured and started the first quantum revolution in the 1950s to 1960s, with semiconductors and lasers leading the way to modern-day technology. Photons are no longer theoretical constructs; single photons underpin many technological innovations, such as solar cells and smartphone cameras. Further groundbreaking applications of quantum physics include the global positioning system (GPS), which relies on atomic clocks to measure distances, and magnetic

resonance imaging (MRI), where the quantum properties of nuclear spins are put to good use for medical diagnosis.

Quantum physics enabled the development of transistors and other semiconductor elements that process digital signals in every modern computer. However, quantum mechanics imposes limits on what can be achieved with classical signals. The miniaturisation approach that has innovated the semiconductor industry for decades is inherently limited by pure quantum effects, such as tunnelling, at the scale where a logic element reaches the size of an atom. The continual improvement of computing hardware that has seen, for example, an exponential increase of component density over the years [Moo98], is already slowing down. Nevertheless, thanks to a series of technological advances, certain quantum mechanical systems can now be controlled at the single-quantum level [Lei+03; SWM10; Wen17; Mar+18]. Rather than hampering technological progress, these systems have the potential to offer *quantum advantage* – a prospect which emerges from the more general structure of quantum information. In 1981, Richard Feynman acknowledged the potential of controllable quantum systems: "Nature isn't classical, dammit, and if you want to make a simulation of nature you'd better make it quantum mechanical, and by golly it's a wonderful problem, because it doesn't look so easy" [Fey82].

Qubits are two-level systems like bits, but their state is described by wavefunctions that are governed by the laws of quantum mechanics. While all classical circuits can be emulated efficiently using the Turing machine model, quantum information has a fundamentally richer structure: superposition and entanglement are among the distinct features arising from it, unhinging an entirely different computing paradigm [Deu85]. Quantum algorithms seek to harness superposition and entanglement to perform calculations that are believed to be intractable with classical machines, an example of which is prime factoring [Sho99; Lan+07]. Armed with these techniques, quantum computers are poised to outperform the world's most powerful supercomputers, with applications ranging from drug discovery to logistics [Blu+22; Ban+20; Lan+10; Fed+22].

Quantum information research has also led to noteworthy applications in cryptography. The laws of quantum mechanics can provide much stronger security than conventional approaches that make assumptions about the computational capabilities of an adversary. Protocols exist for information-theoretically secure ('unbreakable') key distribution [BB84; Eke91], digital signatures [GC01], anonymous communication [Bra+07], private database queries [GLM08], and random number generation [Pir+10].

Quantum computers and quantum cryptography are cornerstones of the 'quantum internet', which has the potential to revolutionise the way we distribute and process information [Kim08; Ben+93; Huc+15; Kóm+14; Mat+08; Hen+15]. Such networks are likely to provide similar services as their classical counterpart, but with enriched features, enhanced performance, and better security. Among these services, cloud computing stands out due to the flexibility, scalability, and security that it can provide to users.

1.1 Secure cloud computing

Cloud computing enables users to tap into the resources of powerful servers from anywhere in the world. This centralised architecture (see Figure 1.1) has been

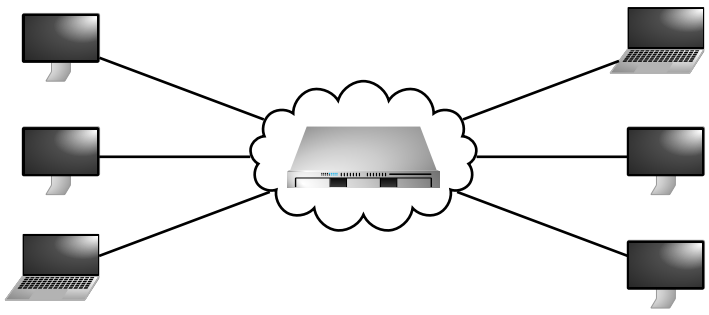

Figure 1.1: Cloud computing in a centralised architecture where users can delegate tasks to a server.

extremely successful, but it has challenged cryptographers to develop encryption schemes that could protect confidential data from the server and eavesdroppers on the way. An example where privacy is of paramount importance is healthcare; the

multi-billion-dollar healthcare cloud computing industry is continually threatened by the security risk associated with retaining private data in the cloud [Hea].

Blind classical computing. To address the issue of data privacy in cloud computing applications, clients are required to store the plaintext exclusively on private or trusted storage. To process this data securely with the help of an untrusted cloud server, the plaintext must be converted into cyphertext by application of an encryption scheme before it enters the public domain (e.g. the internet). Cryptographers distinguish between perfect, information-theoretic security, and computational security. In the first case the security is guaranteed even against arbitrarily powerful adversaries, whereas in the latter case, the security relies on assumptions of computational hardness of certain mathematical problems. For communication for example, the one-time-pad encryption is information-theoretically secure, whereas the Rivest–Shamir–Adleman (RSA) cryptosystem derives its security from the hardness of prime factorisation, which can be undermined with sufficient computational power.

For secure cloud computing, codemakers came up with homomorphic encryption [RAD+78], which proceeds in four steps: key generation, encryption and subsequent transfer of the plaintext to the server, evaluation of the cyphertext, and decryption of the result by the client using the private key. In 2009, Gentry [Gen09] presented the first fully homomorphic encryption (FHE) scheme, which enabled the use of arbitrary algorithms to process the cyphertext – a significant step forward at the time, as all predating homomorphic encryption schemes had been limited to a subset of operations, such as addition-only. The security of Gentry's approach is only computational; it is conjectured that efficient information-theoretically-secure FHE is possible, but, to the best of my knowledge, only approximate perfect security [HP13] has been proven.

Besides data privacy, cryptographers are working on incorporating circuit privacy into existing FHE schemes [DD22]. These approaches aim to reduce the information contained in the processed cyphertext, i.e. the data returned from the server to the

client, about the algorithm that was used by the server to process the cyphertext. Circuit privacy does not aim to hide the algorithm from the server; it only refers to information that could be inferred by eavesdroppers from analysing the transmitted data. Therefore, circuit privacy is not as relevant for the client as it is for a server providing computations with proprietary algorithms.

Blind quantum computing. As quantum processors control delicate quantum states, they are necessarily complex and physical access to high-performance systems is limited. Cloud-based approaches are likely to be the only working model in the near term and beyond; many users already perform computations on commercially available devices for state-of-the-art research [Sar+19; ALP20; Pro+22; Ama+22; Kir+22].

Delegating quantum computations to a server carries the same privacy and security concerns that bedevil classical cloud computing. While the possibility of leveraging quantum mechanics to establish an efficient FHE scheme with circuit privacy has been ruled out [YPF14], the slightly different approach of universal blind quantum computing (BQC) [Chi05; BFK09] presents an alternative that is even stronger. The main difference is that BQC is an interactive protocol, whereas FHE schemes execute the circuit without involvement of the client. The advantage of this is that interactive protocols are more versatile, and, as such, the approach taken for BQC can go beyond circuit privacy in the conventional sense. First, the same phenomena that enable quantum computing can leave the server 'blind' in a way that conceals the client's input, output, and algorithm [BFK09; FK17; GKK19]; because quantum information cannot be copied and measurements irreversibly change the quantum state, information stored in these systems can be protected with information-theoretic security. Secondly, BQC enables resource-efficient verification, which means that incorrect operation of the server or attempted attacks can be detected.

Verification has been a major motivation for BQC: "If a quantum experiment solves a problem which is proven to be intractable for classical computers, how can one verify the outcome of the experiment?" [GKK19]. In the context of verification, the client and server are referred to as verifier and prover, respectively. The task of the prover is to convince the verifier that it is indeed solving the problem correctly. Most verification schemes make use of the prover's lack of knowledge of the quantum circuit (blindness), which enables the verifier to delegate a classically tractable problem and check the result against the predicted solution. Even with unbounded computational power, a blind prover cannot distinguish the actual computation from these tests, and must therefore behave honestly at all times to pass the verifier's security bar. Protocols for this proceed in multiple rounds (polynomial in the size of the input to the problem) and are classified as interactive-proof systems. At the end of a delegated computation, the verifier should accept a correct solution with overwhelming probability, and reject otherwise [FK17; Bro18]. A comprehensive review of existing verification schemes can be found in Reference [GKK19].

Interactive-proof systems are designed to reduce the resource requirements for the verifier to bounded-error probabilistic polynomial time (BPP) and for the prover to bounded-error quantum polynomial time (BQP), which encompass the problems that can be solved efficiently (in polynomial time) on a classical and a quantum computer, respectively. Existing verification schemes can be classified into multi-prover protocols and single-prover protocols; in the former case, a purely classical verifier is sufficient if the provers are not allowed to communicate (which is hard to ensure in practice), whereas in the latter case, the verifier needs a constant-size quantum processor (and a quantum interface to exchange quantum information with the prover).[1] For a single-prover protocol, the verifier needs to be able to perform single-qubit measurements (*receive-and-measure*) or prepare

[1]Integrating constant-size quantum resources into the verifier formally does not change its complexity class, as the number of qubits necessary at any one time is independent of the problem size, and simulating a constant-size quantum computer can be done in constant time [GKK19]. This is just a formality, as the client's quantum capabilities must be real due to the interactive-proof system requiring a working quantum interface connecting it to the prover.

single-qubit states (*prepare-and-send*), in order to perform verified BQC using an interactive-proof system.

Previous experiments were based on purely photonic systems with up to four qubits [Bar+12; Bar+13; Gre+16]. In the first demonstration of BQC [Bar+12], the client generated a four-qubit entangled 'cluster state' (see Section 6.1.1) and sent the qubits to the server to be measured. The shortcomings of this implementation go beyond the fact that the client operated a universal photonic quantum processor and the server performed the trivial task of detecting photons. Unavoidable photon loss, either due to limited photon detection efficiencies or absorption on the way to the client, resulted in information leaks. In subsequent experiments, the same group of researchers verified a Clauser-Horne-Shimony-Holt (CHSH) inequality test [Bar+13] and implemented an improved version of photonic blind quantum computing that required the client to perform only measurements. In this approach, the resources provided (publicly) by the server are general while the measurements are performed locally by the client, which guarantees perfect privacy of the client's data and algorithm [Gre+16]. However, all existing photonic implementations necessitate post-selection of outcomes because of their inability to adapt the measurement basis of photons in real time to the measurement outcomes of previous photons from the same cluster state. Moreover, a single lost photon voids the entire computation. Solutions to these problems exist in theory in the form of fault-tolerant encodings, but they come with substantial overheads, which seem challenging to overcome in the near term [Li+15].

It is therefore desirable to establish an interface between photons – the 'flying' quantum information carrier [Bli+04] – and stationary memory qubits, which enable deterministic processing of quantum information with high fidelity. The ability to retain quantum information on the server then enables the client to perform adaptive mid-circuit adjustments in order to execute the target computation deterministically and securely, remedying the problem of photon losses in the link by

heralding, i.e., allowing for repetition without sacrificing the progress of the entire computation. Combining two completely different platforms at the single-quantum level is technically challenging [Pfa+14; Huc+15]; so far, quantum network nodes with a photonic interface and integrated memory qubits have been realised with solid state systems [Kal+17; Sta+22] and trapped ions [Inl+17].

1.2 Trapped ions and photons

Among quantum technological platforms, trapped ions stand out due to their exceptionally long coherence times [Wan+21] and the ability to initialise, manipulate, entangle, and read them out with high fidelity [Chr+20; Har+14; Sri+21; Gae+16; Cla+21]. Moreover, trapped ions readily interact with optical fields, providing a natural interface between their electronic state and photons. While trapped ion systems have demonstrated state-of-the-art quantum logic and quantum networking interfaces independently, integrating these aspects within one quantum network node is challenging because an ion species suitable for quantum communication does not necessarily also provide a good memory qubit with sufficient isolation from network activity. One possibility is to use a single ion species and shuttle ions individually into dedicated interaction zones using electric fields, thereby establishing the isolation requirement by spatial separation. However, this approach is slow ($\sim 1\,\mathrm{ms}$ per shuttling operation) and prone to excess heating of the ion's motion, which adversely affects the performance of subsequent quantum logic operations.

Here we use two different atomic species, $^{88}\mathrm{Sr}^+$ for the network interface and $^{43}\mathrm{Ca}^+$ for the quantum memory, to the effect that network activity and logic operations are well isolated from each other in the frequency domain. This minimises crosstalk between the species without requiring spatial separation or individually addressing laser beams. In addition, ions of the networking species can also be employed for sympathetic cooling, which enables continued operation in the presence of heating, and for mid-circuit measurements [Inl+17; Neg+18].

Of course, controlling a second atomic species inevitably increases the experimental complexity of the system. Atomic species such as $^{133}\mathrm{Ba}^+$ or $^{171}\mathrm{Yb}^+$ [Chr+20;

Yan+22] have been proposed to circumvent this issue by utilising the *OMG* (optical-frequency, metastable-state, and ground-state) architecture [All+21], where qubits encoded in long-lived metastable states serve as an effective second species; however, the development of the required experimental techniques is still ongoing. Nonetheless, trapping and controlling mixed-species ion crystals is a well-established technique, which has become a key component of highly advanced ion trap systems [Mos+23].

In this thesis I present the first implementation of coherent transfer of information from a communication photon onto a memory qubit within a mixed-species quantum network node [Drm+23]. This is an important milestone on the path towards building practically relevant quantum networks because it allows for the processing and storage of network information with high fidelity without degradation due to network activity.

1.3 Thesis outline

Chapter 2 reviews theoretical aspects of atomic/quantum physics that are central to the experimental work presented in this thesis:

- Spontaneous emission from the $P_{1/2}$ transition in $^{88}Sr^{+}$ is treated theoretically, as this process is key to generating ion-photon entanglement and remote steering (Section 2.1).
- The structures of motional modes of single- and mixed-species crystals are derived using classical equations of motion (Section 2.2). A good understanding of the motional mode structure is a prerequisite for performing quantum gates with low cross-coupling and with high fidelity.
- A framework for atom-laser interactions (Section 2.3) is presented which discusses techniques for coherent quantum state manipulation of hyperfine qubits, optical qubits, and motional modes.
- A short analysis of the indispensable Ramsey method is presented in the context of noise filtering by dynamical decoupling (Section 2.4).
- Randomised benchmarking is introduced in Section 2.5.

Chapter 3 summarises relevant standard techniques of ion trapping, such as loading, cooling, state preparation and readout. Moreover, I discuss aspects of the experimental setup that have not been covered in the D. Phil. theses of previous students who worked on the same setup [Ste19; Nad22; Nic22], but are relevant to the experiments presented in this thesis.

- Section 3.2 discusses the generation of static electrode signals for trapping, shuttling, splitting and merging, with a focus on the static components that define the properties of a single well. The decomposition into components is constructive and enables fast scanning of certain trap parameters.
- The client-side photonic detection system that is used for BQC experiments (see Chapter 6) is described in Section 3.3. This section focusses on practical aspects of the design and assembly process, attempting to provide step-by-step instructions for the key routines involved in characterising the device.
- The general architecture of the experimental control system is explained in the first part of Section 3.4. I then describe a collection of extensions to this system that I developed or modified over the course of my studies.

Chapter 4 presents quantum operations on qubits encoded in $^{88}Sr^{+}$ and $^{43}Ca^{+}$, characterisation experiments thereof, and a discussion of error sources.

I present the first main result of this thesis, the transfer of ion-photon entanglement from the $^{88}Sr^{+}$ network qubit to a memory qubit in $^{43}Ca^{+}$, in Chapter 5, which is published in Reference [Drm+23].

The second main result of this thesis, the first demonstration of deterministic and verifiable BQC (Chapter 6), builds on the integration of mixed-species quantum logic into a quantum network node, as described in Chapter 5, and is published in Reference [Drm+24]. Here, the quantum network node (server) is connected to the fast polarisation analyser (client) via the photonic fibre link.

Lastly, an outlook is presented in Chapter 7, which encompasses ideas, both vague and concrete, which are extensions of this work. Besides the undeniable prospect of more complex client-server protocols, our twin trap apparatus' main purpose – the generation of high-fidelity remote entanglement at high rates – will be the prevalent resource for implementing those ideas.

2

Theory

Contents

2.1 Dipole emission into free space

The first pillar of our experiments is the generation of single photons that are entangled with an ion. Here we derive expressions for the dipole emission from a stationary[1] atom into free space. We employ a quantum description of the process [BKD08], starting from the Hamiltonian,

$$\hat{H} = \underbrace{\frac{\hat{\boldsymbol{p}}^2}{2m} - \frac{1}{4\pi\epsilon_0}\frac{Ze^2}{\hat{r}}}_{H_{\text{electron}}} + \underbrace{\sum_{\boldsymbol{k}}\sum_{u=1}^{2}\hbar\omega\left(\hat{a}^\dagger_{\boldsymbol{k},u}\hat{a}_{\boldsymbol{k},u} + \frac{1}{2}\right)}_{H_{\text{field}}} + \underbrace{\mathrm{i}\frac{\hbar e}{m}\hat{\boldsymbol{A}}\cdot\hat{\boldsymbol{p}}}_{H_{\text{int}}} ,$$

of an electron with mass m bound to a charge Z in the presence of and interacting with an electromagnetic field,

$$\hat{\boldsymbol{A}} = A_0\sum_{\boldsymbol{k}}\sum_{u=1}^{2}\left(\hat{a}_{\boldsymbol{k},u}\boldsymbol{\epsilon}_{\boldsymbol{k},u}\,\mathrm{e}^{\mathrm{i}(\boldsymbol{k}\cdot\boldsymbol{r}-\omega_{\boldsymbol{k}}t)} + \hat{a}^\dagger_{\boldsymbol{k},u}\boldsymbol{\epsilon}^*_{\boldsymbol{k},u}\,\mathrm{e}^{-\mathrm{i}(\boldsymbol{k}\cdot\boldsymbol{r}-\omega_{\boldsymbol{k}}t)}\right) .$$

We use the bosonic commutation relations $[\hat{a}_{\boldsymbol{k},u}, \hat{a}^\dagger_{\boldsymbol{k'},u'}] = \delta_{u,u'}\delta(\boldsymbol{k}-\boldsymbol{k'})$, $[\hat{a}_{\boldsymbol{k},u}, \hat{a}_{\boldsymbol{k'},u'}] = [\hat{a}^\dagger_{\boldsymbol{k},u}, \hat{a}^\dagger_{\boldsymbol{k'},u'}] = 0$ and the Coulomb gauge condition implying $\boldsymbol{k}\cdot\boldsymbol{\epsilon}_{\boldsymbol{k},u} = 0$, where u is a binary variable identifying two orthogonal polarisations. The transition probability amplitude from $|i\rangle = |e, J_e, m_e\rangle \otimes |0\rangle$ to $|f\rangle = |g, J_g, m_g\rangle \otimes \hat{a}^\dagger_{\boldsymbol{K},U}|0\rangle$ in first-order perturbation theory is proportional to

$$\begin{aligned}\langle f|\, H_{\text{int}}\,|i\rangle &\propto \langle f|\,\hat{\boldsymbol{A}}\cdot\hat{\boldsymbol{p}}\,|i\rangle \\ &= \langle g, J_g, m_g|\,\boldsymbol{\epsilon}^*_{\boldsymbol{K},U}\cdot\hat{\boldsymbol{p}}\,\mathrm{e}^{-\mathrm{i}(\boldsymbol{K}\cdot\boldsymbol{r}-\omega_{\boldsymbol{K}}t)}\,|e, J_e, m_e\rangle \ . \end{aligned} \tag{2.1}$$

In the next step, we apply the dipole approximation $\mathrm{e}^{-\mathrm{i}\boldsymbol{K}\cdot\boldsymbol{r}} \approx 1$, assuming that the wavelength of the electromagnetic radiation is considerably larger than the extent of the ion. From $\frac{\mathrm{d}}{\mathrm{d}t}\hat{\boldsymbol{r}}_{\mathrm{H}} = \frac{\hat{\boldsymbol{p}}_{\mathrm{H}}}{m} = \frac{\mathrm{i}}{\hbar}[H, \hat{\boldsymbol{r}}_{\mathrm{H}}]$ in the Heisenberg picture it follows that $\langle f|_{\mathrm{H}}\,\hat{\boldsymbol{p}}_{\mathrm{H}}\,|i\rangle_{\mathrm{H}} = \frac{m\mathrm{i}}{\hbar}\,\langle f|_{\mathrm{H}}\,[H, \hat{\boldsymbol{r}}_{\mathrm{H}}]\,|i\rangle_{\mathrm{H}} = m\mathrm{i}(\omega_f - \omega_i)\,\langle f|_{\mathrm{H}}\,\hat{\boldsymbol{r}}_{\mathrm{H}}\,|i\rangle_{\mathrm{H}}$. Therefore, $\langle f|\,\hat{\boldsymbol{p}}\,|i\rangle \propto \langle f|\,\hat{\boldsymbol{r}}\,|i\rangle$. Returning to the transition probability, we may now write

$$\langle f|\, H_{\text{int}}\,|i\rangle \propto \langle g, J_g, m_g|\,\boldsymbol{\epsilon}^*_{\boldsymbol{K},U}\cdot\hat{\boldsymbol{d}}\,|e, J_e, m_e\rangle \ , \tag{2.2}$$

where $\hat{\boldsymbol{d}} = -e\hat{\boldsymbol{r}}$ is the electric dipole moment operator.

[1] This implies that we ignore the centre-of-mass motion of the atom here.

To highlight more of the structure contained in Equation (2.2), we apply the Wigner-Eckart theorem,

$$\langle \alpha, J, M_J | \, T_q^{(\kappa)} \, | \alpha, J', M_J' \rangle = \underbrace{\langle \alpha, J \| T^{(\kappa)} \| \alpha, J' \rangle}_{\text{reduced matrix element}} \langle J', M_J', \kappa, q | J, M_J \rangle \ ,$$

which holds for spherical tensor operators[2] $T_q^{(\kappa)}$, where κ is the rank (for example $\kappa = 0$ for scalar operators, $\kappa = 1$ for vector operators), $q = -\kappa, \ldots, 0, \ldots, \kappa$ and α stands for all other quantum numbers. It allows us to separate the dependency of the matrix element on the magnetic quantum numbers, as the reduced matrix element cancels in all relative calculations, such as the branching ratio. To be able to apply the Wigner-Eckart theorem approximately[3] to Equation (2.2), we expand (subscripts indicate component index) $\hat{\boldsymbol{d}} = \sum_{q=-1}^{1} \hat{d}_q \boldsymbol{e}_q^*$ and $\boldsymbol{\epsilon}^* = \sum_{p=-1}^{1} \epsilon_p^* \boldsymbol{e}_p$ in the spherical basis,

$$\begin{aligned} \boldsymbol{e}_{+1} &= -\tfrac{1}{\sqrt{2}}(\boldsymbol{e}_x + \mathrm{i}\boldsymbol{e}_y) \ , \\ \boldsymbol{e}_0 &= \boldsymbol{e}_z \ , \\ \boldsymbol{e}_{-1} &= \tfrac{1}{\sqrt{2}}(\boldsymbol{e}_x - \mathrm{i}\boldsymbol{e}_y) \ , \end{aligned} \tag{2.3}$$

for which $\boldsymbol{e}_q \cdot \boldsymbol{e}_p^* = \delta_{q,p}$. Note that with these definitions, σ^+-polarisation is described by $\boldsymbol{e}_1$, σ^--polarisation by $\boldsymbol{e}_{-1}$ and π-polarisation by $\boldsymbol{e}_0$. The scalar product of $\boldsymbol{\epsilon}^*$ and $\hat{\boldsymbol{d}}$ in terms of spherical components is

$$\boldsymbol{\epsilon}^* \cdot \hat{\boldsymbol{d}} = \sum_{q=-1}^{1} \sum_{p=-1}^{1} \epsilon_p^* \hat{d}_q \ \boldsymbol{e}_p \cdot \boldsymbol{e}_q^* = \sum_{q=-1}^{1} \epsilon_q^* \hat{d}_q$$

and the interaction matrix element reads (re-introducing subscripts)

$$\begin{aligned} \langle f | H_{\mathrm{int}} | i \rangle &\propto \sum_{q=-1}^{1} (\epsilon_{\boldsymbol{K},U})_q^* \, \langle g, J_g, m_g | \hat{d}_q | e, J_e, m_e \rangle \\ &= \langle g, J_g \| \hat{d}^{(1)} \| e, J_e \rangle \sum_{q=-1}^{1} (\epsilon_{\boldsymbol{K},U})_q^* \, \langle J_e, m_e, 1, q | J_g, m_g \rangle \ . \end{aligned}$$

The factors $\langle g, J_g \| \hat{d}^{(1)} \| e, J_e \rangle$ are called reduced matrix elements and the coefficients $\langle J_e, m_e, 1, q | J_g, m_g \rangle$ are the so-called Clebsch-Gordan coefficients, which determine the relative strength between decay branches to different magnetic sublevels and hence give rise to dipole selection rules. For a quantitative analysis of the transition

[2] A spherical tensor operator is defined as a tensor operator which, upon rotation, can be written as a linear combination over its elements: $U^\dagger T_q^{(\kappa)} U = \sum_{q'} D_{q,q'}^{(\kappa)} T_{q'}^{(\kappa)}$

[3] The radial wavefunctions of g and e are not identical in general.

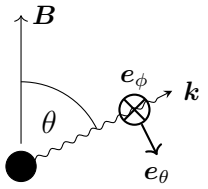

Figure 2.1: Geometry of spontaneous emission from a single atom.

amplitude in different directions, we use spherical coordinates,

$$\begin{aligned}
\boldsymbol{e}_r &= \sin\theta\cos\phi\boldsymbol{e}_x + \sin\theta\sin\phi\boldsymbol{e}_y + \cos\theta\boldsymbol{e}_z \\
&= -\tfrac{1}{\sqrt{2}}\sin\theta\exp(\mathrm{i}\phi)\boldsymbol{e}^*_{-1} + \cos\theta\boldsymbol{e}^*_0 + \tfrac{1}{\sqrt{2}}\sin\theta\exp(-\mathrm{i}\phi)\boldsymbol{e}^*_{+1} \ , \\
\boldsymbol{e}_\theta &= \cos\theta\cos\phi\boldsymbol{e}_x + \cos\theta\sin\phi\boldsymbol{e}_y - \sin\theta\boldsymbol{e}_z \\
&= \tfrac{1}{\sqrt{2}}\cos\theta\exp(-\mathrm{i}\phi)\boldsymbol{e}^*_{-1} - \sin\theta\boldsymbol{e}^*_0 - \tfrac{1}{\sqrt{2}}\cos\theta\exp(\mathrm{i}\phi)\boldsymbol{e}^*_{+1} \ , \\
\boldsymbol{e}_\phi &= -\sin\phi\boldsymbol{e}_x + \cos\phi\boldsymbol{e}_y \\
&= -\tfrac{1}{\sqrt{2}}\mathrm{i}\exp(-\mathrm{i}\phi)\boldsymbol{e}^*_{-1} - \tfrac{1}{\sqrt{2}}\mathrm{i}\exp(\mathrm{i}\phi)\boldsymbol{e}^*_{+1} \ .
\end{aligned}$$

With $\boldsymbol{K} = |\boldsymbol{K}|\boldsymbol{e}_r$, a natural choice is $\boldsymbol{\epsilon}_{\boldsymbol{K},1} = \boldsymbol{e}_\theta$ and $\boldsymbol{\epsilon}_{\boldsymbol{K},2} = \boldsymbol{e}_\phi$, which automatically fulfils the transversality constraint (see Figure 2.1). Using the amplitudes shown

Transition	q	Amplitude $(\epsilon_{\boldsymbol{K},1})^*_q$	$(\epsilon_{\boldsymbol{K},2})^*_q$	Clebsch-Gordan coefficient
σ^-	$+1$	$-\frac{1}{\sqrt{2}}\cos\theta\exp(-\mathrm{i}\phi)$	$\frac{1}{\sqrt{2}}\mathrm{i}\exp(-\mathrm{i}\phi)$	$\langle J_e, m_e, 1, +1 \vert J_g, m_g\rangle$
π	0	$-\sin\theta$	0	$\langle J_e, m_e, 1, 0 \vert J_g, m_g\rangle$
σ^+	-1	$\frac{1}{\sqrt{2}}\cos\theta\exp(\mathrm{i}\phi)$	$\frac{1}{\sqrt{2}}\mathrm{i}\exp(\mathrm{i}\phi)$	$\langle J_e, m_e, 1, -1 \vert J_g, m_g\rangle$

Table 2.1: Transition probability amplitudes and coefficients for spontaneous emission of light polarised along the orthogonal directions $\boldsymbol{\epsilon}_{\boldsymbol{K},1} = \boldsymbol{e}_\theta$ and $\boldsymbol{\epsilon}_{\boldsymbol{K},2} = \boldsymbol{e}_\phi$, which are perpendicular to the wave vector $\boldsymbol{K} = \mathrm{abs}(\boldsymbol{K})\boldsymbol{e}_r$.

in Table 2.1, we define the (unnormalised) states of polarised fields emitted from a dipole:

$$\begin{aligned}
|\boldsymbol{A}_\pi\rangle &= -\sin\theta\,\hat{a}^\dagger_{\boldsymbol{K},1}\,|0\rangle \ , \\
|\boldsymbol{A}_{\sigma^\pm}\rangle &= \tfrac{1}{\sqrt{2}}\,\mathrm{e}^{\pm\mathrm{i}\phi}\left(\pm\cos\theta\,\hat{a}^\dagger_{\boldsymbol{K},1} + \mathrm{i}\,\hat{a}^\dagger_{\boldsymbol{K},2}\right)|0\rangle \ .
\end{aligned}$$

2.1.1 Ion-photon state

In our apparatus, we trap $^{88}\mathrm{Sr}^+$ ions for the purpose of generating ion-photon entanglement by fast excitation and spontaneous emission on the $S_{1/2} \leftrightarrow P_{1/2}$

Dipole transition (see Figure 2.2). The ground state manifold of $^{88}Sr^{+}$ contains two magnetic sublevels, $|S_{1/2},\, m_J{=}-\frac{1}{2}\rangle = |{\downarrow_{\mathrm{N}}}\rangle$ and $|S_{1/2},\, m_J{=}\frac{1}{2}\rangle = |{\uparrow_{\mathrm{N}}}\rangle$, which are split by the Zeeman effect by $\hbar\Omega_Z \approx 2\mu_{\mathrm{B}}|\boldsymbol{B}|$, where $\boldsymbol{B}$ is a static magnetic field and $\mu_{\mathrm{B}} \approx 9.274 \times 10^{-24}\,\mathrm{J\,T^{-1}}$ is the Bohr magneton. We refer to this qubit, $\{|{\downarrow_{\mathrm{N}}}\rangle, |{\uparrow_{\mathrm{N}}}\rangle\}$, as the network qubit throughout this thesis (see also Figure 3.2).

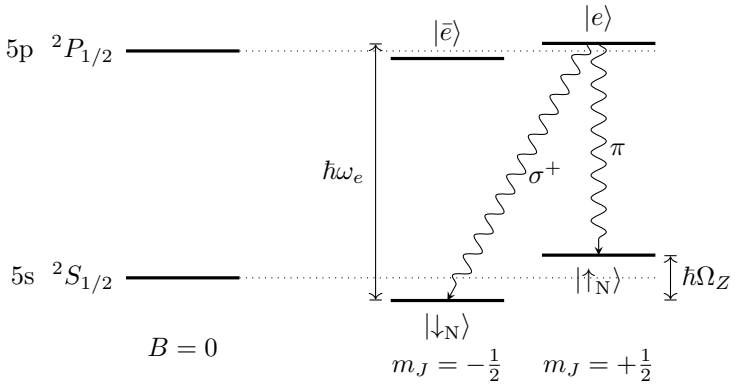

Figure 2.2: Spontaneous emission from the $|P_{1/2},\, m_J{=}\frac{1}{2}\rangle$ level (fine structure splittings to scale).

The ion is prepared in $|{\downarrow_{\mathrm{N}}}\rangle$ by optical pumping (see Section 3.1.5) and then coherently excited with a $\sim 10\,\mathrm{ps}$ laser pulse to the $|e\rangle = |P_{1/2},\, m_J{=}\frac{1}{2}\rangle$ state, from where it decays spontaneously (see Figure 2.2) into either $|{\uparrow_{\mathrm{N}}}\rangle$ via emission of a π-polarised 422 nm photon (linear polarisation in plane spanned by $\boldsymbol{B}$ and $\boldsymbol{K}$), back into $|{\downarrow_{\mathrm{N}}}\rangle$ via emission of a σ^+-polarised 422 nm photon (polarisation depends on the direction of $\boldsymbol{K}$ with respect to $\boldsymbol{B}$)[4], or with $\sim 5\,\%$ probability into the $D_{3/2}$ level via emission of a 1092 nm photon (see level diagram in Figure 3.2). As the picosecond excitation is about three orders of magnitude faster than the spontaneous decay, it can be treated as an instantaneous π-pulse. Since the optical fibre in our photonic interface does not transmit infrared wavelengths, we can ignore the decay into $D_{3/2}$ in the following. Referring to the treatment of spontaneous emission in Section 2.1,

[4] σ^+ photons emitted into the direction of the magnetic field are circularly polarised. However, in the plane perpendicular to the magnetic field, their polarisation is linear. In this case, the angular momentum is contained in the orbital angular momentum of the photon's wavefunction.

the joint state of the ion and the emitted photon is

$$\begin{aligned}|\Psi\rangle &\propto \sum_f \langle f|\hat{H}_{\text{int}}|e\rangle\,|f\rangle \otimes |0\rangle \\ &= |\uparrow_{\text{N}}\rangle \otimes |\boldsymbol{A}_\pi\rangle \left\langle \tfrac{1}{2},\tfrac{1}{2},1,0 \,\middle|\, \tfrac{1}{2},\tfrac{1}{2}\right\rangle + |\downarrow_{\text{N}}\rangle \otimes |\boldsymbol{A}_{\sigma^+}\rangle \left\langle \tfrac{1}{2},\tfrac{1}{2},1,-1 \,\middle|\, \tfrac{1}{2},-\tfrac{1}{2}\right\rangle \\ &= \sqrt{\frac{1}{3}}\,|\uparrow_{\text{N}}\rangle \otimes |\boldsymbol{A}_\pi\rangle + \sqrt{\frac{2}{3}}\,|\downarrow_{\text{N}}\rangle \otimes |\boldsymbol{A}_{\sigma^+}\rangle \ ,\end{aligned}$$

where $|0\rangle$ is the vacuum state and $\langle \frac{1}{2},\frac{1}{2},1,q|\frac{1}{2},q+\frac{1}{2}\rangle$ are the Clebsch-Gordan coefficients for the transitions that change the angular momentum by q. The states $|\boldsymbol{A}_\pi\rangle$ and $|\boldsymbol{A}_{\sigma^+}\rangle$ describe π- and σ^+-polarised isotropic emission from a dipole into vacuum. Restricting ourselves to a geometry in which we collect photons only perpendicular to the magnetic field, i.e. with $\theta = \pi/2$ and $\phi = \pi/2$ (arbitrary), the Clebsch-Gordan coefficients cancel the difference in amplitude and we are, after normalisation, left with

$$\begin{aligned}|\Psi\rangle &= \tfrac{1}{\sqrt{2}}\left(|\uparrow_{\text{N}}\rangle \otimes \hat{a}^\dagger_{K\boldsymbol{e}_y,\boldsymbol{e}_z}\,|0\rangle + |\downarrow_{\text{N}}\rangle \otimes \hat{a}^\dagger_{K\boldsymbol{e}_y,\boldsymbol{e}_x}\,|0\rangle\right) \\ &= \tfrac{1}{\sqrt{2}}\left(\,|\downarrow_{\text{N}}\rangle \otimes |H\rangle + |\uparrow_{\text{N}}\rangle \otimes |V\rangle\right) , \end{aligned} \tag{2.4}$$

where $\hat{a}^\dagger_{K\boldsymbol{e}_y,\boldsymbol{e}_x}\,|0\rangle = |H\rangle$ and $\hat{a}^\dagger_{K\boldsymbol{e}_y,\boldsymbol{e}_z}\,|0\rangle = |V\rangle$ are single-photon Fock states in the horizontally and vertically polarised mode, respectively, where vertical lies along the direction of $\boldsymbol{B}$. In an experiment with free-space optics, however, photons will always be collected from within a finite solid angle, e.g. in our setup by an NA = 0.6 objective. Therefore, σ^+-polarised photons collected off-axis will contribute to the vertically polarised field mode, mixing into the π decay channel and, thus, decreasing the fidelity of ion-photon entanglement. This detrimental effect can be avoided by filtering the emission through a single-mode optical fibre, which preserves maximal entanglement for arbitrary numerical apertures at the cost of increased photon loss [Ste+20]. Detailed calculations involving the photon collection geometry and ion-photon entanglement generation can be found in Reference [Nad22].

Equation (2.4) presumes the definiteness of the spontaneous decay by excluding the excited state amplitude.[5] For a description of our experiments, this presumption is justified, as the photon detection heralds the occurrence of spontaneous decay and triggers any subsequent experimental sequence (cases where no photon is detected are simply ignored). The only remaining practical question concerns the phase relation between the states – information that is necessary for coherent manipulation of the system – and is addressed in the following sections.

2.1.2 Quantum jumps

So far, we have derived the polarisation-dependent transition probability amplitudes and spatial emission patterns, but neglected the time evolution of the dipole emission process. In the presence of a time- and polarisation-resolving photon detector, the state of the decaying ion is subject to a continuous measurement process on the electromagnetic field, i.e., whether a photon was emitted yet, and if so, with what polarisation. The quantum jump formalism provides a description of the state evolution during the decay process in the presence of these detectors and will prove useful for understanding steering (see Section 2.1.3).

The relaxation operator for many dissipative processes can be written as [MCD93]

$$\mathcal{L}_{\text{relax}}(\hat{\rho}) = -\frac{1}{2}\sum_q \left(\hat{C}_q^\dagger \hat{C}_q \hat{\rho} + \hat{\rho}\hat{C}_q^\dagger \hat{C}_q\right) + \sum_q \hat{C}_q \hat{\rho} \hat{C}_q^\dagger \ ,$$

where $\hat{C}_q$ are jump operators and $\hat{\rho}$ is the density matrix of the (small) system (as opposed to the reservoir, or bath, which the system is dissipating into). The evolution of the system can then be calculated from

$$\frac{\mathrm{d}}{\mathrm{d}t}\hat{\rho} = \frac{\mathrm{i}}{\hbar}\left[\hat{\rho}, \hat{H}\right] + \mathcal{L}_{\text{relax}}(\hat{\rho}) \ ,$$

[5] Under the assumption that the photon propagates freely and indefinitely, the above description of the ion-photon state (2.4) could be extended by introducing time-resolved photon modes weighted by the probability amplitude at time t after the excitation, which is given by $\sqrt{\Gamma}\mathrm{e}^{-\frac{\Gamma}{2}t}$ in the Wigner-Weisskopf approximation [WW30], where Γ^{-1} is the lifetime of the $P_{1/2}$ level. The length of the photonic wavepacket is therefore on the order of $\frac{c}{\Gamma}$, where c is the speed of light. In our experimental realisation, this length ($\sim 2\,\mathrm{m}$) is comparable to the distance from the atom to the photon detector.

where $\hat{H}$ is the (hermitian) system Hamiltonian. However, this density matrix formalism is not the only way to describe stochastic dissipative processes.

The Monte-Carlo wavefunction (MCWF) method [MCD93] (also known as quantum-jump/trajectories approach) works by evaluating random realisations of the system's wavefunction, $|\psi(t)\rangle$, which form an ensemble, and can be used to calculate any quantity that could also be obtained from $\hat{\rho}$. The evolution of a sample state $|\psi(t)\rangle$ can be simulated numerically by repeating the following two-step procedure at every time step, δt.

1. Evolve $|\psi(t)\rangle$ with the non-hermitian Hamiltonian

$$\hat{H}_{\mathrm{nh}} = \hat{H} - \frac{\mathrm{i}\hbar}{2}\sum_q \hat{C}_q^\dagger \hat{C}_q \ .$$

   The resulting state, $|\tilde{\psi}(t+\delta t)\rangle$ is sub-normalised: $\langle\tilde{\psi}(t+\delta t)|\tilde{\psi}(t+\delta t)\rangle = 1-\delta p$, $\delta p > 0$, due to the diffusive, non-hermitian propagation.

2. Draw a random number $0 \leq \epsilon \leq 1$. If $\epsilon < \delta p$, the wavefunction is subjected to a quantum jump (q randomly chosen according to the branching ratios), to $\hat{C}_q\,|\psi(t)\rangle$, and normalised. Otherwise, no quantum jump occurs and the updated normalised wavefunction is $|\psi(t+\delta t)\rangle = |\tilde{\psi}(t+\delta t)\rangle\,/\sqrt{1-\delta p}$.

The density matrix can be constructed as a classical mixture of these trajectories, $\hat{\rho}(t) \approx \sum_{n=1}^{N} |\psi_n(t)\rangle\langle\psi_n(t)|$, where N must be sufficiently large to reduce the statistical error. If the jump operators can be implemented physically through a suitable detection scheme, a trajectory resulting from this model can be interpreted as the real single-shot evolution of the system. This can be useful in cases where experiments are conditioned on particular outcomes, such as for time-resolved heralding of spontaneous emission from an atom.

Specifically, for spontaneous decay from $P_{1/2}$ to the $S_{1/2}$ ground state in $^{88}\mathrm{Sr}^+$, with

$$\hat{H}_{\mathrm{SP}} = \hbar\Omega_Z\,|{\uparrow_{\mathrm{N}}}\rangle\langle{\uparrow_{\mathrm{N}}}| + \hbar\omega_e\,|e\rangle\langle e| + \hbar\left(\omega_e - \tfrac{1}{3}\Omega_Z\right)|\bar{e}\rangle\langle\bar{e}|$$

containing only the relevant state energies relative to $|\downarrow_{\mathrm{N}}\rangle$ as shown in Figure 2.2, the jump operators for the atomic qubit upon measuring the decay channel $q \in \{-1, 0, 1\}$ are

$$\begin{aligned}
\hat{C}_{-1} &= \sqrt{\frac{\Gamma}{2}}\sqrt{\frac{2}{3}}\,|\uparrow_{\mathrm{N}}\rangle\langle\bar{e}| \ , \\
\hat{C}_{0} &= \sqrt{\frac{\Gamma}{2}}\sqrt{\frac{1}{3}}\,(|\uparrow_{\mathrm{N}}\rangle\langle e| + |\downarrow_{\mathrm{N}}\rangle\langle\bar{e}|) \ , \\
\hat{C}_{+1} &= \sqrt{\frac{\Gamma}{2}}\sqrt{\frac{2}{3}}\,|\downarrow_{\mathrm{N}}\rangle\langle e| \ ,
\end{aligned}$$

such that $\sum_{q=-1}^{1} \hat{C}_q^\dagger \hat{C}_q = \Gamma(|e\rangle\langle e| + |\bar{e}\rangle\langle\bar{e}|)$, where Γ^{-1} is the radiative lifetime of the $P_{1/2}$ level. Using the same collection geometry as above leading up to Equation (2.4), the weights of the jump operators must be modified by the relative dipole emission amplitude of the π and σ decay channels, and renormalised. Moreover, in the following we will ignore the unpopulated $|\bar{e}\rangle$ state, such that we are looking at the same scenario as depicted in Figure 2.2.

The non-hermitian Hamiltonian for spontaneous decay from $P_{1/2}$,

$$\hat{H}_{\mathrm{nh}} = \hat{H}_{\mathrm{SP}} - \frac{\mathrm{i}\hbar}{2}\Gamma\,|e\rangle\langle e| \ , \tag{2.5}$$

matches the intuition that energy from the excited state gradually dissipates into the field. Following the MCWF algorithm to evolve the initial state $|e\rangle$ using Equation (2.5), the probability for no quantum jump to occur for a period Δt is $p_0(\Delta t) = \langle\tilde{\psi}(t+\Delta t)|\tilde{\psi}(t+\Delta t)\rangle$. With

$$\begin{aligned}
|\tilde{\psi}(t+\Delta t)\rangle &= \mathrm{e}^{-\frac{\mathrm{i}}{\hbar}\hat{H}_{\mathrm{nh}}\Delta t}\,|\psi(t)\rangle \\
&= \mathrm{e}^{-\frac{\mathrm{i}}{\hbar}\hat{H}_{\mathrm{nh}}\Delta t}\,|e\rangle \\
&= \mathrm{e}^{-\mathrm{i}\omega_e\Delta t}\mathrm{e}^{-\frac{\Gamma}{2}\Delta t}\,|e\rangle \ ,
\end{aligned}$$

this probability evaluates to $p_0(\Delta t) = \mathrm{e}^{-\Gamma\Delta t}$, showing that the duration without a quantum jump is Poisson-distributed with mean waiting time Γ^{-1}.

2.1.3 Steering

If we identify the angular momentum change $q \in \{0, +1\}$ in a jump from $|e\rangle$ to $|\downarrow_{\mathrm{N}}\rangle$ or $|\uparrow_{\mathrm{N}}\rangle$ as the angular momentum of the emitted photon, measuring the polarisation of this photon in the basis $\{|H\rangle, |V\rangle\}$ implements the jump operators

$$\hat{C}_\pi = |\uparrow_{\mathrm{N}}\rangle\langle e| \ ,$$
$$\hat{C}_\sigma = |\downarrow_{\mathrm{N}}\rangle\langle e| \ .$$

This detection scheme can be adapted to unitarily rotated polarisation measurement bases, $\{\hat{U}_P |H\rangle, \hat{U}_P |V\rangle\}$, in order to transform the jump operators as

$$\hat{C}_q \mapsto \hat{J}\hat{U}_P\hat{J}^\dagger\hat{C}_q \ ,$$

where $\hat{J} = |\downarrow_{\mathrm{N}}\rangle\langle H| + |\uparrow_{\mathrm{N}}\rangle\langle V| + |e\rangle\langle e|$ reflects the fact that the ion-photon state (2.4) is maximally entangled.

The polarisation measurement basis transformation $\hat{U}_P$, the photon detection time t_0, and the polarisation measurement outcome q, define the evolution of the atomic qubit initially prepared in $|\psi(0)\rangle = |e\rangle$:

$$|\psi(t)\rangle = \begin{cases} \mathrm{e}^{-\mathrm{i}\omega_e t}|e\rangle & t < t_0 \\ \mathrm{e}^{-\mathrm{i}\omega_e t_0}\mathrm{e}^{-\mathrm{i}\Omega_Z|\uparrow_{\mathrm{N}}\rangle\langle\uparrow_{\mathrm{N}}|(t-t_0)}\hat{J}\hat{U}_P\hat{J}^\dagger\hat{C}_q|e\rangle & t \geq t_0 \end{cases} \ . \tag{2.6}$$

This MCWF picture suggests that the phase of the ground state superposition starts to evolve at the time of the quantum jump, t_0, which relates to the time of photon detection by a constant offset. For remote steering of the qubit state by measuring the photon polarisation, this offset needs to be taken into account – hence the importance of time-resolved detection of the photon, as the qubit state would otherwise appear dephased (see Section 2.1.4).

When we discussed the ion-photon state (2.4), we assumed that the photon had not been measured, but the decay already occurred. Equation (2.6) now implies that the phase of the state after the decay depends on the time of the jump, which is unknown until the detection of the photon. A time-resolved polarisation-maintaining non-demolition measurement of the photon number would be required to make t_0 known without affecting the spin-polarisation entanglement (Equation (2.6)). In

most experiments, including ours, however, photons are measured in a destructive manner by absorption in a detector. We therefore obtain both t_0 and q together in one measurement. Then, even at the earliest time at which the phase of the entangled state (2.4) can be known, the photon is already destroyed and its polarisation state collapsed, leaving the atomic qubit unentangled and in a deterministic state. This process forms the basis for the remote state preparation (RSP) step in the BQC implementation described in Chapter 6.

The non-classical correlations between the photon polarisation and atomic spin, which are exploited for steering, stem from entanglement between the two systems at times prior to the destruction of the photon (see Chapter 5). This entanglement is not properly captured by the quantum jump formalism, as the electromagnetic field is treated as the reservoir and its state is traced out in order to gain insights into the dissipative dynamics of the atom. The fact that local operations and classical communication (LOCC) are required in order to harness this entanglement is no restriction, because classical communication is a fundamental requirement for any protocol utilising remote entanglement.[6] Here, local operations that depend on the photon measurement outcome need to be applied to the atomic system before the quantum correlations can be exploited.

2.1.4 Error due to timing uncertainties

We analyse the effect of different timestamping capabilities for the photon detection on the fidelity of the steered qubit state,

$$\mathcal{F}[\hat{\rho}] = \langle + | \hat{\rho} | + \rangle \ ,$$

with respect to the target state $|+\rangle = \frac{1}{\sqrt{2}}(|\downarrow_{\mathrm{N}}\rangle + |\uparrow_{\mathrm{N}}\rangle)$, where we are moving into a frame rotating at Ω_Z to emphasise those phases that contribute to dephasing. For this demonstration, without loss of generality, we override $\hat{J}\hat{U}_P\hat{J}^\dagger\hat{C}_q = |+\rangle\langle e|$ in Equation (2.6) to obtain the target state without the complication of different outcomes q. The density matrix for the qubit contains a statistical mixture of

[6] Faster-than-light communication is not possible (except in *Star Trek*). Thus, analysing outcomes from the systems in isolation reveals nothing but the maximally mixed state.

trajectories, e.g., states with different jump times, t_0, and fluctuating phase errors due to noise in the electronic detection system. As established earlier, the jumps are Poisson distributed with mean waiting time Γ^{-1}. We introduce a response function of the timestamping electronics, $h(\Delta t) = h(t - t_0)$, to describe the distribution of timestamps t with respect to a photon impinging on the detector at time t_0. Here, t is the reference time used by the control system for subsequent phase-coherent manipulation of the qubit; it determines the phase of the control field in the rotating frame of the qubit. Consequently, any error in the knowledge of t propagates to the observed qubit phase and causes dephasing.

Combining the distribution of jump times with the effect of noisy timestamping yields the mixed state

$$\hat{\rho} = \int_{-\infty}^{\infty} \int_{0}^{\infty} \Gamma \mathrm{e}^{-\Gamma t_0} h(t - t_0) \, |\phi(t - t_0)\rangle\langle\phi(t - t_0)| \, \mathrm{d}t_0 \, \mathrm{d}t \ , \text{where}$$
$$|\phi(\Delta t)\rangle = \tfrac{1}{\sqrt{2}} \left(|\downarrow_{\mathrm{N}}\rangle + \mathrm{e}^{-\mathrm{i}\Omega_Z \Delta t} \, |\uparrow_{\mathrm{N}}\rangle \right) \ .$$

For a perfect detector, $h(\Delta t) = \delta(\Delta t)$ is the Dirac distribution, and the observed state would be $\phi(t_0) = |+\rangle$ independent of the time of the jump, realising steering with unit fidelity.

2.1.4.1 No time-resolving capabilities

Assuming the photon detector only heralds the presence of a photon, its response $h(\Delta t)$ is time-independent (constant within the detection window), and the fidelity of steering a superposition state becomes

$$\mathcal{F}_{\mathrm{no}} = \frac{1}{2} \left[1 + \frac{1}{1 + \left(\frac{\Omega_Z}{\Gamma} \right)^2} \right] \approx 1 - \frac{1}{2} \left(\frac{\Omega_Z}{\Gamma} \right)^2 \ . \tag{2.7}$$

For $^{88}\mathrm{Sr}^+$ in a 0.5 mT magnetic field, $\frac{\Omega_Z}{2\pi} \approx 14\,\mathrm{MHz}$ and $\Gamma^{-1} \approx 7.4\,\mathrm{ns}$, the infidelity is significant, $1 - \mathcal{F}_{\mathrm{no}} \approx 0.2$, showing that time-resolved photon detection is a necessity for high-fidelity steering.

2.1.4.2 Time-resolved detection with jitter

The timing resolution in our experiments is limited by the digital inputs to 1 ns. We model their response as a square window of length 2σ,

$$h(\Delta t) = \frac{1}{2\sigma}\left[\Theta(\Delta t + \sigma) - \Theta(\Delta t - \sigma)\right] \ .$$

The steering fidelity for this scenario is

$$\mathcal{F}_{\mathrm{sq}} = \frac{1}{2}\left[1 + \mathrm{sinc}(\Omega_Z \sigma)\right] \approx 1 - \frac{1}{12}(\Omega_Z \sigma)^2 \ .$$

The infidelity evaluates to $1 - \mathcal{F}_{\mathrm{sq}} \approx 2 \times 10^{-4}$ with the above parameters for $^{88}\mathrm{Sr}^+$ and $\sigma = 0.5$ ns. This value is negligible compared to other errors in our system.[7]

2.2 Motional dynamics of trapped ions

In this section I present a classical approach for calculating the normal modes of motion of one ion (Section 2.2.1) and two different ions (Section 2.2.2). The motional properties of a single ion are mainly used to characterise the trapping potential. When multiple ions are trapped together in the same potential, the individual trapping potential is modified to include the Coulomb potential of all other ions and the ions distribute to balance the external confinement provided by the trap with the Coulomb force pushing the ions away from each other. This pairwise interaction gives rise to $3N$ motional modes, where N is the number of ions in the trap. In the limit of small excitations, that is the linear regime, these modes are described by harmonic oscillators that can be quantised straight-forwardly (Section 2.2.3). It is therefore possible to transfer single quanta of energy between the internal state of an ion and the motion. Since the modes are shared by all ions, this process can be used to mediate a coupling between the electronic states of different ions. The prevailing methods to generate entanglement between trapped-ion qubits all – this work being no exception – operate on this principle (see Chapter 4).

[7] If the input were clocked by the default 125 MHz system clock, for which $\sigma = 4$ ns, the infidelity of 0.01 would be significant, showing that the use of these faster inputs is crucial.

2.2.1 Single ion

A particle of mass m and charge q in a Paul trap experiences the time-averaged potential [Hom13]

$$\phi(\boldsymbol{r}) = \phi(\boldsymbol{r}) + \Phi(\boldsymbol{r}, m) \ ,$$

where ϕ is a static field and the ponderomotive part $\Phi(\boldsymbol{r}, m) \propto m^{-1}$ remaining after eliminating fast dynamics driven by the radio frequency (RF) field from the time-dependent potential [Deh69]. We assume a conventional four-rod trap geometry, where the principal axes of the static and the ponderomotive potentials are aligned.[8] The potential energy can be expanded in a Taylor polynomial around the origin:

$$\begin{aligned} q\phi(\boldsymbol{r}) &\approx \frac{1}{2}\left(ax^2 + by^2 + cz^2\right) \ , \\ q\Phi(\boldsymbol{r}, m) &\approx \frac{1}{2m}\left(\kappa_x^2 x^2 + \kappa_y^2 y^2 + \kappa_z^2 z^2\right) \ , \end{aligned}$$

where $a+b+c = 0$ and $\kappa_x+\kappa_y+\kappa_z = 0$ in order to fulfil Laplace's equation. Further, we assume cylindrical RF confinement, for which $\kappa_z = 0$, restricting the potential to

$$\begin{aligned} q\phi(\boldsymbol{r}) &\approx \frac{1}{2}(ax^2 + by^2 - (a+b)z^2) \ , \\ q\Phi(\boldsymbol{r}, m) &\approx \frac{\kappa^2}{2m}(x^2 + y^2) \ . \end{aligned}$$

The Lagrangian formalism can be used to derive the normal modes of motion from this potential. For a single ion, the system of equations

$$\begin{aligned} L = T - V = \frac{1}{2}m\dot{\boldsymbol{r}}^2 - q\phi(\boldsymbol{r}) - q\Phi(\boldsymbol{r}, m) \\ \text{and } m\ddot{\boldsymbol{r}} = -\boldsymbol{\nabla}(q\phi(\boldsymbol{r}) + q\Phi(\boldsymbol{r}, m)) \end{aligned} \tag{2.8}$$

is solved using the ansatz $\boldsymbol{r}(t) = \boldsymbol{R}\exp(\mathrm{i}\omega t)$. The set of coupled linear second-order differential equations (2.8) reduces to the eigenvalue problem

$$M \cdot \boldsymbol{R} = \omega^2 \boldsymbol{R} \ , \tag{2.9}$$

[8] While this is usually not the case in surface electrode traps, the treatment presented here is sufficiently accurate for our purpose.

with the matrix

$$M = \frac{1}{m}\begin{pmatrix} a+\frac{\kappa^2}{m} & 0 & 0 \\ 0 & b+\frac{\kappa^2}{m} & 0 \\ 0 & 0 & -(a+b) \end{pmatrix} .$$

The normal modes of a single ion in this potential are trivially aligned with the Cartesian coordinate system and oscillate at frequencies

$$\omega_x = \sqrt{\frac{1}{m}\left(a+\frac{\kappa^2}{m}\right)} ,$$
$$\omega_y = \sqrt{\frac{1}{m}\left(b+\frac{\kappa^2}{m}\right)} ,$$
$$\omega_z = \sqrt{\frac{-a-b}{m}} .$$

These equations can be inverted to calculate the trap parameters a, b and κ from measured trap frequencies:

$$a = \frac{m}{2}\left(\omega_x^2 - \omega_y^2 - \omega_z^2\right) ,$$
$$b = \frac{m}{2}\left(\omega_y^2 - \omega_x^2 - \omega_z^2\right) ,$$
$$\kappa^2 = \frac{m^2}{2}\left(\omega_x^2 + \omega_y^2 + \omega_z^2\right) .$$

2.2.2 Two ions

The motion of co-trapped ions of masses m_1 and m_2 is described by the Lagrangian

$$L = \frac{1}{2}m_1|\dot{\boldsymbol{r}}_1|^2 + \frac{1}{2}m_1|\dot{\boldsymbol{r}}_2|^2 - V \text{ with} \tag{2.10}$$
$$V = q\phi(\boldsymbol{r}_1) + q\phi(\boldsymbol{r}_2) + q\Phi(\boldsymbol{r}_1, m_1) + q\Phi(\boldsymbol{r}_2, m_2) + \frac{q^2}{4\pi\epsilon_0|\boldsymbol{r}_2 - \boldsymbol{r}_1|} . \tag{2.11}$$

The equilibrium distance between two ions in a compensated axial configuration is independent of their mass because on axis, the mass-dependent ponderomotive force, $-q\boldsymbol{\nabla}\Phi$, is zero due to its cylindrical symmetry, and the static Coulomb repulsion depends only on their charge. The ions lie on the z axis at a distance

$$z_0 = \frac{d}{2} = \left(\frac{-q^2}{16\pi\epsilon_0(a+b)}\right)^{\frac{1}{3}} \tag{2.12}$$

from the origin. The Lagrangian (2.10) can be transformed into a dimensionless quantity by expressing energies in units of $\frac{q^2}{4\pi\epsilon_0 z_0}$. Furthermore, the mass dependence of the kinetic energy can be absorbed into a new set of degrees of freedom,

$$\boldsymbol{u}_i = \frac{\sqrt{m_i}}{2z_0}\boldsymbol{r}_i \ .$$

The transformed Lagrangian reads

$$\begin{aligned}
\tilde{L} &= \frac{1}{2}\frac{-1}{a+b}\left(|\dot{\boldsymbol{u}}_1|^2 + |\dot{\boldsymbol{u}}_2|^2\right) - \tilde{V} \text{ with} \\
\tilde{V} &= \frac{1}{2}\frac{-1}{a+b}\left[q\phi\left(\frac{\boldsymbol{u}_1}{\sqrt{m_1}}\right) + q\phi\left(\frac{\boldsymbol{u}_2}{\sqrt{m_2}}\right) + q\Phi\left(\frac{\boldsymbol{u}_1}{\sqrt{m_1}}, m_1\right) + q\Phi\left(\frac{\boldsymbol{u}_2}{\sqrt{m_2}}, m_2\right)\right] \\
&\quad + \frac{1}{2}\left|\frac{\boldsymbol{u}_2}{\sqrt{m_2}} - \frac{\boldsymbol{u}_1}{\sqrt{m_1}}\right|^{-1} \ .
\end{aligned}$$

Proceeding analogously to the case of a single ion, solving the Euler-Lagrange equation leads to the eigenvalue problem (2.9) with

$$\begin{aligned}
M &= -(a+b)(\boldsymbol{\nabla}^{\mathrm{T}}\boldsymbol{\nabla})\tilde{V} \\
&= \begin{pmatrix}
\omega_x^2 - \frac{\omega_z^2}{2} & 0 & 0 & \frac{\omega_z^2}{2\sqrt{\mu}} & 0 & 0 \\
0 & \omega_y^2 - \frac{\omega_z^2}{2} & 0 & 0 & \frac{\omega_z^2}{2\sqrt{\mu}} & 0 \\
0 & 0 & 2\omega_z^2 & 0 & 0 & -\frac{\omega_z^2}{\sqrt{\mu}} \\
\frac{\omega_z^2}{2\sqrt{\mu}} & 0 & 0 & \frac{(1+\mu)\omega_x^2+(1-\mu)\omega_y^2+(1-2\mu)\omega_z^2}{2\mu^2} & 0 & 0 \\
0 & \frac{\omega_z^2}{2\sqrt{\mu}} & 0 & 0 & \frac{(1-\mu)\omega_x^2+(1+\mu)\omega_y^2+(1-2\mu)\omega_z^2}{2\mu^2} & 0 \\
0 & 0 & -\frac{\omega_z^2}{\sqrt{\mu}} & 0 & 0 & \frac{2\omega_z^2}{\mu}
\end{pmatrix}
\end{aligned}$$

in terms of the mode frequencies ω_x, ω_y, ω_z of a single ion of mass m_1 in the same trap (Section 2.2.1), and $\mu = \frac{m_2}{m_1}$. By diagonalising M, we find the normal modes of motion and their eigenfrequencies, ω_α. By construction of the matrix M, the eigenvectors $\boldsymbol{m}^\alpha$ are concatenations of the participation vectors, $\boldsymbol{v}_i^\alpha$, of the individual ions ($i = 1, 2$).

The main results of this thesis involve trapping two different ion species, $^{88}\mathrm{Sr}^+$ and $^{43}\mathrm{Ca}^+$, and performing entangling gates between them. To do that in the presence of motional heating, it is favourable to select a motional mode with high frequency, where the heating is generally lower. The potential required to create linear ion chains also leads to the radial modes having higher frequency than the

axial modes. However, the participation, i.e. oscillation amplitude, in radial modes is highly imbalanced between two ions of different mass, rendering these modes unsuitable for performing mixed-species entangling gates. Therefore, the axial modes of motion ($\boldsymbol{v}_i^\alpha \parallel \boldsymbol{e}_z$) are of particular interest to our experiments. The axial in-phase (IP) and axial out-of-phase (OOP) modes are found at

$$\omega_{\text{ip}} = \omega_z \sqrt{\frac{1+\mu-\sqrt{1+\mu(\mu-1)}}{\mu}} \qquad \text{with } \boldsymbol{e}_z \cdot \boldsymbol{v}_i^{\text{ip}} = \begin{bmatrix} \cos(\gamma) \\ \sin(\gamma) \end{bmatrix}_i ,$$

$$\omega_{\text{oop}} = \omega_z \sqrt{\frac{1+\mu+\sqrt{1+\mu(\mu-1)}}{\mu}} \qquad \text{with } \boldsymbol{e}_z \cdot \boldsymbol{v}_i^{\text{oop}} = \begin{bmatrix} \sin(\gamma) \\ -\cos(\gamma) \end{bmatrix}_i ,$$

where

$$\tan(\gamma) = \frac{1-\mu+\sqrt{1+\mu(\mu-1)}}{\sqrt{\mu}} .$$

We plot the motional mode spectrum for different ion species pairs in Figure 2.3

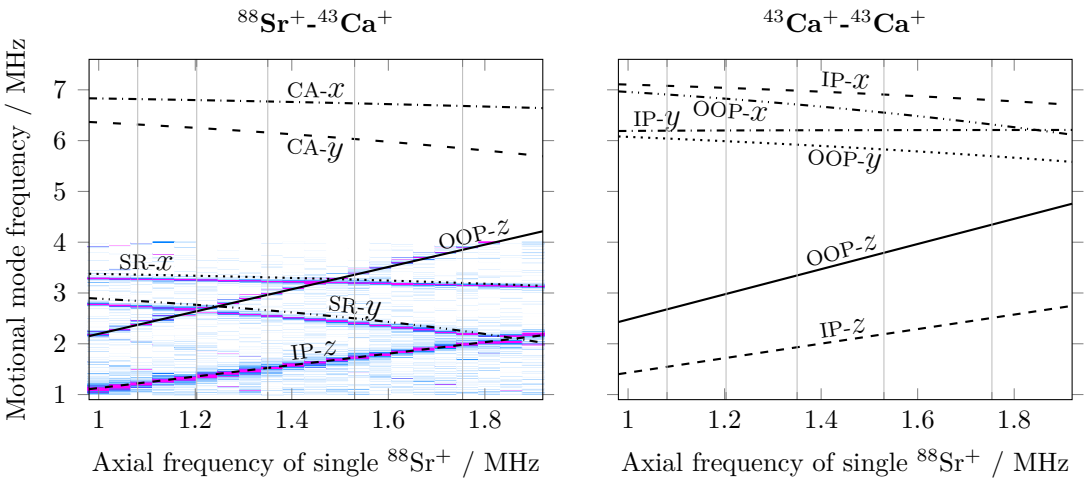

Figure 2.3: Calculated motional mode frequencies for different ion species pairs as a function of axial confinement (black lines). The horizontal axis is expressed in terms of the axial mode frequency of a single trapped ^{88}Sr$^+$ in the same trap with $\omega_x^2 + \omega_y^2 + \omega_z^2 = (2\pi \times 4.7\,\text{MHz})^2$. The vertical grid lines indicate where the ion spacing matches a half-integer multiple of the 401.543 nm Raman laser wavelength projected onto the trap axis (at 45°) – at these values, two-qubit entangling light shift gates on the out-of-phase (OOP) axial mode (Section 4.2) are maximally efficient. For the mixed-species crystal, an experimental scan of probing the motional sidebands of the 674 nm transition in ^{88}Sr$^+$ is shown in the background for comparison with the theoretical prediction.

for a typical RF voltage of $\sim 160\,\text{V}$. The majority of experiments presented in this thesis were performed with an axial frequency of a single ^{88}Sr$^+$ of 1.52 MHz.

2.2.3 Quantisation

The classical normal modes of motion of an ion chain, labelled by $\alpha \in \mathcal{N}$, are each characterised by a resonance frequency, ω_α, and an ion participation vector, $\boldsymbol{v}_i^\alpha$, with three entries per ion. In the regime of small motional excitations[9], the modes can be treated as independent quantum harmonic oscillators, with Hamiltonian

$$\hat{H} = \sum_{\alpha \in \mathcal{N}} \hbar \omega_\alpha \hat{a}_\alpha^\dagger \hat{a}_\alpha \ , \tag{2.13}$$

where $\hat{a}_\alpha$ and $\hat{a}_\alpha^\dagger$ are annihilation and creation operators for mode α, which obey the commutation relations $[\hat{a}_\alpha, \hat{a}_\beta^\dagger] = \delta_{\alpha,\beta}$. The observable $\hat{n} = \hat{a}_\alpha^\dagger \hat{a}_\alpha$ counts the energy quanta (excitations of $\hbar\omega_\alpha$ each) that are contained in a motional state. The average number of energy quanta in a motional state $\hat{\rho} = \sum_{n=0}^{\infty} \rho_n \, |n\rangle\langle n|$ can be calculated using $\bar{n} = \mathrm{Tr}(\hat{\rho}\hat{n}) = \sum_{n=0}^{\infty} \langle n|\hat{\rho}|n\rangle$, where $\{|n\rangle\}_{n\geq 0}$ are Fock states (energy eigenstates of Equation (2.13)).

2.2.4 Motional heating

The motional modes of a trapped-ion chain can be cooled into the ground state and coupled to the internal states of the ions in the chain to mediate an entangling operation between ions. Trapped ions provide exceptionally well-isolated qubits, but their charge makes them susceptible to electric fields, which affects the collective motion.

Often, the underlying noise mechanism is as mundane as technical noise in the electronics that supply voltages to the electrodes. However, 'anomalous' heating is present even if technical noise can be eliminated [Bro+15]. The physical mechanism for this is not fully understood; based on empirical evidence, a power law, $\dot{\bar{n}} \propto \omega_\alpha^{-2} d^{-4}$, can be used to model the scaling with motional mode frequency ω_α and ion-electrode distance d [DCG09; Bro+15]. The observed d^{-4} scaling is not compatible with blackbody radiation and Johnson noise alone, or any spatially correlated noise for that matter, for which a d^{-2} scaling would be expected. A candidate

[9] Anharmonicities in the potential lead to higher-order terms and mode mixing. In addition to experimental imperfections, there are unavoidable intrinsic anharmonicities, such as that generated by relative motion between two ions, which gives rise to Kerr cross-couplings [Roo+08].

explanation for the d^{-4} scaling is given by fluctuating patch potentials present on the electrode surface [Tur+00].

The interaction of a fluctuating electric field $\boldsymbol{\mathcal{E}}(\boldsymbol{r}_i, t)$ with an N-ion chain is captured by the Hamiltonian $\hat{H}(t) = -|e| \sum_{i=1}^{N} \hat{\boldsymbol{r}}_i \cdot \boldsymbol{\mathcal{E}}(\boldsymbol{r}_i, t)$, where $\hat{\boldsymbol{r}}_i$ is the position operator of the i^{th} ion in the chain. Assuming that the electric field noise is stationary with correlation times short compared to spin dynamics in the chain, the heating rate of a mode $\alpha \in \mathcal{N}$ is approximately given by [Hom13; Bro+15]

$$\dot{\bar{n}} = \frac{e^2}{4\hbar\omega_\alpha} S_\alpha(\omega_\alpha) \ ,$$

where $S_\alpha(\omega)$ is the spectral density

$$S_\alpha(\omega) = 2 \int_{-\infty}^{\infty} \mathrm{e}^{\mathrm{i}\omega\tau} \xi_\alpha(\tau) \xi_\alpha(0) \, \mathrm{d}\tau$$

of $\xi_\alpha(t) = \sum_{i=1}^{N} \frac{1}{\sqrt{m_i}} \boldsymbol{v}_i^\alpha \cdot \boldsymbol{\mathcal{E}}(\boldsymbol{r}_i, t)$, with the participation vector $\boldsymbol{v}_i^\alpha$ in mode α and the mass m_i of the i^{th} ion in the chain. For same-species chains, modes in which ions are moving antisymmetrically (out-of-phase) with respect to the centre of the chain exhibit zero heating rate. On the other hand, heating of the centre-of-mass motion of an N-ion string is N times higher than for a single ion. For a mixed-species ion chain, the situation is more complex: purely antisymmetric modes with $\dot{\bar{n}} \approx 0$ exist only in chains of more than two ions and tend to be rare [Hom13].

Assuming that the electric field noise $\boldsymbol{\mathcal{E}}(\boldsymbol{r}, t) = \mathcal{E}(t) \boldsymbol{e}_\mathcal{E}$ is spatially uniform and, without loss of generality, directed in a constant direction with unit vector $\boldsymbol{e}_\mathcal{E}$, the spectral density simplifies to

$$S_\alpha(\omega) = 2 \int_{-\infty}^{\infty} \mathrm{e}^{\mathrm{i}\omega\tau} \mathcal{E}(\tau) \mathcal{E}(0) \, \mathrm{d}\tau \underbrace{\sum_{i,j=1}^{N} \frac{(\boldsymbol{v}_i^\alpha \cdot \boldsymbol{e}_\mathcal{E})(\boldsymbol{v}_j^\alpha \cdot \boldsymbol{e}_\mathcal{E})}{\sqrt{m_i m_j}}}_{g_\alpha} \ ,$$

which contains a spectral factor and a geometric factor, g_α. In the following, we consider only axial modes and electric field noise in the axial direction, i.e. with $\boldsymbol{e}_\mathcal{E} = \boldsymbol{e}_z$. For a single ion, $g_\alpha = \frac{1}{m}$. For the mixed-species two-ion configuration specified in Section 2.2.2, the geometry factors evaluate to

$$g_{\text{oop}} = \frac{1}{m_2} \left(\cos(\gamma) - \sqrt{\mu} \sin(\gamma)\right)^2 \ ,$$
$$\text{and } g_{\text{ip}} = \frac{1}{m_2} \left(\sqrt{\mu} \cos(\gamma) + \sin(\gamma)\right)^2 \ .$$

Further, including the empirical frequency scaling of the heating rate, $\dot{\bar{n}} \propto \omega^{-2}$, and given the heating rate $\dot{\bar{n}}_z$ of the axial mode of a single ion of mass m_1 at ω_z, the heating rate of an axial mode $\alpha \in \{\text{oop}, \text{ip}\}$ after adding an ion of mass m_2 into the same trap, is expected to be

$$\dot{\bar{n}}_\alpha = \dot{\bar{n}}_z \frac{m_1}{g_\alpha} \frac{\omega_z^2}{\omega_\alpha^2} \ . \tag{2.14}$$

For example, with $\mu = \frac{43}{88}$ for a $^{88}\text{Sr}^+$-$^{43}\text{Ca}^+$ pair, the axial OOP and axial IP mode heating rates relate to the heating rate of a single $^{88}\text{Sr}^+$ in the same trap as $\frac{\dot{\bar{n}}_{\text{oop}}}{\dot{\bar{n}}_{\text{sr}}} \approx 0.095$ and $\frac{\dot{\bar{n}}_{\text{ip}}}{\dot{\bar{n}}_{\text{sr}}} \approx 0.910$, respectively.

As entangling gates with trapped ions rely on the quantum state of the motion, heating can constitute a significant source of error. In simulations of quantum dynamics using the master equation, white-noise motional heating can be modelled by the Lindblad operators $\dot{\bar{n}}_\alpha^{\frac{1}{2}} \hat{a}_\alpha$ and $\dot{\bar{n}}_\alpha^{\frac{1}{2}} \hat{a}_\alpha^\dagger$. These operators result from a treatment of the coupling of a harmonic oscillator with a thermal amplitude reservoir [Tur+00].

A related effect is motional dephasing, which stems from the coupling of a harmonic oscillator with a phase-damping reservoir, and can be modelled by $\sqrt{\kappa_\alpha} \hat{a}_\alpha^\dagger \hat{a}_\alpha$, where κ_α is the variance of random phase shifts imprinted onto the first excited Fock state during the interaction with the reservoir.

2.2.5 Micromotion

Using the ponderomotive force approximation in Section 2.2.1 allowed us to investigate the secular dynamics in closed form. However, this approach hides another, very important characteristic of Paul trap dynamics. In addition to harmonic motion at the secular frequency, trapped particles experience driven (micro)motion at the RF frequency. Static electric fields, such as generated by stray charges, can push the particles away from the RF null, amplifying this effect. Using controlled voltages on dedicated electrodes, the unknown electric field can be compensated. Assuming that the RF null is found along a line parallel to the trap axis due to the symmetry of the trap, compensating micromotion reduces to

a two-dimensional optimisation problem. Several methods exist for detecting and minimising micromotion. The choice of the method depends on the type of trap, the optical access and on the availability of narrow-linewidth transitions and the corresponding lasers. With conventional three-dimensional four-rod 'blade' traps, lasers can easily be aligned along linearly independent radial directions, which enables full micromotion compensation by minimising the correlations between fluorescence photons and the trap RF drive [Kel+15], or by minimising the Rabi frequency of the micromotion sideband on a narrow-linewidth transition [Chw09]. For surface traps, optical access is more restricted, which hinders the installation of linearly independent radial beams. Alternative approaches have been developed for those geometries seeking to provide a signal perpendicular to the trap surface, such as camera-based methods. In this work we parametrically excite the motion of a trapped ion by modulating the trap RF [Nad+21] (see Section 2.2.5.1).

2.2.5.1 Parametric excitation

For this derivation, we consider the one-dimensional[10] second-order linear differential equation,

$$\ddot{x}(t) + 2\zeta\dot{x}(t) + \left(\frac{\Omega_{\mathrm{rf}}}{2}\right)^2 \left[a + 2q\cos(\Omega_{\mathrm{rf}}t)\right] x(t) = \frac{EZe}{m} \ ,$$

describing the motion of an ion with mass m and charge Ze in a Paul trap with Mathieu parameters $|a| \ll |q| \ll 1$ and trap RF frequency Ω_{rf}. The ion is offset by an external static electric field E, and laser-cooled with damping parameter ζ. To transfer energy to this system it can either be driven by an external force, such as by varying the external field in time, or by varying the Mathieu parameters in time (parametric excitation). Here we vary q by modulating the amplitude of the RF confinement at a frequency ω_{pe}:

$$\ddot{x}(t) + 2\zeta\dot{x}(t) + \left(\frac{\Omega_{\mathrm{rf}}}{2}\right)^2 \left\{a + 2q\left[1 + h\cos(\omega_{\mathrm{pe}}t)\right]\cos(\Omega_{\mathrm{rf}}t)\right\} x(t) = \frac{EZe}{m} \ ,$$

[10] For a Paul trap where the principal axes of the RF potential align with the principal axes of the DC potential, the equations of motion separate into individual equations for each principal coordinate. While this is usually not the case in surface traps where the DC potential is rotated to enable efficient Doppler cooling in all directions, the pseudopotential approximation is still reasonably accurate in the relevant parameter regime.

where h is the modulation index. To transform this into dimensionless form, we substitute $\xi = \frac{\Omega_{\mathrm{rf}} t}{2}$, $d = \frac{2\zeta}{\Omega_{\mathrm{rf}}}$, $\nu = \frac{2\omega_{\mathrm{pe}}}{\Omega_{\mathrm{rf}}} \ll 1$, and $u = \frac{x}{x_0}$, where $x_0 = \frac{4eZE}{m\Omega_{\mathrm{rf}}}$:

$$u''(\xi) + 2du'(\xi) + \{a + 2q\,[1 + h\cos(\nu\xi)]\cos(2\xi)\}\,u(\xi) = 1\ . \tag{2.15}$$

We separate the slowly-varying excursion $\bar{u} = u - \delta$ from fast oscillations $\delta \ll \bar{u}$. Solving for fast oscillations under the approximations $\delta' \gg \bar{u}'$ and $d \ll 1$, we obtain

$$\delta(\xi) = -\frac{\bar{q}(\xi)\bar{u}(\xi)}{2}\cos(2\xi)\ ,$$

where $\bar{q}(\xi) = q\,[1 + h\cos(\nu\xi)]$. By averaging Equation (2.15) over one period of this oscillation and treating $\bar{u}$ and $\bar{q}$ as a constant over this period, we obtain

$$\bar{u}''(\xi) + 2d\bar{u}'(\xi) + \left\{a + \frac{q^2}{2}\,[1 + h\cos(\nu\xi)]^2\right\}\bar{u}(\xi) = 1 \tag{2.16}$$

for the slowly-varying component $\bar{u}(\xi)$. With the definitions

$$\nu_0^2 = a + \frac{q^2}{2}\left(1 + \frac{h^2}{2}\right)\ ,$$
$$\tilde{h} = \frac{q^2 h}{2\nu_0^2}\ ,$$

Equation (2.16) can also be written as

$$\bar{u}''(\xi) + 2d\bar{u}'(\xi) + \nu_0^2\left[1 + 2\tilde{h}\cos(\nu\xi) + \frac{h\tilde{h}}{2}\cos(2\nu\xi)\right]\bar{u}(\xi) = 1\ .$$

To first order in h and after transforming back into dimensional form, the slowly-varying ion position $\bar{x}(t)$ is thus described by another Mathieu equation,

$$\ddot{\bar{x}}(t) + 2\zeta\dot{\bar{x}}(t) + \left(\frac{\omega_{\mathrm{pe}}}{2}\right)^2\left[A + 2Q\cos(\omega_{\mathrm{pe}}t)\right]\bar{x}(t) = \frac{EZe}{m}\ , \tag{2.17}$$

with stability parameters $A = \left(\frac{2\omega_0}{\omega_{\mathrm{pe}}}\right)^2$ and $Q = \tilde{h}A$, where $\omega_0 = \frac{\Omega_{\mathrm{rf}}}{2}\nu_0$. While for Paul traps stable solutions of the Mathieu equation with $|a| \ll |q| \ll 1$ are typically considered, here, $Q < A$, and we are interested in the onsets of parametric instabilities, which occur at modulation frequencies $\omega_{\mathrm{pe}} = \frac{2\omega_0}{n}$, where $n \in \mathbb{N}$ is the resonance index (see Figure 2.4). For $n = 2$ ($\omega_{\mathrm{pe}} = \omega_0$), the boundary of the stability region depends on the modulation index and the damping via $\tilde{h} \approx \frac{2\zeta}{\omega_0}$ [Nad+21]. A derivation of approximate analytical bounded solutions to Equation (2.17) using

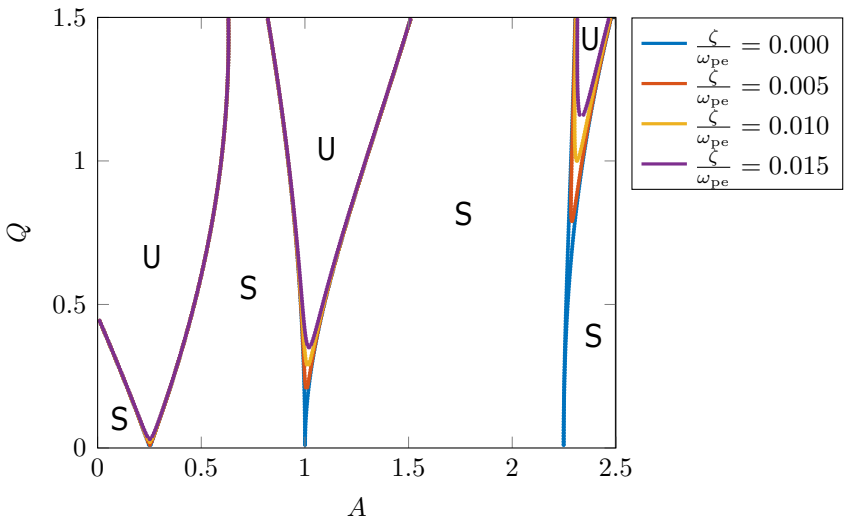

Figure 2.4: Stability diagram of parametric excitation as a function of Mathieu parameters $A = \left(\frac{2\omega_0}{\omega_{pe}}\right)^2$ and $Q = \tilde{h}A$. Stable regions are labelled S and unstable regions U. As the damping coefficient ζ is increased, the modulation index that is required to reach an unstable region also increases. Reproduced with permission from G. Araneda.

a Floquet analysis approach can be found in Reference [Nad22]. In the limit of weak excitation (to first order in $\tilde{h}$), the solution to Equation (2.17) resembles that of a driven harmonic oscillator,

$$\bar{x}(t) \approx c_0 + \Re\left(C e^{-i\omega_{pe}t}\right) \ ,$$

where $c_0 = \frac{EZe}{m\omega_0^2}$ is the offset of the ion position due to the external electric field, and C is the complex amplitude of the parametrically driven motion. Crucially, $|C| \propto |c_0|$, i.e., the amplitude of the modulation is linear in the electric field. We exploit this property to compensate stray electric fields (see Section 3.2.3).

2.3 Atom-laser interactions

We model N atoms as individual two-level systems governed by the Pauli operators $\hat{\sigma}_\xi^{(i)} = \hat{1}^{\otimes(i-1)} \otimes \hat{\sigma}_\xi \otimes \hat{1}^{\otimes(N-i)}$, $\xi \in \{x, y, z\}$, $i = 1, \ldots, N$, and their shared normal modes of motion as harmonic oscillators with creation and annihilation operators $\hat{a}_\alpha^\dagger$, $\hat{a}_\alpha$, $\alpha \in \mathcal{N}$. The Hamiltonian of the composite system is

$$\hat{H} = \underbrace{\hat{H}_0^{(\text{atom})} + \hat{H}_0^{(\mathcal{N})}}_{\hat{H}_0} + \hat{H}(t) = \sum_{i=1}^{N} \frac{\hbar\omega_i}{2}\hat{\sigma}_z^{(i)} + \sum_{\alpha\in\mathcal{N}} \hbar\omega_\alpha \hat{a}_\alpha^\dagger \hat{a}_\alpha + \sum_i \hat{H}_i(t) \ , \qquad (2.18)$$

including an interaction term for each individual atom. This interaction is driven by an electromagnetic plane wave with resonant Rabi frequency Ω_i, wavevector $\boldsymbol{k}$, associated angular frequency $\omega = c|\boldsymbol{k}|$, and global phase offset ϕ, and can be expressed as

$$\hat{H}_i(t) = \frac{\hbar}{2}\Omega_i \left(\hat{\sigma}_+^{(i)} + \hat{\sigma}_-^{(i)}\right)\left(\mathrm{e}^{\mathrm{i}(\boldsymbol{k}\cdot\hat{\boldsymbol{r}}_i - \omega t + \phi)} + \mathrm{e}^{-\mathrm{i}(\boldsymbol{k}\cdot\hat{\boldsymbol{r}}_i - \omega t + \phi)}\right) , \tag{2.19}$$

where $\hat{\sigma}_+^{(i)} = \frac{1}{2}(\hat{\sigma}_x^{(i)} + \mathrm{i}\hat{\sigma}_y^{(i)})$, $\hat{\sigma}_-^{(i)} = (\hat{\sigma}_+^{(i)})^\dagger$, and $\hat{\boldsymbol{r}}_i$ is the position operator of the i^{th} atom. In terms of the normal modes of motion,

$$\boldsymbol{k}\cdot\hat{\boldsymbol{r}}_i = \phi_i + \sum_{\alpha\in\mathcal{N}} \eta_{\alpha,i}(a_\alpha + a_\alpha^\dagger) ,$$

where $\eta_{\alpha,i}$ are the Lamb-Dicke parameters and ϕ_i the spatial phase of the wave at the rest position of the atom. The square of the Lamb-Dicke parameter equates to the number of motional energy quanta ($\hbar\omega_\alpha$) that can be injected into the motional mode α (participation vectors $\boldsymbol{v}_i^\alpha$) by emission of a photon (wavevector $\boldsymbol{k}$) from the i^{th} atom (mass m_i):

$$\eta_{\alpha,i}^2 = \frac{E_\gamma}{\hbar\omega_\alpha} ,$$

which depends on the atom's mass and the overlap of the wavevector with the motional mode, $\tilde{k}_{\text{eff}} = \boldsymbol{k}\cdot\boldsymbol{v}_i^\alpha$, via the recoil energy $E_\gamma = \frac{(\hbar\tilde{k}_{\text{eff}})^2}{2m_i}$. An electromagnetic wave therefore only interacts with motional modes for which at least one irradiated atom oscillates in the propagation direction of the wave.

This description holds for electromagnetic waves in the RF, microwave, and optical regime, as well as for Raman transitions after adiabatic elimination of the upper level [JJ07] and substituting the effective frequency, $\omega = \omega_2 - \omega_1$, and effective wavevector, $\boldsymbol{k} = \boldsymbol{k}_2 - \boldsymbol{k}_1$, using the difference of the values of the two Raman beams.

We transform Equation (2.18) into the interaction picture[11] with respect to $\hat{H}_0$:

$$\begin{aligned}\hat{\mathcal{H}}(t) &= \mathrm{e}^{\mathrm{i}\hat{H}_0 t/\hbar}\hat{H}(t)\mathrm{e}^{-\mathrm{i}\hat{H}_0 t/\hbar} \\ &= \sum_{i=1}^{N}\frac{\hbar}{2}\Omega_i\left(\mathrm{e}^{-\mathrm{i}\omega_i t}\hat{\sigma}_+^{(i)} + \mathrm{e}^{\mathrm{i}\omega_i t}\hat{\sigma}_-^{(i)}\right)\left\{\mathrm{e}^{-\mathrm{i}(\omega t - \phi - \phi_i)}\exp\left[\mathrm{i}\sum_{\alpha\in\mathcal{N}}\eta_{\alpha,i}\left(\mathrm{e}^{-\mathrm{i}\omega_\alpha t}\hat{a}_\alpha + \mathrm{e}^{\mathrm{i}\omega_\alpha t}\hat{a}_\alpha^\dagger\right)\right]\right. \\ &\qquad \left. + \mathrm{e}^{\mathrm{i}(\omega t - \phi - \phi_i)}\exp\left[-\mathrm{i}\sum_{\alpha\in\mathcal{N}}\eta_{\alpha,i}\left(\mathrm{e}^{-\mathrm{i}\omega_\alpha t}\hat{a}_\alpha + \mathrm{e}^{\mathrm{i}\omega_\alpha t}\hat{a}_\alpha^\dagger\right)\right]\right\} .\end{aligned}$$

[11] For this calculation, useful identities are $\mathrm{e}^{\mathrm{i}\frac{\xi}{2}\hat{\sigma}_z}\hat{\sigma}_+\mathrm{e}^{-\mathrm{i}\frac{\xi}{2}\hat{\sigma}_z} = \mathrm{e}^{-\mathrm{i}\xi}\hat{\sigma}_+$ and $\mathrm{e}^{\mathrm{i}\zeta\hat{a}^\dagger\hat{a}}\hat{a}\mathrm{e}^{-\mathrm{i}\zeta\hat{a}^\dagger\hat{a}} = \mathrm{e}^{-\mathrm{i}\zeta}\hat{a}$.

Neglecting fast-oscillating terms $\propto \mathrm{e}^{\pm\mathrm{i}(\omega+\omega_i)t}$ in the rotating wave approximation (RWA) and defining $\varphi_i = \phi + \phi_i$, the interaction becomes

$$\hat{\mathcal{H}}(t) \overset{\text{RWA}}{\approx} \sum_{i=1}^{N} \frac{\hbar}{2}\Omega_i \hat{\sigma}_+^{(i)} \mathrm{e}^{-\mathrm{i}(\delta_i t+\varphi_i)} \exp\left[-\mathrm{i}\sum_{\alpha\in\mathcal{N}} \eta_{\alpha,i}\left(\mathrm{e}^{-\mathrm{i}\omega_\alpha t}\hat{a}_\alpha + \mathrm{e}^{\mathrm{i}\omega_\alpha t}\hat{a}_\alpha^\dagger\right)\right] + \text{h.c.}, \quad (2.20)$$

with the detunings from the atomic resonances $\delta_i = \omega_i - \omega$.

In the following, we assume the Lamb-Dicke approximation (LDA), which holds if the wavelength of the radiation is significantly larger than the extent of the atom's wavefunction. This condition is typically fulfilled for trapped ions cooled close to the motional ground state and implies $\eta_{\alpha,i} \ll 1$, such that

$$\mathrm{e}^{\pm\mathrm{i}\sum_{\alpha\in\mathcal{N}}\eta_{\alpha,i}(a_\alpha+a_\alpha^\dagger)} \approx 1 \pm \sum_{\alpha\in\mathcal{N}} \mathrm{i}\eta_{\alpha,i}(a_\alpha + a_\alpha^\dagger)\ . \quad (2.21)$$

Inserting Equation (2.21) into Equation (2.20), the interaction Hamiltonian becomes

$$\hat{\mathcal{H}}(t) \overset{\text{LDA}}{\approx} \sum_{i=1}^{N} \frac{\hbar}{2}\Omega_i \hat{\sigma}_+^{(i)} \mathrm{e}^{-\mathrm{i}(\delta_i t+\varphi_i)} \left[1 - \sum_{\alpha\in\mathcal{N}} \mathrm{i}\eta_{\alpha,i}\left(\mathrm{e}^{-\mathrm{i}\omega_\alpha t}\hat{a}_\alpha + \mathrm{e}^{\mathrm{i}\omega_\alpha t}\hat{a}_\alpha^\dagger\right)\right] + \text{h.c.} \quad (2.22)$$

For every ion and motional mode, Equation (2.22) contains three resonances that can be addressed individually with sufficiently narrow-linewidth radiation:

1. **Carrier.** If $\delta_i = 0$, the interaction of the electromagnetic wave with the i^{th} atom is given by

   $$\hat{\mathcal{H}}_{\text{carrier}} = \frac{\hbar}{2}\Omega_i\left(\mathrm{e}^{-\mathrm{i}\varphi_i}\hat{\sigma}_+^{(i)} + \mathrm{e}^{\mathrm{i}\varphi_i}\hat{\sigma}_-^{(i)}\right)\ .$$

   The qubit dynamics resulting from the carrier are called Rabi flops, which drive the $|\downarrow\rangle \otimes |n\rangle \leftrightarrow |\uparrow\rangle \otimes |n\rangle$ (no changes to the motional state), at a rate Ω_i. Including second-order terms $\propto \eta_{\alpha,i}^2$ in Equation (2.22), the carrier Rabi frequency decreases with increasing motional excitation number n as $\Omega_i(1-\eta_{\alpha,i}^2 n^2)$.

2. **Red sideband.** If $\delta_i = \omega_\alpha$, the spin of the i^{th} atom is coupled with the motional mode α by the Jaynes-Cummings Hamiltonian

   $$\hat{\mathcal{H}}_{\text{rsb}} = \frac{\hbar}{2}\eta_{\alpha,i}\Omega_i\left(\mathrm{e}^{-\mathrm{i}\varphi_i}\hat{\sigma}_+^{(i)}\hat{a}_\alpha + \mathrm{e}^{\mathrm{i}\varphi_i}\hat{\sigma}_-^{(i)}\hat{a}_\alpha^\dagger\right)\ .$$

   This interaction implements Rabi flops between the spin-motion states $|\downarrow\rangle \otimes |n+1\rangle \leftrightarrow |\uparrow\rangle \otimes |n\rangle$ at a rate reduced by $\eta_{\alpha,i}\sqrt{n}$ compared to the carrier flops.

3. **Blue sideband.** If $\delta_i = -\omega_\alpha$, the spin of the i^{th} atom is coupled with the motional mode α by the anti-Jaynes-Cummings Hamiltonian

$$\hat{\mathcal{H}}_{\text{bsb}} = \frac{\hbar}{2}\eta_{\alpha,i}\Omega_i \left(\mathrm{e}^{-\mathrm{i}\varphi_i}\hat{a}_\alpha^\dagger \hat{\sigma}_+^{(i)} + \mathrm{e}^{\mathrm{i}\varphi_i}\hat{a}_\alpha \hat{\sigma}_-^{(i)}\right) .$$

This interaction implements Rabi flops between the spin-motion states $|{\downarrow}\rangle \otimes |n\rangle \leftrightarrow |{\uparrow}\rangle \otimes |n+1\rangle$ at a rate reduced by $\eta_{\alpha,i}\sqrt{n+1}$ compared to the carrier flops.

The majority of coherent atom-laser interactions for quantum information processing can be described based on this model if the motional state is close to the ground state. Considering only the carrier and the first sideband interactions is sufficient in most cases, as the coupling strengths of the next-order sidebands are suppressed by $\eta_{\alpha,i}$. Outside of the Lamb-Dicke regime, the effective Rabi frequency of all interactions listed above decrease asymptotically with the motional occupation number, n. The Lamb-Dicke parameter for RF and microwave radiation is negligible; the motional state can only change if significant momentum can be transferred from the field to the atom, and visible lasers fulfil this requirement. It is possible to enhance the coupling of microwave radiation to the motion using a magnetic field gradient [MW01], but the related techniques are not employed in the experimental apparatus used for this thesis. Raman beams can be aligned in different geometries; this can be exploited to set $\boldsymbol{k} = \boldsymbol{0}$ and eliminate the coupling to all motional modes using a collinear geometry, or selectively set $\boldsymbol{k} \parallel \boldsymbol{v}_\alpha$ and maximise the coupling to a particular motional mode. For cooling and multi-qubit gates, the latter geometry is used, while the former is beneficial for single-qubit gates, as their performance is then insensitive to the motion (see Figure 2.5).

2.3.1 Sideband dynamics

The spin-motion couplings derived above, the red and the blue sideband interaction, can change the motional state of the harmonic oscillator along with the spin state. The different $|n\rangle$ states of the harmonic oscillator are driven at different rates, resulting in complex dynamics if the initial state is not a pure eigenstate. With the

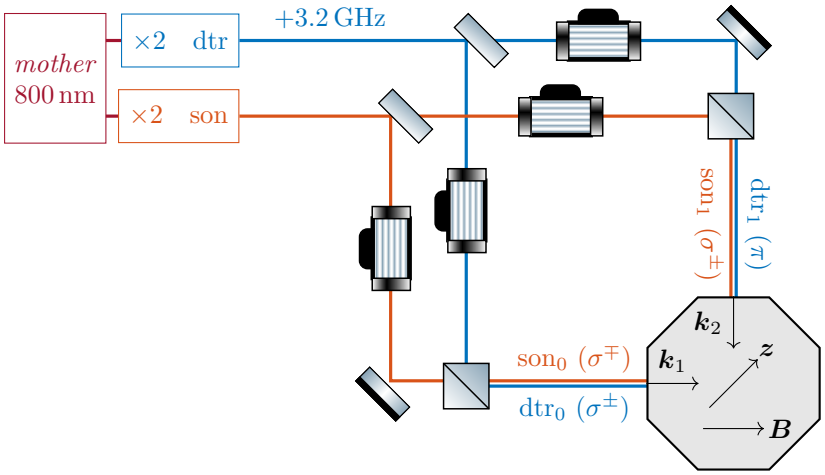

Figure 2.5: The Raman lasers are derived from the same source by second harmonic generation. The *dtr* laser includes an EOM that creates a frequency offset equal to the ground state hyperfine splitting of $^{43}Ca^{+}$. This enables addressing of all transitions in the $S_{1/2}$ manifold using the AOMs to tune into resonance. The beam geometry enables these qubits to be addressed with either $\Delta\boldsymbol{k} = \boldsymbol{k}_2 - \boldsymbol{k}_1 = 0$ or $\Delta\boldsymbol{k} = \frac{2\pi}{\sqrt{2}\lambda_R}\boldsymbol{z}$; the former suppresses the coupling to the motion and is therefore used for carrier transitions; the latter must be used in order to drive motional sidebands, such as for sideband cooling (SBC).

spin initialised in $|{\downarrow}\rangle$, and the harmonic oscillator state populations $P(n)$, a blue sideband pulse of duration τ flips the spin with probability $1 - P_{\downarrow}$, where [Mee+96]

$$P_{\downarrow}(\tau) = \sum_{n=0}^{\infty} P(n)\cos^2(\eta\Omega\sqrt{n+1}\tau) \ . \tag{2.23}$$

For a thermal state of the motion,

$$\hat{\rho}_{\text{therm}} = \sum_{n=0}^{\infty} \underbrace{\frac{\bar{n}^n}{(1+\bar{n})^{n+1}}}_{P(n)} |n\rangle\langle n| \ ,$$

the probability distribution $P(n)$ is parametrised by a single parameter, the mean occupation number $\bar{n}$. Equation (2.23) can be used to obtain estimates for the parameters η and $\bar{n}$ from experimental data points $(\tau, P_{\downarrow})$ by performing a least-squares fit.

2.3.2 Single-qubit gates

Single-qubit gates can be performed by applying radiation resonant with the carrier for a duration $T = \theta/\Omega_i$ with phase φ, where θ is the pulse area. The unitary

operation implemented by this pulse is

$$\hat{R}(\theta,\varphi) = \cos\frac{\theta}{2}\hat{1} - \mathrm{i}\sin\frac{\theta}{2}\left[\cos(\varphi)\hat{\sigma}_x + \sin(\varphi)\hat{\sigma}_y\right] \ . \tag{2.24}$$

The action of $\hat{R}(\theta,\varphi)$ on a qubit state can be visualised on the Bloch sphere as a rotation by an angle θ around an axis in the equatorial plane with polar angle φ. For instance, a 'π pulse' with phase $\varphi = 0$ implements the X gate, a 180° rotation around the $\hat{\sigma}_x$ axis. In order to rotate around the $\hat{\sigma}_y$ axis to implement a Y gate, the phase needs to be changed to $\varphi = \frac{\pi}{2}$. Another ubiquitous choice, the '$\frac{\pi}{2}$ pulse' takes the prepared $|{\downarrow}\rangle$ state to $|{+}\rangle = \frac{1}{\sqrt{2}}(|{\downarrow}\rangle + |{\uparrow}\rangle)$ – a prerequisite for any Ramsey experiment (see Section 2.4) and an indispensable element of most quantum circuits.

Rotations around the $\hat{\sigma}_z$ axis can be synthesised using three consecutive pulses:

$$\mathrm{e}^{\mathrm{i}\frac{\theta}{2}\hat{\sigma}_z} = \hat{R}\left(\frac{\pi}{2},0\right)\hat{R}\left(\theta,\frac{\pi}{2}\right)\hat{R}\left(\frac{\pi}{2},\pi\right) \ .$$

Alternatively, an altogether different effect can be used to obtain a $\hat{\sigma}_z$ rotation, namely the AC-Stark shift.

2.3.3 AC-Stark shift

So far, we have investigated resonant qubit-light interactions and now turn to the other extreme. Under illumination of radiation that is far off-resonant from any transition in the atom, the state populations do not change (rendering the phase of the field unimportant). Here we assume no spatial dependence of the intensity of the field such that the motion can be neglected (drop $\boldsymbol{k}\cdot\boldsymbol{r}$ coupling). The following derivation is for a single atom (drop subscript i). In the idealised picture of a two-level system with transition frequency ω_0 interacting with a field of frequency ω and coupling strength characterised by Rabi frequency Ω, the Hamiltonian is

$$\begin{aligned}\hat{H}_{\mathrm{AC}} &= \frac{\hbar}{2}\omega_0\hat{\sigma}_z + \frac{\hbar}{2}\Omega\left(\hat{\sigma}_+ + \hat{\sigma}_-\right)\left(\mathrm{e}^{-\mathrm{i}\omega t} + \mathrm{e}^{\mathrm{i}\omega t}\right) \\ &= \underbrace{\frac{\hbar}{2}\omega\hat{\sigma}_z}_{\hat{H}_{\mathrm{frame}}} + \frac{\hbar}{2}(\omega_0-\omega)\hat{\sigma}_z + \frac{\hbar}{2}\Omega\left(\hat{\sigma}_+ + \hat{\sigma}_-\right)\left(\mathrm{e}^{-\mathrm{i}\omega t} + \mathrm{e}^{\mathrm{i}\omega t}\right) \ ,\end{aligned}$$

where we have added zero in the last step to obtain a term with detuning $\Delta = \omega_0 - \omega$. Moving into the interaction picture with respect to $\hat{H}_{\text{frame}}$,

$$\begin{aligned}\mathcal{H}_{\text{AC}} &= \mathrm{e}^{\frac{\mathrm{i}}{\hbar}\hat{H}_{\text{frame}}t}(\hat{H}_{\text{AC}} - \hat{H}_{\text{frame}})\mathrm{e}^{-\frac{\mathrm{i}}{\hbar}\hat{H}_{\text{frame}}t} \\ &= \frac{\hbar}{2}\Delta\hat{\sigma}_z + \frac{\hbar}{2}\Omega\left(\mathrm{e}^{-\mathrm{i}\omega t}\hat{\sigma}_+ + \mathrm{e}^{\mathrm{i}\omega t}\hat{\sigma}_-\right)\left(\mathrm{e}^{-\mathrm{i}\omega t} + \mathrm{e}^{\mathrm{i}\omega t}\right) \\ &\overset{\text{RWA}}{\approx} \frac{\hbar}{2}\Delta\hat{\sigma}_z + \frac{\hbar}{2}\Omega\hat{\sigma}_x \ ,\end{aligned}$$

where rapidly oscillating terms $\propto \mathrm{e}^{\pm 2\mathrm{i}\omega t}$ were again neglected in the last step with the RWA. The eigenvalues of this Hamiltonian,

$$\begin{aligned}E_\pm &= \pm\frac{\hbar}{2}\sqrt{\Delta^2 + \Omega^2} \ , \\ &\approx \pm\left(\frac{\hbar}{2}\Delta + \hbar\frac{\Omega^2}{4\Delta}\right) \ \text{for} \ \Delta \gg \Omega,\end{aligned}$$

correspond to energies in the rotating frame where the unperturbed system ($\Omega \to 0$) appears to have energy levels $\pm\frac{\hbar}{2}\Delta$ that depend on the detuning of a field with zero amplitude. The actual shift of the levels must therefore be taken as the difference to the unperturbed case,

$$\Delta E_\pm = \pm\hbar\frac{\Omega^2}{4\Delta} \ ,$$

and the transition frequency shift $\Delta\omega_0 = \frac{1}{\hbar}(\Delta E_+ - \Delta E_-)$. In reality, many transitions contribute to the Stark shift of a level. Furthermore, the shift depends on the polarisation of the light field and the quantum numbers of the qubit level via the Rabi frequency, Ω. To probe the shift experimentally, spin-echo Ramsey experiments can be used, where a pulse of the detuned light is applied only to the first delay and nothing during the second delay to compensate for systematic frequency offsets from other sources.

The AC-Stark shift is a useful experimental tool, as it allows to lift degeneracies, detune levels from resonance with other control fields, e.g. for electromagnetically-induced transparency (EIT) cooling, to measure the intensity profile or the polarisation purity of laser beams. However useful, the Stark shift is a stubborn source of errors for laser-based gate schemes and precision metrology. The light shift

causes a $\hat{\sigma}_z$ rotation, which can only be corrected if other operations commute with this rotation. As this is not always possible, minimising the effect with great precision is the only option in these cases. It is thus expedient to perform $\hat{\sigma}_z \otimes \hat{\sigma}_z$ entangling gates, where the unwanted evolution can be reversed using a simple spin-flip π pulse during the gate.

2.3.4 Light shift gate

We implement a two-qubit gate mechanism based on the light shift coupled with the motion – a spin-dependent 'light shift force'. We have seen above that radiation far-detuned from any transition in an atom shifts the energy levels. This is also true for the two laser beams that drive Raman transitions. Raman lasers are operated at a common detuning from a dipole transition (e.g. $S-P$) and their beat note can be adjusted to match the frequency of a target transition ($\sim$ kHz $-$ GHz). The qubit is assumed to reside in the $S_{1/2}$ manifold. In the case of $^{43}Ca^+$, we use the hyperfine levels $|S_{1/2},\, F{=}4,\, m_F{=}4\rangle = |{\downarrow_{\mathrm{L}}}\rangle$ and $|S_{1/2},\, F{=}3,\, m_F{=}3\rangle = |{\uparrow_{\mathrm{L}}}\rangle$ and refer to this qubit, $\{|{\downarrow_{\mathrm{L}}}\rangle, |{\uparrow_{\mathrm{L}}}\rangle\}$, as the logic qubit throughout this thesis (see Figure 3.2). In the case of $^{88}Sr^+$, we use the network qubit (ground state Zeeman levels, see Figure 3.2), $\{|{\downarrow_{\mathrm{N}}}\rangle, |{\uparrow_{\mathrm{N}}}\rangle\}$. The following treatment is general, but we will refer to these levels specifically in examples.

The Rabi frequency for transitions *between* qubit levels, Ω_0, and for the light shift of *individual* qubit levels, $\Omega_\uparrow$ and $\Omega_\downarrow$, can be calculated using transition matrix elements between the $S_{1/2}$ ground state and excited states $|e\rangle$ in the P manifolds, $\mathcal{M}_{1/2}$ and $\mathcal{M}_{3/2}$: [Sch18]

$$\Omega_0 \propto \sum_{J=\frac{1}{2},\frac{3}{2}} \frac{1}{\Delta_J} \sum_{|e\rangle \in \mathcal{M}_J} \langle \downarrow | \hat{\boldsymbol{d}} \cdot \boldsymbol{\epsilon}_1 | e \rangle \langle e | \hat{\boldsymbol{d}} \cdot \boldsymbol{\epsilon}_2 | \uparrow \rangle \ ,$$

$$\Omega_\uparrow \propto \sum_{J=\frac{1}{2},\frac{3}{2}} \frac{1}{\Delta_J} \sum_{|e\rangle \in \mathcal{M}_J} \langle \uparrow | \hat{\boldsymbol{d}} \cdot \boldsymbol{\epsilon}_1 | e \rangle \langle e | \hat{\boldsymbol{d}} \cdot \boldsymbol{\epsilon}_2 | \uparrow \rangle \ ,$$

$$\Omega_\downarrow \propto \sum_{J=\frac{1}{2},\frac{3}{2}} \frac{1}{\Delta_J} \sum_{|e\rangle \in \mathcal{M}_J} \langle \downarrow | \hat{\boldsymbol{d}} \cdot \boldsymbol{\epsilon}_1 | e \rangle \langle e | \hat{\boldsymbol{d}} \cdot \boldsymbol{\epsilon}_2 | \downarrow \rangle \ ,$$

where $\hat{\boldsymbol{d}}$ is the dipole operator, $\boldsymbol{\epsilon}_1$ and $\boldsymbol{\epsilon}_2$ are the polarisation vectors of the two beams, and Δ_J are the detunings of the Raman laser from the respective P_J manifold. The carrier Rabi frequency for qubits with $|\Delta m_F| = 1$ evaluates to

$$\Omega_0 \propto \mathcal{E}^2 g_{\uparrow\downarrow}^{\text{magn}} \frac{\omega_P}{\Delta(\Delta - \omega_P)} \left[(\boldsymbol{\epsilon}_1 \cdot \boldsymbol{e}_{-1})(\boldsymbol{\epsilon}_2 \cdot \boldsymbol{e}_0) + (\boldsymbol{\epsilon}_1 \cdot \boldsymbol{e}_0)(\boldsymbol{\epsilon}_2 \cdot \boldsymbol{e}_1)\right] \ , \tag{2.25}$$

where ω_P is the fine structure splitting between the $P_{1/2}$ and $P_{3/2}$ levels, $\mathcal{E}$ the electric field magnitude, and $g_{\uparrow\downarrow}^{\text{magn}}$ a numerical factor that depends on the magnetic structure of the isotope and the quantum numbers of the chosen qubit state. For the network qubit in $^{88}\text{Sr}^+$ and the logic qubit in $^{43}\text{Ca}^+$, we obtain $g_{\uparrow\downarrow_\text{N}}^{\text{magn}} = \frac{\sqrt{2}}{6}$ and $g_{\uparrow\downarrow_\text{L}}^{\text{magn}} = \frac{\sqrt{7}}{12}$, respectively.

The key realisation for the light shift gate is that for polarisations without π-polarised component, i.e.,

$$\boldsymbol{\epsilon}_1 \cdot \boldsymbol{e}_0 = \boldsymbol{\epsilon}_2 \cdot \boldsymbol{e}_0 = 0 \ , \tag{2.26}$$

the individual light shifts $\Omega_\downarrow$, $\Omega_\uparrow$ are adjustable (see Figure 2.6), but the carrier Rabi frequency (Equation (2.25)) vanishes. The consequence of $\Omega_0 = 0$ is the elimination of the $\hat{\sigma}_x$ term, the interaction Hamiltonian (2.19) that was responsible for all qubit dynamics discussed so far. Without this term, the way is paved for a pure $\hat{\sigma}_z^{\otimes N}$ interaction with all of its benefits.

In the present case, the AC-Stark shift between a single qubit level and all P levels gives rise to a new term,

$$\hat{H}^{\text{LS}}(t) = \hat{1}^{\otimes N} \sum_{i=1}^{N} \hat{H}_i^{\text{LS}}(t)$$

in Equation (2.18), which, after adiabatic elimination of the P levels, commutes with $\hat{\sigma}_z^{\otimes N}$:

$$\begin{aligned}\hat{H}_i^{\text{LS}}(t) &= \sum_{s=\downarrow,\uparrow} -\frac{\hbar}{2}\Omega_{i,s} \left|s\right\rangle\!\left\langle s\right|_i \left(\mathrm{e}^{\mathrm{i}(\boldsymbol{k}\cdot\hat{\boldsymbol{r}}_i - \omega t + \phi)} + \mathrm{e}^{-\mathrm{i}(\boldsymbol{k}\cdot\hat{\boldsymbol{r}}_i - \omega t + \phi)}\right) \\ &\overset{\text{LDA}}{\approx} \sum_{s=\downarrow,\uparrow} -\frac{\hbar}{2}\Omega_{i,s} \left|s\right\rangle\!\left\langle s\right|_i \left[\mathrm{e}^{-\mathrm{i}(\omega t - \varphi_i)} \left(1 + \sum_{\alpha\in\mathcal{N}} \mathrm{i}\eta_{\alpha,i}(\hat{a}_\alpha + \hat{a}_\alpha^\dagger)\right) + \text{h.c.}\right] \ ,\end{aligned}$$

where the notation $|s\rangle\langle s|_i$ denotes the projector on the qubit state $|s\rangle$ of the i^{th} atom. This implies that identities $\hat{1}_{j\neq i}$ act on all other atoms. Proceeding analogously to above, we move into the interaction picture with respect to $\hat{H}_0$:

$$\begin{aligned}\hat{\mathcal{H}}_{\text{LS}}(t) = \hat{1}^{\otimes N}\sum_{i=1}^{N}\sum_{s=\downarrow,\uparrow} -\frac{\hbar}{2}\Omega_{i,s}\,|s\rangle\langle s|_i \\ \left[2\cos(\omega t-\varphi_i) + \left(\mathrm{e}^{-\mathrm{i}(\omega t-\varphi_i)} - \mathrm{e}^{\mathrm{i}(\omega t-\varphi_i)}\right)\sum_{\alpha\in\mathcal{N}}\mathrm{i}\eta_{\alpha,i}\left(\mathrm{e}^{-\mathrm{i}\omega_\alpha t}\hat{a}_\alpha + \mathrm{e}^{\mathrm{i}\omega_\alpha t}\hat{a}_\alpha^\dagger\right)\right] \\ \overset{\text{RWA}}{\approx} \hat{1}^{\otimes N}\sum_{i=1}^{N}\sum_{s=\downarrow,\uparrow} -\frac{\hbar}{2}\Omega_{i,s}\,|s\rangle\langle s|_i \\ \left[2\cos(\omega t-\varphi_i) - \sum_{\alpha\in\mathcal{N}}\mathrm{i}\eta_{\alpha,i}\left(\mathrm{e}^{-\mathrm{i}(\delta_\alpha t+\varphi_i)}\hat{a}_\alpha - \mathrm{e}^{\mathrm{i}(\delta_\alpha t+\varphi_i)}\hat{a}_\alpha^\dagger\right)\right]\,,\end{aligned} \tag{2.27}$$

where $\delta_\alpha = \omega_\alpha - \omega$ denotes the detuning of the driving field from a motional mode, and fast oscillations $\propto \mathrm{e}^{\mathrm{i}(\omega_\alpha+\omega)t}$ are neglected in the RWA. The terms $\propto \Omega_{i,s}\,|s\rangle\langle s|_i\cos(\omega t-\varphi_i)$ cause time-dependent light shifts of the individual states independent of each other and the motion. By pulse shaping using a smooth profile $\Omega_{i,s}(t)$, with $\Omega_{i,s}(t) \ll \omega$ and pulse duration $\gg \frac{1}{\omega_\alpha}$, i.e. ramping the Rabi frequency over multiple periods of the relevant motional modes, the thereby accumulated single-qubit phases can be made negligible [Bal14]. The resulting interaction Hamiltonian for the light shift interaction on multiple ions and multiple modes is then

$$\hat{\mathcal{H}}_{\text{LS}}(t) = \hat{1}^{\otimes N}\sum_{i=1}^{N}\sum_{s=\downarrow,\uparrow}\frac{\hbar}{2}\Omega_{i,s}(t)\,|s\rangle\langle s|_i\sum_{\alpha\in\mathcal{N}}\mathrm{i}\eta_{\alpha,i}\left(\mathrm{e}^{-\mathrm{i}(\delta_\alpha t+\varphi_i)}\hat{a}_\alpha - \mathrm{e}^{\mathrm{i}(\delta_\alpha t+\varphi_i)}\hat{a}_\alpha^\dagger\right)\,. \tag{2.28}$$

Equation (2.28) gives rise to a spin-dependent force. In the polarised wave picture, the interference of the two Raman beams beating at the difference frequency ω and polarised linearly in mutually orthogonal directions, results in a travelling wave with polarisation transitioning through regions that are linear, left circular, linear, right circular, and so on, at any given point in time, with a spatial periodicity depending on the beat note frequency. As the light shift of the spin states, $s \in \{\downarrow,\uparrow\}$ varies with the field's polarisation (see Figure 2.6), the energy $E_s(\boldsymbol{r})$ is position-dependent and implies a spin-dependent force $\boldsymbol{F}_s = e\boldsymbol{\nabla}E_s(\boldsymbol{r})$.

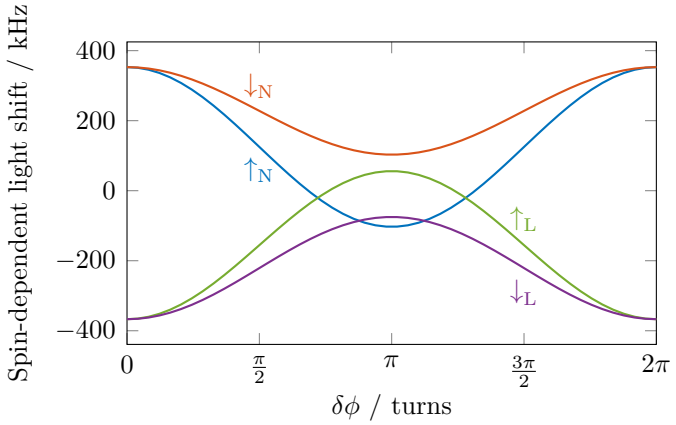

Figure 2.6: The spin-dependent light shift Rabi frequency generated by a pair of Raman laser beams (son_0 and son_1) on the states comprising the $^{88}\text{Sr}^+$ network qubit and the $^{43}\text{Ca}^+$ logic qubit (see level diagram in Figure 3.2). In the geometry shown in Figure 2.5, the π polarisation component of both beams is zero. The polarisation of son_1 is fixed to $\boldsymbol{\epsilon}_1 = \frac{1}{\sqrt{2}}(\boldsymbol{e}_{+1} + \boldsymbol{e}_{-1})$ and the ellipticity of son_0 is varied: $\boldsymbol{\epsilon}_2 = \frac{1}{\sqrt{2}}\left(\boldsymbol{e}_{+1} + \mathrm{e}^{\mathrm{i}\delta\phi}\boldsymbol{e}_{-1}\right)$. The curves are calculated for a Raman laser wavelength of 401.543 nm and a power of 1 mW per beam at a waist radius of 15 µm.

Experimental scenario. To be more concrete, let $N = 2$, $\boldsymbol{k} = \boldsymbol{k}_1 - \boldsymbol{k}_2 = \boldsymbol{z}$ and $\boldsymbol{k}_1 \cdot \boldsymbol{k}_2 = 0$, i.e., consider two ions illuminated by a pair of Raman lasers aligned at 45° to the $\boldsymbol{z}$ axis, such that the effective wavevector $\boldsymbol{k}$ only couples to the axial modes of motion (see Figure 2.5).

We deliberately choose to align them along the axis because the radial modes, which would otherwise be preferable due to their higher frequency, do not couple well to both ions in a mixed-species crystal. Without loss of generality, we set the static phase of the first ion to $\phi_1 = 0$. Consequently, $\phi_2 = \frac{2\pi}{\lambda_{\text{eff}}}d$, where d is the inter-ion distance (see Equation (2.12)) and $\lambda_{\text{eff}} = \frac{\lambda_{\text{R}}}{\sqrt{2}}$ is the wavelength of the Raman laser projected onto the axis.

The efficiency of the light shift gate depends on the axial confinement via d: for $\phi_2 \equiv 0 \pmod{2\pi}$, both ions experience a light shift force in the same direction, whereas for $\phi_2 \equiv \pi \pmod{2\pi}$, the force acts in opposite directions. Hence, for coupling to the axial IP (OOP) mode, the former (latter) configuration is more efficient. For a same-species crystal, the coupling even reaches zero on the suppressed mode when the force couples maximally to the other mode because the mode participation vectors are symmetric for equal masses (see Section 2.2.2). This

situation is exploited for experimentally finding the optimal inter-ion distance (see Section 4.2.5). Between the two axial modes, the OOP mode offers a lower heating rate, as the electric fields that cause heating are approximately uniform over the extent of the crystal and thus induce predominantly common-mode oscillations (see Section 2.2.4). We therefore mean to excite the anti-symmetric OOP mode using the spin-dependent force to generate entanglement while seeking to suppress excitations on the IP mode. To this end, we require an inter-ion distance such that $\phi_2 \equiv \pi \pmod{2\pi}$, which is found at an offset of $\frac{\lambda_{\text{eff}}}{2}$ from integer multiples of λ_{eff} (see vertical grid lines in Figure 2.3).

2.4 Ramsey experiments

The Ramsey technique has been among the most impactful inventions of quantum technology so far. It is based on the evolution of a superposition state,

$$\exp(-\mathrm{i}E_0 t/\hbar)\,|0\rangle + \exp(-\mathrm{i}E_1 t/\hbar)\,|1\rangle \ ,$$

whose phase depends on the energy difference $\hbar\omega_0 = E_1 - E_0$ between the two states and the duration t of the free evolution. The initial phase at $t = 0$ is arbitrarily chosen to be zero. The probability of finding the system in the state $|0\rangle + \exp(\mathrm{i}\varphi)\,|1\rangle$ is $\cos^2\left(\frac{1}{2}(\omega_0 t + \varphi)\right)$, where $\varphi \in [0, 2\pi)$ is the analysis phase. Assuming $\varphi = \omega_{\text{LO}} t$ is the phase of a local oscillator, such as a laser, RF or microwave signal, small frequency differences $(\omega_0 - \omega_{\text{LO}})$ can be resolved with increasing precision as the probe duration t is increased. This technique is particularly well-suited for timekeeping applications, such as atomic clocks. Moreover, it enables precise measurements of any effect that influences the energy difference between the states in the superposition, such as shifts due to electric or magnetic fields. However, there is a limit to the maximum duration t which can be used to probe the system — decoherence effects can be due to imperfections in either the system holding the superposition state (e.g. due to uncontrolled environmental parameters which affect the state energies) or the local oscillator (e.g. due to phase noise).

2.4.1 Frequency domain analysis

To quantify the effect that a noisy energy difference has on the coherence of the superposition state, we use the Hamiltonian

$$\hat{\mathcal{H}}(t) = -\frac{\hbar}{2}(\bar{E}_1 - \bar{E}_0)\hat{\sigma}_z - f(t)\hat{\sigma}_z \ ,$$

where $f(t)$ is the unwanted time-dependent energy shift and $\bar{E}$ is the time-averaged value of the state energy. In the following, we average the dynamics over an ensemble of functions f that are drawn from a stationary Gaussian stochastic density, and evaluate the expectation $\mathbb{E}$. The power spectral density of the noise is equivalent to the Fourier-transform $\tilde{K}(\omega)$ of the covariance $K(t-t') = \mathbb{E}[f(t)f(t')] = \iint_{-\infty}^{\infty} f_1 f_2 p(f_1, f_2, t, t')\,\mathrm{d}f_1\,\mathrm{d}f_2$, where p denotes the joint probability density function to find f in $[f_1, f_1 + \mathrm{d}f_1]$ at time t and also in $[f_2, f_2 + \mathrm{d}f_2]$ at t'. A useful formula is [Pre06]

$$\mathbb{E}\left[\exp\left(\int_a^b f(t)g(t)\,\mathrm{d}t\right)\right] = \exp\left(\frac{1}{2}\iint_a^b g(t)K(t-t')g(t')\,\mathrm{d}t\,\mathrm{d}t'\right) \ . \tag{2.29}$$

In the interaction picture, the time evolution of $\hat{\rho} = \rho_{11}\,|1\rangle\langle 1| + \rho_{00}\,|0\rangle\langle 0| + \rho_{01}\,|0\rangle\langle 1| + \rho_{10}\,|1\rangle\langle 0|$ is

$$\begin{aligned}\hat{\rho}(t) &= \exp\left(\frac{\mathrm{i}}{\hbar}\int_0^t f(t')\,\mathrm{d}t'\hat{\sigma}_z\right)\hat{\rho}(0)\exp\left(-\frac{\mathrm{i}}{\hbar}\int_0^t f(t')\,\mathrm{d}t'\hat{\sigma}_z\right) \\ &= \rho_{11}(0)\,|1\rangle\langle 1| + \rho_{00}(0)\,|0\rangle\langle 0| + \rho_{01}(0)\exp\left(\frac{2\mathrm{i}}{\hbar}\int_0^t f(t')\,\mathrm{d}t'\right)|1\rangle\langle 0| \\ &\quad + \rho_{10}(0)\exp\left(-\frac{2\mathrm{i}}{\hbar}\int_0^t f(t')\,\mathrm{d}t'\right)|0\rangle\langle 1| \ .\end{aligned} \tag{2.30}$$

From Equation (2.30) it becomes apparent that the noise can cause dephasing, as the diagonal elements of $\hat{\rho}$ remain unchanged, but the off-diagonal elements evolve. Using Equation (2.29), the expected decay of the off-diagonal elements after a waiting time τ is

$$\begin{aligned}\mathbb{E}\left[\exp\left(\pm\frac{2\mathrm{i}}{\hbar}\int_0^\tau f(t)\,\mathrm{d}t\right)\right] &= \exp\left(-\frac{2}{\hbar^2}\int_0^\tau\int_0^\tau K(t-t')\,\mathrm{d}t\,\mathrm{d}t'\right) \\ &= \exp\left(-\frac{1}{\pi\hbar^2}\int_{-\infty}^{\infty}\tilde{K}(\omega)\int_0^\tau\int_0^\tau \mathrm{e}^{-\mathrm{i}\omega(t-t')}\,\mathrm{d}t\,\mathrm{d}t'\,\mathrm{d}\omega\right) \\ &= \exp\left(-\frac{1}{\pi\hbar^2}\int_{-\infty}^{\infty}\tilde{K}(\omega)W(\omega)\,\mathrm{d}\omega\right)\end{aligned} \tag{2.31}$$

with the spectral window

$$W(\omega) = \frac{1}{\omega^2}\left[2\sin\left(\frac{\omega\tau}{2}\right)\right]^2 . \tag{2.32}$$

Equation (2.31) shows that the Ramsey experiment is subject to decoherence due to low-frequency noise sources, particularly at frequencies $|\omega| < 2\pi/\tau$. White noise, for example, causes an exponential decay of the coherence $\propto \exp(-\Gamma\tau)$; coloured noise generally results in much more complex behaviour. As we will see below, dynamical decoupling sequences modify the shape of this spectral window, enabling the controlled suppression or enhancement of chosen frequency bands.

2.4.2 Dynamical decoupling

The detrimental effects of decoherence have stimulated the development of methods that make the Ramsey technique more robust. Most of these techniques stem from research on nuclear magnetic resonance (NMR) technology, where decoherence effects are particularly strong.

The Hahn spin-echo [Hah50] technique forms the basis of these protocols, where a π pulse (see Section 2.3.2) flips the state populations. If a dynamical decoupling sequence contains many π pulses, composite sequences, such as XY4 (Section 2.4.2.2) or Knill dynamical decoupling (KDD) (Section 2.4.2.3), are favourable for they reduce the sensitivity to common pulse imperfections.

2.4.2.1 CPMG

The $1/f$ noise amplitude scaling 'law' and the sensitivity curve of a Ramsey experiment, characterised by the filter function Equation (2.32), motivates the use of techniques that target low-frequency components in particular. The simplest method to deal with such noise is the Hahn spin-echo technique [Hah50]. By applying a π pulse mid-way through the delay, the direction of the phase evolution is reversed and returns to the initial state after the second half of the evolution. With spin-echo, the decay of the off-diagonal elements (Equation (2.31)) is not sensitive

to static offsets (zero frequency noise) anymore, as can be seen in Figure 2.7 comparing the modified filter function

$$W(\omega) = \frac{1}{\omega^2}\left[2\sin\left(\frac{\omega T}{4}\right)\right]^4 \tag{2.33}$$

to the one without spin-echo (Equation (2.32)).

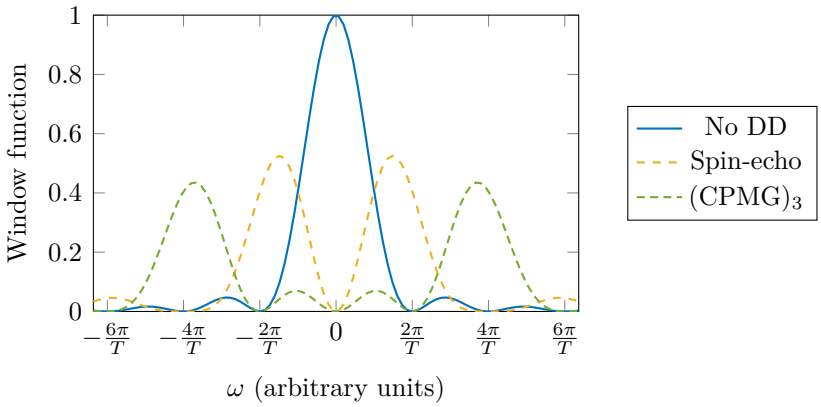

Figure 2.7: Spectral windows quantifying the weight of different noise frequencies causing dephasing in a Ramsey (solid, no spin flips), spin-echo (dashed, one spin flip) and $CPMG_3$ (densely dashed, three spin flips) experiment.

By extension, adding more spin-echo π pulses and thereby decreasing the inter-pulse delays, τ, increases the passband frequency $\omega_{\text{peak}} \sim \frac{\pi}{\tau}$ (see Figure 2.7). The two most successful methods, Carr-Purcell Meiboom-Gill (CPMG) and Uhrig dynamical decoupling (UDD), only differ in the pulse timing: the $(CPMG)_n$ sequence consists of n equidistantly-spaced π pulses, whereas the $(UDD)_n$ distributes them in a way that yields maximum suppression of low-frequency noise. Experimentally, however, the two methods have been found to perform similarly well under the same conditions [Szw+11]. In this thesis, only sequences with equidistant pulses are used.

If the π pulses used in the spin-echo, CPMG, and UDD sequences rotate around the same axis, inaccuracies accumulate as an error that depends on the initial state of the qubit; given an initial Y eigenstate, pulses that rotate around the Y axis do not alter this state, but still effectively decouple it from external noise sources. Even in a noise-free environment, any other initial state would rapidly diverge with

increasing number of imperfect spin flip pulses.

The following two 'universal' sequences (see Section 2.4.2.2 and Section 2.4.2.3) achieve uniform suppression of decoherence independent of the initial state of the qubit by incorporating composite pulse techniques.

2.4.2.2 Periodic dynamical decoupling

A concatenation of $(\mathrm{CPMG})_2$ sequences in the X and the Y basis, i.e.

$$\left(\frac{\tau}{2} - \pi|_x - \tau - \pi|_y - \frac{\tau}{2}\right)^2 , \tag{2.34}$$

where τ denotes the inter-pulse spacing, can be used to suppress decoherence while compensating π pulse imperfections equally for all initial states. The alternating structure of $\pi|_x$ and $\pi|_y$ pulses adds robustness to the sequence, as it partially compensates for errors in the pulse area. As this sequence implements the identity operation overall, it can be repeated as required to achieve the targeted inter-pulse spacing τ for optimal suppression of environmental noise.

2.4.2.3 Knill dynamical decoupling

While the $\mathsf{XY}4$ sequence (Equation (2.34)) has the required properties to suppress decoherence of arbitrary initial states, its robustness to pulse imperfections is limited. More effective composite pulse techniques were developed to reduce the sensitivity of pulses to as many error sources as possible, foremost pulse area and frequency detuning errors. As the number of π pulses can grow large (~ 100), this property is highly desirable. The 20-pulse KDD sequence,

$$\mathrm{KDD} = \left[\mathrm{KDD}_0 - \mathrm{KDD}_{\frac{\pi}{2}}\right]^2 ,$$
$$\mathrm{KDD}_\phi = \frac{\tau}{2} - \pi|_{\frac{\pi}{6}+\phi} - \tau - \pi|_\phi - \tau - \pi|_{\frac{\pi}{2}+\phi} - \tau - \pi|_\phi - \tau - \pi|_{\frac{\pi}{6}+\phi} - \frac{\tau}{2} ,$$

combines the spectral noise filtering by dynamical decoupling with the pulse error suppression of the Knill composite pulse sequence. This sequence excels in comparison with other sequences [SÁS11] and was used to achieve world-record coherence results with trapped ions [Wan+21].

2.5 Randomised benchmarking

As quantum computers grow in size and complexity, it becomes increasingly difficult to assess their performance comprehensively. Understanding the errors involved in a few qubits is manageable, but as the number of qubits increases, the number of free parameters becomes exponentially larger, rendering a full characterisation impossible. Furthermore, different quantum algorithms and tasks have their unique requirements and complexities, and devising a benchmark that accurately captures a quantum computer's overall capability is still an active area of research.

Randomised benchmarking (RBM) [EAŻ05; MGE12; Kni+08] involves running many random sequences of Clifford gates that have the useful property of being efficiently simulatable on classical computers, which ensures the scalability of this approach. The method works by comparing the experimental results with the expected outcomes of each sequence to obtain an average 'survival probability', $S(m)$, which decays with the number of Clifford gates in the sequence, m, and thereby reveals the average error per Clifford gate from the decay rate, and the state preparation and measurement (SPAM) error via $S(0)$.

Protocol 2.5.1. *Randomised benchmarking.*

- Repeat these steps for different randomisations and sequence lengths, m:
  1. Prepare all qubits in $|{\downarrow}\rangle$.
  2. Apply $m-1$ Clifford gates, $\hat{\mathcal{S}}_{m-1} = \hat{C}_{m-1} \cdots \hat{C}_1$, each selected uniformly at random from the n-qubit Clifford group.
  3. Apply one last Clifford gate to the qubits, which is chosen as the inverse of the sequence up to a random Pauli gate on each qubit, i.e. $\hat{\Sigma} = \hat{\sigma}_{k_1} \otimes \cdots \otimes \hat{\sigma}_{k_n}$ with $\hat{\sigma}_{k_i}$ chosen uniformly at random from $\{\hat{1}, \hat{\sigma}_x, \hat{\sigma}_y, \hat{\sigma}_z\}$. The final Clifford gate is therefore $\hat{C}_m = (\hat{\Sigma}\hat{\mathcal{S}}_{m-1})^{-1}$. The resulting sequence implements $\hat{\Sigma}^{-1}$, which randomises the expected outcome of each qubit between $\downarrow$ and $\uparrow$ and thereby avoids systematics due to SPAM errors.

4. Measure all qubits in the $\hat{\sigma}_z$ basis. The probability of finding them in the expected eigenstate is called survival probability, $S(m)$.

- Fit a decay model (see Equation (2.35) and Equation (2.36)) to the measured survival probabilities $S(m)$ to extract the average error rate.

The n-qubit Clifford group $\boldsymbol{C}_n = \{\hat{C}_i\}_i$ is here defined as the normaliser of the Pauli quotient group,[12]

$$\boldsymbol{P}_n/\boldsymbol{U}(1) = \left\{\hat{\sigma}_{k_1} \otimes \cdots \otimes \hat{\sigma}_{k_n} \,|\, \hat{\sigma}_{k_i} \in \{\hat{1}, \hat{\sigma}_x, \hat{\sigma}_y, \hat{\sigma}_z\}\right\} \ ,$$

where $\boldsymbol{U}(1)$ is the unitary group of degree 1.

Protocol 2.5.1 yields a survival probability after application of a sequence that is equivalent to a single Pauli gate in the noise-free case. In the presence of a noise channel, Λ, the fidelity of this identity is given by the survival probability averaged over all possible initial states $|\psi\rangle$, [MGE12]

$$\bar{\mathcal{F}} = \int \langle\psi|\Lambda[|\psi\rangle\langle\psi|]|\psi\rangle \ \mathrm{d}\psi \ .$$

Crucially, the Clifford group is a unitary 2-design, which means that after 'twirling' the noise channel Λ over the Clifford group, i.e., averaging Λ under the composition $\mathcal{C}_i^\dagger \circ \Lambda \circ \mathcal{C}_i$ for Clifford operations $\mathcal{C}_i[\hat{\rho}] = \hat{C}_i\hat{\rho}\hat{C}_i^\dagger$ chosen uniformly from the Clifford group, the noise becomes depolarising,

$$\sum_i (\mathcal{C}_i^\dagger \circ \Lambda \circ \mathcal{C}_i)[\hat{\rho}] \sim p\hat{\rho} + (1-p)\frac{\hat{1}}{d} \ ,$$

where d is the dimension of the Hilbert space. The twirling operation preserves the fidelity $\bar{\mathcal{F}}$ of Λ [Dan+09], which connects it to the measurable depolarising probability,

$$p = \frac{\bar{\mathcal{F}}d - 1}{d-1} \ .$$

Moreover, the Gottesman-Knill theorem [Got98] states that circuits composed only of Clifford gates can be simulated efficiently in polynomial time on a classical computer.

[12] The elements g of a subgroup H of a group G that fulfil $g^{-1}Hg = H$ are said to be the normaliser $N_G(H)$ with respect to H. The normaliser $N_G(H)$ is also a subgroup of G, which trivially contains H.

These two properties, the 'lumping' of arbitrary errors into a simple depolarising channel and the scalability guaranteed by the Gottesman-Knill theorem, make this method a useful benchmarking tool.

The decay of the survival probability, $S(m)$, can be described using the model [MGE12]

$$S^{(1)}(m) = \frac{1}{d} + B_1 p^m + C_1(m-1)(q-p^2)p^{m-2} \ , \tag{2.35}$$

where d is the dimension of the Hilbert space, B_1 and C_1 account for SPAM error offsets, and $(q-p^2)$ quantifies the degree of gate- and time-dependence of the errors. For gate- and time-independent errors, the survival probability (Equation (2.35)) simply decays exponentially:

$$S^{(0)}(m) = \frac{1}{d} + B_0 p^m \ . \tag{2.36}$$

The constraints for these models are, $\forall m$,

$$\begin{aligned} \frac{1}{d} < S(m) \leq 1 \ , \\ S(m+1) \leq S(m) \ . \end{aligned} \tag{2.37}$$

3 Experimental setup

Contents

In this chapter, I introduce the experimental platform that enabled the experiments described in later chapters. The first part gives a brief summary of

important standard techniques, such as trapping ions, driving them dissipatively with lasers for cooling, state preparation and readout (Section 3.1), and controlling their position using electric fields (Section 3.2). The second part gives more detail on major sections of the experimental system which I developed or modified myself (Section 3.3, Section 3.4.3, and Section 3.4.4).

3.1 Standard techniques in ion trapping

3.1.1 Ion trap

The experiments presented in this thesis were performed with surface Paul traps (Sandia *HOA2*). The design of these traps combines segmented electrodes (70 µm pitch) to enable ion transport and a central slot (60 µm width) to allow imaging of the ions from both sides of the trap (NA 0.25 to the back side). We drive the RF rails with $\sim 160\,\mathrm{V}$ at $\sim 50\,\mathrm{MHz}$ to generate radial confinement, and supply $\pm 10\,\mathrm{V}$ to the 15 central DC electrode pairs, as well as to compensation electrodes, which extend along the entire length of the trap. More details about the ion trap assembly can be found in [Mau16; Ste19].

3.1.2 Atomic species

Which atomic species is used in an experiment depends on many variables. However, a convenient choice of isotope fulfils the following criteria:

- The isotope must be sufficiently stable and abundant, as the atomic source is preferably kept inside the UHV chamber for weeks to years at a time.
- The isotope must have a level structure permitting an efficient cooling scheme, or be compatible with another species for sympathetic cooling.
- The wavelengths required to control the electronic states of the isotope must be accessible with current technology.

The electronic configuration of singly-ionised alkaline earth metals, certain transition metals, and lanthanides resembles that of atomic hydrogen, which is well understood and simple, and thus facilitates experimental control schemes in the quantum regime.

The optimal choice of ion depends on the application at hand – for atomic clocks, minimising systematic errors due to energy shifts takes precedence over the ability to perform high-fidelity quantum gates, which are, however, a key requirement for universal quantum computing; for quantum network interfaces, the species should permit an efficient scheme for generating single photons. Table 3.1 lists isotopes that have been trapped in the past alongside with properties that are relevant for ion trapping. The nuclear spin I determines the hyperfine structure of the species; isotopes with $I = 0$ are generally easier to be cooled, but don't offer magnetic field-insensitive qubits, which is one of the benefits of isotopes with $I > 0$. For those isotopes with hyperfine structure, the nuclear g factor, g_{nuc}, determines the hyperfine splitting; large hyperfine spitting is generally good for reducing quantum logic errors.

Atomic species are often chosen according to simulated properties, such as fundamental error sources pertinent to quantum logic gates. For instance, the leading fundamental error for laser-driven Raman gates is photon scattering, which was calculated early on for $^{43}Ca^{+}$ [Ste97], $^{9}Be^{+}$ and $^{199}Hg^{+}$ [Win+98] in the limit of large Raman laser detunings. Detailed calculations followed with increasing levels of generality [Win+03; Oze+07; Uys+10], and are continuing to be improved [Moo+23].[1] Experimental tests of these models have been performed on several occasions [Oze+05; Bog+23].

Among many suitors for quantum logic applications, $^{43}Ca^{+}$ has shown some of the best qubit performances in any platform, with high-fidelity state preparation and readout (with 7×10^{-4} error) [Har+14], single-qubit gates (laser-based with 7×10^{-5} error), and two-qubit gates (laser-based with 1×10^{-3} error) [Bal+16; Har+14] having been demonstrated in this group. Moreover, the hyperfine structure of the ground $S_{1/2}$ ground state features magnetic field-insensitive transitions at particular magnetic field strengths, enabling long coherence times ($T_2^* > 45\,\mathrm{s}$) [Luc+07]. An added benefit is that the shortest laser wavelength involved in

[1] While scattering errors pose fundamental limits to the gate fidelities, the issue can be avoided by performing laser-free gates using magnetic field gradients [MW01]. Here, the mass of the ion and its magnetic structure plays a key role.

Isotope	I	g_{nuc}	Abundance	$\lambda_{\mathrm{Doppler}}$	Reference
$^{9}Be^{+}$	3/2	-0.78495	100 %	313 nm	[Tur+98]
$^{24}Mg^{+}$	0	0	78.99 %	280 nm	[Ber+03]
$^{26}Mg^{+}$	0	0	11.01 %		
$^{25}Mg^{+}$	5/2	-0.34218	10.00 %		[Osp+11]
$^{27}Al^{+}$	5/2	+1.4566028	100 %	—	Atomic clock [Bre+19]
$^{40}Ca^{+}$	0	0	96.941 %	397 nm	[Luc+04a]
$^{42}Ca^{+}$	0	0	0.647 %		
$^{44}Ca^{+}$	0	0	2.086 %		
$^{46}Ca^{+}$	0	0	0.004 %		
$^{48}Ca^{+}$	0	0	0.187 %		
$^{43}Ca^{+}$	7/2	-0.37637	0.135 %		Clock qubit [Luc+07]
$^{64}Zn^{+}$	0	0	48.63 %	203 nm	[Mat+03]
$^{66}Zn^{+}$	0	0	27.90 %		
$^{68}Zn^{+}$	0	0	18.75 %		
$^{70}Zn^{+}$	0	0	0.62 %		
$^{67}Zn^{+}$	5/2	+0.350192	4.10 %		—
$^{86}Sr^{+}$	0	0	9.86 %	422 nm	[LBC11]
$^{87}Sr^{+}$	9/2	-0.24284	7.00 %		[Bar+03]
$^{88}Sr^{+}$	0	0	82.58 %		Networking [Bro07]
$^{111}Cd^{+}$	1/2	-1.18977	12.80 %	215 nm	Ion-photon entanglement [Bli+04]
$^{112}Cd^{+}$	0	0	24.13 %		[Bli+02]
$^{114}Cd^{+}$	0	0	28.73 %		
$^{115}In^{+}$	9/2	+1.2313	95.71 %	231 nm	Atomic clock [Kel15; PHW94]
$^{133}Ba^{+}$	1/2	-1.5433	0 %	493 nm	Clock qubit [Chr+20]
$^{135}Ba^{+}$	3/2	+0.55863	6.592 %		[BW83]
$^{137}Ba^{+}$	3/2	+0.62491	11.232 %		[An+22]
$^{138}Ba^{+}$	0	0	71.698 %		[Cro+19; HSQ22]
$^{171}Yb^{+}$	1/2	+0.98734	14.28 %	369 nm	Clock qubit [Lan+22]
$^{172}Yb^{+}$	0	0	21.83 %		Sympathetic cooling [Cet+22]
$^{173}Yb^{+}$	5/2	-0.2592	16.13 %		
$^{174}Yb^{+}$	0	0	31.83 %		[Vri+19]
$^{175}Lu^{+}$	7/2	+0.6378	97.4 %	—	[Arn+16]
$^{176}Lu^{+}$	7	+0.4517	2.6 %	646 nm	[Kae+19]
$^{198}Hg^{+}$	0	0	9.97 %	194 nm	[BIW87]
$^{199}Hg^{+}$	1/2	+1	16.87 %		[Poi+96]
$^{201}Hg^{+}$	3/2	0	13.18 %		
$^{202}Hg^{+}$	0	0	29.86 %		
$^{226}Ra^{+}$	0	0	0 %	468 nm	Atomic clock [Hol+22]

Table 3.1: Chosen isotopes from the ion trapping history. The wavelengths $\lambda_{\mathrm{Doppler}}$ are given for the transitions that were used for Doppler cooling (none where sympathetic cooling with a second species was used).

manipulation of $^{43}Ca^{+}$ is 393 nm, meaning that all required lasers operate in the visible range,[2] where solid-state-diode lasers and high-quality optical components are commercially available. These properties make $^{43}Ca^{+}$ an ideal choice for an 'application qubit' inside our quantum network node.

For the networking ion, we prefer an ion species of similar mass as $^{43}Ca^{+}$, as this simplifies motional dynamics, which are essential for mixed-species quantum logic and sympathetic cooling [Hom13]. We choose $^{88}Sr^{+}$ because the laser wavelengths needed to cool and manipulate this ion are also in the visible spectrum (see Table 3.1), and a toolbox of techniques has already been developed for this isotope [Bro07]. Moreover, the absence of hyperfine structure due to the nuclear spin $I = 0$ is advantageous for generating single photons at high rate, which is an essential property for a photonic network link.

3.1.3 Loading

Inside the vacuum chamber, there is one oven filled with strontium and another filled with calcium. To evaporate strontium (calcium) atoms from the source, the ovens are resistively heated to 280 °C (310 °C) [Bal+18]. The atoms reaching the trapping region are ionised in an isotope-selective two-step photo-ionisation process [Gul+01; Luc+04b; Van+06] (see Figure 3.1). The first laser, at 423 nm (461 nm), excites the neutral strontium (calcium) on the $5s^2 \leftrightarrow 5s5p$ ($4s^2 \leftrightarrow 4s4p$) transition. The second laser, at 378 nm, provides sufficient energy for ionisation from this excited state, but not from the ground state. Therefore, the frequency of the 461 nm laser can be used to select the calcium isotope to be ionised, given that the line-width (~ 35 MHz) is much smaller than the isotope shift involved (~ 1 GHz). For the work reported in this thesis, we typically load the calcium isotope $^{43}Ca^{+}$, but occasionally choose $^{40}Ca^{+}$ for diagnostic purposes.

[2] The exception is the 378 nm laser used to ionise atomic calcium. However, only low power is required and the frequency does not have to be stabilised because this laser is responsible for ejecting electrons into the continuum.

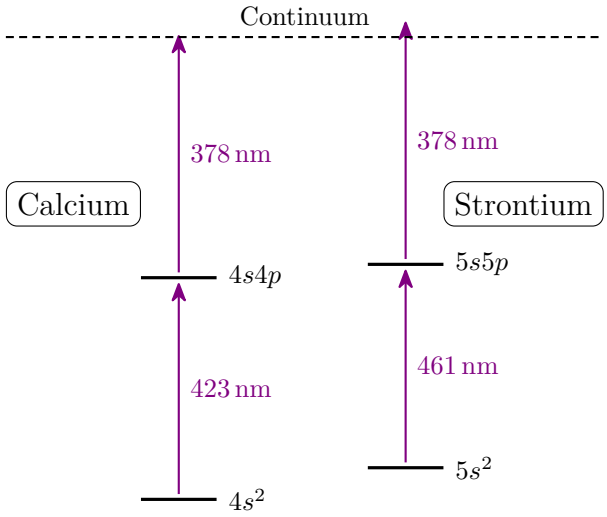

Figure 3.1: Diagram of energy levels relevant for photo-ionisation of strontium and calcium (to scale).

3.1.4 Cooling

Once the atoms have been ionised, they are subject to the electric trapping potential. The thermal kinetic energy of the ions is of the same order of magnitude as the typical potential depth of $\sim 0.1\,\mathrm{eV}$ and would quickly escape if their excess kinetic energy is not removed. Moreover, through interaction with the environment, trapped ions inadvertently experience heating and collisions with residual gas particles, which necessitate cooling beyond the initial trapping step. Depending on the initial temperature, the target temperature, and the heating rate, different cooling methods are applicable. In this section, we will introduce the cooling methods chosen for the experiments discussed in this thesis. Level diagrams are shown in Figure 3.2 for both species to aid this discussion. A typical mixed-species experiment starts with ground-state cooling of the axial motion (see Protocol 3.1.1).

Protocol 3.1.1. *Mixed-species axial ground state cooling.*

1. Doppler-cool both species simultaneously for $\sim 1\,\mathrm{ms}$ with empirically optimised laser powers and detunings.
2. EIT-cool (using $^{88}Sr^{+}$) for $\sim 500\,\mu\mathrm{s}$ with parameters optimised for the OOP mode.

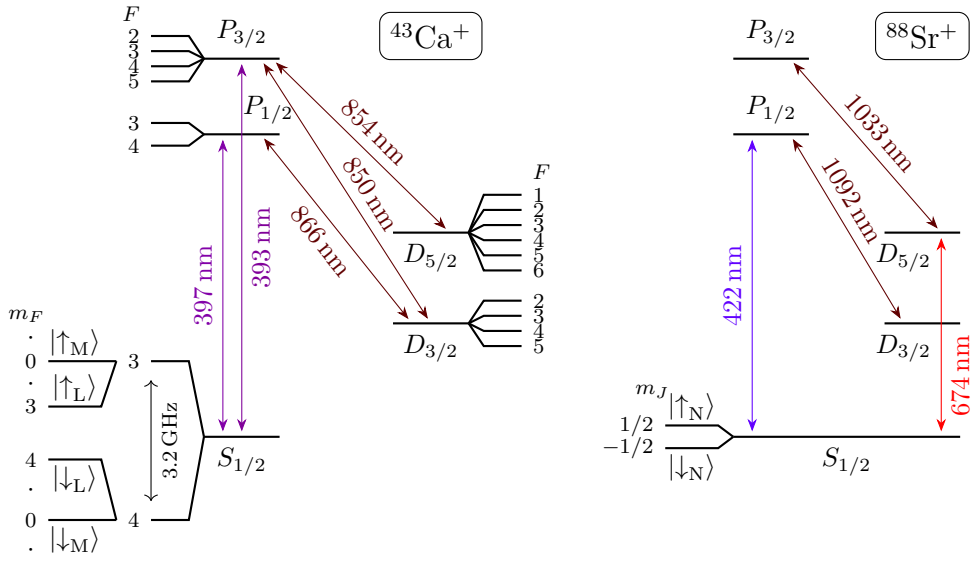

Figure 3.2: Energy level diagram of $^{43}Ca^+$ (left) and $^{88}Sr^+$ (right), not to scale. Laser wavelengths are shown for the transitions used in this work, except the Raman laser at 401.543 nm. The network qubit N, the logic qubit L, and the memory qubit M are shown explicitly within the (hyper)fine structure of the species. The network qubit and the logic qubit can be prepared efficiently by optical pumping. The memory qubit M comprises the $m_F = 0$ states in the $^{43}Ca^+$ $S_{1/2}$ manifold and is nearly magnetic field-insensitive at low magnetic fields.

3. Perform SBC on the OOP mode (using Raman a transition in $^{43}Ca^+$).
4. Alternate ~ 50 times between EIT cooling (using $^{88}Sr^+$) of the IP and the OOP mode, for a total of ~ 1 ms.

As the heating rate of the IP mode exceeds the cooling rate of SBC in our apparatus, this mode can only be ground-state cooled using EIT cooling. To maintain a sufficient EIT cooling rate on the IP mode during this step, the OOP mode is pre-cooled using a standard cooling sequence (Doppler, EIT, SBC). Then, to maintain the final temperature of the OOP mode during the last EIT cooling step targeting the IP mode, we interleave short EIT cooling pulses on the OOP mode.

3.1.4.1 Doppler cooling

Trapped ions are typically observed by illuminating them with light tuned to the $S_{1/2} \leftrightarrow P_{1/2}$ transition (422 nm in Sr^+, 397 nm in Ca^+) and detecting scattered photons using an imaging system. To avoid population getting stuck in the

metastable $D_{3/2}$ levels via dipole-allowed spontaneous decay from $P_{1/2}$ (branching ratio $\sim 5\,\%$), we saturate the $D_{3/2} \leftrightarrow P_{1/2}$ transition using a repumper laser (1092 nm in Sr^+, 866 nm in Ca^+). Since the photon scattering process involves a momentum transfer, this mechanism can be used to cool the ions. The line shape of the transition is broadened by the Doppler effect, which shifts the resonance frequency of the transitions depending on the direction and speed of the particle's motion in the wave of the driving laser. If the cooling laser is red-detuned from the line center of the transition, it becomes more likely for the ion to scatter light when it is moving towards the laser source. The net momentum transferred from the photons to the ion is negative, which cools the ion. The minimum temperature achievable with Doppler cooling is limited by the recoil of scattered photons, which causes a random walk in phase space, and is given by $T_{\text{Doppler}} = \frac{\hbar\Gamma}{2k_B}$, where Γ is the natural linewidth of the cooling transition. For $^{88}Sr^+$, $\Gamma = 2\pi \times 20.1\,\text{MHz}$ and the Doppler limit is therefore $T_{\text{Doppler}} = 484\,\mu\text{K}$. Any mode that has a projection onto the Doppler cooling beam can be cooled using this method.

3.1.4.2 EIT cooling

As we have seen in the previous section, the lowest temperature that can be reached by Doppler cooling is limited by the natural width of the cycling transition. In order to decrease the temperature further, we exploit EIT, which is an interference effect that occurs in Λ-shaped level structures, such as that formed by the 422 nm π and σ transition in $^{88}Sr^+$. Driving this system creates spectral features that are narrow compared to the natural linewidth of the transition. The method is convenient in that no additional hardware is required, as the same beams are installed for Doppler cooling and state preparation. The alignment of the EIT beams sets the difference between their wavevectors, $\boldsymbol{\Delta k} = \boldsymbol{k}_\pi - \boldsymbol{k}_\sigma$; all normal modes that overlap with $\boldsymbol{\Delta k}$ can be EIT-cooled simultaneously [Lec+16].

3.1.4.3 Sideband cooling

In Section 2.3 we derived Hamiltonian terms that couple the spin state of an ion with its motional state in the harmonic trapping potential. Notably, the red sideband

interaction, which arises when the light field is detuned below the qubit resonance by the frequency of a motional mode, induces Rabi flops $|\downarrow\rangle |n+1\rangle \leftrightarrow |\uparrow\rangle |n\rangle$ on the joint state of spin and motion. A π pulse on this transition thus reduces the occupation number of the harmonic oscillator by one, and flips the spin of the ion. If followed by a state preparation pulse to return the spin to $|\downarrow\rangle$, repeating this procedure removes energy quanta from the harmonic oscillator until all population is in the ground state[3]. Once the motional state is in the ground state, the transition ceases to occur, leaving the ion in the $|\downarrow\rangle$ state after subsequent red sideband π pulses – a clear experimental signal that ground state cooling has been achieved. In the presence of heating, the final temperature that can be reached with SBC is limited. After all, the repetition rate must be high enough to combat the heating rate, necessitating a fast state preparation sequence and elevated laser powers in order to compensate for the Rabi frequency scaling with the (small) Lamb-Dicke factor, to perform the sideband transition in a short time.

3.1.5 State preparation and measurement

Among the requirements for universal quantum computing is the ability to prepare qubits in a pure state and to perform single-qubit measurements [DiV00]. At the time of writing, the lowest reported SPAM infidelity (9×10^{-5}) has been reported for a trapped $^{137}Ba^{+}$ ion [An+22].

3.1.5.1 Optical pumping

To prepare trapped ions in a pure state, we employ the lasers of the same wavelengths as for Doppler cooling (Section 3.1.4.1), but exploit geometrical or spectral features of the transition spectrum to drive dissipative dynamics that pump population from all electronic levels into a single state. Optical pumping exploits the dependence of these dissipative dynamics on the branching ratios, the polarisation and frequency of the light fields such that the atom eventually decays into the target state (typically a level in the ground state or a metastable excited state) and remains there even under

[3] or trapped in a high-n state due to the more complicated n dependence of the sideband Rabi frequency, which has been omitted from Section 2.3.

persistent illumination of the pumping fields. The state preparation scheme used in this work rely on the polarisation purity of the laser beams used for optical pumping, which is experimentally more challenging than frequency-selective pumping, but nevertheless provides high-fidelity state preparation with infidelities $\lesssim 10^{-3}$. For Sr^+ (Ca^+), a pulse of σ^--polarised 422 nm (397 nm) light together with a repumper at 1092 nm (866 nm) pumps population into $|\downarrow_N\rangle$ ($|\downarrow_L\rangle$).

3.1.5.2 State discrimination

Readout is performed by fluorescence detection after shelving of one of the qubit states into a state outside of the Doppler cooling cycle, e.g. into the $D_{5/2}$ manifold. For $^{88}Sr^+$, state-selective shelving is straight-forwardly achieved using the 674 nm laser that addresses this quadrupole transition directly. For example, the superposition $\alpha\,|\downarrow_N\rangle + \beta\,|\uparrow_N\rangle$ in the ground-state Zeeman qubit is mapped to $\alpha\,|\downarrow_N\rangle + \beta\,|D\rangle$ using a π pulse on the 674 nm transition, where we typically select $|D\rangle = |D_{5/2},\, m_J = -\frac{3}{2}\rangle$ because this transition has the lowest sensitivity to magnetic field noise. For $^{43}Ca^+$, the same could be done using a 729 nm quadrupole-addressing laser. However, such a laser is not part of our system yet. Instead, a polarisation-selective pumping scheme was implemented [Mye+08; Szw09] (see Protocol 3.1.2).

Protocol 3.1.2. *Shelving process for $^{43}Ca^+$.*
Using ~ 5 repetitions of the following steps, population from $|\downarrow_L\rangle$ is shelved to the $D_{5/2}$ levels with high fidelity. If the same method is applied to shelve population from $|\downarrow_M\rangle$, the lowest achievable error is 4×10^{-3} [Bal14].

1. A 393 nm pulse with 0.7 µW power pumps population from $|S_{1/2},\, F=4,\, m_F=4\rangle$ into $|P_{3/2},\, F=5,\, m_F=5\rangle$ for 40 µs, from where it decays with 6 % into the $D_{5/2}$ shelf. The other allowed decay is back to the initial state, and with 0.7 % to a $D_{3/2}$ state.
2. The fraction of population now left in $D_{3/2}$ is recovered using two pulses on the 850 nm transition: first with 15 µW and σ polarisation for 7.5 µs to clear the $|D_{3/2},\, F=4,\, m_F=4\rangle$ and $|D_{3/2},\, F=5,\, m_F=4\rangle$ states, and then with 35 µW and π polarisation for 6.5 µs to clear the $|D_{3/2},\, F=5,\, m_F=5\rangle$ state.

After shelving, the Doppler cooling lasers implement a strong measurement given by the positive operator-valued measurements (POVMs) $\{|\downarrow\rangle\langle\downarrow|, |D\rangle\langle D|\}$. If the superposition collapses into $|D\rangle$, the ion remains dark and fluorescence detection only captures background light (e.g. scatter from the Doppler cooling laser, which has the same frequency as the fluorescence photons). To distinguish between the two outcomes we use a threshold for the number of fluorescence photons, c_{thr}, above which we regard the ion as fluorescing. The difference between the signal c_{sig} and the background c_{bg} can be calibrated by counting photons from an unshelved ion with and without enabling the repumper beam, respectively (1092 nm for strontium, 866 nm for calcium). Disabling the repumper ensures that the ions do not fluoresce, as they are pumped into the metastable $D_{3/2}$ level, and enables a precise measurement of the background counts. Neglecting spontaneous emission and accidental shelving during the background and signal calibration, respectively, the optimal threshold for state discrimination is given by [Bur10]

$$c_{\mathrm{thr}} = \frac{c_{\mathrm{sig}} - c_{\mathrm{bg}}}{\ln(c_{\mathrm{sig}}) - \ln(c_{\mathrm{bg}})} \ .$$

3.1.6 Ion loss detection

Collisions of the trapped ions with residual gas particles in the vacuum chamber occasionally eject the ions from the trap. The collision rate between an ion of mass m_{ion} and a molecule of mass m_{molecule} can be estimated using [Aik+20]

$$\gamma = \frac{ep}{k_B T}\sqrt{\frac{\pi\alpha}{\mu\epsilon_0}} \ ,$$
$$\text{where } \mu = \frac{m_{\mathrm{ion}} m_{\mathrm{molecule}}}{m_{\mathrm{ion}} + m_{\mathrm{molecule}}}$$

and α is the polarisability of the molecule [Nat22], e the electron charge, and ϵ_0 the vacuum permittivity. For example, N_2 or H_2O molecules in the background with a partial pressure of 1×10^{-10} mbar collide with a trapped $^{88}Sr^+$ on average every ~ 10 min.

To determine whether the correct number, n, of ions are trapped, we detect fluorescence photons and if the count falls within $\pm\frac{1}{2}RT_1$ of the expected number

nRT_1, where R is the known average photon collection rate for a single ion, the routine indicates no ion loss. If, however, a loss event is suspected after a short detection window of duration T_1, the ion is re-cooled for $T_{\mathrm{recool}} = 25\,\mathrm{ms}$, and a second window of duration $T_2 > T_1$ is opened to double-check the result. The purpose of the long re-cooling delay between the detection windows is to recover from background gas collisions which could leave the ion in a hot orbit where Doppler cooling is inefficient.

The number of photons per window of length T is Poisson-distributed with mean value RT. The probability of a correct classification after a window duration T is therefore

$$p(T) = \sum_{k=(n-\frac{1}{2})RT}^{(n+\frac{1}{2})RT} \frac{\mathrm{e}^{-RT}(RT)^k}{k!}$$

and can be approximated by

$$p(T) \approx Q\left(1 + \left(n + \frac{1}{2}\right)RT, nRT\right) - Q\left(1 + \left(n - \frac{1}{2}\right)RT, nRT\right) \ ,$$

where $Q(a, x)$ is the regularised upper incomplete gamma function. Our method optimises the two window durations, T_1 and T_2, such that when there is the correct number of ions, the average duration of this procedure, Equation (3.1), is minimal. Furthermore, we constrain this optimisation such that the overall classification success probability, Equation (3.2), exceeds p_{target}:

$$f_{\mathrm{objective}}(T_1, T_2) = T_1 + (1 - p(T_1))(T_2 + T_{\mathrm{recool}}) \to \min, \tag{3.1}$$

$$g_{\mathrm{constraint}}(T_1, T_2) = p(T_1) + (1 - p(T_1))p(T_2) \geq p_{\mathrm{target}} \ . \tag{3.2}$$

The average duration of the optimised ion loss procedure is plotted for different values of p_{target} in Figure 3.3. Subdividing the ion loss detection into more than two windows could further reduce the average duration spent, as was demonstrated previously for fluorescence readout [Bur10]. The main difference between ion readout and the ion loss detection procedure described here lies in the comparatively long recooling delay needed to recover from decrystallisation events.

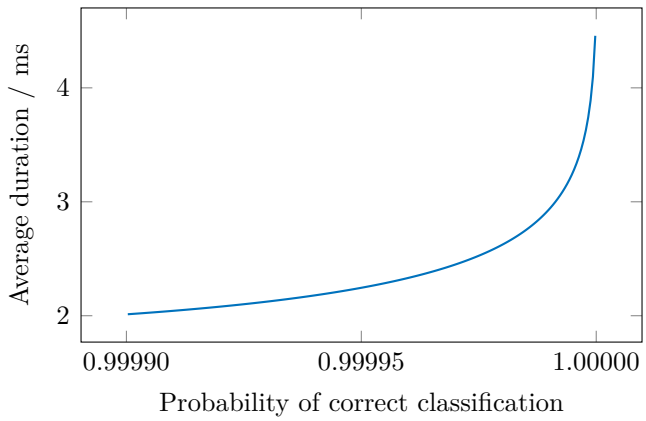

Figure 3.3: Average duration spent detecting ion loss assuming a count rate $R = 16\,\mathrm{kHz}$ (representative for $^{88}Sr^{+}$ in our system).

3.1.7 Ion order

To avoid systematic errors in mixed-species experiments, we take care to control the order of ions in a chain comprising a single $^{88}Sr^{+}$ ion and a single $^{43}Ca^{+}$. This requires reliable and efficient detection of the current ion order and a method that enables the order to be changed, which could be necessary after collisions with background gas, decrystallisation due to excessive heating, or simply because the ion order is random after loading. To detect the current ion order, we have three options:

1. *Camera method.* The image of each ion species can be imaged onto different areas of an electron-multiplying charge-coupled device (EMCCD) sensor. Using an appropriate image analysis, the position of each ion can be determined with respect to a reference image.
2. *Split method.* The ions can be split into two separate wells using ion transport (see Protocol 3.2.3 in Section 3.2.2), and fluorescence detection performed on both sides individually.
3. *High-NA method.* The extent of the point spread function of the NA = 0.6 objective that is used for the photonic interface is significantly smaller than the ion separation ($\sim 3.3\,\mu\mathrm{m}$). If the ion order changes and the $^{88}Sr^{+}$ ion no longer fluoresces in its focus, the collected light drops to the background level. To distinguish reordering events from ion loss, this method is always paired with ion loss detection (see Section 3.1.6).

The camera method is impractical because switching from photomultiplier tube (PMT) readout to the EMCCD camera is very slow (a motorised mirror must be moved), and it requires a dedicated image processing routine. The split method is significantly faster than the camera method, but the high-NA method beats both other methods in simplicity. The split method is used only here to characterise the reordering algorithm (remainder of this section). All other mixed-species experiments reported in this thesis use the high-NA method to detect reordering events.

When a reordering event is detected, we attempt to recover the correct order automatically using ion transport techniques. In principle, the segmentation of electrodes in our trap support arbitrary rotations of the normal modes of the trapping potential to be implemented. Unfortunately, our digital to analogue converter (DAC) voltage range is presently insufficient to faithfully execute this approach. Instead, our reordering algorithm, Protocol 3.1.3 (see Figure 3.4(a)), aims to disturb the trapping potential in a principled way, following a similar procedure as described in Reference [Neg18]:

Protocol 3.1.3. *Reordering protocol for a mixed-species chain of two ions.*

1. Increase the axial confinement to incentivise the ions to align radially.
2. At the same time, displace the ions radially to increase the micromotion. Since the masses of the ions differ, they experience different ponderomotive potentials. The heavier mass tends to be displaced further away from the trap axis. This effect provides the deterministic element of the routine.
3. Delay.
4. Tilt the radial motional mode towards the trap axis. The sign of the tilt sets the final ordering on the axis, but there could be a preferred direction due to asymmetries in the trapping potential.
5. Delay.

6. Revert the radial displacement (step 2). This reduces the micromotion and stabilises the ion order.
7. Delay.
8. Reset the axial confinement (step 1). The ions return into a purely axial formation.
9. At the same time, reset the radial tilt (step 4).
10. Determine the ion order and return if it was successfully restored.

As this procedure is probabilistic (though with a small failure probability), we allow up to eight repetitions until the routine reverts to checking for ion losses (Section 3.1.6).

We diagnose the reliability of the reordering algorithm by scrambling the order of a $^{88}Sr^{+}$-$^{43}Ca^{+}$ chain (ratio between different configuration ~ 0.35), executing the reordering algorithm, and finally measuring the order using the split method. In particular, the direction of the radial displacement applied in step (2) above determines the final configuration (see Figure 3.4(b)).

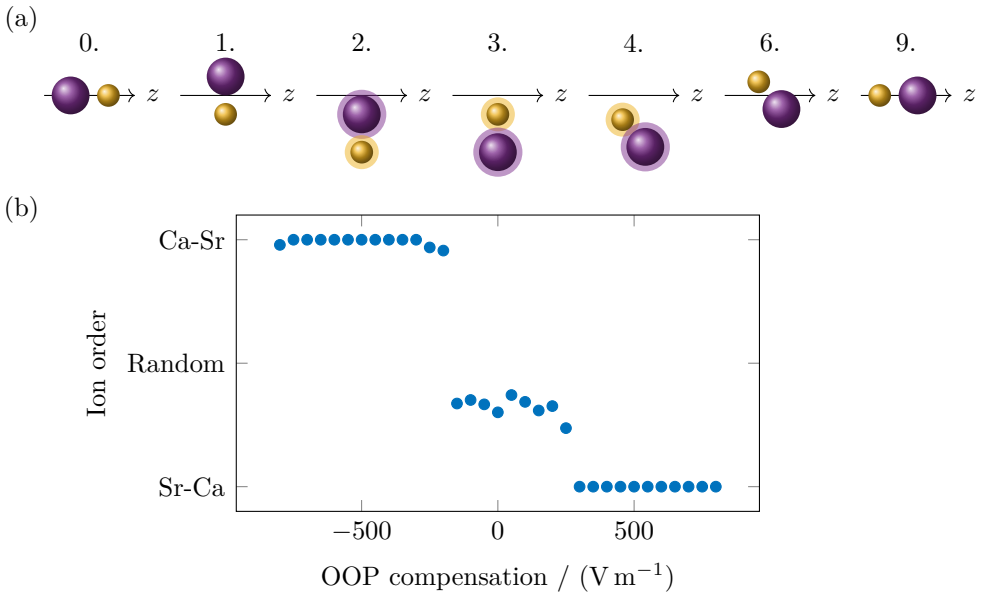

Figure 3.4: (a) Visualisation of the steps in Protocol 3.1.3. (b) We plot the probability of obtaining one particular order (arbitrarily chosen) as a function of the radial compensation field, which is applied in a tight axial trap to induce a mass-dependent radial displacement at steps 2-5 of the reordering protocol.

3.2 Ion transport

Surface Paul traps with segmented electrodes allow precise control of the electric potential confining ions above it. The electrostatic field produced by the electrodes is combined with the RF field produced by dedicated electrodes. In the pseudopotential approximation, the fast varying RF term of the potential is neglected and an effective radial pseudopotential $\phi_{\mathrm{RF}}(|x^m - x_0^m(z)|)$ is introduced. In this section we use index notation (e.g. $\boldsymbol{x} \equiv x^m$) and Einstein summation convention. In linear Paul traps, the experimentally relevant parameters are defined near the position of the RF null $x_0^m(z)$.

1. The compensation fields $F^i(x^m) = \partial_i \phi(x^m)$ are used to shift the potential minimum to coincide with the RF null at the target position z along the trap axis.

2. The field curvatures $f^{ij}(x^m) = \partial_i \partial_j \phi(x^m)$ define the eigenfrequencies of the trapped particle's motion and the rotation of the respective motional modes.

3. Higher derivatives of the potential are only relevant for linear transport operations. In particular, for splitting and merging (inverse splitting), $\partial_z^3 \phi(x^m)$ and $\partial_z^4 \phi(x^m)$ along the trap axis z are of interest.

To this end, the potential can be approximated by a Taylor polynomial around the point $z^m = (0, 0, z_0)$ on the trap axis, with $x^m = (x, y, z) = z^m + r^m$:

$$\phi(x^m) = \phi(z^m) + r^i \partial_i \phi(z^m) + \frac{1}{2} r^i r^j \partial_i \partial_j \phi(z^m) + \frac{1}{6}(z - z_0)^3 \partial_z^3 \phi(z^m) + \frac{1}{24}(z - z_0)^4 \partial_z^4 \phi(z^m) \, .$$

The static electric field $\chi_\ell(x^m)$ produced by electrode ℓ is linear in the applied voltage v^ℓ. Due to the linearity of Maxwell's equations, the total static electric field produced by all electrodes is $\phi_{\mathrm{DC}}(x^m) = \chi_\ell(x^m) v^\ell$. The total effective potential experienced by a charge in the trap is therefore

$$\phi(x^m) = \phi_{\mathrm{RF}}(x^m) + \chi_\ell(x^m) v^\ell \, .$$

We use the Julia library SURF [Web22] for all transport operations. At the time of writing, SURF implements three solvers: the static solver, the dynamic solver, and the splitting solver.

Static solver. The aim of the static SURF solver is to find the voltages v^ℓ such to produce a potential whose relevant Taylor coefficients match the target values within a given width w around the axial position z_0 of the potential minimum. On a technical level, this is achieved by sampling the model at discrete grid points z_k along the trap axis. A cost function quantifying the deviation from the target potential at significant points z_k (weighted by a Gaussian $G(z_k; w)$) is minimised using a quadratic programming approach.

Dynamic solver. The dynamic solver connects wells with varying parameters (usually shuttling a well along the axis) while also minimising the voltage changes along the trajectory.

Splitting solver. Splitting and merging is generally more complex than shuttling because it involves a point where the quadratic confinement reaches zero, and the ions become sensitively exposed to electric field noise causing heating. For more information on the implementation, see Reference [Web22]. By varying the axial displacement of the crystal we can control the ion split ratio into the two wells.

3.2.1 Principal component analysis

In some situations, calling the SURF solver at runtime is prohibitively expensive. For a single stationary trap well, most parameters are typically fixed. The goal of this section is to develop a linear model for the electrode voltages as a function of the compensation fields, the trap depth, the axial confinement, and a small axial offset. Electrode voltages found by SURF for a set of target well parameters are linearised using principal component analysis (PCA). The target wells were chosen with common field curvatures (rotated by 0.5 rad around the axis) and no axial compensation (no displacement from the axial trap centre). For a set $(F^x, F^y, w)_n$ of N varying target radial compensation and width parameter combinations, voltage solutions v_n^ℓ are calculated using the static SURF solver. Care is needed in choosing the parameter ranges such that the voltages do not reach the maximum solver constraint. The untagged matrix v_n^ℓ was processed by PCA to extract the strongest

principal components totaling >99 % of the variance. Owing to the linearity of the problem, the first three principal components already account for 99.99 % of the variance in the voltage set. Two principal components correlate naturally with the original compensation tags F^x and F^y, whereas the third component is correlated with the well depth d along the trap axis rather than the original width tag w.

To be able to reconstruct voltage solutions for a trap with given radial compensation and certain depth d, a linear regression is performed on the correspondence between physical trap parameters F^x, F^y, and d of a solution v_n^ℓ and its principal components. A constant offset vector is included in the linear regression. The result from the regression is then used to transform the principal voltage vectors into a basis spanned by the parameters $p^q = (1, d, F^y, F^x)$. The columns of this basis, ${V^\ell}_q$, contain voltage vectors representing the transformed principal components. With the mean voltage $v_\mathrm{c}^\ell = \sum_n v_n^\ell / N$, the trapping solution is parameterised by

$$v_n^\ell = v_\mathrm{c}^\ell + {V^\ell}_q \, p^q \ . \tag{3.3}$$

The solutions (3.3) obtained from this method are practical because they are parameterised by physical quantities, easy to calculate, and reliable. However, there are often more characteristic properties that are relevant in practice. The following sections describe transformations that change the axial frequency and axial offset of the solution without affecting the principal components.

3.2.1.1 Axial frequency

The constant component v_c^ℓ alone sets the mode frequencies and the mode rotations, as per construction, the principal components have no influence on those parameters. It is possible to tune the axial confinement by scaling the voltages by a scalar factor, α. This rescaling does not affect the compensations F^x and F^y, but the axial trap depth, which naturally follows the strength of the axial confinement. To compensate for this, we adjust the depth parameter post-hoc to $d + \beta(1 - \alpha)$, where β is a scalar correction factor. Having this procedure adds the axial frequency to the set of independently controllable physical parameters. It should be mentioned that,

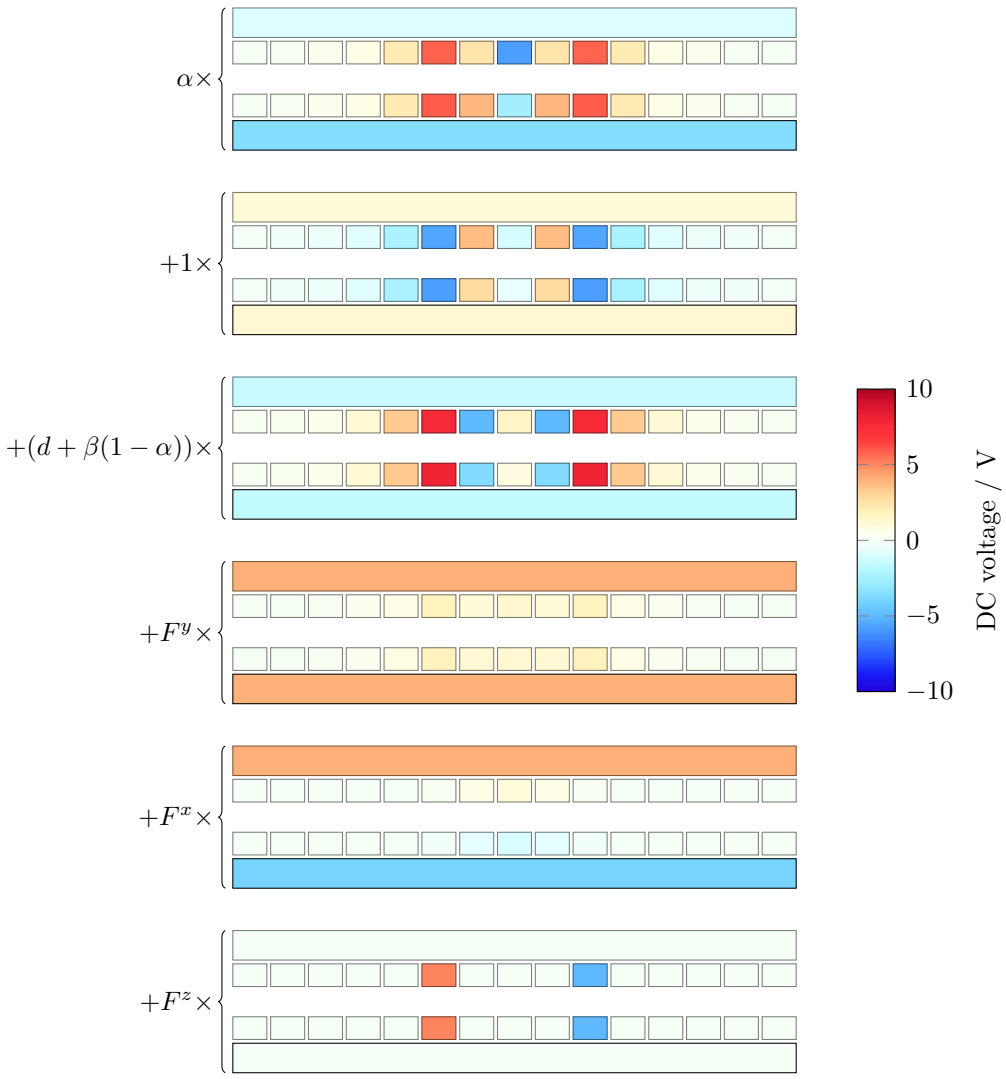

Figure 3.5: Principal components of voltages for a typical trapping configuration.

due to Gauss's law $\partial_i \phi^i(x^m) = 0$, the square sum of the three mode frequencies is a constant. Therefore, tuning the axial frequency also changes the radial confinement. By the initial construction of SURF solutions with fixed high-frequency radial modes, the axial frequency and the lower radial frequency are always affected with opposite sign, whereas the higher radial frequency remains unchanged.

3.2.1.2 Axial shift

To apply a static axial force $F^z(x^m) = -\partial_z \phi(x^m)$, the potential ϕ should be linear in z. In electrostatics, this is readily achieved in the free-space region between two differently charged parallel surfaces. This picture illustrates the principle that

is applied in segmented electrode chip traps in order to displace the ion in space. However, the linearity of the potential depends on the electrode geometry in a given direction. Perpendicular to the trap axis in the trap plane, the idealised picture holds accurately, so that an asymmetric potential applied to opposing electrodes enacts a homogeneous force to charges between them. Along the trap axis, the situation is different insofar as there are no electrodes on either side of the trapped ion. For small displacements, the required potential gradient along the z axis is achieved by adding a symmetrical voltage difference to the second-nearest-neighbour electrodes. This choice of electrodes is made to avoid changing the trap curvatures while retaining a sufficiently large gradient with reasonable voltages.

3.2.2 Splitting and merging

We use a splitting/merging subroutine for mixed-species ion loading and single-qubit addressing in same-species crystals. The DAC update rate for the following protocols is 100 kHz.

Protocol 3.2.1. *Splitting (reverse merging).*

1. Interpolate (in 20 DAC steps) to the initial configuration of the split waveform.
2. Split (in 15 DAC steps) the well into two wells, as shown in Figure 3.6.
3. Interpolate (in 20 DAC steps) to two wells located at $z_1 = -150\,\mu\text{m}$ and $z_2 = 150\,\mu\text{m}$, respectively.

Protocol 3.2.2. *Shuttle loading.*

1. Load the first ion into a potential well at $z_1 = 0$.
2. Spawn (in 5 DAC steps) an empty potential well at $z_2 = -300\,\mu\text{m}$.
3. Shuttle (in 25 DAC steps) this well to $z_2 = 0$ while transporting the other well to $z_1 = 300\,\mu\text{m}$, far from the focus of the photo-ionisation lasers.
4. Load the second ion into the well at $z_2 = 0$.
5. Shuttle (in 25 DAC steps) the wells to $z_2 = -150\,\mu\text{m}$ and $z_1 = 150\,\mu\text{m}$, respectively.

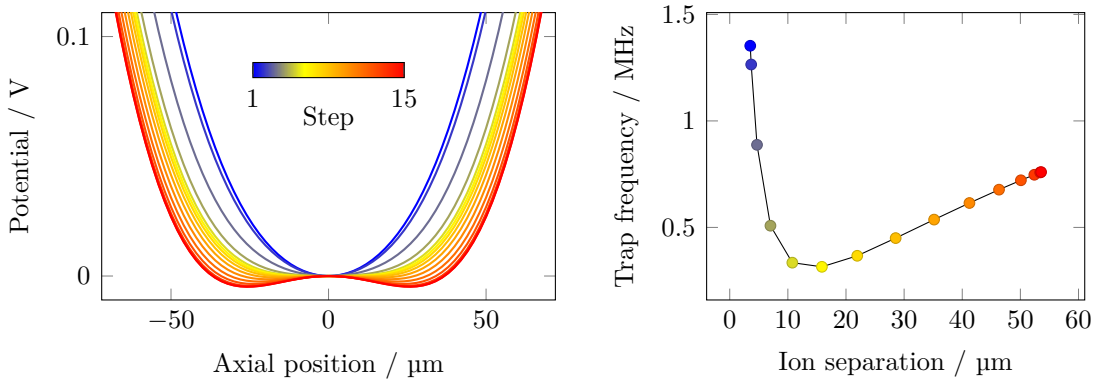

Figure 3.6: Left: waveform used to split an ion chain into two parts. At the critical point, the potential is purely quartic as the quadratic term transitions from positive to negative. Right: The trap frequency, expressed in terms of the axial mode frequency of a single $^{88}Sr^{+}$ ion. At the point where the trap frequency is minimal, near the critical point, the ions are highly sensitive to electric field noise and jerk due to stepped waveform updates. For merging, the same waveform can be used in reverse.

6. Merge using the reverse splitting routine (Protocol 3.2.1), finishing in the default potential well.

Protocol 3.2.3. *Split readout.*

1. Split using Protocol 3.2.1.
2. Shuttle (in 30 DAC steps) the first well to $z_1 = 0$ while transporting the other well to $z_2 = 300\,\mu m$, far from the readout beams.
3. Perform fluorescence readout of the ions in the well at $z_1 = 0$.
4. Shuttle (in 60 DAC steps) the other well to $z_2 = 0$ while transporting the previous well to $z_1 = -300\,\mu m$.
5. Perform fluorescence readout of the ions in the well at $z_2 = 0$.
6. Shuttle (in 25 DAC steps) the wells to $z_2 = -150\,\mu m$ and $z_1 = 150\,\mu m$, respectively.
7. Merge using the reverse splitting routine (Protocol 3.2.1), finishing in the default potential well.

We demonstrate the reliability of Protocol 3.2.3 on a chain of six $^{88}Sr^{+}$ ions with varying axial potential gradient during the split to control the number of ions in the left and right well (see Figure 3.7).

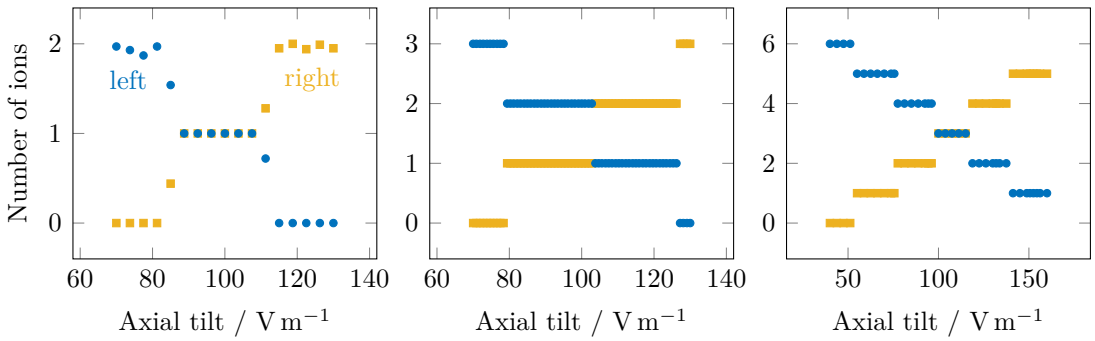

Figure 3.7: We perform splitting of a chain with up to 6 $^{88}Sr^{+}$ ions, count the fluorescence in each well by shuttling them sequentially into the laser interaction zone, and finally merge them again (see Protocol 3.2.3). The axial tilt can be adjusted for different ion split ratios into the left and the right well.

3.2.3 Micromotion compensation by parametric excitation

Modulating the amplitude of the trap RF [Nad+21] leads to parametrically driven motion of the Doppler-cooled ion (see Section 2.2.5.1). We detect the arrival times of fluorescence photons on a PMT and demodulate them digitally at the parametric excitation frequency (see Figure 3.8) to extract the correlation number $C \in \mathbb{C}$. The amplitude $|C|$ quantifies the fraction of photons that are correlated with the excitation drive and $\arg(C)$ measures the phase offset with respect to the drive (see Figure 3.8(b)).

For this application, we choose the resonance index $n = 2$ to avoid the phase ambiguity that arises at the first resonance with $n = 1$, where the excitation frequency is twice the mode frequency and the initial correlated phase of the motion can therefore be either 0 or π with equal probability at every repetition.[4] The second resonance with $n = 2$ is found at the mode frequency. We find that the correlated motion stabilises, i.e., the parametric excitation balances with Doppler cooling, after $\sim 250\,\mu s$ (see Figure 3.8(c-d)).

At the micromotion-compensated point, the ion does not respond to the parametric excitation, resulting in vanishing correlated amplitude. The correlated

[4]The ambiguity can be removed by seeding the motion by exciting briefly on the second resonance with $n = 2$. We have confirmed that this approach recovers a deterministic phase relation between the motion and the subsequent excitation on the first resonance with $n = 1$. As the first resonance is much stronger, the modulation index required for the same signal-to-noise ratio, is significantly smaller, and the ion is more likely to escape the trap.

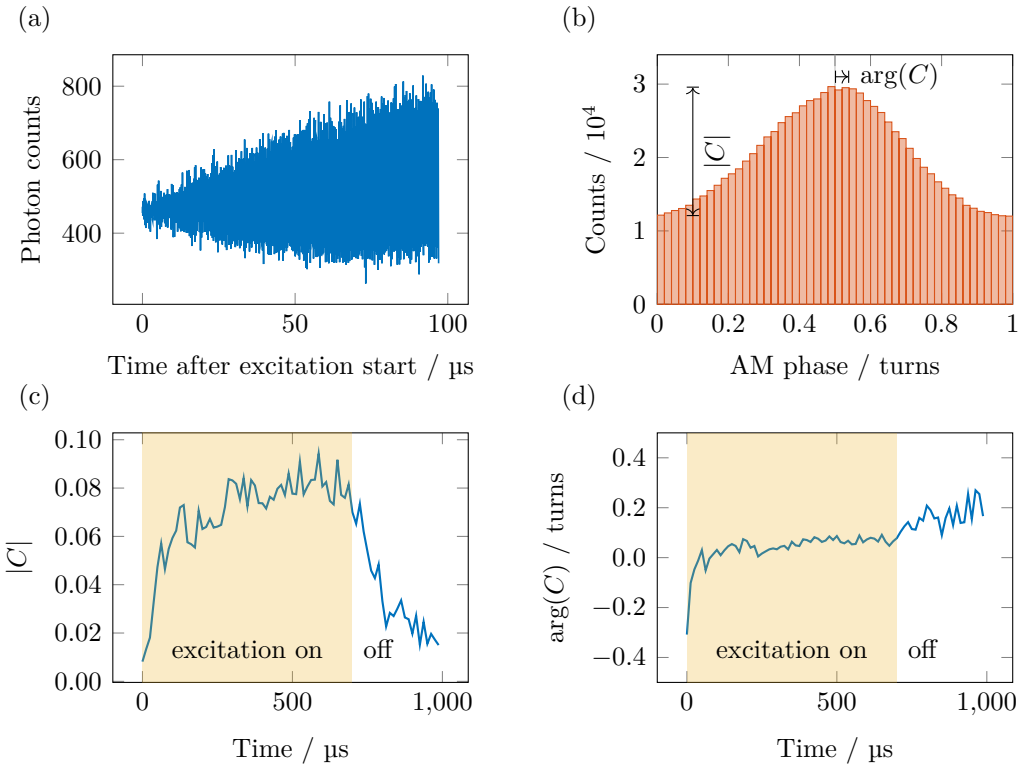

Figure 3.8: Dynamics of timestamped fluorescence photon detection during and after parametric excitation. (a) Fluorescence photons detected over multiple repetitions of the parametric excitation with periods of cooling in between, are accumulated in 50 ns bins. The photon number oscillates with increasing amplitude due to the onset of parametrically driven motion. (b) Evaluating the phase of the photon timestamps from (a) with respect to the parametric drive shows that they are correlated with the drive. Demodulating the timestamps like this yields the correlated amplitude, $|C|$, and the correlated phase offset, $\arg(C)$. (c-d) In a second experiment, we resolve the correlated amplitude (c) and phase (d) during and after parametric excitation. The correlated motion stabilises within $\sim 100\,\mu s$.

amplitude increases linearly and the phase of the correlated amplitude changes by π, as the ion is moved away from the micromotion null along the direction of the driven motional mode. It is therefore possible to detect micromotion in both radial directions with a single set of Doppler cooling beams. As long as the Doppler cooling laser has overlap with both radial modes, the motional excitation of this mode is imprinted in the timings of fluorescence photons. Only the excitation frequency has to be changed in order to sense micromotion along another motional mode direction.

The phase jump of the correlation number C provides a highly robust signal for micromotion compensation [Nad+21]. Moreover, the sensitivity of the signal

increases as $\tilde{h}^{-1}$. Therefore, it is possible to maintain a short averaging duration even close to the optimal compensation, where the correlated signal would otherwise be small, by increasing the modulation index, $\tilde{h}$.

3.2.3.1 Pre-calibrated mode frequencies

In Reference [Nad+21], an algorithm is presented for two-dimensional micromotion compensation using the parametric excitation method; the implementation of this algorithm was used throughout this thesis. Here I present a similar implementation that uses a pre-calibrated first-order approximation of the motional mode frequencies f_α, where $\alpha \in \{\mathrm{LF}, \mathrm{HF}\}$ labels the radial modes of a single ion, as a function of the compensation fields E_x and E_y, around an initial working point, $(\tilde{E}_x, \tilde{E}_y)$:

$$f_\alpha(E_x, E_y) \approx A + (E_x - \tilde{E}_x)B + (E_y - \tilde{E}_y)C \ .$$

The parameters A, B, C are obtained during the pre-calibration from a least-squares fit to ~ 6 mode frequency measurements on a triangular lattice of $\sim 50\,\mathrm{V\,m^{-1}}$ radius around the working point. This parameter region is large enough to tolerate typical day-to-day drifts of the compensation voltages.

To find the compensated point, we minimise the correlated fraction along both radial mode directions simultaneously, as illustrated in Figure 3.9. Using our knowledge of the mode rotation in the radial plane, this can be done with only two successive applications of a one-dimensional (noisy) root-finding problem, starting from an initial guess. Each mode is compensated along a line in the compensation parameter space whose slope is given by the known mode rotation and whose offset is determined by measuring the position of the phase jump along the orthogonal direction. Taking Figure 3.9 for example, the dashed (dotted) line indicates the line along which the HF (LF) mode is compensated, which is the direction orthogonal to that mode's normal vector. The compensated point is found at the intersection of these two lines.

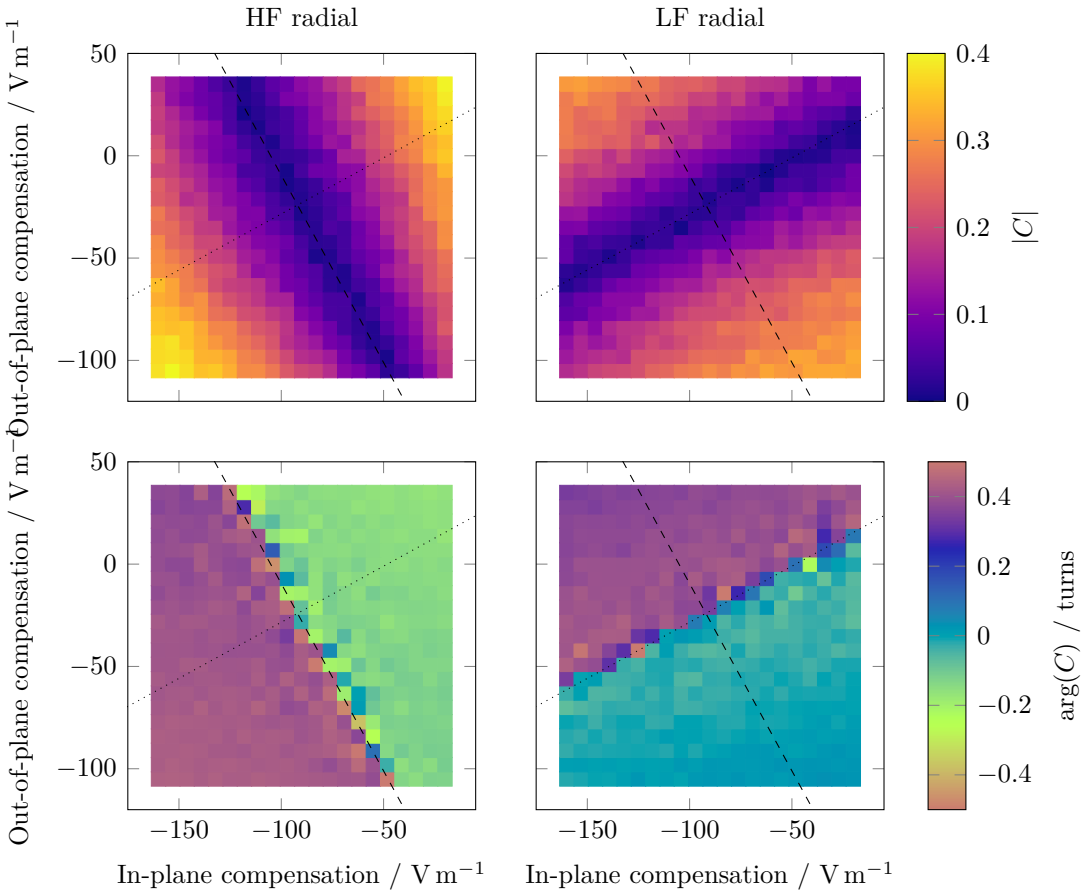

Figure 3.9: We parametrically excite the motion of a $^{88}Sr^{+}$ ion and extract the correlated fraction (top row) and correlated phase (bottom row) of the photons with the parametric excitation drive. We detune the drive by 15 kHz from the pre-calibrated mode frequency at each point. The left (right) column show the result for the radial mode with higher (lower) frequency. The dashed (dotted) line is a fit to the phase step of the HF (LF) radial mode. The fits indicate a mode rotation around the axis of 0.500(3) rad, which matches exactly the intended rotation of 0.5 rad. The crossing point of the fitted lines corresponds to the compensated point.

3.3 Fast polarisation analyser

In this section I introduce the photonic detection system that is used by the client in a demonstration of blind quantum computing (Chapter 6). In order to meet the timing requirements for rapid manipulation of the photon polarisation, electro-optic modulators (EOMs)[5] were selected for their fast switching speeds. Two electro-optic modulators in series provide the necessary degrees of freedom to be able to realise any polarisation measurement basis (Figure 3.16).

3.3.1 Temperature stability of EOMs

Even though the EOMs are manufactured in a dual-crystal configuration, which provides passive cancellation of the differential temperature dependence between the ordinary and extraordinary axes, significant temperature-dependent polarisation drifts were observed in a preliminary investigation [Tom19]. Therefore, the final optical layout of the client apparatus is designed with shared temperature stabilisation of the EOMs (Figure 3.10). A two-layer enclosure with added thermal

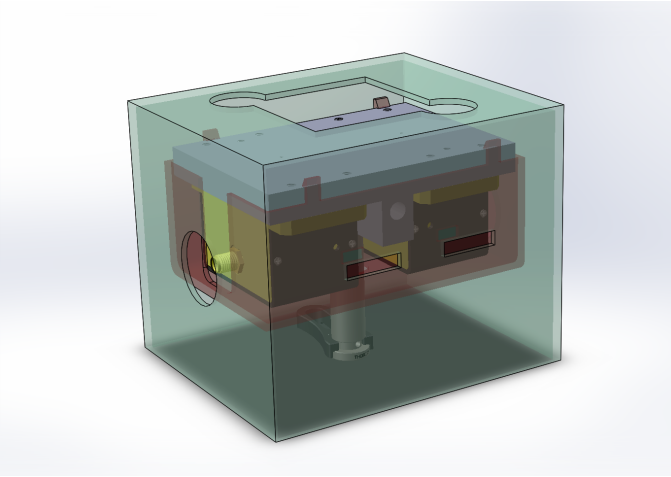

Figure 3.10: Mechanical assembly of the mount for both electro-optic modulators (EOMs). Two enclosures (shown transparently) surround the modulators for improved thermal shielding. The top recess in the outermost enclosure is fitted for a Peltier element with heatsink and fan (not included in drawing) attached to the aluminium mount. Aperture slits at the front are for beam delivery and circular openings at the sides are for SMA-type connectors supplying the high voltage driving the EOM.

[5] Thorlabs, EO-AM-NR-C4.

insulation surrounds the EOM modules. In addition, active stabilisation is employed using a Peltier element on the top surface of the mount, with a heatsink and a fan for ducted heat removal. A thermistor is placed close to the crystals inside the metalwork to provide feedback to the Peltier element via a home-built proportional-gain, integral-gain, differential-gain (PID) controller. The controller adjusts the Peltier current I_{Peltier} according to

$$\Delta = T - T_{\text{set}}$$
$$I_{\text{Peltier}}(t) = k_p \Delta(t) + k_i \int_0^t \Delta(\tau)\,\mathrm{d}\tau + k_d \frac{\mathrm{d}\Delta(t)}{\mathrm{d}t} \ ,$$

where the gains k_p, k_i, k_d have to be chosen appropriately for the particular transient performance of the system [ZN42]. From the step response measurement shown in

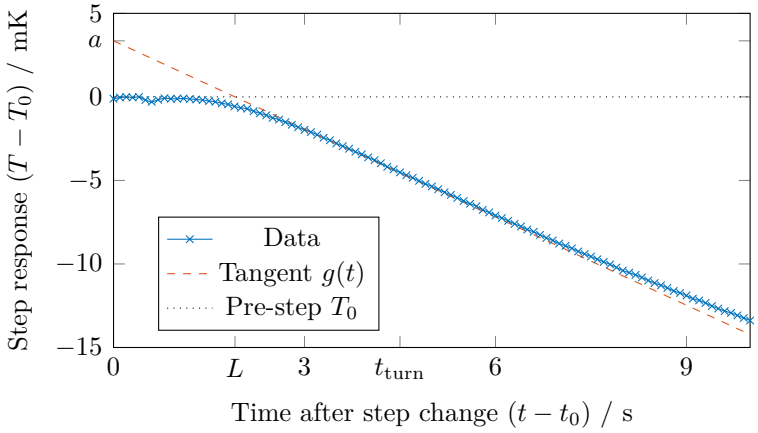

Figure 3.11: The Ziegler-Nichols method is used to determine suitable PID gains from the step response. The thermistor data shown is corrected for a slow linear ambient temperature drift. The Peltier current was switched from 0.4 A to 0.5 A at $t = t_0$. The pre-step temperature was $\approx 20\,^{\circ}\text{C}$. In this example, $a = 0.089$, $L = 1.908$, and therefore, $k_p = 13.52$, $k_i = 3.54$, $k_d = 12.9$ are suggested as suitable PID gains.

Figure 3.11, we extract the tangent $g(t)$ at the turning point t_{turn} (dashed line in Figure 3.11) and determine its intersection $L : g(L) = T_0$ with the pre-step steady-state (dotted line in Figure 3.11), as well as its extrapolated value at the time of the step change normalised by the response step magnitude, $a = g(t_0)/(T_0 - T_\infty)$.

The recommended PID gains are then

$$k_p = \frac{1.2}{a} ,$$
$$k_i = \frac{k_p}{2L} ,$$
$$k_d = \frac{k_p L}{2} .$$

The thermal response of the system presented here evolves on different time scales simultaneously. For active stabilisation, only the shorter, transient time constants are relevant. For this reason, we do not take T_∞ as the thermalised limit (which is typically reached after ∼1 h). Instead, we artificially symmetrise the response around the turning point, for which $T_0 - T_\infty = 2(T_0 - g(t_{\text{turn}}))$. With the gains

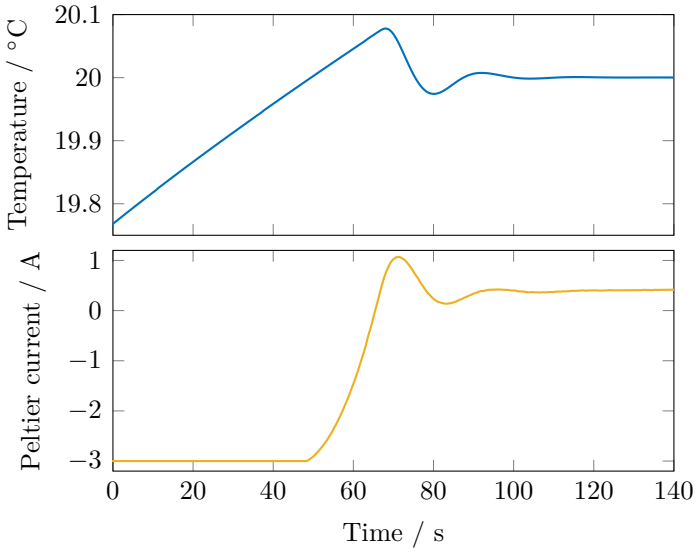

Figure 3.12: Temperature settling behaviour with active stabilisation and two-layer insulation.

calibrated as described above, the temperature settles within ∼ 2 min and reaches a stability below 0.1 mK under typical operating conditions (Figure 3.12).

3.3.2 Optical components

In this section, I introduce the optical components that were used to build the fast polarisation analyser and characterise them.

3.3.2.1 Polarising beamsplitter

The polarising beamsplitter (PBS) is the heart of the polarisation measurement, as it effects a spatial separation between s- and p-polarised components of an incident beam. The action of a lossless beamsplitter on the polarisation state of light can be parameterised by two angles θ_s and θ_p:

$$U_{\mathrm{BS}} = \begin{pmatrix} \cos(\theta_p) & \cos(\theta_s) \\ \mathrm{i}\sin(\theta_p) & \mathrm{i}\sin(\theta_s) \end{pmatrix} ,$$

where the right-hand basis states identify as s- and p-polarisation and the left-hand basis corresponds to the two spatially separated output modes. For a perfect PBS, $\theta_p = 0$ and $\theta_s = \pi$. In reality, however, a small fraction always leaks into the opposite channel, which motivates the 'extinction ratio' – the ratio of maximum to minimum output power – as a measure of imperfection of PBS cubes. Experimentally, we determine the extinction ratio by a two-dimensional search over the rotation angles of a quarter- and a half-waveplate pair (Figure 3.13) to minimise and maximise the output power in the transmitted and reflected beams. Using this

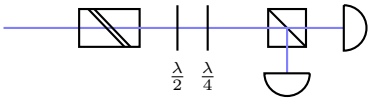

Figure 3.13: Setup used to characterise polarising beamsplitters. A Glan-Taylor PBS with high polarisation extinction ratio is used to clean up the input polarisation. Two waveplates create the necessary degrees of freedom to maximise and minimise the transmission through the 'PBS under test', and photodiodes record the intensity at both of its output ports.

method, we determine an extinction ratio $T_s/T_p = 0.5 \times 10^{-4}$ in transmission and $R_p/R_s = 1.3 \times 10^{-4}$ in reflection (Table 3.2) for the PBS used.

Powermeter	T_{max}	T_{min}	R_{max}	R_{min}	$T_{\mathrm{max}} : T_{\mathrm{min}}$	$R_{\mathrm{max}} : R_{\mathrm{min}}$
1	2.821 mW	109 nW	372 nW	2.800 mW	25686 : 1	7584 : 1
2	1.566 mW	71.2 nW	207.3 nW	1.524 mW	21403 : 1	7555 : 1

Table 3.2: Extinction ratio measurement on the same PBS cube with two different powermeter sensors. The PBS is an optically contacted cube for 397 nm, AR-coated for 422 nm (source: Acal BFi UK Ltd).

3.3.2.2 Waveplates

We use optically contacted zero-order waveplates, customarily designed for 422 nm. At this wavelength, the manufacturer (CASTECH) specifies 0.50006 and 0.2504 retardance for the half-waveplates (WPZO-127-1/2-W422) and quarter-waveplates (WPZO-127-1/4-W422), respectively. In-situ measurements of the retardances showed that the half-waveplates were near-perfect, but the quarter-waveplates did not meet this specification. To characterise them, we use 650 µW horizontally polarised 422 nm light, rotate the waveplate to minimise the power transmitted by a PBS, and record the power split after the PBS (Figure 3.14).

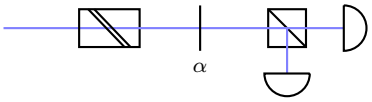

Figure 3.14: Setup used to calibrate waveplates. A Glan-Taylor polarising beamsplitter with high polarisation extinction ratio is used to clean up the input polarisation. Detectors are placed at the input and output ports of a PBS to record the horizontally and vertically polarised components after the 'waveplate under test'.

We model the action of a waveplate whose distinct birefringent axes are aligned with the coordinate system as a unitary transformation acting on the polarisation state of light:

$$U_{\mathrm{WP}}(\alpha, \beta = 0) = \begin{pmatrix} \mathrm{e}^{\mathrm{i}\frac{\alpha}{2}} & 0 \\ 0 & \mathrm{e}^{-\mathrm{i}\frac{\alpha}{2}} \end{pmatrix} ,$$

where α is the retardance – the difference in optical path length experienced by basis-aligned linear polarisation states when passing through the birefringent element. A waveplate rotated by an angle β around the optical axis is described by

$$U_{\mathrm{WP}}(\alpha, \beta) = R(\beta) U_{\mathrm{WP}}(\alpha, 0) R^{\mathrm{T}}(\beta)$$

with the rotation matrix

$$R(\beta) = \begin{pmatrix} \cos(\beta) & -\sin(\beta) \\ \sin(\beta) & \cos(\beta) \end{pmatrix} .$$

For horizontal polarisation passing through the waveplate, the fractional horizontal polarisation component of the outgoing light is

$$T(\alpha, \beta) = |\langle H | U_{\mathrm{WP}} | H \rangle|^2 = [3 + \cos(4\beta) + 2\cos(\alpha)\sin^2(2\beta)]/4 .$$

At the minimum with respect to the rotation angle $T_{\min} = T(\alpha, \pi/4)$, this expression can be inverted to retrieve the retardance

$$\alpha = 2 \arccos(\sqrt{T_{\min}}) \ .$$

Experimentally, both the horizontally polarised power P_H and the vertically polarised power P_V were measured to estimate $T_{\min} = P_H/(P_H + P_V)$. This method was applied to several nominal quarter-waveplates from the same batch (Table 3.3).

WP	Angle	min P_H	max P_V	Inferred retardance
2	25	318 µW	335 µW	0.254
2	116	326 µW	324 µW	0.250
3	128	319 µW	325 µW	0.251
3	218	310 µW	337 µW	0.257
5	342	314 µW	330 µW	0.254
5	72	330 µW	316 µW	0.247
6	47	307 µW	334 µW	0.257
6	321	302 µW	350 µW	0.262
7	330	316 µW	338 µW	0.255
7	60	324 µW	333 µW	0.252
8	330	314 µW	339 µW	0.256
8	238	319 µW	337 µW	0.254
9	350	312 µW	340 µW	0.257
9	80	325 µW	329 µW	0.251

Table 3.3: Quarter-waveplate retardance measurements. The table lists local minima (maxima) of the power transmitted (reflected) by a PBS cube after passing through the 'waveplate under test' (see Figure 3.14).

3.3.2.3 Electro-optic modulators

The EOMs used in this work consist of MgO-doped congruent $LiNbO_3$ crystals, which belong to the uniaxial symmetry group 3m, thus restricting the electro-optic tensor to the form [YY03]

$$r_{ijk} = \begin{pmatrix} \begin{pmatrix} 0 & -r_{22} & r_{13} \end{pmatrix}_k & \begin{pmatrix} -r_{22} & 0 & 0 \end{pmatrix}_k & \begin{pmatrix} r_{51} & 0 & 0 \end{pmatrix}_k \\ \begin{pmatrix} -r_{22} & 0 & 0 \end{pmatrix}_k & \begin{pmatrix} 0 & r_{22} & r_{13} \end{pmatrix}_k & \begin{pmatrix} 0 & r_{51} & 0 \end{pmatrix}_k \\ \begin{pmatrix} r_{51} & 0 & 0 \end{pmatrix}_k & \begin{pmatrix} 0 & r_{51} & 0 \end{pmatrix}_k & \begin{pmatrix} 0 & 0 & r_{33} \end{pmatrix}_k \end{pmatrix}_{ij} \ ,$$

where the coefficients r_{ij} carry the unit $\mathrm{m\,V^{-1}}$ and depend on the temperature and the wavelength. The refractive index ellipsoid of a uniaxial crystal depends on the applied electric field $E = (E_1, E_2, E_3)$ via the electro-optic tensor r_{ijk} as

$$1 = (x_1^2 + x_2^2) n_{\mathrm{o}}^{-2} + x_3^2 n_{\mathrm{e}}^{-2} + \sum_{\{ijk\}=1}^{3} r_{ijk} x_i x_j E_k \ ,$$

where $x_i = (x, y, z)_i$ and n_o and n_e are the ordinary and extraordinary index of refraction, respectively. The wavelength- and temperature-dependence of the principal refractive indices can be modelled using Sellmaier equations [Gay+08; She+92]. Here, for demonstration purposes only, we use the model given in [Gay+08] at 20 °C and 422 nm and the electro-optic coefficients according to [YJT07; YJT08].

Property	Value	Reference
n_o	2.40132	[Gay+08]
n_e	2.29222	[Gay+08]
r_{22}	$9.065\,56\,\mathrm{pm\,V^{-1}}$	[YJT07]
r_{13}	$12.17\,\mathrm{pm\,V^{-1}}$	[YJT08]
r_{33}	$34.8168\,\mathrm{pm\,V^{-1}}$	[YJT08]

Table 3.4: Refractive properties of MgO-doped $LiNbO_3$ at 20 °C and 422 nm.

In $LiNbO_3$, the coefficient r_{33} dominates the electro-optic activity (Table 3.4). Therefore, for this crystal, the electric field is aligned along x_3, the extraordinary axis. In this configuration, the refractive index ellipsoid reduces to

$$1 = (x_1^2 + x_2^2)\left(n_\mathrm{o}^{-2} + r_{13}E_3\right) + x_3^2\left(n_\mathrm{e}^{-2} + r_{33}E_3\right) \ . \tag{3.4}$$

The principal axes of ellipsoid (3.4) do not depend on the electric field E_3, but the respective refractive indices are tuned according to

$$n_1 = n_2 = n_\mathrm{o} - n_\mathrm{o}^3 r_{13} E_3/2 \ ,$$
$$n_3 = n_\mathrm{e} - n_\mathrm{e}^3 r_{33} E_3/2 \ .$$

A beam of wavelength λ propagating through the crystal with wavevector

$$\boldsymbol{k} = \frac{2\pi}{\lambda}\begin{pmatrix}\sin\vartheta_\mathrm{c}\cos\varphi_\mathrm{c}\\ \sin\vartheta_\mathrm{c}\sin\varphi_\mathrm{c}\\ \cos\vartheta_\mathrm{c}\end{pmatrix} \ ,$$

expressed in principal coordinate system of the crystal, experiences the refractive indices

$$n_\mathrm{o}(\vartheta_c, \varphi_c) = n_1 \ ,$$
$$n_\mathrm{e}(\vartheta_c, \varphi_c) = \left(\frac{\cos^2\vartheta_c}{n_2^2} + \frac{\sin^2\vartheta_c}{n_3^2}\right)^{1/2} \ ,$$

and therefore accumulates a dynamic phase

$$\phi_{\mathrm{dyn}} = \frac{2\pi}{\lambda} \frac{L}{\sin\vartheta_c \sin\varphi_c} \left(n_{\mathrm{o}}(\vartheta_c, \varphi_c) - n_{\mathrm{e}}(\vartheta_c, \varphi_c)\right) \ .$$

By placing the crystal between two crossed polarisers and illuminating this system with divergent light, a conoscopic interference pattern – the isochromate – is observed with amplitude $(1 - \cos\phi_{\mathrm{dyn}})/2$ (Figure 3.15). The conoscopic method is a useful

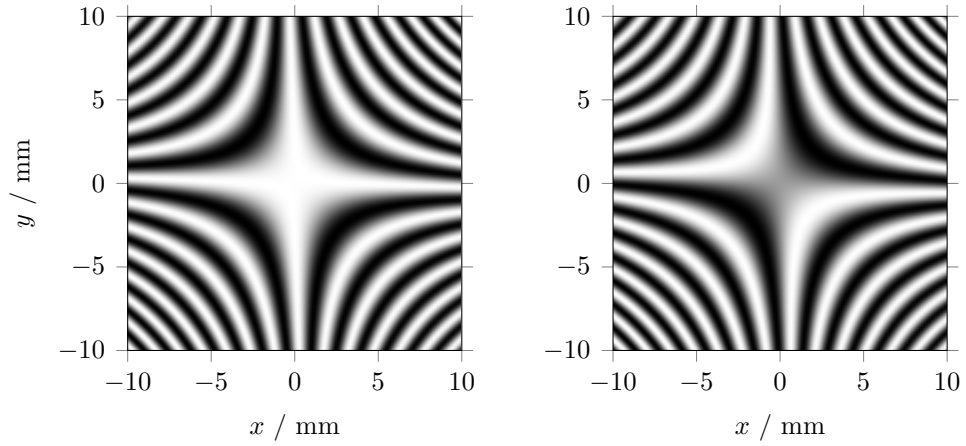

Figure 3.15: Conoscopic interference pattern of a uniaxial crystal with and without applied electric field. In this simulation, the diverging beams propagate conically along the ordinary principal axis x_2 of the crystal and illuminate a screen placed 15 cm away from the crystal. Left: $0\,\mathrm{V\,m^{-1}}$ – A symmetric pattern is formed. Right: $63\,\mathrm{V\,m^{-1}}$ – The electric field breaks the symmetry.

tool for initially aligning a laser beam with the crystal axis.

The dynamic phase acquired by a plane wave with wavevector $\boldsymbol{k} = \frac{2\pi}{\lambda}\boldsymbol{e}_y$ can be tuned by the electric field $E_3 = \frac{V}{d}$ along the extraordinary axis, where d is the spacing between the electrodes producing the electric field. The voltage required to produce a phase shift of π is called half-wave voltage V_π and can be calculated from Equation (3.3.2.3) with $\vartheta_c = \pi/2$, $\varphi = \pi/2$:

$$V_\pi = \frac{d\lambda}{L}\left(r_{33}n_{\mathrm{e}}^3 - r_{13}n_{\mathrm{o}}^3\right)^{-1} \ . \tag{3.5}$$

The manufacturer (Thorlabs) specifies a linearisation to Equation (3.5) as a function of wavelength,

$$V_\pi(\lambda) \approx \lambda\, 0.361\,\mathrm{V\,nm^{-1}} - 23.844\,\mathrm{V} \ .$$

Optical impurities The incoming light is focussed into the first EOM, then recollimated and focussed into the second EOM, using 300 mm plano-convex lenses. Focussing the light through the crystals significantly reduces depolarising effects due to spatial inhomogeneities in the EOM crystals.

3.3.3 Internal birefringence cancellation

The action of an ideal EOM is to rotate the polarisation around a fixed axis represented by the unitary transformation

$$\hat{R}(U) = \exp\left[-\mathrm{i}\frac{\phi(U)}{2}\hat{X}\right] ,$$

where the rotation angle ϕ is a function of the voltage U applied across the crystal and $\hat{X} = |H\rangle\langle V| + |V\rangle\langle H|$ in the basis given by the extraordinary axis of the EOM. For a pair of ideal EOMs to be able to reach any output polarisation from an arbitrary input, the rotation axes must be made orthogonal to each other. This can in principle be achieved by placing a quarter waveplate between the EOMs; in practice, however, there is an unknown amount of static birefringence from each optical element including the EOM crystals and mirrors. To compensate this exactly, the inverse unitary operation has to be constructed with optical elements. It can be shown that at least a triplet of waveplates, e.g. two quarter-wave and one half-wave, are required to implement the most general unitary acting on the polarisation qubit [SCS12]. In Figure 3.16, all optical components that could affect the polarisation are labelled with a unitary operator. The operators $\hat{E}_1$ and $\hat{E}_2$ capture the unknown static birefringence in the two EOMs. We adjust the waveplate triplets $\hat{W}_1$ and $\hat{W}_2$ to approximately cancel all unwanted sources of birefringence, such that

$$\hat{P}_{\mathrm{BS}}\underbrace{\hat{W}_2\hat{M}_6\hat{M}_5\hat{E}_2}_{1}\hat{R}(U_b)\underbrace{\hat{W}_1\hat{M}_4\hat{M}_3}_{\hat{Q}_{\mathrm{WP}}}\hat{R}(U_a)\underbrace{\hat{E}_1\hat{M}_2\hat{M}_1\hat{F}\,|\psi\rangle}_{|\tilde{\psi}\rangle} = \hat{P}_{\mathrm{BS}}\hat{R}(U_b)\hat{Q}_{\mathrm{WP}}\hat{R}(U_a)\,|\tilde{\psi}\rangle ,$$

where $\hat{P}_{\mathrm{BS}} = \hat{Z} = |H\rangle\langle H| - |V\rangle\langle V|$ is the projector implemented by the PBS and $\hat{Q}_{\mathrm{WP}} = \exp(\mathrm{i}\frac{\pi}{4}\hat{Z})$ is the unitary of an ideal quarter waveplate aligned with a principal axis. We do not correct the transformation from the input state $|\psi\rangle$ to $|\tilde{\psi}\rangle$ because this merely rotates the overall coordinate system.

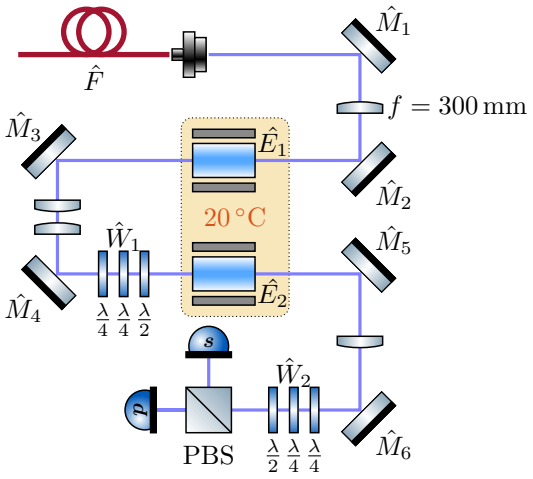

Figure 3.16: Detailed beam path for the fast photon polarisation analyser used by the client. The EOMs are thermally shielded and actively stabilised to 20 °C with 0.1 mK stability. The waveplate triplets $\hat{W}_1$ and $\hat{W}_2$ are used to cancel unwanted birefringence in the sections comprising $\{\hat{M}_3, \hat{M}_4\}$ and $\{\hat{E}_2, \hat{M}_5, \hat{M}_6\}$, respectively. The birefringence in components $\{\hat{F}, \hat{M}_1, \hat{M}_2, \hat{E}_1\}$ is absorbed into the calibration of the device.

In Protocol 3.3.1, we describe the two-step procedure that was used to adjust the waveplate triplets. This method implements by construction the inverse of an unknown system $\hat{X}$ in a waveplate triplet

$$\hat{W}(\beta_{q_1}, \beta_{q_2}, \beta_h) = \hat{U}_{\mathrm{WP}}\left(\frac{\pi}{2}, \beta_{q_1}\right) \hat{U}_{\mathrm{WP}}\left(\frac{\pi}{2}, \beta_{q_2}\right) \hat{U}_{\mathrm{WP}}(\pi, \beta_h)$$

consisting of two quarter- and one half-waveplate. Let

$$\hat{W}(\tilde{\beta}_{q_1}, \tilde{\beta}_{q_2}, \tilde{\beta}_h) = \hat{X}^{-1}\hat{U} \ ,$$

where $\hat{U}$ can be an arbitrary additional unitary transformation. The overall target operator $\hat{U} = \hat{X}\hat{W}(\tilde{\beta}_{q_1}, \tilde{\beta}_{q_2}, \tilde{\beta}_h)$ can be fully characterised by its mapping

$$|R\rangle \mapsto |\psi_R\rangle = \hat{U}\,|R\rangle \ , \tag{3.6}$$

$$|H\rangle \mapsto |\psi_H\rangle = \hat{U}\,|H\rangle \ . \tag{3.7}$$

In practice, any state can be created and projected onto using only a PBS, a quarter- and a half-waveplate. In particular, no half-waveplate is needed to create the states $|H\rangle$ and $|R\rangle$. The state $|R\rangle$ exhibits the special property of being an eigenstate of the half-waveplate operator $\hat{U}_{\mathrm{WP}}(\pi, \beta_h)$ irrespective of its rotation angle β_h. Therefore, $|\psi_R\rangle = \hat{X}\hat{W}(\beta_{q_1}, \beta_{q_2}, \beta_h)\,|R\rangle$ depends only on the quarter-waveplate angles.

Protocol 3.3.1. *Birefringence cancellation using two quarter-waveplates and one half-waveplate.*

1. With input $|R\rangle$, project the output on the target state $|\psi_R\rangle$. Maximising the overlap $|\langle\psi_R|\hat{X}\hat{W}(\beta_{q_1},\beta_{q_2},\beta_h)|R\rangle|$ by adjusting β_{q_1} and β_{q_2} implements the mapping (3.6).

2. With input $|H\rangle$, project the output on the target state $|\psi_H\rangle$. Maximising the overlap $|\langle\psi_H|\hat{X}\hat{W}(\tilde{\beta}_{q_1},\tilde{\beta}_{q_2},\beta_h)|H\rangle|$ by adjusting only β_h satisfies the mapping (3.7).

In our system (Figure 3.16), Protocol 3.3.1 is applied to $\hat{X}_1^\dagger = \hat{M}_4\hat{M}_3$ via the waveplate triplet $\hat{W}_1$ to create U_Q and to $\hat{X}_2^\dagger = \hat{M}_6\hat{M}_5\hat{B}$ via the waveplate triplet $\hat{W}_2$ to create $\hat{1}$. We back-propagate light through the output PBS and follow the procedure in this direction. We use quarter-waveplates 2 and 5 (Table 3.3) for creating and measuring circular states at different locations in the apparatus. For the cancellation of $\hat{X}_2$, projection optics are inserted between $\hat{B}\hat{E}_2$ and $\hat{W}_1$, which are then rearranged to create the input states for the adjustment of $\hat{W}_1$, for which projection optics are inserted between $\hat{M}_3$ and $\hat{E}_1\hat{A}$. Using that, the mappings $\hat{1} : |R\rangle \mapsto |R\rangle, |H\rangle \mapsto |H\rangle$ and $\hat{Q}_{\mathrm{WP}} : |R\rangle \mapsto |D\rangle, |H\rangle \mapsto |H\rangle$ are implemented using the waveplate triplets W_2 and W_1, respectively.

3.3.4 Validation

Prior to connecting the polarisation analyser to the single-photon interface of the ion trap, we validate its performance ex-situ using continuous-wave (CW) laser light at 422 nm.

3.3.4.1 Switching dynamics

Significant drift behaviour was observed after changing the electric field across the crystal [Tom19]. This can be attributed to charging of the crystal by the high-voltage electrodes attached to it. We therefore apply compensation pulses after each pulse with the same duration and amplitude, but opposite sign, in order

to zero the time-averaged electric field. A systematic analysis of the pulse duration, settling time and the duty cycle showed that with compensation pulses in place the detrimental effects, which otherwise dominate, can be fully removed. We determine the switching speed by recording the intensity of the transmitted fraction over time (Figure 3.17). The intensity settles to 1 % of the final value within 18 µs,

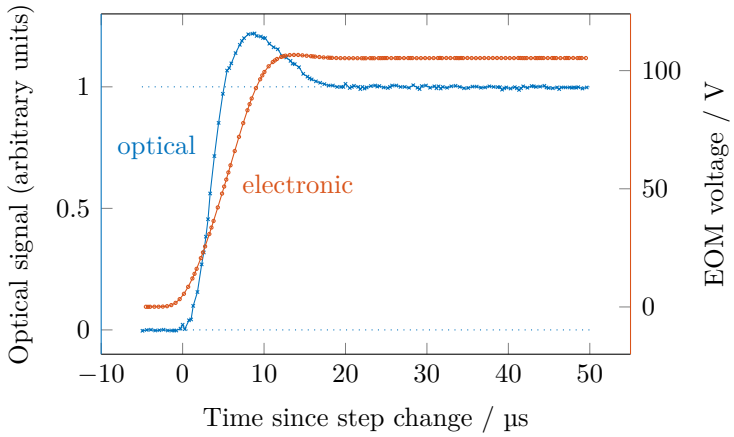

Figure 3.17: Example trace of settling behaviour of the EOM control voltage (red dots) and the horizontal polarisation component exiting the electro-optic modulator (blue crosses).

in synchronisation with the settling of the driving voltage, which is generated by amplifying (using Thorlabs HVA200) the signal from a DAC (Zotino). We therefore identify the driving electronics as the speed-limiting factor.

3.3.4.2 Polarisation measurement basis

To characterise the action of the client setup on arbitrary polarisation inputs, we use motorised waveplates following a Glan-Taylor polariser at the input. For this characterisation, we use $\sim 1\,\mathrm{mW}$ of continuous-wave laser light at 422 nm. The fraction of horizontally polarised output power contains information about the state amplitudes, but not their phase. To gain knowledge of the phase, amplitude information of linearly independent input states must be combined. We collect data for all combinations of quarter-waveplate (measured retardance $2\pi \times 0.2584(4)\,\mathrm{rad}$) angles $q \in \{-\pi/4, 0, \pi/4\}\,\mathrm{rad}$ and half-waveplate (measured retardance $2\pi \times 0.5000(1)\,\mathrm{rad}$) angles $h \in \{-\pi/8, 0, \pi/8, \pi/4\}\,\mathrm{rad}$ in random order. These waveplate settings

produce input polarisations from the set $\{|H\rangle, |V\rangle, |R\rangle, |L\rangle, |D\rangle, |A\rangle\}$ (the six nodes of an octahedron inscribed into the Bloch sphere). Figure 3.18 shows the fraction of horizontally polarised light at the output of the polarisation analyser as a function of the EOM control voltages for calibrated input polarisations[6].

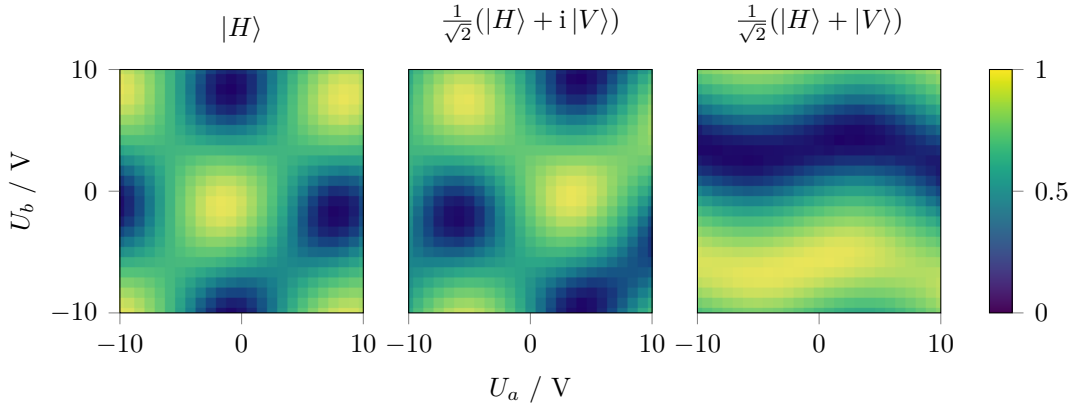

Figure 3.18: EOM control voltage scans of the transmitted fraction with different input states.

For each EOM voltage setting, we perform a nonlinear fit to the waveplate scan data using the model

$$t = \left|\langle\psi|\hat{Q}_{\mathrm{WP}}(q)\hat{H}_{\mathrm{WP}}(h)|H\rangle\right|^2 \tag{3.8}$$

for the transmitted fraction t, where $|\psi\rangle = \cos(\vartheta/2)\,|H\rangle + \sin(\vartheta/2)\exp(\mathrm{i}\varphi)\,|V\rangle$, the waveplate angles (q, h) are varied in the scan, and (ϑ, φ) are adjusted during the optimisation. The result of this analysis is shown in Figure 3.19. Using a density matrix formulation of Equation (3.8), the purity of the reconstructed states is found to be consistent with $\mathrm{Tr}(\rho^2) = 1$ for all EOM voltage settings used.

Orthogonal measurements In order to achieve perfect blindness, the measurements implemented by the client apparatus must not leak information to the server. One possibility for this to happen would be secret-dependent noise, such as imperfections that depend on the EOM voltage settings (Section 6.5). Using the same measurement setup as described at the beginning of this section, we record data for

[6]Calibrated using Schäfter + Kirchhoff, SK010PA-UV.

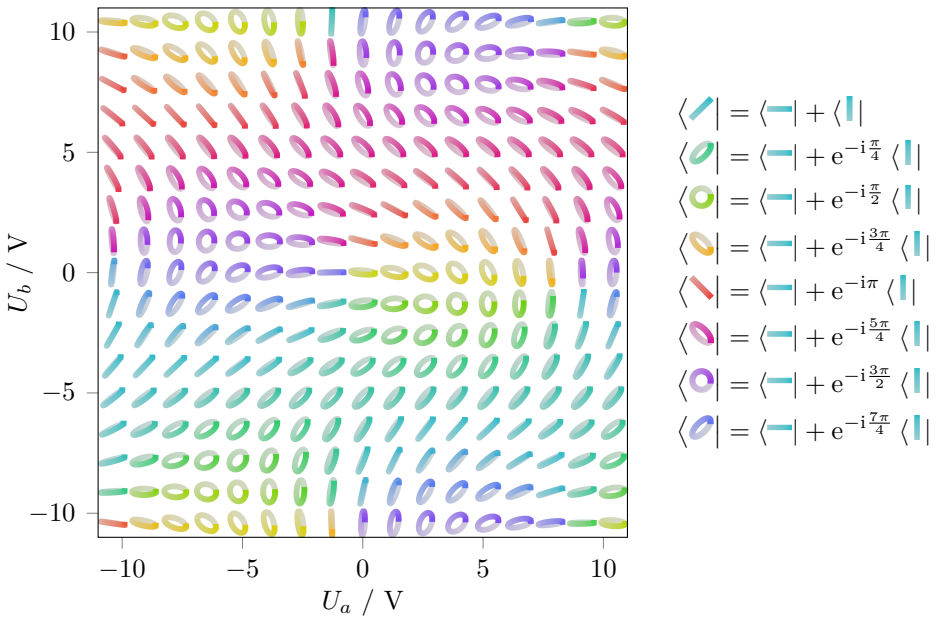

Figure 3.19: CW laser light is used to reconstruct the measurement basis implemented by the device as a function of the control voltages. Polarisation ellipses are shown for the basis states heralded by the horizontally polarised detector, where the colour highlights the phase of these states.

an exhaustive list of quarter- and half-waveplate angles (overlap between adjacent polarisation states $\approx 3 \times 10^{-4}$). For each EOM voltage pair (U_a, U_b) scanned, we select the two input polarisation states $|\psi^+_{ab}\rangle$ and $|\psi^-_{ab}\rangle$ created by these waveplates that respectively maximise the power transmitted and reflected by the PBS. The overlap $\left|\langle\psi^-_{ab}|\psi^+_{ab}\rangle\right|^2$ shown in Figure 3.20 averages to 0.0016 (median value).

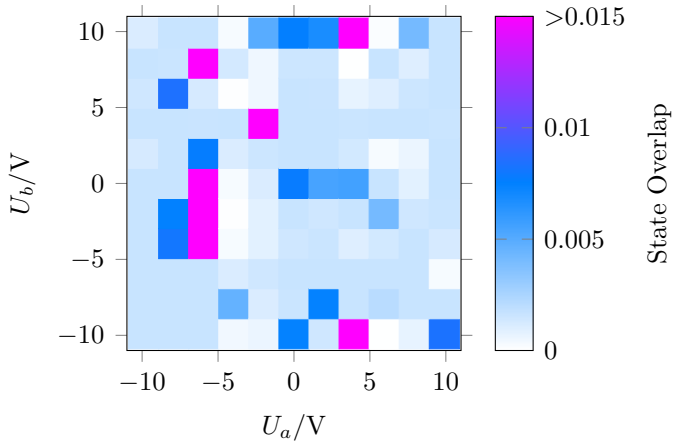

Figure 3.20: Overlap of polarisation input states which produce orthogonal polarisation measurement outcomes.

3.3.4.3 Long-term stability

The stability of the polarisation analyser was independently examined *ex situ* using repeated tomography measurements over the same set of EOM control voltages for 62 h (Figure 3.21). Over this time period, the infidelity due to polarisation drifts was less than 3×10^{-4}, limited by the accuracy of the measurement.

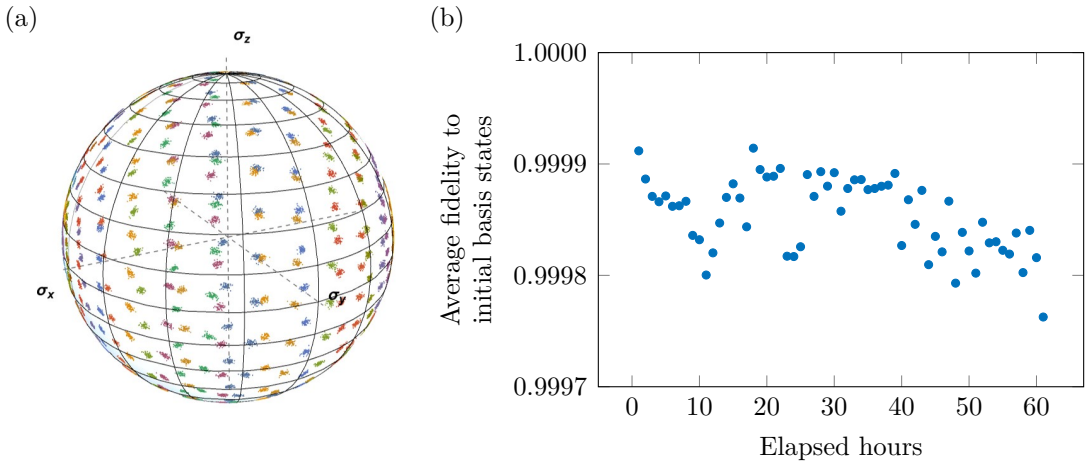

Figure 3.21: Long-term stability of the polarisation measurement basis implemented by the client apparatus. We repeatedly measure the laser intensity transmitted by the polarisation analyser's PBS for an over-complete set of input polarisation states to perform tomography of the polarisation measurement basis implemented by the device. (a) Reconstructed polarisation eigenstates of the measurement bases on a Poincaré sphere. Clusters of points with common colour correspond to states created by the same EOM voltage settings at different times. (b) For each EOM voltage setting we evaluate the fidelity of the measurement basis states w.r.t. the initial measurement over time and plot the average of values for all EOM voltage settings.

3.4 Experimental control system

3.4.1 ARTIQ

Both ion trap nodes, Alice and Bob, are controlled by independent instances of the ARTIQ ('advanced real-time infrastructure for quantum physics') control system [Bou+21]. Each system runs the ARTIQ master process on their own host computer, which manages the typical workflow consisting of experiment submission, prioritised scheduling, compilation of kernels, handling asynchronous remote procedure calls (RPCs), collecting, broadcasting, analysing and archiving data.

Kernels are programs that are executed on the coredevice[7] rather than on the host computer. The coredevice orchestrates events for execution in real-time – with 1 ns precision – on hardware from the open-source Sinara [Kas+20] ecosystem, which includes Eurocard modules with special-purpose functionality, such as digital input/output (DIO), direct digital synthesis (DDS), analogue to digital converter (ADC), and DAC cards. Additionally, custom gateware cores can be implemented on the coredevice field-programmable gate array (FPGA), such as digital signal processing, feedback loops (Section 3.4.2.1), and complex state machines (Section 3.4.4.1). Peripheral modules and corresponding gateware cores are directly accessible from a kernel program by a unique real-time input/output (RTIO) channel number. Input and output events are composed of a timestamp, an RTIO channel number and a 32-bit data word. They are distributed to and from the corresponding gateware core via the RTIO system. Output events are placed in a first-in, first-out (FIFO) buffer of the RTIO system ahead of time and strobed into the target core when the specified output timestamp matches the global real-time clock value. Each RTIO channel has an input event FIFO buffer, which captures events strobed by the respective gateware core. The kernel program is responsible for fetching these input events from the buffers.

Since the kernel is executed on a soft-core central processing unit (CPU) inferred on the same FPGA as the RTIO system, this architecture is sufficiently flexible and ex-

[7] 'Kasli' FPGA carrier.

tensible for most atomic, molecular and optical physics (AMO) experiments. If more channels are needed than the main coredevice provides, the distributed real-time input/output (DRTIO) system can be used to forward events to downstream 'satellite' coredevices, which have no processor for kernels, but provide RTIO interfaces to further peripherals attached to additional gateware cores at potentially different locations, via industry-standard small form-factor pluggable (SFP) transceivers. This solution works well for applications where the event rate is sufficiently constrained to be generated on the fly in a single kernel. Future quantum computing devices will likely require parallel processing capabilities in order to sustain the high event rates required for complex ion transport operations or pulse shaping.

On the other end of the infrastructure is the user interface – the 'dashboard'. The dashboard provides an interface to perform actions on the processes and data hosted by the master computer, such as submitting experiments, plotting broadcasted data, and modifying calibration parameters. Any number of client computers can subscribe to the same master at the same time.

Experiments are written in an object-oriented dialect of Python. The ARTIQ compiler generates kernels for the embedded coredevice architecture based on the control flow expressed in the experiment script.[8]

3.4.2 Coherent control

The majority of quantum operations with trapped ions are driven by RF signals, microwaves, or lasers. Lasers are best operated continuously at a suitable setpoint and switched downstream using acousto-optic modulators (AOMs). This not only benefits their stability, but it also allows the laser to be easily shared between users, each possibly requiring multiple laser beams with different amplitudes, phases and frequencies. AOMs are ubiquitous in quantum optics laboratories. They consist of a crystal with a piezo transducer attached to one side, which is driven via a resonant RF circuit. If an RF signal is applied, an acoustic wave travels through the crystal and imprints a modulation of the refractive index, which acts as an optical

[8]This choice is debatable, as it prioritises a low entry bar for new users, who might already be familiar with Python, over the suitability of the language for embedded programming.

grating. The intensity, phase and frequency of the diffracted light depends on the amplitude, phase and frequency of the RF drive. Typically, the first diffraction peak is spatially isolated from other components using an iris or by coupling it into a single-mode optical fibre.

Whether RF signals are used directly to address the ions using an antenna, or indirectly via an AOM to address an optical transition, the amplitude, phase and frequency of the RF signal is responsible for the operation either way. While it is straightforward to adjust the frequency and amplitude of RF signals, establishing absolute phase control across multiple distributed channels is non-trivial, as it requires precise timing of updates when the phase or frequency parameters are changed. To generate RF, we employ the AD9910 variant of the Urukul DDS card. The AD9910 chip ships with features for deterministic multi-chip phase synchronisation and is therefore well suited to our purpose.

3.4.2.1 Phase-coherent amplitude stabilisation

The laser power reaching the ion is subject to uncontrollable environmental effects, such as fibre birefringence depending on temperature and strain, AOM diffraction and fibre coupling efficiency variations. To obtain repeatable results, the intensity needs to be stabilised. To this end, we monitor the intensity on a pickoff photodiode module and feed back onto the amplitude of the RF driving the corresponding AOM. The digital signals for 8-16 RF channels can be processed by a single pipelined proportional-gain, integral-gain (PI) filter using the samples from 8 ADC channels. The bandwidth of this filter is currently limited by the DDS programming latency, as the AD9910 chip requires 72 bits, including 8-bit address, 14-bit amplitude, 32-bit frequency, and 16-bit phase information, to be written at every update, even if only the amplitude is changing. For phase-coherent control, this creates an important difficulty, as the phase cannot be set independently of the amplitude. Moreover, since the PI loop iterations cannot be synchronised with the RF frequency of all channels, the gateware core needs to keep track of the phase of all RF channels, such that the output phase is reproducible when switching between frequencies.

3.4.2.2 Arbitrary waveform generation

The AD9910 DDS chip exhibits a random access memory (RAM) modulation feature that can be used to program the amplitude, frequency, phase, or both amplitude and phase simultaneously (polar mode) to an arbitrary waveform. The RAM can store 1024 samples, which can be supplied to the DDS at a programmable sampling rate. Up to eight different waveforms can be concatenated, where each waveform can be played at its individual speed, but with a common destination (amplitude, frequency, phase, or polar). Figure 3.22(a) shows an example of amplitude modulation and

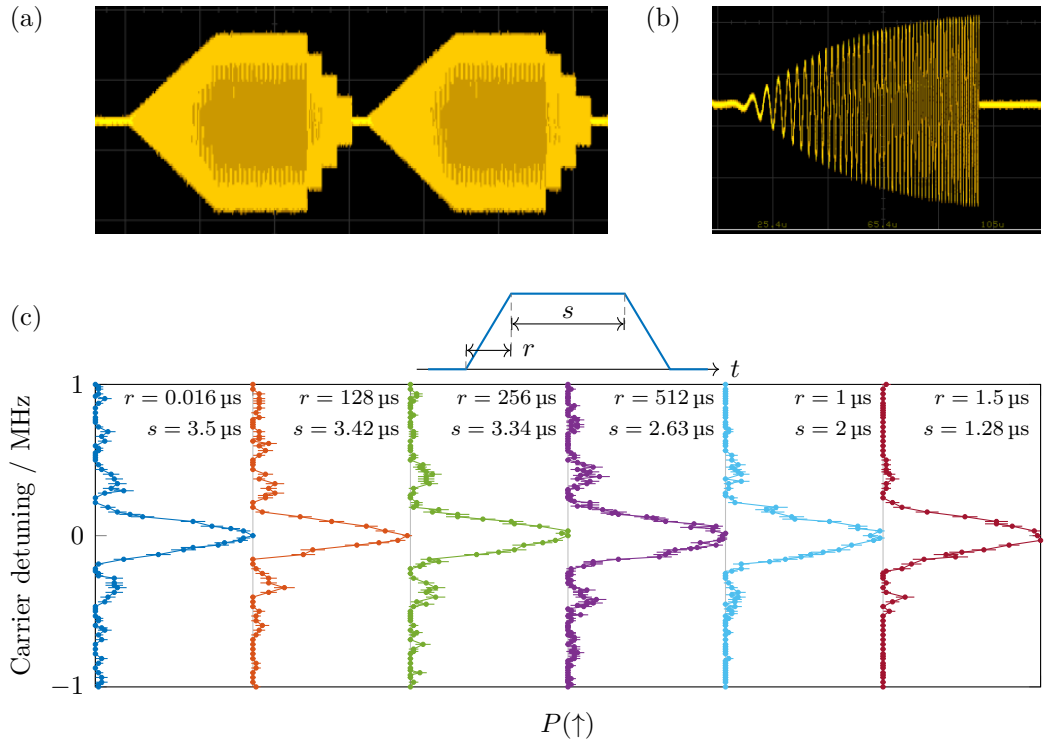

Figure 3.22: The AD9910 RAM feature can be used for arbitrary waveform generation. (a-b) Amplitude modulation (a) and chirping of the frequency (b) of an RF pulse. (c) Rabi detunig scans on the 674 nm transition in $^{88}Sr^{+}$ with varying linear pulse ramp duration, r. The duration of the flat top, s, is adjusted to maintain a pulse area of π. The 'wings' of the frequency response are increasingly suppressed as r is increased.

Figure 3.22(b) an example of a frequency chirp. In (a), a linear rising edge is generated using the first waveform and a high density of samples, and the following constant waveforms are each represented by only two samples in memory, independent of the step duration. In (b), a single waveform is used to increase the

frequency of the pulse over time, starting at 0 Hz. The simultaneous change in amplitude is a result of the high-pass filtering property of the RF chain.

Moreover, we evaluate this pulse shaping feature on a single $^{88}Sr^{+}$ ion by probing the narrow-linewidth quadruople transition at 674 nm (see Figure 3.22(c)). The observed lineshape is well approximated by the spectrum of the driving pulse, as the linewidth of the transition is ~ 5 orders of magnitude smaller than the carrier Rabi frequency.

Going forward, the arbitrary waveform generation feature of the AD9910 RAM could be used to suppress off-resonant excitation errors that can arise in two-qubit gates without changing the existing hardware. For the experiments presented in this thesis, pulse shaping for two-qubit gates was performed using a different approach (see Section 3.4.3.1).

3.4.3 Hardware extensions

3.4.3.1 Pulse shaper

Square pulses are produced by simply switching the RF on and off with a sharp edge. As a consequence, the frequency spectrum around the carrier Ω falls off slowly with $1/\omega$. In many cases, however, transitions are closely spaced and nearby transitions are driven even though they were not addressed. Pulse shaping usually refers to smoothening the edges of a pulse, but more complex shapes have been used in the past [Sch+18]. We implement basic pulse shapes using a custom-built multiplier circuit: a low-pass-filtered TTL pulse is multiplied with the RF signal (see Figure 3.23). The bandwidth of the filter is selectable between fifth-order Bessel low-pass filters with 230 kHz and 700 kHz cutoff frequency (see Figure 3.23). The measured cutoff frequencies of 238(7) kHz and 720(10) kHz deviate by $< 5\,\%$ from the design values in accordance with known component tolerances.

3.4.3.2 Fast photodiode trigger

Because the pulsed laser is not locked to the control system clock, the duration from a request until the arrival of the excitation laser pulse is random and can be as long

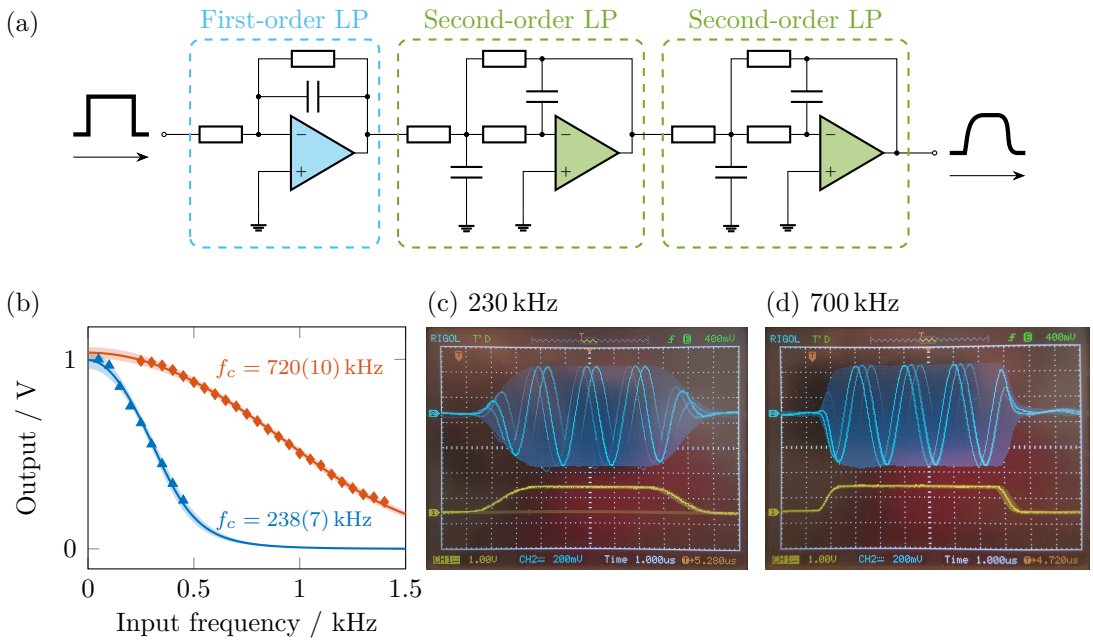

Figure 3.23: We produce shaped RF pulses by multiplying an RF carrier signal with an envelope that is generated by filtering a square pulse with a fifth-order low-pass Bessel filter, see circuit (a). (b) The amplitude response of two selectable filters (same circuit, different components) is measured by filtering a square wave of varying frequency. Solid lines show fits of the theoretical filter response to the data, with 90 % confidence intervals indicated by shaded areas. (c-d) RF pulses are shaped (blue trace) by multiplying a continuous RF signal with the low-pass-filtered envelope (yellow trace) obtained with the 230 kHz (c) and 700 kHz (d) filter setting.

as the laser pulse interval of 12.5 ns. However, the arrival time of the excitation pulse triggers the acceptance window for the single photon detectors. The electronics used to detect inputs require at least 1.5 V signal for 8 ns into 50 Ω. Previously, a bare photodiode[9] was placed in the residual infrared beam after second harmonic generation. However, even with ∼ 20 nJ incident pulse energy, this photodiode did not reliably trigger the digital input. To resolve this issue, a monostable circuit with > 1 GHz input bandwidth was required to resolve the ∼ 1 ns pulses from a weakly-driven (∼ 10 pJ pulses) bare photodiode (Figure 3.24 and [Nad16], Fig. 3.20) with less than 500 ps timing jitter. Unfortunately, there is no off-the-shelf component with those specifications. Together with D. Nadlinger, I developed a design which uses an ultra-high-speed comparator with positive emitter coupled logic (PECL) differential

[9] Hamamatsu, S5973.

output[10], a PECL flip-flop[11] with a feedback *RC* element to create a delayed reset signal and two PECL-LVTTL translators[12] in parallel. A precision voltage reference[13] drives a potentiometer that supplies a variable reference voltage to the comparator. As an additional feature, a current-shunt monitor[14] is included for power monitoring. The performance of the implemented circuit meets all specifications, featuring 6 ps

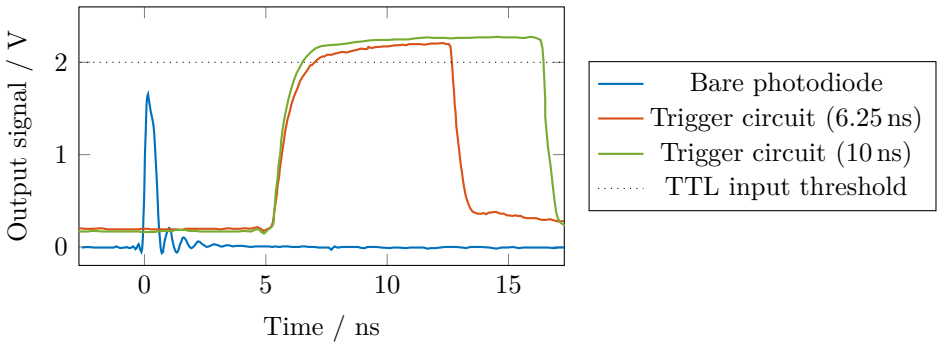

Figure 3.24: Photodiode output signals into 50 Ω. The solid line shows the response of a weakly driven, bare photodiode upon incidence of ∼ 20 pJ pulse energy, which neither reaches the TTL input threshold of 2 V, nor the required pulse width of 8 ns. The dashed and dashdotted lines show the output of a fast, low-jitter monostable trigger circuit for 10 pJ incident laser pulse energy. The length of the trigger pulse above the TTL input threshold was initially set to 6.25 ns (red line) to accommodate an 80 MHz pulse train, and then increased to 10 ns (green line) to reach the length required to reliably trigger the control system.

timing jitter, ∼ 10 pJ detection threshold, and perfect reliability (no missed trigger since installation). Figure 3.24 shows oscilloscope traces of the circuit's output with different time constants compared to a bare photodiode signal.

3.4.4 Gateware extensions

As the advanced real-time infrastructure for quantum physics (ARTIQ) control system is open-source, it is possible to modify and extend it. We make use of this possibility for cases where the timing requirements are particularly high.

[10]Analog Devices, ADCMP582.
[11]ON Semiconductor, MC100EP51.
[12]ON Semiconductor, MC100LVELT23.
[13]Linear Technology, LT1461.
[14]Texas Instruments, INA210.

3.4.4.1 Entangler core

The attempt loop for generating single photons (see Section 5.1.1) requires a high density of RTIO events following a logical decision (success, repeat, or fail). To reach the maximum possible repetition rate, the soft-core CPU cannot be involved in this decision. Furthermore, for two-party protocols, the systems must coordinate their timing and the decisions. We use a custom gateware core to handle the specific task of issuing transistor-transistor logic (TTL) pulses, registering input events within an acceptance window, and to synchronise the two systems. The finite-state machine (FSM) of this core has three operating modes:

- **Standalone.** The system runs independently without communication overheads.
- **Follower.** The system follows the commands received from the 'leader'. In this mode, the system does not make decisions by itself; it can only fail with a timeout while waiting for the leader to initiate an attempt.
- **Leader.** The system synchronises with the 'follower', issuing a command (success, repeat, or fail) at every iteration.

The main state of the FSM executes a single attempt to generate a photon. This state is independent of the operating mode. A counter provides the time base for the event placement in this state.

Outputs. Each TTL output is assigned an *on* and an *off* time; specialised 'sequencer' cores compare the current time base value with the programmed times and switch the output accordingly when they match. These outputs include

1. the 422 nm single-pass AOM switch and
2. the 1092 nm AOM switch for fast state preparation, and
3. the picosecond excitation pulse trigger to request an excitation pulse from the pulse picker. The pulse picker selects a single pulse out of the 80 MHz pulse train. As the pulsed laser is not locked to the control system, the jitter between this trigger and the picked optical pulse is between 0 ns and 12.5 ns.

An additional TTL output switches the 422 nm double-pass AOM off as soon as the attempt loop terminates in order to reduce errors due to laser leakage.

Inputs. Each TTL input core monitors the signal for rising edges between an assigned *start* and *end* time after a reference event. The fast photodiode trigger (see Section 3.4.3.2) detects the arrival of the excitation pulse with an accuracy of 1 ns and provides this reference event to the four gated avalanche photodiode (APD) inputs to remove the jitter that was introduced by the pulse picker. Each APD input core can be triggered by a rising signal edge within the assigned window after the fast photodiode reference trigger.

Heralder. This core compares the triggered APD input pattern with up to four different herald patterns. For the single-photon experiments using the Bell state analyser (Chapter 5), we use the patterns $\{0001, 0010, 0100, 1000\}$, for the experiments presented in Chapter 6, $\{0100, 1000\}$, and for heralding remote entanglement between two systems, the coincidence patterns $\{0011, 0101, 1010, 1100\}$. If at the end of the global time base counter a match is indicated by the heralder, the state machine signals completion. The analysis sequence can either be played directly from memory (see Section 3.4.4.3), or handled by the soft-core CPU.

3.4.4.2 Core-link transaction

Passing digital signals between two FPGAs falls into the category of clock domain crossings, which require special attention to ensure the signals are correctly received. Here we transmit a data nybble (4 bits) in parallel from the leader to the follower. We add a write-enable (WE) bit to the bus, which the leader asserts in parallel with the data to indicate to the follower that the data is valid. The follower registers the five incoming bits in the local clock domain using two consecutive flip-flops to reduce the probability for metastabilities. If the follower's state machine is ready to perform the command encoded in the data, it responds by asserting the acknowledgement (ACK) bit. The leader also uses two consecutive flip-flops to

stabilise the incoming ACK bit, and if it detects a rising edge within the expected time frame, the interaction is assumed to have succeeded.

The default transaction contains 1 `trigger` bit, 1 `success` bit, and 2 `reason` bits. The bits `trigger` (no success, immediately start next attempt) and `success` are mutually exclusive, but if neither is asserted, the leader has timed out and the state machine is about to return. The `reason` bits are only relevant in case of a success, and contains additional information about the outcome of the attempt. For example, `reason` may encode the index of the herald pattern which led to the success (e.g. for the experiments reported in Chapter 5).

For BQC (Chapter 6), the client must communicate one of eight possible phase angles for every detected photon. To accommodate the additional information, we implement a second core-link transaction, extending `reason` from two to six bits. The extra bits are also used to indicate the start and end of a computation round, such that low-latency direct memory access (DMA) playback (see Section 3.4.4.3) can be used in all cases (we note that in our BQC protocol, the first and the last step of a computation differ from intermediate steps).

3.4.4.3 Low-latency DMA playback

When the entangler core returns, successful or not, and the soft-core CPU retakes control of the experiment, a delay of $\sim 60\,\mu s$ is typically necessary before the first event can be issued. In the past, this delay has caused noticeable dephasing of the $^{88}Sr^{+}$ network qubit due to magnetic field noise [Ste+20]. Better magnetic field stabilisation has relieved this issue [Mai20], but to further improve the situation, I developed a gateware core that interfaces the entangler core with the DMA engine. Using this gateware core reduces the latency to $\sim 0.1\,\mu s - 3\,\mu s$. The interface can store 31 references to DMA sequences that can be linked to specific entangler core reason codes; one extra sequence is reserved for unsuccessful attempt loops (e.g. due to timeout).

4 Quantum operations

Contents

In this chapter I present results from the integration of entangling gates into one of our trapped-ion network nodes. The prevailing method to generate entanglement between ions trapped in the same potential is via excitations of their collective

motion. The motional states are therefore a crucial component of a trapped-ion quantum processor and must therefore be controlled with sufficient precision. For this reason, we start the discussion by characterising the ions' motion (Section 4.1). We then describe several aspects of the spin-dependent force (SDF) that enables the desired gate operation (Section 4.2), and finally analyse its performance on different ion crystals with different methods (Section 4.3 and Section 4.4).

4.1 Characterisation of the motion

The normal modes of trapped-ion motion can be described by independent quantum harmonic oscillators coupled to a surrounding amplitude reservoir and a phase bath. The dynamics of the motional states are therefore dissipative in nature. When we use the motion to mediate entanglement between two ions, these dissipative processes corrupt the quantum information contained in the system, which poses an irreversible source of error[1] (as opposed to coherent errors, which could, in principle, be corrected by using advanced control schemes). To quantify the effect of these couplings on the fidelity of our gates (Section 4.2), we measure both the heating rate and the dephasing rate of the relevant motional modes.

4.1.1 Temperature and Lamb-Dicke parameter

We perform thermometry of the motion using the sideband ratio method [Mee+96] (see Section 2.3.1), which yields an estimate of $\bar{n}$ alongside the effective Rabi frequency, $\eta\Omega_0$, where η is the Lamb-Dicke parameter that characterises the coupling strength of the probe laser with the motion, and Ω_0 is the carrier Rabi frequency. In order to determine the value of η, we measure Ω_0 independently using the same Raman beams at the same powers as were used to probe the sidebands (see Figure 4.1).

[1] This assumes that the state of the system's environment is beyond our control. Through the use of quantum error correction, where information is stored redundantly in a larger system, a limited amount of dissipation can nevertheless be tolerated [Ste03].

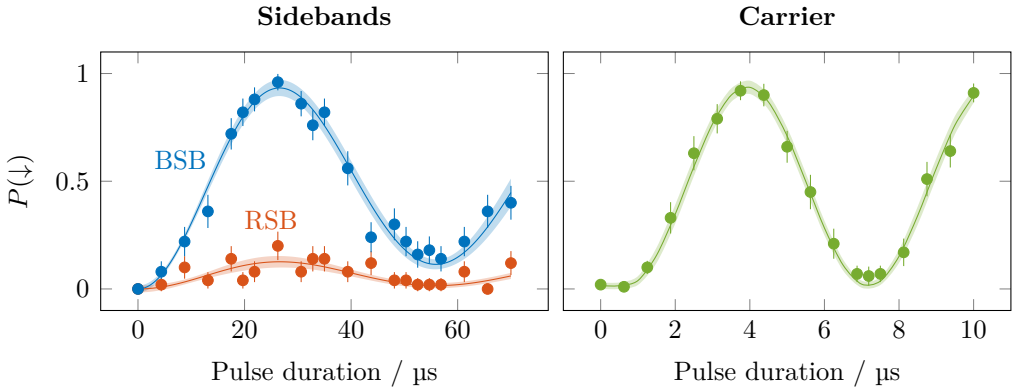

Figure 4.1: Measurement of the temperature and the Lamb-Dicke parameter on the axial OOP mode of the mixed-species $^{88}Sr^{+}$-$^{43}Ca^{+}$ crystal at 3.354 MHz using the Raman beams on the logic qubit of $^{43}Ca^{+}$. Left: flops on the red and the blue sideband, respectively; we measure $\eta_{\mathrm{exp}}\frac{\Omega_0}{2\pi} = 18(9)\,\mathrm{kHz}$ and $\bar{n} = 0.16(3)$. Right: flops on the carrier transition with the same beam parameters yield $\frac{\Omega_0}{2\pi} = 153(2)\,\mathrm{kHz}$. Shaded areas show the 90 % confidence intervals around the mean predicted by the fits (solid curves). Combining the results, the corresponding Lamb-Dicke parameter is $\eta_{\mathrm{exp}} = 0.11(6)$, which matches well with the theoretical value of $\eta_{\mathrm{th}} = 0.12$.

4.1.2 Heating rate

The coupling with a surrounding amplitude reservoir leads to heating as the system thermalises with the bath. Amplitude heating is described by the Lindblad operators $\dot{\bar{n}}^{\frac{1}{2}}\hat{a}$ and $\dot{\bar{n}}^{\frac{1}{2}}\hat{a}^{\dagger}$ [Tur+00] (see Section 2.2.4). The increase of the average occupation number of the motional state, $\bar{n}$, is linear in time and the rate, $\dot{\bar{n}}$, is called heating rate. It is important to know the heating rate because heating leads to residual entanglement between the motion and the ions after applying the SDF. As heating is a stochastic process, this process is irreversible and causes an error in the gate operation.

To find the rate of change in temperature of the motion, we scan the sideband pulse duration at variable delays after ground state cooling. Using a single $^{88}Sr^{+}$, we measure the heating rate in all three motional modes (see Figure 4.2). The radial modes were rotated by 0.5 rad around the trap axis to enable Doppler cooling of both radial modes using the same lasers. This rotation also increases the overlap of the in-plane radial (higher frequency) mode with electric field noise from the trap surface and complicates a direct interpretation in terms of the frequency scaling of

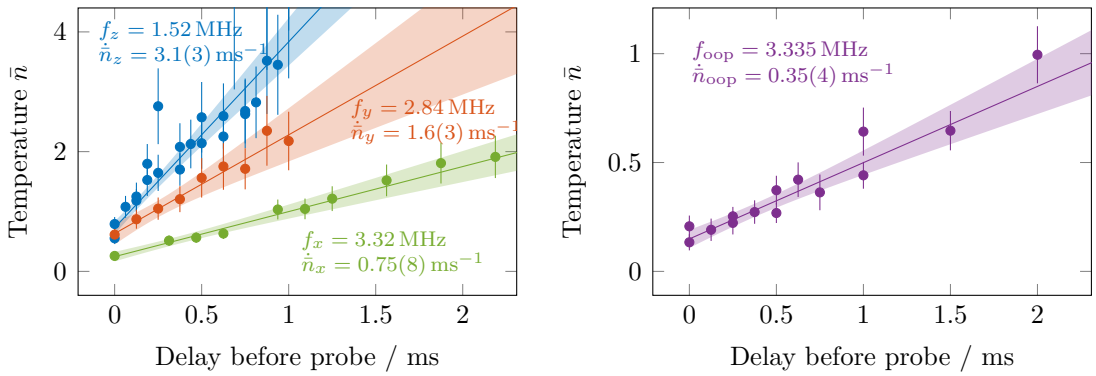

Figure 4.2: Heating rate measurements of all three modes of a single $^{88}Sr^+$ (left) and of the axial OOP mode of the mixed-species configuration (right). Error bars span one standard deviation. Shaded areas show 90 % confidence bands around the predicted mean (solid lines).

the heating rate (see Section 2.2.4). We perform a measurement of the (mostly) in-plane radial mode also with 0.25 rad rotation around the axis, and observe a heating rate of $370(30)\,\mathrm{s}^{-1}$, which is significantly lower than the $750(80)\,\mathrm{s}^{-1}$ found at a mode rotation of 0.5 rad. This observation is consistent with the prevailing theory that the majority of electric field noise originates from the trap surface.

For the mixed-species gates described in the following section (Section 4.2), the axial OOP mode is the most relevant mode, followed by the axial IP mode, and radial 'rocking' modes (ions oscillating out of phase). We measure the heating rate of the axial OOP mode (see Figure 4.2) and obtain $350(40)\,\mathrm{s}^{-1}$. A measurement of the IP mode heating rate was attempted and we obtained $2100(1300)\,\mathrm{s}^{-1}$ (n.b. the error is 63 % – no more reliable measurement was possible as the mode resisted being cooled below $\bar{n}_{\mathrm{ip}} \approx 3$)[2]. These measurements can be used to test the prediction of Equation (2.14) based on the axial heating rates of a single $^{88}Sr^+$, and we find reasonable agreement (with 26 % confidence, equivalent to a 1.12-sigma discrepancy).

The radial modes of the mixed-species crystal decouple into single-ion motional modes with $\lesssim 1\,\%$ participation of the other species. The rocking modes are dominated by the heavier ion, $^{88}Sr^+$, and the in-phase radial modes by the lighter

[2]For the sideband thermometry to return accurate results, we found that an initial temperature of $\bar{n} \lesssim 2$ is required, as the sensitivity of the method decreases, and thus increases the sampling and stability requirements considerably for discerning the red sideband (RSB) from the blue sideband (BSB) amplitude with confidence at $\bar{n} \sim 3$.

ion, $^{43}Ca^{+}$. We therefore assume that the rocking modes of the mixed-species crystal appear with similar frequency and heating rate as the radial modes of a single $^{88}Sr^{+}$ ion, which have been measured independently (see Figure 4.2). As the in-phase radial modes are found at $\sim 2\times$ higher frequencies than the rocking modes, their heating rates are expected to be $\sim 4\times$ lower than those of the rocking modes.

In suspicion of the quality of the trap RF, we performed heating rate measurements of the radial mode of $^{88}Sr^{+}$ at 1.7 MHz at different offsets of the ion from the radially compensated point. We observed no significant increase in the heating rate with displacement fields of up to $160\,\mathrm{V\,m^{-1}}$.

4.1.3 Motional decoherence

To measure the motional coherence time, we perform Ramsey experiments on the motional mode (Protocol 4.1.1), where the motional 'qubit' is encoded in the Fock states $|0\rangle_\alpha$ and $|1\rangle_\alpha$.

Protocol 4.1.1. *Motional Ramsey experiment.* [Tur+00]

1. Initially, the motion is cooled close to the ground state and one ion is prepared in $|+\rangle = \frac{1}{\sqrt{2}}(|\downarrow\rangle + |\uparrow\rangle)$ using a carrier $\frac{\pi}{2}$ pulse.
2. A RSB sideband π pulse maps this state to the motion: $|+\rangle \otimes |0\rangle_\alpha \rightarrow |\downarrow\rangle \otimes \frac{1}{\sqrt{2}}(|0\rangle_\alpha + |1\rangle_\alpha)$.
3. Optionally, the motional states can be flipped to echo out slow changes in the mode frequency. This is done by mapping the superposition from the motion to the ion using a RSB π pulse, applying a carrier π pulse to the ion, and returning the state to the motion using another RSB π pulse.
4. A final RSB π pulse returns the superposition to the spin for readout.
5. The remaining coherence of this state is analysed by scanning the phase of a $\frac{\pi}{2}$ carrier pulse, which maps the phase information onto the populations, which can be detected using standard fluorescence readout.

The coherence of a superposition of motional states, e.g. $|+\rangle_\alpha = \frac{1}{\sqrt{2}}(|0\rangle_\alpha + |1\rangle_\alpha)$, degrades (dephases) over time due to amplitude and phase heating, which are formally described by coupling the system to an amplitude and phase bath [Tur+00].

Amplitude heating (see Section 4.1.2) is characterised by the heating rate, $\dot{\bar{n}}_\alpha$ and is conventionally referred to as heating, but it also affects the coherence of the motional state. In the absence of phase heating, amplitude heating alone causes the contrast of the motional superposition between $|0\rangle$ and $|1\rangle$ to decrease with [Tur+00]

$$\langle +|_\alpha \hat{\rho}_\alpha(t)|+\rangle_\alpha = \frac{1}{2}\left[1 + \left(1 + \dot{\bar{n}}_\alpha t\right)^{-2}\right] \ .$$

Phase heating on the other hand does not increase the average motional occupation number, but contributes to motional decoherence. This effect can be modelled by the Lindblad operator $(2/\tau_\alpha)^{\frac{1}{2}}\hat{a}_\alpha^\dagger \hat{a}_\alpha$, where τ_α is the motional coherence time. In the absence of amplitude heating ($\dot{\bar{n}}_\alpha = 0$), phase heating alone leads to an exponential decay of the Ramsey contrast with [Tur+00]

$$\langle +|_\alpha \hat{\rho}_\alpha(t)|+\rangle_\alpha = \frac{1}{2}\left(1 + \mathrm{e}^{-\frac{t}{\tau_\alpha}}\right) \ .$$

In reality, phase and amplitude heating act simultaneously. Moreover, heating causes population leaking from the qubit subspace to higher-energy Fock states. Additionally, the initial motional state is a thermal mixture, lowering the maximum achievable contrast and causing errors in mapping between the ion's spin and $|1\rangle_\alpha$, introducing spin dephasing as an additional error source. Spin dephasing has no significant effect on the time constant of the Ramsey contrast decay; it merely lowers the initial contrast. With a spin echo in place, spin dephasing is negligible.

Same-species (two $^{43}Ca^+$). As both ions participate equally in the same-species axial OOP motion, this mode experiences a very low heating rate; we measure $\sim 5\,\mathrm{s}^{-1}$ at 3.8 MHz. Therefore, the contrast decay observed in a motional coherence experiment (Protocol 4.1.1) can be attributed entirely to phase heating.

As we do not have single-ion addressing capabilities, we 'hide' one ion in the $D_{5/2}$ states. To do this, we apply a global $\frac{\pi}{2}$ pulse and perform fluorescence

readout. We repeat this process until the fluorescence counts are consistent with one ion being bright and the other one being dark. After state preparation without repumper beams, Protocol 4.1.1 can be executed without further precautions. Using the motional spin echo, we obtain the best-fit estimate of the dephasing time constant of $\tau_{\mathrm{oop}}^{\mathrm{CC}} = 7.4(5)\,\mathrm{ms}$.

Mixed-species ($^{88}\mathrm{Sr}^+$ and $^{43}\mathrm{Ca}^+$). We perform Protocol 4.1.1 on the axial OOP mode of the mixed-species crystal. We use the sidebands of the logic qubit in $^{43}\mathrm{Ca}^+$ for manipulating the motional state.[3] We observe that motional dephasing contributes significantly to the decay of the Ramsey contrast, both with and without spin echo (see Figure 4.3); we obtain best-fit estimates of the dephasing time constant of $\tau_{\mathrm{oop}}^{*} = 3.4(4)\,\mathrm{ms}$ and $\tau_{\mathrm{oop}} = 0.67(4)\,\mathrm{ms}$ in these two cases, respectively. The discrepancy points towards the presence of low-frequency technical

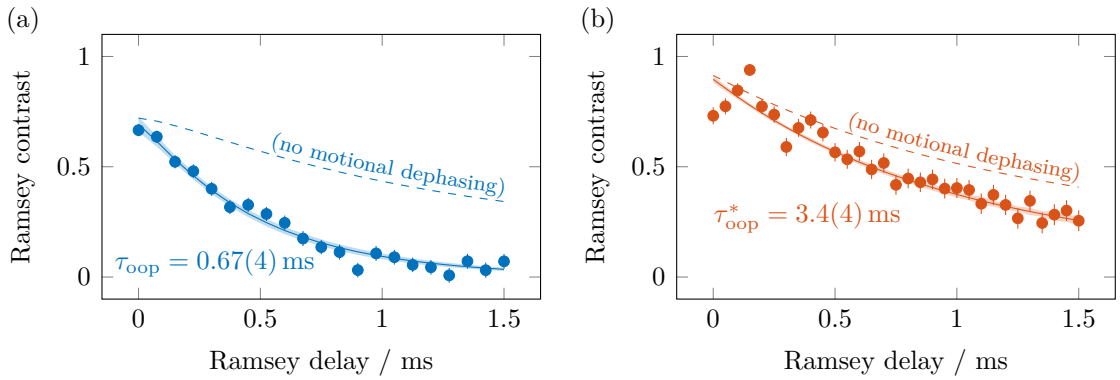

Figure 4.3: Motional coherence of the mixed-species axial OOP mode is measured using motional Ramsey experiments, (a) without and (b) with spin echo (see Protocol 4.1.1), via the motional sidebands of the logic qubit of $^{43}\mathrm{Ca}^+$. We simulate the spin-motion dynamics by solving the master equation; we assume an initial temperature of $\bar{n}_{\mathrm{oop}} = 0.15$, a heating rate of $\dot{\bar{n}}_{\mathrm{oop}} = 350\,\mathrm{s}^{-1}$ (see Figure 4.2), a RSB pulse duration of 27 µs, and an instantaneous, error-free carrier π pulse; the dephasing time constants of the spin and the motion are optimised in a least-squares fitting routine to fit the data (solid curves with shaded 90 % confidence intervals). The dashed curves show the simulated decay model for $\tau \to \infty$, but with all other imperfections (finite temperature, heating rate, and spin dephasing) the same.

noise in our setup.[4]

[3] In hindsight, it would have been advantageous to use the sidebands of the clock qubit in $^{43}\mathrm{Ca}^+$, as this would eliminate spin dephasing from the resulting decay.

[4] A long and unsuccessful 'hunt' for potential noise sources was abandoned for the benefit of a DPhil student's mental health.

The results obtained with spin echo in the same-species case and the mixed-species case differ by a factor of ~ 2. This discrepancy was not further investigated, but it is plausible that the asymmetric motional mode structure affects the coupling of the mixed-species crystal to the phase reservoir in a similar way as that to the amplitude reservoir.

4.2 Implementation of the light shift gate

We perform two-qubit $\hat{\sigma}_z \otimes \hat{\sigma}_z$ geometric phase gates using the light shift SDF generated by a single pair of $\sim 20\,\mathrm{mW}$ Raman laser beams at 401.543 nm (see Section 4.2.1). Only one pair is required to drive both $^{88}Sr^+$ and $^{43}Ca^+$ thanks to their compatible electronic level structure [Hug+20] (see Figure 3.5 in Reference [Sch18]). The main advantage of this scheme over Cirac-Zoller and Mølmer-Sørensen gates is its robustness to qubit frequency shifts. The Raman beams are aligned to address the axial motion of the two-ion crystal [Hug+20] (see *son* beams in Figure 2.5). For maximum gate efficiency on the OOP mode, the ion spacing is set to a half-integer multiple of the effective wavelength $\lambda_R/\sqrt{2}$ (see Section 4.2.5). As the memory qubit in $^{43}Ca^+$ does not experience a light shift, this interaction is performed on the logic qubit instead. In $^{88}Sr^+$, the ground state Zeeman levels are used (network qubit, see Figure 3.2 for an energy level diagram). Walsh-1 modulation compensates for the SDF imbalance between the hyperfine qubit states and between the two species (see Table 4.1). Additionally, it reduces the sensitivity of the gate to detuning and pulse area offsets (see Section 4.2.8).

The same gate mechanism has been used previously to generate entanglement between different atomic species [Hug+20; Hug21; Thi19; Sch18; Bal+15], including $^{43}Sr^+$ and $^{43}Ca^+$. We revisit the essential aspects of the gate mechanism in this section and supplement them with insights from integrating it into a photonically interconnected quantum network node. For the present work, the gates are needed as a tool to generate entanglement between 422 nm photons and a memory qubit in $^{43}Ca^+$ (see Chapter 5). We therefore do not focus as much on the characterisation of the gate fidelity and associated error mechanisms here.

Ion (i)	Mode (α)	$\tilde{\eta}_{\alpha,i}$	$v_{\alpha,i}$	$\Omega_{i\downarrow}/(2\pi)$	$\Omega_{i\uparrow}/(2\pi)$
$^{88}Sr^+$	IP	0.13	0.89	330 kHz	−330 kHz
	OOP	0.09	0.45		
$^{43}Ca^+$	IP	0.18	0.45	−180 kHz	240 kHz
	OOP	0.13	−0.89		

Table 4.1: Breakdown of components factoring into the SDF strength on the axial modes of the mixed-species configuration with $\frac{\omega_{\text{oop}}}{2\pi} = 3.335\,\text{MHz}$ and $\frac{\omega_{\text{ip}}}{2\pi} = 1.715\,\text{MHz}$. The bare Lamb-Dicke parameter, $\tilde{\eta}_{\alpha,i} = \eta_{\alpha,i}/v_{\alpha,i}$, is related to the effective Lamb-Dicke parameter, $\eta_{\alpha,i}$, by normalisation with the mode participation, $v_{\alpha,i}$. $\Omega_{i,s}$ is calculated for the network qubit in $^{88}Sr^+$ and the logic qubit of $^{43}Ca^+$, using 20 mW per beam with a 15 µm waist. Overall, the interaction is asymmetric due to the mass imbalance, the level structure, and the hyperfine structure of $^{43}Ca^+$.

4.2.1 Raman wavelength optimisation

The optimal wavelength of the Raman beams to use is determined by numerically simulating the spin-echo light shift gate using the interaction Hamiltonian (2.28) including motional heating, motional dephasing, Raman scattering, and Rayleigh scattering, via the master equation. Using the experimental parameters of our system, the infidelity is minimised at 402.6 nm (see top panel in Figure 4.4). However, the tuning range of the laser was not sufficiently large to reach this wavelength; we operate the laser at 401.543 nm. As the same laser is used for coherent manipulation of the $^{43}Ca^+$ hyperfine states, keeping the wavelength closer to the 397 nm dipole transition enables more efficient single-qubit gates (see bottom panel in Figure 4.4).

4.2.2 Raman polarisation optimisation

The aim of this optimisation is to create perfect $\sigma^{\pm}$ and $\sigma^{\mp}$ polarisation of the two light shift SDF beams at the position of the ion. As shown in Figure 2.5, the *dtr* and *son* beams are combined at a polarising beam splitter at both viewports to the vacuum system, resulting in orthogonal polarisations at the ions (assuming unitary birefringence in the optics). We use waveplates to fine-tune the polarisations of the beam pairs entering the two vacuum windows using a two-step process.

1. Raman beams with $\boldsymbol{k}_1 \perp \boldsymbol{B}$: we perform Rabi flops on the $^{88}Sr^+$ Zeeman qubit using the combination $\text{son}_0 + \text{son}_1$ and minimise the observed Rabi

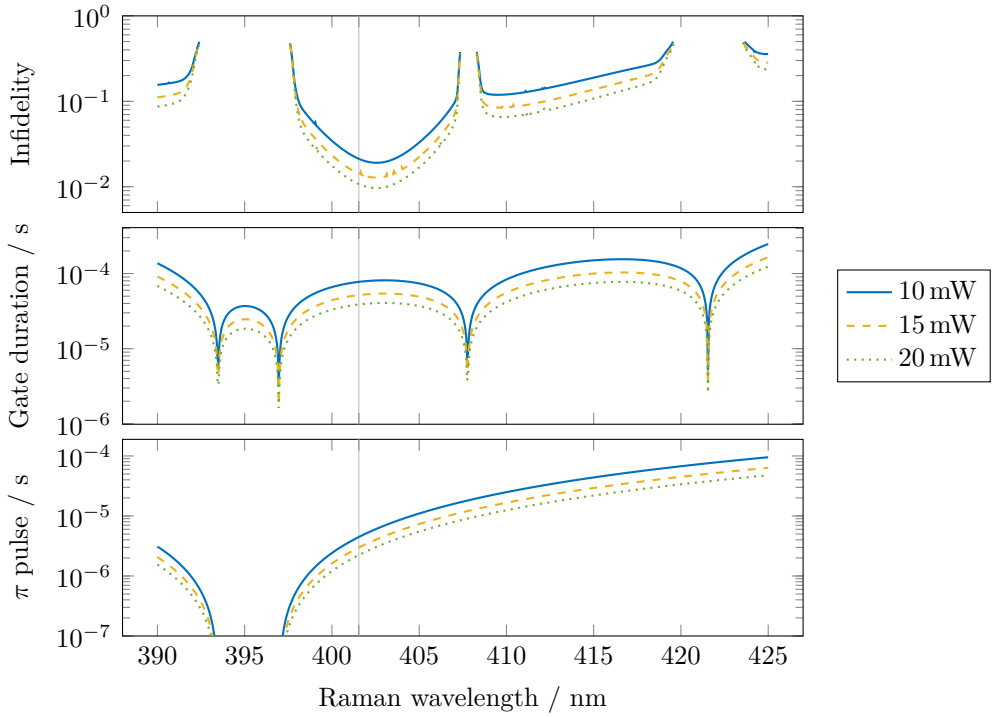

Figure 4.4: The mixed-species gate infidelity (top panel) is optimised via simulations as a function of the Raman laser wavelength. The simulation includes errors due to amplitude and phase heating, and (negligible) Raman scattering errors. The optimum is found at 402.6 nm, but the laser tuning range limited the closest achievable wavelength to 401.543 nm (vertical line). Middle panel: the respective gate duration. Bottom panel: with the same beam parameters, the duration of a single-qubit π pulse on the logic qubit of $^{43}Ca^{+}$.

frequency by adjusting the waveplates in the beam path of the $(\mathrm{son}_1, \mathrm{dtr}_1)$ pair. This minimises the π component of son_1, which maximises that of dtr_1 at the same time.

2. Raman beams with $\boldsymbol{k}_2 \parallel \boldsymbol{B}$: with the son_1 beam polarisation adjusted to $\sigma^{\pm}$ in the previous step, we aim to create the orthogonal polarisation, $\sigma^{\mp}$, on son_0. The π polarisation component is suppressed geometrically as the beam is copropagating with the high-fidelity state preparation beam at 397 nm. The target ratio and phase between σ^{+} and σ^{-} polarisation can be obtained by maximising the SDF created by $\mathrm{son}_0 + \mathrm{son}_1$ on the $^{88}Sr^{+}$ Zeeman qubit or the $^{43}Ca^{+}$ logic qubit. However, the starting point given by the PBS is near optimal, and the gate efficiency depends only quadratically on the polarisation rotation at this point, rendering such a maximisation very imprecise.

A second figure of merit for this optimisation is given by the non-ellipticity of the polarisation of all Raman beams. Experimentally, this can be measured directly via the differential light shift, $\Delta \propto (\boldsymbol{\epsilon} \cdot \boldsymbol{e}_{-1})^2 - (\boldsymbol{\epsilon} \cdot \boldsymbol{e}_{+1})^2$, of the $^{88}Sr^+$ Zeeman qubit or the $^{43}Ca^+$ logic qubit [Sch18]. After step 1 above, the differential light shift due to son_1 and dtr_1 were $< 100\,\mathrm{Hz\,mW^{-1}}$ (see Figure 4.5). The polarisations of the son_0

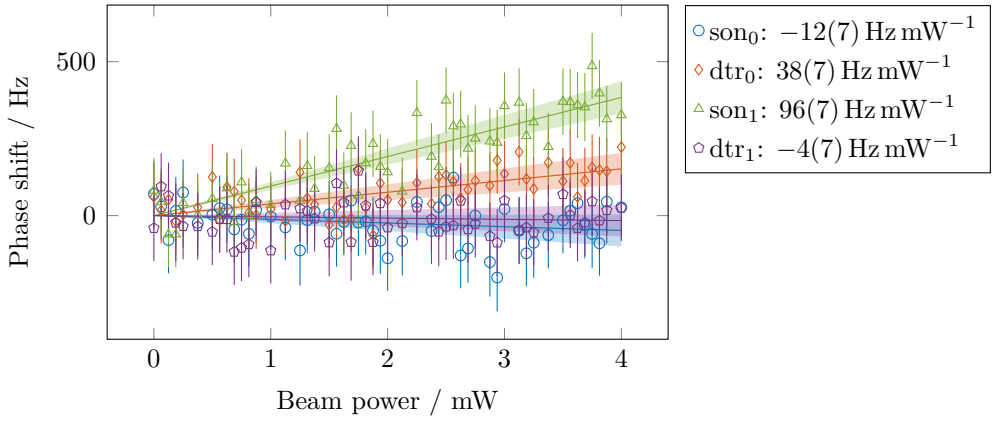

Figure 4.5: Differential light shift of the $^{88}Sr^+$ Zeeman qubit for each individual Raman beam, measured using (Bayes-optimal) Ramsey experiments.

and dtr_0 beams were then adjusted to minimise the differential light shift. As the beam geometry with respect to the magnetic field (see Figure 2.5) ensures $\boldsymbol{\epsilon} \cdot \boldsymbol{e}_0 = 0$, by minimising Δ we obtain equal intensity of σ^+ and σ^- polarisation. The phase degree of freedom (the rotation of the linear polarisation around the magnetic field axis) was set initially by the PBS and was not significantly changed in the process of minimising the differential light shift. Nevertheless, we expect that the magnitude of the SDF could be optimised by exploring this degree of freedom further.

4.2.3 Pulse shaping

As explained in Section 2.3.4, the gate interaction comes with a time-dependent single-qubit light shift term (see Equation (2.27)), which can be a significant source of error if the pulses are not shaped smoothly with a rise/fall time several times greater than the motional mode period [Bal14]. Furthermore, the spectral intensity component at nearby modes can be suppressed using pulse shaping due to the faster

fall-off behaviour from the centre frequency (see Figure 3.22). This reduces the probability of exciting spectator modes off-resonantly.

In the following we use the electronics described in Section 3.4.3.1 to shape the Raman beam intensity of the son_1 beam. It is sufficient to shape only one Raman beam because the time-dependent light shift error term is due to the interference of both beams and differential AC Stark shifts of individual beams are nulled during the polarisation optimisation (see Section 4.2.2). As the active amplitude stabilisation would counteract the pulse shaping, we deactivate this feature during the gate pulses.

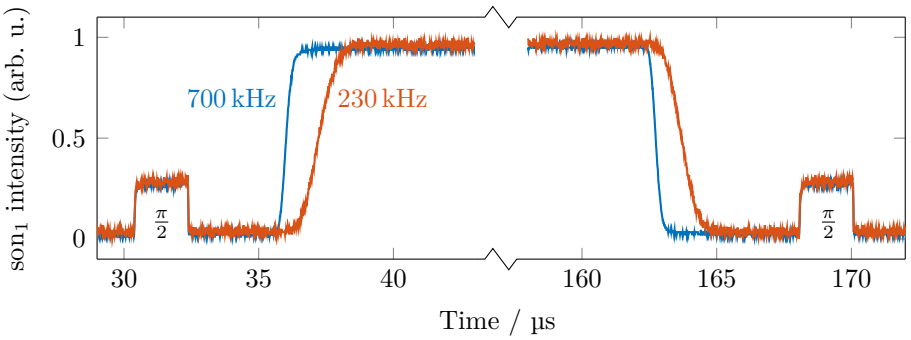

Figure 4.6: The pulse shapes of the son_1 Raman beam is measured over the course of a light shift gate experiment using a pickoff photodiode. The $\frac{\pi}{2}$ pulses at the start and at the end are not shaped, while the SDF pulse is shaped using one of two bandwidth settings of the pulse shaping circuit.

Both cutoff frequency settings of the low-pass filter were tested against the gate performance, but no difference was resolved at the current level of gate fidelities. We maintain the 230 kHz cutoff frequency setting for all SDF pulses in the following. With this setting, we measure an optical rise/fall time of $\sim 4\,\mu\mathrm{s}$ (see Figure 4.6). This is significantly longer than the motional mode period of $(3.335\,\mathrm{MHz})^{-1} \approx 300\,\mathrm{ns}$; errors due to uncontrollable single-qubit light shifts are therefore expected to be negligible.

4.2.4 Spin-dependent force signature

We investigate the properties of the SDF experimentally on a single ion using spin-echo Ramsey experiments. We apply the SDF and observe its effect through

motional decoherence following the displacement it generates in phase space (see Figure 4.7). The spin-echo pulse of the Ramsey sequence reverses the initial direction of displacement due to the spin dependence of the SDF (see Table 4.1). Consequently, the motion returns to the origin at the end of the sequence if the SDF was in resonance with the motion, or if the phase space trajectory forms a closed loop. The measurements shown in Figure 4.7 confirm this behaviour. Performing

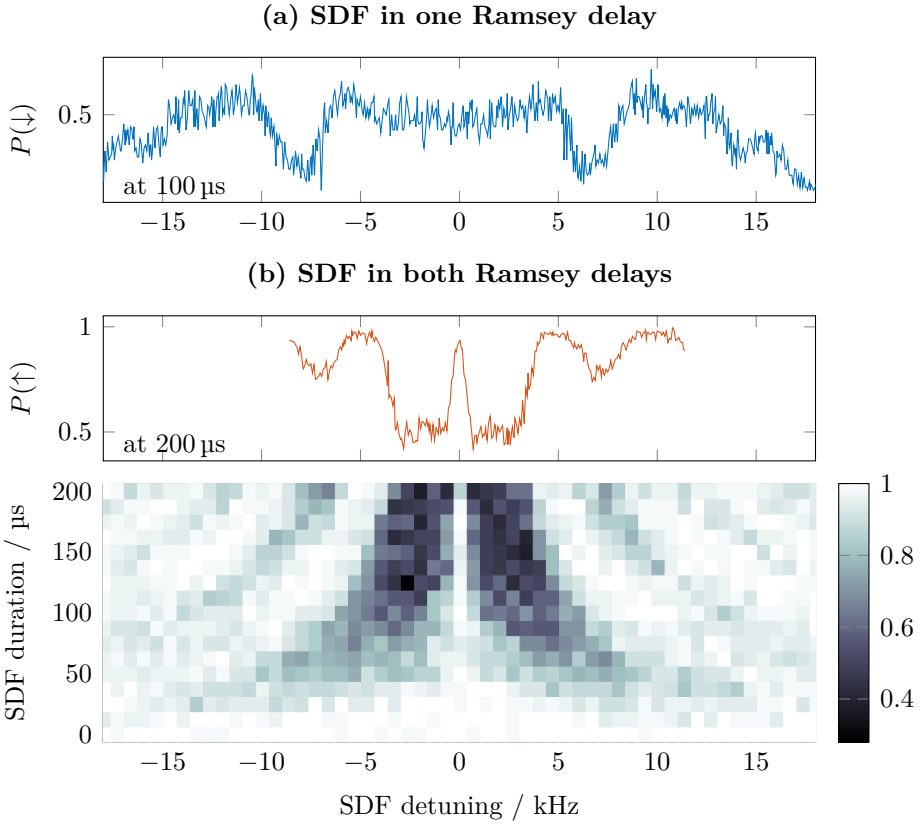

Figure 4.7: We apply the SDF to the axial mode (a) of a $^{88}Sr^{+}$ ion during one arm and (b) of a $^{43}Ca^{+}$ ion during both arms of a spin-echo Ramsey experiment on (a) the Zeeman and (b) the logic qubit. The SDF entangles the spin with the motion, such that the spin coherence becomes affected by motional decoherence. (a) The blue curve shows the probability to find the spin in the initial state after a total of 100 µs of exposure to the SDF during the first half of the spin-echo experiment. (b) The red curve show the result of applying the SDF for 200 µs in each arm of the spin-echo experiment. After the spin flip, the SDF acts in the opposite direction, returning the motion to the origin and disentangling it from the spin state if the SDF is on resonance or completes a full loop in phase space. The bottom panel extends this scan to different pulse durations. As the SDF pulse duration is increased, the features become narrower in frequency.

these experiments on the logic qubit of $^{43}Ca^{+}$ shows the same features. These

experiments confirm key characteristic properties of the SDF and have proven useful to our understanding of the SDF prior to performing entangling gates on two ions.

4.2.5 Ion spacing

After establishing the presence of a SDF on both ion species, we move towards applying the SDF to two cotrapped ions in order to generate entanglement. As discussed in Section 2.3.4, for maximum efficiency of a gate on the axial OOP mode, the ion spacing must be set to a half-integer multiple of the effective Raman wavelength, $\lambda_R/\sqrt{2}$. We choose the $(11 + \frac{1}{2})^{\text{th}}$ multiple of the effective Raman wavelength, which corresponds to an ion spacing of $d = 3.265\,\mu\text{m}$ and a single-$^{88}Sr^+$ axial frequency of $\approx 1.52\,\text{MHz}$ (see Figure 2.3). Experimentally, this is done by finding the axial confinements that correspond to adjacent integer multiples of the effective wavelength, i.e. the 11^{th} and 12^{th} multiple, as minimising the coupling of the SDF to the OOP mode is much more precise than maximising it.[5] The sought-after axial confinement at which the SDF couples maximally to the OOP mode is found halfway between these frequencies.

To measure the motional excitation by the SDF we prepare the spins of two same-species ions ($^{88}Sr^+$ in the following) in $|\downarrow\downarrow\rangle$ and cool the motion to near its ground state, apply the SDF on resonance for a sufficient duration, and then map the motional excitation to the spins using a RSB π pulse. In the low-excitation regime, the spin flip probability increases with the SDF pulse duration. The rate of this increase quantifies the coupling strength between the SDF and the motional mode. At each step, we change the axial confinement, compensate micromotion in the new potential, calibrate the RSB and SDF resonance frequencies (Section 4.2.6), and then measure the motional excitation. We increase the SDF excitation pulse duration as necessary to enhance the sensitivity as we approach the minimum coupling. Figure 4.8(a) shows the probability for no spin flip around the minima of the 11^{th} and 12^{th} multiple of the effective Raman wavelength. Figure 4.8(b) shows

[5] Alternatively, the coupling to the IP mode can be minimised, which directly maximises the coupling to the OOP mode. In our apparatus, however, the high heating rate of the IP mode and the consequent inability to cool the mode to the ground state significantly limited the precision of this measurement.

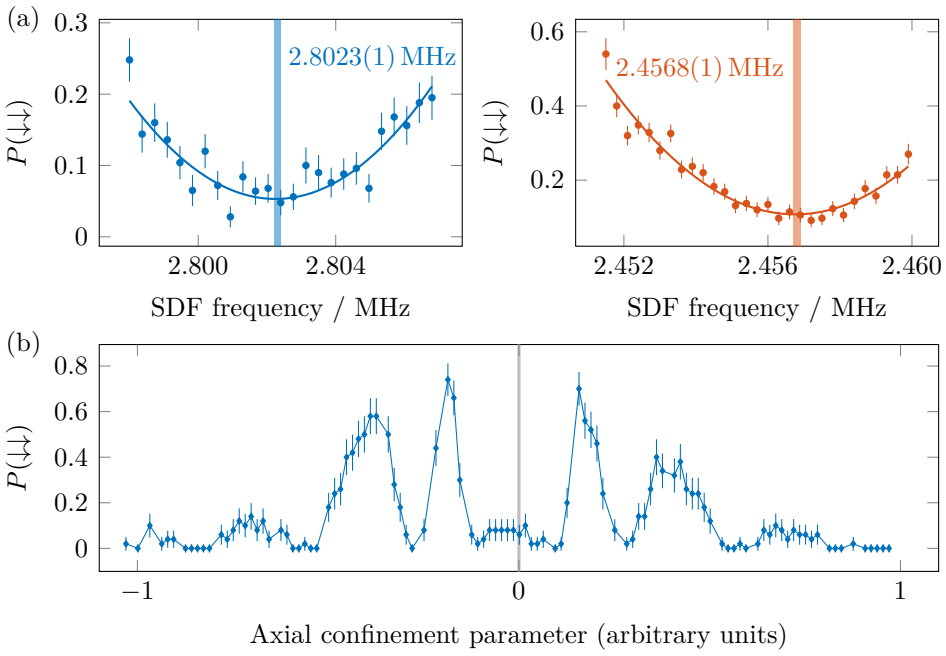

Figure 4.8: Steps to optimise the ion spacing for maximum coupling of the SDF with the axial OOP mode. (a) We find two adjacent OOP mode frequencies where the coupling is minimised, which correspond to ion spacings that are different by one effective wavelength of the SDF. (b) Exciting with the SDF halfway between these frequencies, at 2.6295 MHz, we search for the symmetry point of the signal as a function of the parameter that changes the ion spacing (axial confinement).

the probability for no spin flip with the SDF at the frequency halfway between theses optima as a function of axial confinement. As the axial mode frequencies do not scale exactly linearly with the axial confinement parameter, we search for the point of symmetry in this scan, which is expected to correspond to the point of maximum coupling between the SDF and the axial OOP mode.

4.2.6 Frequency calibration

To calibrate the resonance frequency of the SDF with the motional mode, we probe the motional excitation caused by the SDF as above, using a RSB π pulse and qubit readout. The frequency resolution of this method is inversely proportional to the SDF pulse duration and limited by the heating rate. We typically choose a pulse duration of ~ 1 ms to resolve the frequency at the ~ 1 kHz level (see Figure 4.9).

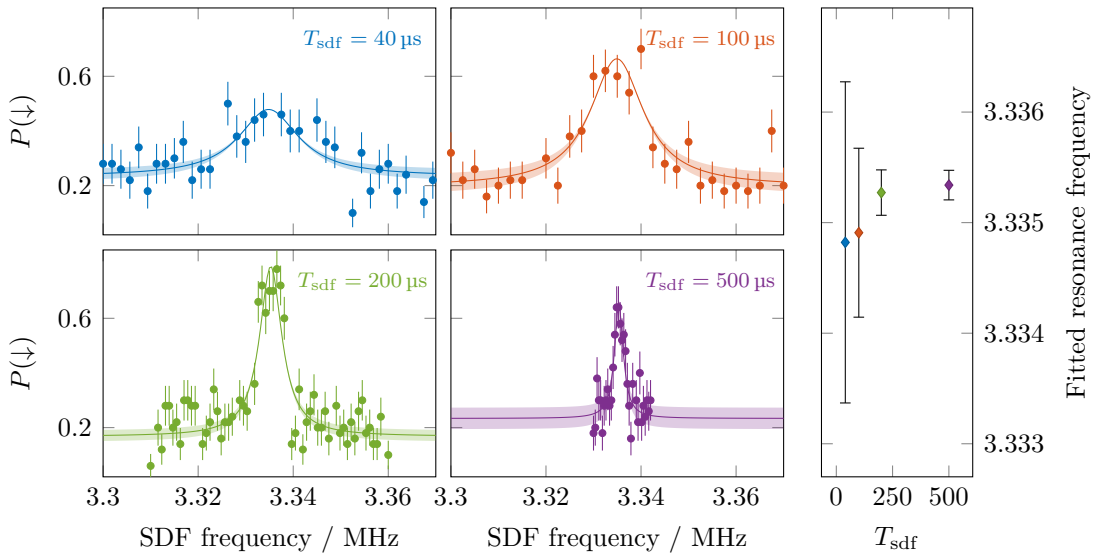

Figure 4.9: Calibration of the SDF frequency using motional excitation with increasing SDF pulse duration. In this example, the axial OOP motion of the mixed-species crystal is ground state cooled. Then, an SDF pulse is applied for a duration T_{sdf}. Finally, the motional excitation is mapped to the spin using a RSB pulse for readout. Left: Individual scans. Solid lines show the predicted mean and shaded areas span the 90 % confidence interval. Right: The frequency resolution increases $\propto T_{\mathrm{sdf}}^{-1}$. Error bars span one standard deviation from the fitted resonance frequency.

4.2.7 Fidelity estimation

Estimating the fidelity of a gate is a non-trivial task which is often reduced to simply measuring the fidelity of generating a particular Bell state from a separable state. However, quantum gates should act in a defined way on any possible input state; characterising them fully, i.e. for a complete set of input states and measurement bases, is called process tomography. The number of measurements required for full process tomography scales exponentially with the number of qubits; characterising a two-qubit gate in our apparatus takes ~ 10 min. RBM is more efficient, scaling polynomially with the number of qubits, but instead of a full description of the process, it estimates the fidelity by averaging the outcomes of random sequences, which are constructed to act as the identity overall. For optimising the gate fidelity, however, even this approach is prohibitively slow; we resort to optimising the fidelity of generating a particular Bell state, and only bring out the 'big guns', process tomography or RBM, to characterise the final performance.

The fidelity of an arbitrary two-qubit state, $\hat{\rho} = \sum_{a,b,c,d\in\{\downarrow,\uparrow\}} \rho_{abcd} \, |ab\rangle\langle cd|$, with respect to an even Bell state is given by [Neg18; Thi19]

$$\mathcal{F}(\hat{\rho}) = \frac{1}{2} \left(\rho_{\downarrow\downarrow\downarrow\downarrow} + \rho_{\uparrow\uparrow\uparrow\uparrow} + 2|\rho_{\downarrow\downarrow\uparrow\uparrow}| \right) \ . \tag{4.1}$$

This suggests that the minimum number of measurements required to estimate the fidelity is three. Without single-ion addressed readout, the distinguishable population readout results are

$$\begin{aligned} P_0(\hat{\rho}) &= \mathrm{Tr}(|\downarrow\downarrow\rangle\langle\downarrow\downarrow| \, \hat{\rho}) = \rho_{\downarrow\downarrow\downarrow\downarrow} \ , \\ P_1(\hat{\rho}) &= \mathrm{Tr}\left[(|\downarrow\uparrow\rangle\langle\downarrow\uparrow| + |\uparrow\downarrow\rangle\langle\uparrow\downarrow|)\hat{\rho} \right] = 1 - \rho_{\downarrow\downarrow\downarrow\downarrow} - \rho_{\uparrow\uparrow\uparrow\uparrow} \ , \\ P_2(\hat{\rho}) &= \mathrm{Tr}(|\uparrow\uparrow\rangle\langle\uparrow\uparrow| \, \hat{\rho}) = \rho_{\uparrow\uparrow\uparrow\uparrow} \ , \end{aligned} \tag{4.2}$$

which correspond to zero, one and two ions whose spin has flipped, respectively. Adding a global $\hat{U}(\phi) = \hat{R}(\frac{\pi}{2}, \phi)^{\otimes 2}$ pulse before the population measurement implements effectively a parity measurement with phase ϕ, for which the one-bright probability is

$$Q_1(\hat{\rho}, \phi) = P_1\left(\hat{U}(\phi)\hat{\rho}\hat{U}(\phi)^\dagger \right) = \frac{1}{2} - \Re(\rho_{\downarrow\uparrow\uparrow\downarrow}) + |\rho_{\downarrow\downarrow\uparrow\uparrow}| \cos(2\phi + \phi_0) \ , \tag{4.3}$$

with a state-dependent phase offset $\phi_0 = \arg(\rho_{\downarrow\downarrow\uparrow\uparrow})$. We use the term 'parity readout' to refer to this type of measurement with $0 \leq Q \leq 1$; the parity $\mathcal{P}$ is related to this quantity via $\mathcal{P} = 2Q - 1$. By combining measurements of the one-bright population (4.2), $P = P_1(\hat{\rho})$, and the contrast of the parity readout signal (4.3), $C = Q_1(\hat{\rho}, \frac{\phi_0}{2}) - Q_1(\hat{\rho}, \frac{\pi - \phi_0}{2})$, the fidelity (4.1) can be expressed as

$$\mathcal{F}(\hat{\rho}) = \frac{1}{2}(1 - P + C) \ . \tag{4.4}$$

To estimate the fidelity of a $(\sigma_z \otimes \sigma_z)$ gate, $\hat{G}_{ZZ}$, we use the gate sequence shown in Figure 4.10. Up to the vertical dashed line, the circuit ideally prepares the Bell state

$$|\Psi\rangle = \frac{1}{\sqrt{2}}(|\downarrow\downarrow\rangle + \mathrm{e}^{\mathrm{i}\phi_0} \, |\uparrow\uparrow\rangle) \ ,$$

with $\phi_0 = -\frac{\pi}{2}$. In practice, the population and parity contrast measurements are performed back-to-back, where each measurement is repeated ~ 100 times (which gives sufficient statistical precision to diagnose infidelities at the 1 % level).

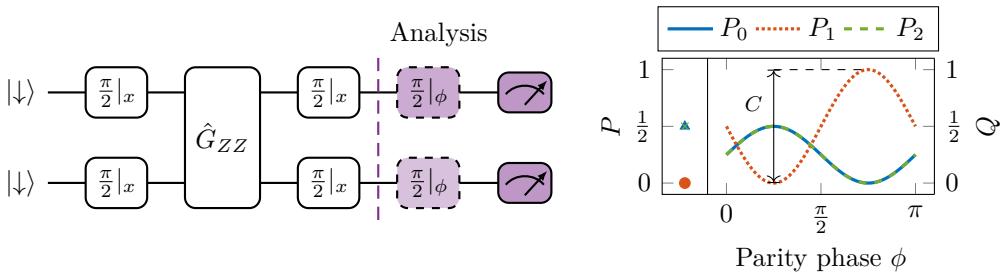

Figure 4.10: Circuit used to estimate the fidelity of a $(\sigma_z \otimes \sigma_z)$ gate, $\hat{G}_{ZZ}$. The optional $\frac{\pi}{2}$ analysis pulse switches from population readout to parity readout. The plot shows the expected populations for a perfect Bell state without (left) and with (right) the analysis $\frac{\pi}{2}$ pulse.

4.2.8 Walsh modulation

Coherent errors, for instance due to frequency offsets or miscalibrated gate duration, can be suppressed by appropriate composite pulse techniques similar to dynamical decoupling discussed in Section 2.4.2. Furthermore, for mixed-species gates between $^{88}Sr^+$ and $^{43}Ca^+$, the spin-dependent Rabi frequencies are asymmetrical between species and spin states; Walsh modulation eliminates any geometrical single-qubit phases by symmetrising the gate propagator.

For Walsh-n modulation, the gate is subdivided into $n+1$ intervals of equal length, where $n+1$ must be a power of 2. The modulated system is supposed to undergo a phase flip when the Walsh function[6], $W_n(m) \in \{-1, 1\}$, changes sign (see Figure 4.11). Experimentally, this phase flip can be implemented either by

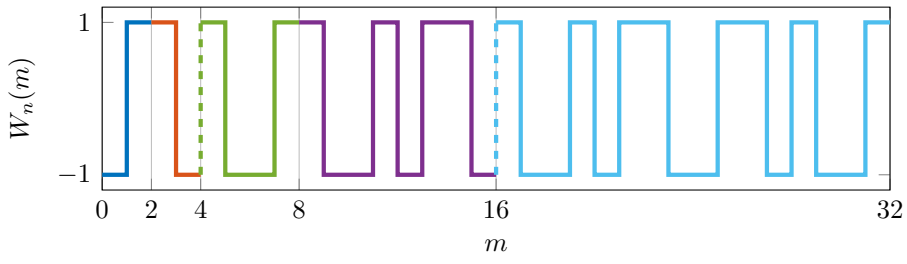

Figure 4.11: Walsh functions $W_n(m)$ for $n = 1, 3, 7, 15, 31$ are shown. For a given order n, the argument m runs from 0 to $n+1$.

advancing the phase of the SDF with respect to the motional mode by π [Hay+12],

[6]We evaluate $W_n(m)$ via the sum of bits in the binary representation of m: if this number is even, $W_n(m) = -1$, and $W_n(m) = 1$ otherwise.

or by flipping the spin states using a carrier pulse on all qubits. The latter approach is used here as it also dynamically decouples the qubit from frequency shifts and compensates for unequal illumination of the two ions. The phase of the spin flip pulses can be alternated between 0 and $\frac{\pi}{2}$ in order to cancel pulse area imperfections, in a way similar to the XY4 dynamical decoupling sequence (see Section 2.4.2.2).

Furthermore, the phase of the SDF is reset to start with the same phase relative to the motional mode at the beginning of every loop. Assuming the SDF strength does not change between loops, this sequence closes the phase space trajectory independent of the SDF detuning (see Figure 4.12(a)). For comparison, without resetting the phase of the SDF or without the spin-echo π pulse, miscalibration of the SDF detuning or strength always causes loop closure errors (see Figure 4.12(b-d)). It is important to note that for the cancellation provided by the phase reset to be effective, the mode frequency must be known with sufficient precision.

Phase space diagrams are a way to visualise motional dynamics. The ground state of the motion is given by a Gaussian probability distribution centered at the origin. In the rotating frame of the mode, the instantaneous phase of the SDF with respect to the motion determines the tangent to the phase space trajectory. Assuming the SDF coupling strength stays constant, the trajectory is circular and returns to the origin after a period equal to $T_g = 2\pi\delta_g^{-1}$, where δ_g is the detuning of the SDF from the motional mode. To reach the best performance, the strength of the SDF is adjusted such that the motion completes a loop in phase space after every interval. This avoids motional errors affecting the spin via any residual spin-motion entanglement while the spin-flip pulses are applied. Moreover, in this configuration, the geometric phase error due to over- or under-rotations is cubically suppressed.[7] Consequently, the best detuning for a Walsh-n-modulated gate is

$$\frac{\delta_g}{2\pi} = \frac{n+1}{T_g} \ ,$$

[7]Let the optimal SDF duration for one loop be $T_1 = \frac{T_g}{2}$ and the error be due to an offset ΔT_1. The area of the circular segment with opening angle $\Delta = \Omega\Delta T_1$ is given by $\frac{1}{4}(\Delta - \sin(\Delta)) \approx \frac{\Delta^3}{24}$, where Ω parameterises the SDF strength and $\Omega T_1 = \frac{\pi}{4}$ for a perfect gate. For a two-loop gate, the total geometric phase error is therefore $\approx \frac{\Delta^3}{12}$.

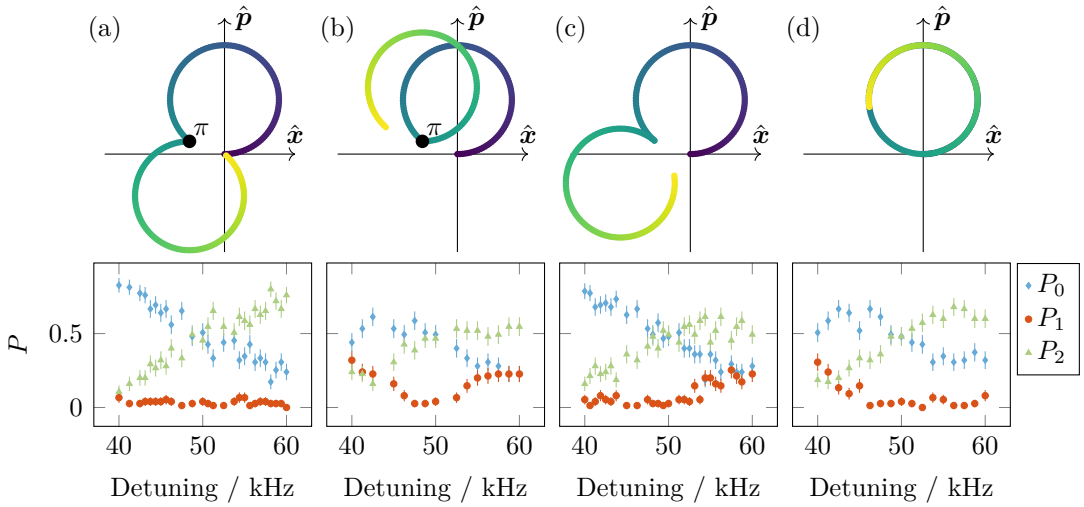

Figure 4.12: Top: Illustration of a phase space trajectory (in the rotating frame of the motion) for an example spin state (here $|\downarrow\uparrow\rangle$) during a two-loop gate with an under-rotation error. We depict four cases for the action between the two loops. (a) Reset SDF phase to 0, with spin echo. (b) Reset SDF phase to π, with spin echo. (c) Advance SDF phase by π, no spin echo. (d) Continuous SDF phase, no spin echo. Bottom: an experiment which prepares an even Bell state between two $^{43}Ca^{+}$ ions (see Figure 4.10) is performed using these modulation schemes. For this target state we require vanishing population in the states $|\uparrow\downarrow\rangle$ and $|\downarrow\uparrow\rangle$, i.e. $P_1 = 0$. However, P_1 is sensitive to loop closure errors, and the data confirms that Walsh-1 case (a) is less sensitive to this error than Walsh-1 case (c) and both non-Walsh cases (b) and (d).

where T_g is the total effective[8] duration of the gate.

With an SDF imbalance (see Table 4.1), the spin echo changes the strength from one phase space loop to the next. At first glance, this effect nullifies the error suppression explained above, as the trajectories no longer return to the origin. However, as pointed out in Reference [Thi19], the trajectories of all spin states end in the same point in phase space. As errors are caused by imperfect overlap of the motional states, the Walsh modulation technique described above is equally effective in systems with imbalanced SDFs.

Increasing the Walsh order from Walsh-n_1 to Walsh-n_2 at constant detuning, the Raman power requirements are relaxed by a factor $\sqrt{\frac{n_1+1}{n_2+1}}$ per beam and the phase space excursion during the loops become smaller, thus reducing the gate's sensitivity to motional errors. In practice, however, this gain must be

[8]The pulse duration must be adjusted to account for the pulse shape. Delays between Walsh intervals, for example due to the finite duration of the spin echo pulses, are irrelevant.

balanced with spin dephasing and accumulated spin-flip pulse errors. In this work, only Walsh-1 sequences were used, as higher-order sequences did not noticeably improve the gate fidelity. In the computational basis the unitary describing the Walsh-1 $(\hat{\sigma}_z \otimes \hat{\sigma}_z)$ gate is

$$W_{ZZ} = \begin{pmatrix} 0 & 0 & 0 & 1 \\ 0 & 0 & -\mathrm{i} & 0 \\ 0 & -\mathrm{i} & 0 & 0 \\ 1 & 0 & 0 & 0 \end{pmatrix} .$$

4.3 Same-species gate results

As the motional dynamics of mixed-species crystals are more complex than for single-species crystals, we start by performing gates between two $^{43}Ca^{+}$ ions. The results in this section were obtained with the Raman laser tuned closer to calcium, to 399 nm. The axial OOP mode of the two-calcium crystal is found at 3.8 MHz (see Figure 2.3). The heating rate on this mode is $\dot{\bar{n}}_{\mathrm{oop}}^{\mathrm{CaCa}} \approx 5\,\mathrm{s}^{-1}$ and the motional dephasing time constant is 7.4(5) ms (see Section 4.1.3). Under these conditions, we simulate Walsh-1-modulated light shift gates and predict that a gate fidelity of $\gtrsim 99\,\%$ could be reached, with gate durations of $\lesssim 240\,\mu\mathrm{s}$.

Unequal illumination. We implement single-qubit rotations of the $^{43}Ca^{+}$ ions using global Raman beams. Due to alignment inaccuracies, the intensity at the position of the two ions is not equal, which causes a difference in Rabi frequency, $\Delta\Omega$ between the individual ions. For the SDF, the light shift imbalance only substantiates the existing asymmetry (see Table 4.1), which is addressed by Walsh modulation. The carrier Rabi frequency imbalance, however, undermines the fidelity of global single-qubit rotations.

A straight-forward diagnostic for this condition is global Rabi flopping, where the probability of a joint spin flip, $|{\downarrow\downarrow}\rangle \rightarrow |{\uparrow\uparrow}\rangle$, undergoes Rabi oscillations with an envelope beating at $\Delta\Omega$ (see Figure 4.13). To measure this faster and more accurately, we combine split readout (Protocol 3.2.3) and Bayes-optimal phase estimation [Nee19]. This signal can be used in real time to equalise the Rabi

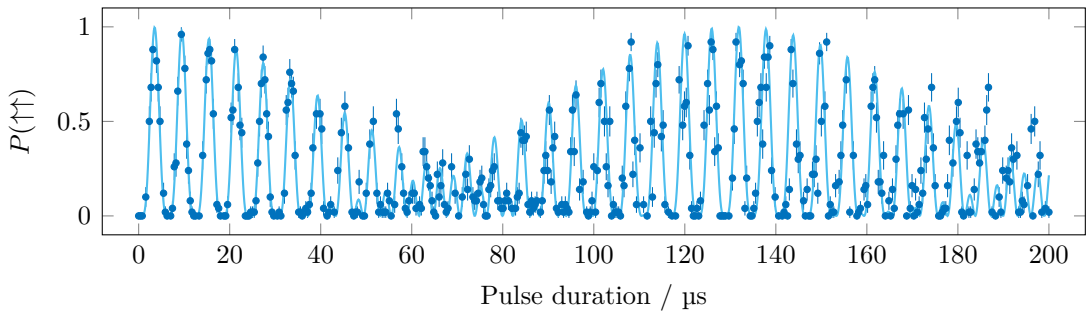

Figure 4.13: We measure the Rabi frequency difference between two $^{43}Ca^{+}$ ions that is caused by unequal illumination by the global Raman beams. In this example, the Rabi frequency is $\frac{\Omega_0}{2\pi} = 163.67(3)\,\text{kHz}$ with an imbalance of $4.67(1)\,\%$ between the two ions. The imbalance causes the individual Rabi flops to rephase after 131 µs.

frequency by adjusting the beam pointing or moving the ions along the axis. To alleviate the issue when the error is still found to be significant, we use the broadband type 1 (BB1) composite pulse sequence [Wim94]

$$\text{BB1} = \theta_0 \text{—} \pi|_\phi \text{—} 2\pi|_{3\phi} \text{—} \pi|_\phi \ , \tag{4.5}$$

where θ is the intended pulse area and $\phi = \arccos(-\frac{\theta}{4\pi})$ is relative to the intended pulse phase (zero in Equation (4.5)). Alternatively, far-field microwaves could be used to drive the transitions to circumvent the issue of unequal illumination, as their wavelength is significantly larger than the ion separation.

Gate fidelity. We apply the procedure outlined in Section 4.2.7 (see Figure 4.10) to estimate the fidelity of two-loop light shift gates on two $^{43}Ca^{+}$ ions with detunings between 10 kHz and 35 kHz. These gates required only between 2 mW and 5 mW per Raman beam at 399 nm, which is only a small fraction of the total available power in our system (~ 30 mW per beam). The gate fidelity varied $\lesssim 0.5\,\%$ across this range of parameters. Figure 4.14 for instance shows the dynamics of a Walsh-1-modulated gate with detuning $\frac{\delta_g}{2\pi} = 11.7\,\text{kHz}$ and duration $T_g = 160\,\mu\text{s}$. BB1 pulses were not employed in this case. We attribute the infidelity of 0.026(3) largely to SPAM errors and single-qubit rotation errors due to unequal illumination. The carrier Rabi frequency imbalance due to unequal illumination was measured as $\frac{\Delta\Omega}{\Omega} \approx 4 \times 10^{-3}$ shortly before attempting the gate. We did not fully characterise

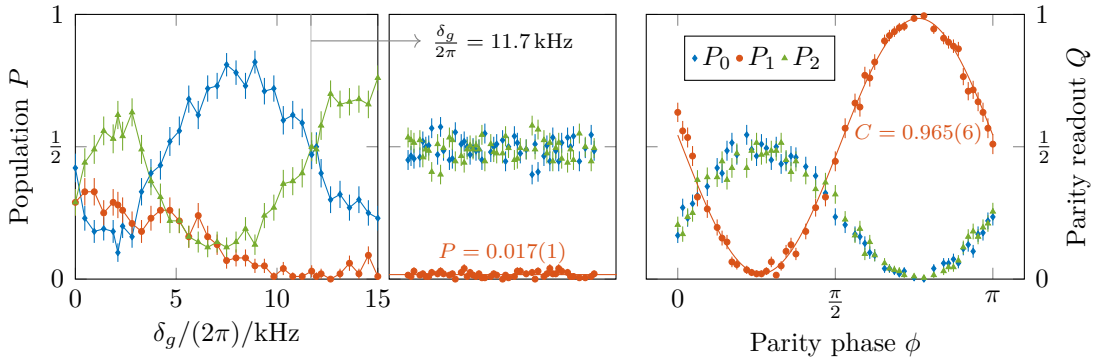

Figure 4.14: We perform the circuit shown in Figure 4.10 to analyse the Bell state prepared between two $^{43}Ca^{+}$ ions by the Walsh-1-modulated light-shift SDF. The leftmost panel shows the final populations depending on the gate detuning, with the vertical line indicating the point where they match the signature of an even Bell state. Middle: extended dataset of populations at the indicated gate detuning to obtain the one-bright population P. Right: estimating the parity readout contrast using the method described in Section 4.2.7. We fit the oscillation using maximum likelihood estimation to obtain the contrast C. Before SPAM correction, the fidelity of this gate evaluates to 0.974(3). Partially correcting for SPAM, this number adjusts to 0.985(5).

the SPAM matrix at this occasion. Instead, we performed a comparison experiment using the same gate sequence, but replaced the SDF pulse by an equivalent delay. We obtain a residual population in the one-bright states of 0.015(2), which may be subtracted from the population obtained in the fidelity measurement. In summary, partially correcting for spurious errors due to unequal illumination and SPAM, the gate fidelity can be placed at 0.985(5).

In Figure 4.15 we compare the three-point fidelity (see Equation (4.4)) with the simulated fidelity for a range of gate detunings and gate durations with constant laser power. The simulation and the experiment agree qualitatively very well, but disagree in the parameters that are required to perform the highest-fidelity gate because the SDF magnitude used in simulations was derived from nominal parameters and not measured directly – experimental imperfections, such as optical losses and aberrations, are likely the cause of this discrepancy.

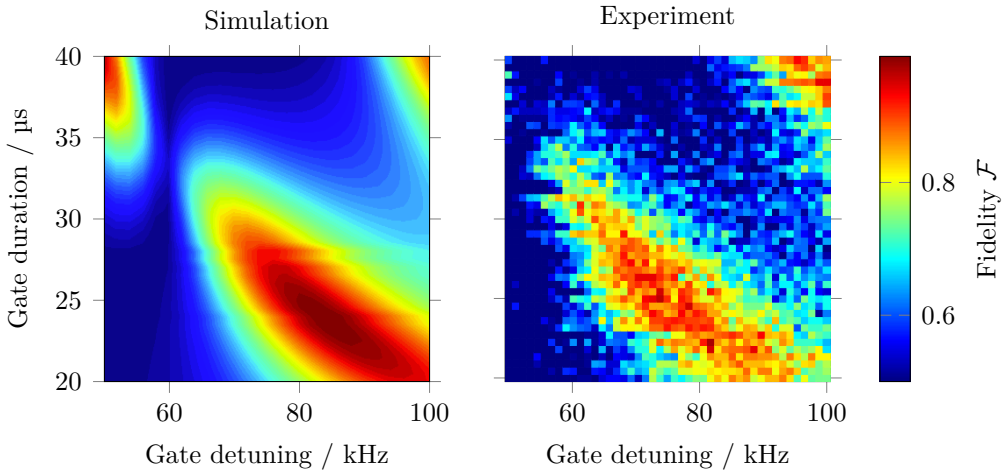

Figure 4.15: Comparison of simulated and experimental fidelities of $^{43}Ca^{+}$-$^{43}Ca^{+}$ light shift gates as a function of gate duration and detuning. The fidelities of preparing a Bell state are measured using three points, including two for the parity and one for the population. The measurements are not corrected for SPAM errors.

4.4 Mixed-species gate results

We load one $^{88}Sr^{+}$ and one $^{43}Ca^{+}$ ion into the trap and ensure their order is consistent between experiments (see Section 3.1.7). Thanks to the spectral isolation of the $^{88}Sr^{+}$ Zeeman qubit and the $^{43}Ca^{+}$ hyperfine qubit, they can be addressed individually with global laser beams. Consequently, single-qubit gates can be calibrated and characterised independently from each other. This enables the use of process tomography to fully characterise the action of a chosen gate. Moreover, single-qubit addressing enables the use of (full[9]) RBM to quantify the overall performance of the two-qubit system in a way that lumps errors together into a single depolarising noise channel (see Section 4.4.4).

In the following, we present the $\hat{W}_{ZZ}$ gate, which is in the CZ class (Section 4.4.1), and two gates from the iSWAP class (Section 4.4.2 and Section 4.4.3), which are gates that can be decomposed into two CZ-type gates and single-qubit rotations. We then discuss the overall performance of the mixed-species two-qubit system on the basis of RBM results. Finally, we compare our measurements with simulations

[9]If qubits can only be addressed globally, i.e., with the same single-qubit unitary acting simultaneously on all qubits, then a variant of RBM, namely subspace RBM, must be used.

of the mixed-species $\hat{W}_{ZZ}$ gate dynamics, including off-resonant excitation of the axial IP mode, to improve our understanding of the error budget.

4.4.1 $\hat{W}_{ZZ}$ gate

The symbol of the $\hat{W}_{ZZ}$ gate is shown in Figure 4.16 alongside with the experimental Walsh-1 pulse sequence, which includes a spin-echo π-pulse on both qubits to protect from slow qubit frequency shifts and asymmetric light shift SDF coupling strengths in the mixed-species case. We characterize the $\hat{W}_{ZZ}$ operation using

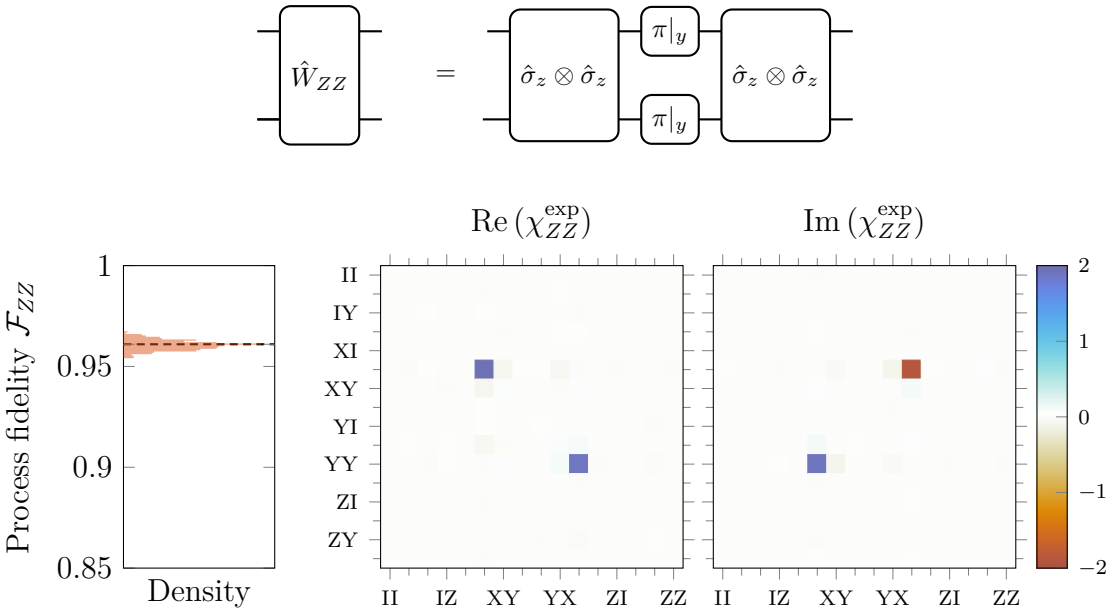

Figure 4.16: Gate sequence (top) and process tomography (bottom) of the $\hat{W}_{ZZ}$ gate. $\hat{\sigma}_z \otimes \hat{\sigma}_z$ symbolises the SDF applied for the duration needed to complete one loop in motional phase space. Bottom left: the process fidelity is obtained from maximum likelihood estimation (dashed line) and its uncertainty from non-parametric bootstrapping (histogram).

process tomography and from the experimental outcomes, we reconstruct the 'χ matrix', χ_{ZZ}^{exp}, by maximum likelihood estimation [Řeh+07; AL12]. Given the χ matrix, it is straight-forward to calculate the process fidelity $\mathcal{F}_{ZZ} = \text{Tr}(\chi_{ZZ}^{\text{id}} \chi_{ZZ}^{\text{exp}})$ with respect to the ideal process χ_{ZZ}^{id}. For the data shown in Figure 4.16, we obtain 0.961(2). This estimate includes errors from the $\hat{W}_{ZZ}$ gate, as well as imperfections in the preparation of the initial states and the implementation of the measurement bases needed for process tomography.

4.4.2 iSWAP gate

The concatenation of the two Clifford gates SWAP and CZ lies within the ISWAP gate class, which contains gates that can be implemented by two $\hat{\sigma}_z \otimes \hat{\sigma}_z$ interactions and single-qubit rotations.[10] Here we define the iSWAP operation by the circuit shown in Figure 4.17. In the computational basis, this circuit implements the unitary

$$U_{\mathsf{iS}} = \begin{pmatrix} 1 & 0 & 0 & 0 \\ 0 & 0 & 1 & 0 \\ 0 & 1 & 0 & 0 \\ 0 & 0 & 0 & -1 \end{pmatrix} .$$

This definition differs from the prototypical ISWAP gate defined in the literature, but note that they are equivalent up to single-qubit rotations.

The iSWAP is useful for swapping an unknown quantum state, $|\psi\rangle$ from one qubit to another qubit that is prepared in $|\downarrow\rangle$:

$$\mathsf{iSWAP} : |\psi\rangle \otimes |\downarrow\rangle \mapsto |\downarrow\rangle \otimes |\psi\rangle \ .$$

A full SWAP gate would also work for the same purpose, but the iSWAP gate requires only two $\hat{W}_{ZZ}$ gates while the SWAP gate requires three.

We characterize the iSWAP operation independently using process tomography [Řeh+07; AL12] to reconstruct the χ matrix, $\chi_{\mathsf{iS}}^{\text{exp}}$, and calculate the process fidelity $\mathcal{F}_{\mathsf{iS}} = \text{Tr}(\chi_{\mathsf{iS}}^{\text{id}} \chi_{\mathsf{iS}}^{\text{exp}})$ with respect to the ideal process $\chi_{\mathsf{iS}}^{\text{id}}$, yielding 0.913(3) (Figure 4.17). This estimate includes errors from the iSWAP gate, as well as imperfections in the preparation of the initial states and the implementation of the measurement bases needed for process tomography.

4.4.3 SWAP · CNOT gate

The concatenation of the two Clifford gates SWAP and CNOT is implemented by two $\hat{\sigma}_z \otimes \hat{\sigma}_z$ interactions, single-qubit rotations, and phase shifts. The circuit implementing the SWAP · CNOT unitary is shown in Figure 4.18. In the computational

[10] Clifford gates that require one (three) $\hat{\sigma}_z \otimes \hat{\sigma}_z$ interaction(s) are part of the CZ (SWAP) gate class. Clifford gate decompositions with $n > 3$ $\hat{\sigma}_z \otimes \hat{\sigma}_z$ interactions can always be reduced to use only $n \pmod 3 + 1 \in \{1, 2, 3\}$ such interactions, as the two-qubit Clifford group is complete with one CZ-type, one iSWAP-type, and a SWAP-type gate, and the Clifford gates from the individual single-qubit groups.

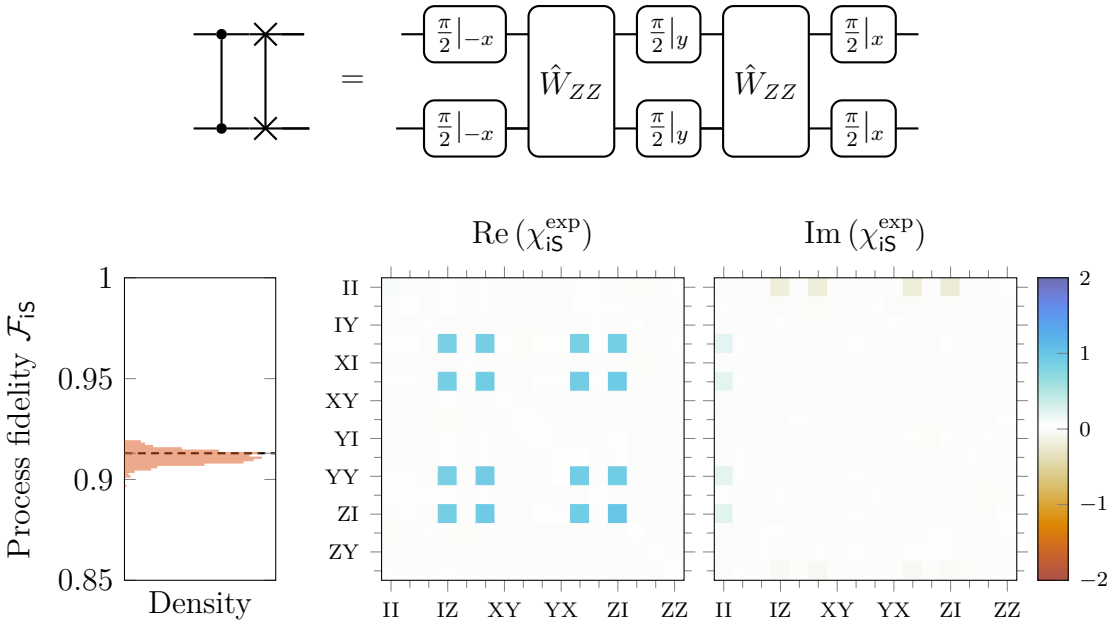

Figure 4.17: Gate sequence (top) and process tomography (bottom) of the iSWAP gate. Bottom left: the process fidelity is obtained from maximum likelihood estimation (dashed line) and its uncertainty from non-parametric bootstrapping (histogram).

basis, this gate takes the form

$$U_{\neg\text{S}} = \begin{pmatrix} \mathrm{i} & 0 & 0 & 0 \\ 0 & 0 & \mathrm{i} & 0 \\ 0 & 0 & 0 & 1 \\ 0 & -1 & 0 & 0 \end{pmatrix} .$$

For tomography experiments, the single-qubit phase shifts are tracked in software and combined with the phase of subsequent analysis pulses. Alternatively, the resulting tracked phase shift φ can be applied to the qubit using a sequence of three $\frac{\pi}{2}$ pulses ($\frac{\pi}{2}|_x$ — $\varphi|_y$ — $\frac{\pi}{2}|_{-x}$).

We characterize the SWAP·CNOT operation using process tomography [Řeh+07; AL12] to reconstruct the Choi process matrix, $C^{\text{exp}}_{\neg\text{S}}$ (now in the computational basis as opposed to χ, which is in the Pauli basis), and calculate the process fidelity $\mathcal{F}_{\neg\text{S}} = \mathrm{Tr}(C^{\text{id}}_{\neg\text{S}} C^{\text{exp}}_{\neg\text{S}})$ with respect to the ideal process $C^{\text{id}}_{\neg\text{S}}$, yielding 0.910(4) (Figure 4.18). This estimate includes errors from the CNOT gate, as well as imperfections in the preparation of the initial states and the implementation of the measurement bases needed for process tomography.

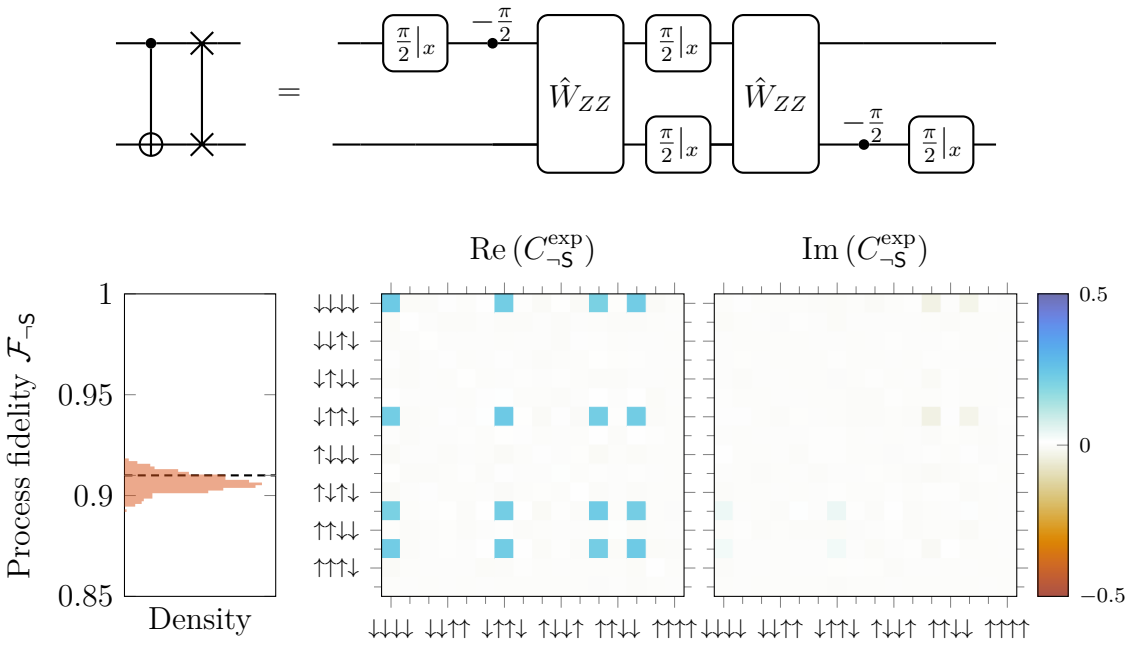

Figure 4.18: Gate sequence (top) and process tomography (bottom) of the SWAP·CNOT gate. Bottom left: the process fidelity is obtained from maximum likelihood estimation (dashed line) and its uncertainty from non-parametric bootstrapping (histogram).

4.4.4 Randomised benchmarking

Here we use RBM (see Section 2.5) to evaluate the overall gate performance that is achieved with this mixed-species two-qubit system. Table 4.2 summarises the number of native gate pulses that are physically required to implement every Clifford gate for the particular decomposition used in the following experiments.[11]

Qubits	Cliffords	π pulses	$\frac{\pi}{2}$ pulses	$\hat{W}_{ZZ}$ gates
1	24	4	20	0
2	11520	1920	22848	17280

Table 4.2: Number of native gate pulses per qubit in the Clifford group decompositions that are used for single- and two-qubit RBM. The decompositions were chosen to minimise the number of required physical gate pulses. The spin-echo π pulses within $\hat{W}_{ZZ}$ are not counted towards the π pulse total.

4.4.4.1 Simultaneous single-qubit RBM

First, we perform interleaved single-qubit RBM of the unentangled $^{88}Sr^+$ Zeeman qubit and $^{43}Ca^+$ logic qubit. For every sequence length m in the scan, two random

[11] Thanks to D. P. Nadlinger for tabulating them for us.

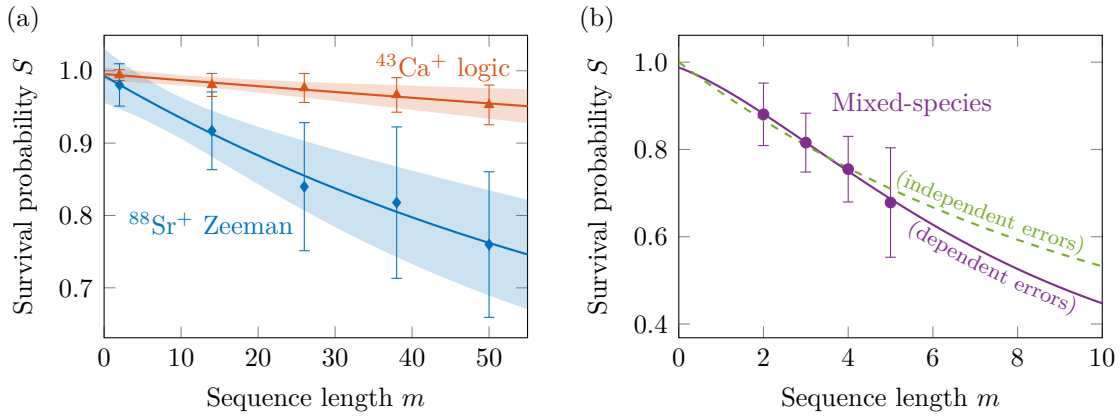

Figure 4.19: Mixed-species single- and two-qubit RBM. The average error per Clifford gate is extracted from the fit (solid lines; shaded area span one-sigma confidence intervals) for (a) interleaved single-qubit Clifford sequences (different random gates per qubit) and (b) the full two-qubit sequences, decomposed using the native $\hat{W}_{ZZ}$ gate to generate entanglement. The average errors per Clifford gate are $0.9(5) \times 10^{-3}$, $6(3) \times 10^{-3}$, and 0.07(5) (0.16(8)) for the ^{43}Ca$^+$ logic qubit, the ^{88}Sr$^+$ Zeeman qubit, and the mixed-species two-qubit case with assumption of independent (dependent) errors, respectively.

sequences of Clifford gates are generated, one for ^{88}Sr$^+$ and one for ^{43}Ca$^+$. The gates from these two sequences are applied to ^{88}Sr$^+$ and ^{43}Ca$^+$ in an interleaved way.

We obtain an average error per Clifford gate of $6(3) \times 10^{-3}$ and $0.9(5) \times 10^{-3}$ on the ^{88}Sr$^+$ Zeeman qubit and the ^{43}Ca$^+$ logic qubit, respectively (see Figure 4.19(a)), using the gate- and time-independent model (2.36).[12] Since a randomly selected Clifford gate contains on average one gate pulse, the error per Clifford gate can be loosely associated with an error per gate pulse.

The error on ^{43}Ca$^+$ is significantly higher compared to non-simultaneous single-qubit RBM, where we typically obtain $\sim 4 \times 10^{-4}$. The dominant cause for the excess error here is the increased inter-pulse delay due to the interleaved ^{88}Sr$^+$ gates and the associated decoherence. Secondly, occasional reordering events cause the ^{43}Ca$^+$ ion to sample a different intensity of the Raman laser; an error similar to unequal illumination in the same-species case (see Section 4.3). The error on the Zeeman qubit is consistent with the combined error of the three optical pulses on the 674 nm transition that are required to perform one rotation on the Zeeman

[12] The use of this model is justified, as an analysis using the extended model (2.35) yields $(q - p^2) \approx 0$.

qubit. Moreover, the optical qubit of $^{88}Sr^{+}$ is less sensitive to changes in ion order due to the wider focus of the 674 nm beam.

4.4.4.2 Full two-qubit RBM

As the $\hat{W}_{ZZ}$ gate is the native entangling gate in our system, we perform RBM using a decomposition of the Clifford group that reflects this choice.

The gate- and time-independent model (2.36) (see dashed curve in Figure 4.19(b)) does not describe our observations under the constraints (2.37). In particular, the SPAM error, $S(0)$, is forced towards the boundary of the constraint $S(0) \leq 1$. The data shows that the error per gate increases with the number of gates. This effect was already observed in Reference [Hug21], but to a lesser extent. In our case, the degradation of the $\hat{W}_{ZZ}$ gate fidelity is likely due to the high heating rate in our system. We find $(q - p^2) = 0.21$ and $p = 0.79$ by fitting the extended model, Equation (2.35), to the observations (see solid line in Figure 4.19(b)).[13] A randomly selected Clifford gate contains on average 1.5 $\hat{W}_{ZZ}$ gates and 2.15 single-qubit rotations per qubit (see Table 4.2). Using the single-qubit RBM results from above to subtract SPAM errors and the contribution of single-qubit Clifford gates, we obtain an estimate of 0.98(1) for the fidelity of the first $\hat{W}_{ZZ}$ gate in a sequence. To compare this estimate to the result obtained with process tomography (see Section 4.4.1), we must take the contribution of SPAM and the single-qubit rotations (1.5 on average per qubit and tomography circuit) that implement the different initial states and measurement bases for process tomography into account. Using only fidelity estimates obtained from single- and two-qubit RBM, we expect a process fidelity of 0.96(1) for the process tomography of the $\hat{W}_{ZZ}$ gate with imperfect state preparation and measurement implementations. This estimate agrees well with the measured process fidelity of 0.961(2) (see Section 4.4.1).

[13] As the number of data points (4) is equal to the number of free model parameters in Equation (2.35), we regularise the fit by including a point at $m = 0$ with the value of the total SPAM that is extracted from the data shown in Figure 4.19(a), $S(0) = 0.988$.

4.4.5 Error analysis

We simulate the $\hat{W}_{ZZ}$ gate using the master equation to quantify the error contributions of known imperfections. The network qubit in $^{88}Sr^+$ and the logic qubit in $^{43}Ca^+$ are each described by a spin-$\frac{1}{2}$ system. The axial OOP and axial IP mode are represented by truncated Fock spaces with cutoff $n_c^{\text{oop}} = 7$ and $15 \leq n_c^{\text{ip}} \leq 50$ (depending on the expected thermal occupation), respectively.

By geometry, the coupling of the SDF to the radial modes is strongly suppressed. In a mixed-species, two-ion crystal, the axial normal modes of motion are found at frequencies

$$\omega^2_{\substack{\text{oop}\\\text{ip}}} = \frac{\left(1+\mu \pm \sqrt{1+(\mu-1)\mu}\right)\omega_1^2}{\mu} \ ,$$

where $\mu = m_2/m_1$ is the mass ratio of the two ions, and ω_1 is the axial frequency of a single ion of mass m_1 in the same trap. For $^{88}Sr^+$ and $^{43}Ca^+$, the ratio $\omega_{\text{oop}}/\omega_{\text{ip}} \approx 1.94486$ is close to 2, which results in unavoidable off-resonant excitation of the second harmonic of the IP mode when addressing the OOP mode [Bru+19]. The first-order coupling of the SDF to the axial IP mode is neglected in the RWA as it is far detuned. It is therefore sufficient to include only the first-order OOP terms, see Equation (2.28) with $\mathcal{N} = \{\text{oop}\}$, and the second-order IP terms,

$$\begin{aligned}\hat{\mathcal{H}}^{\text{ip}^2}_{\text{LS}}(t) = \ &-\hat{1}^{\otimes N}\sum_{i=1}^{N}\sum_{s=\downarrow,\uparrow}\frac{\hbar}{2}\Omega_{i,s}(t)\,|s\rangle\langle s|_i \otimes \\ &\frac{1}{2}\eta^2_{\text{ip},i}\left[\mathrm{e}^{-\mathrm{i}[(2\omega_{\text{ip}}-\omega)t+\varphi_i]}(\hat{a}_{\text{ip}})^2 + \mathrm{e}^{\mathrm{i}[(2\omega_{\text{ip}}-\omega)t+\varphi_i]}(\hat{a}^\dagger_{\text{ip}})^2\right] \ .\end{aligned}$$

For each axial motional mode, $\alpha \in \{\text{ip}, \text{oop}\}$, we include heating with Lindblad operators $\{\dot{\bar{n}}^{\frac{1}{2}}_\alpha \hat{a}_\alpha, \dot{\bar{n}}^{\frac{1}{2}}_\alpha \hat{a}^\dagger_\alpha\}$, and motional dephasing with Lindblad operator $(2/\tau_\alpha)^{\frac{1}{2}}\hat{a}^\dagger_\alpha \hat{a}_\alpha$. For each ion, we include Raman scattering with Lindblad operators $\{\Gamma_x^{\frac{1}{2}}\hat{\sigma}_+^{(i)}, \Gamma_x^{\frac{1}{2}}\hat{\sigma}_-^{(i)}\}$, and Rayleigh scattering and dephasing[14] with Lindblad operator $\Gamma_z^{\frac{1}{2}}\hat{\sigma}_z^{(i)}$, where the scattering rates Γ_x, Γ_z are calculated from theory [Cli+94; Oze+05; Bal14; Sch18]. By simulating the $\hat{W}_{ZZ}$ gate with different error rates we find that heating and motional decoherence of the IP mode does not directly affect the infidelity of the

[14] If this treatment were to be improved, dephasing due to magnetic field noise should be treated stochastically, as any realistic noise spectrum is coloured, i.e. non-white.

$\hat{W}_{ZZ}$ gate (maximum error $\lesssim 5 \times 10^{-4}$ with measured parameters); instead, the high heating rate of the IP mode limits the achievable temperature and thereby indirectly affects the gate fidelity.

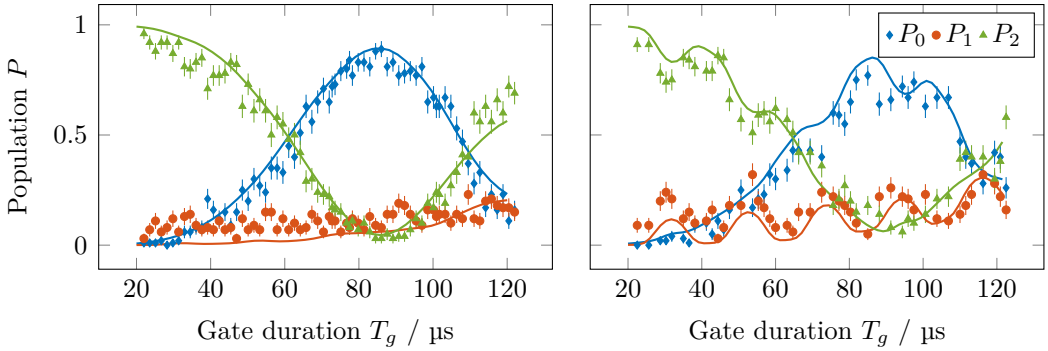

Figure 4.20: Effect of off-resonant excitation of the second harmonic of the IP mode of the mixed-species $\hat{W}_{ZZ}$ gate for different initial temperatures. In these scans, we set $\delta_g = \frac{4\pi}{T_g}$ at every point. Solid lines show simulations. Left: With $\bar{n}_{\mathrm{ip}} \approx 3$, the gate dynamics are dominated by the OOP mode. Right: With $\bar{n}_{\mathrm{ip}} \approx 20$, we observe significant out-of-Lamb-Dicke effects.

To diagnose the effect of second-harmonic excitation on the IP mode experimentally, we scan the gate time T_g at constant power while adjusting the detuning from the OOP gate mode, $\delta_g = -\frac{4\pi}{T_g}$, to always close the phase space loops of the OOP mode. The signature of a hot IP mode is an oscillating feature of P_1 as a function of the gate duration (see Figure 4.20).

We plot the contributions of all known error sources in Figure 4.21 for a range of gate durations, where SDF strength and detuning are adjusted to their corresponding optimal value at which they produce a perfect gate in the case of no imperfections. The sign of the detuning from the OOP mode is chosen to maximise the detuning from the second harmonic of the IP mode. Due to insufficient cooling and the resulting out-of-Lamb-Dicke effects, the excitation of the second harmonic of the IP mode can reduce the fidelity of the gate significantly. Notably, the infidelity due to the IP mode depends on the gate duration (detuning) and is minimised at appropriately chosen values. In this work, we operate close to the minimum near $T_g = 60\,\mu\mathrm{s}$. Other error sources that are included in this model, i.e. motional errors affecting the OOP mode and spin decoherence, increase monotonically with the gate duration.

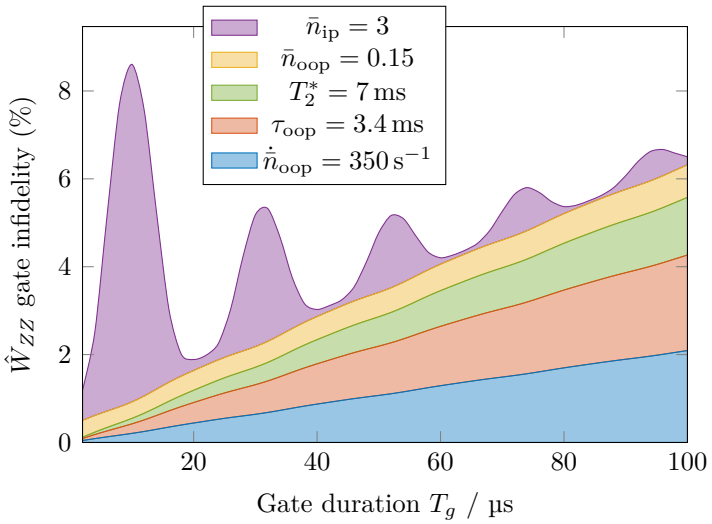

Figure 4.21: Error budget of the mixed-species $\hat{W}_{ZZ}$ gate as a function of total gate duration. Filled areas correspond to the contributions of different known imperfections, which were independently characterised with the exception of T_2^*, which was estimated.

5

Robust ion-photon entanglement memory

Contents

In this chapter I discuss the first experiment in which entanglement between a network qubit and a photon is created and coherently transferred onto a memory qubit for storage. Due to its simple level structure, $^{88}Sr^{+}$ is ideally suited for our ion-photon entanglement (IPE) scheme, whereas the hyperfine structure of $^{43}Ca^{+}$ provides a long-lived memory qubit [Luc+07]. While both IPE and local mixed-species entangling gates have been demonstrated independently [Inl+17], this is the first experiment in which these capabilities are combined. Furthermore, we show that the memory qubit in $^{43}Ca^{+}$ is robust to environmental noise as well as concurrent addressing of $^{88}Sr^{+}$ for the generation of IPE (see Section 5.2.2). We use this property

to store ion-photon entanglement on the memory qubit while the network qubit is entangled with a second photon. Finally, sympathetic cooling of the ion chain using $^{88}Sr^{+}$ between rounds of entanglement generation enables continued operation even in the presence of heating. The availability of a memory qubit in a photonic quantum network node unlocks a number of applications, including entanglement distillation for distributed quantum computing, and increased coherence times for entanglement-enhanced atomic clock comparisons, and delegation of measurement-based quantum computations for BQC, which I present in Chapter 6. The results discussed in this chapter are published in Reference [Drm+23].

5.1 Methods

A schematic of the experimental apparatus used in these experiments is shown in Figure 5.1. The first ion species, $^{88}Sr^{+}$, is the central component of the photonic

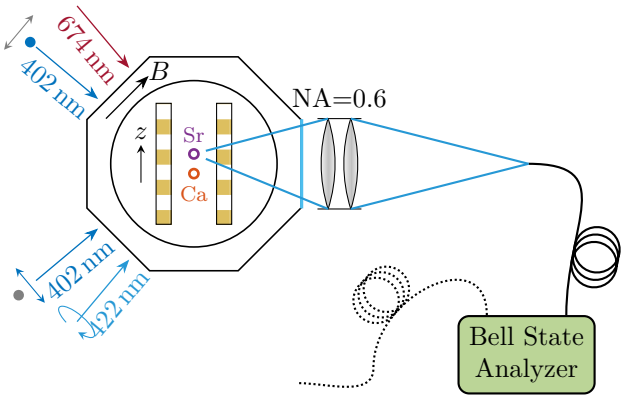

Figure 5.1: Schematic of ion trap and single-photon interface. We show the laser beam geometry; within the plane of the trap surface, the magnetic field B is oriented at 45° to the trap axis z. Perpendicular to this plane, the NA = 0.6 lens collects single photons from a $^{88}Sr^{+}$ ion (violet circle). Single photons are coupled into a single-mode fibre that is connected to a Bell state analyser. Here, only one network node is connected; the same device can herald remote entanglement with a second, identical node [Ste+20]. The state of $^{88}Sr^{+}$ can be mapped onto a co-trapped $^{43}Ca^{+}$ ion (orange circle).

interface, and is used to generate single photons whose polarisation is entangled with the state of the network qubit (see Section 2.1.1). The second ion species, $^{43}Ca^{+}$, is chosen for its excellent coherence properties and the high level of control achieved in previous experiments [Hom+09; Har+14; Bal+16; Sep+19]. The

level structures of $^{88}Sr^+$ and $^{43}Ca^+$ and relevant laser transitions are shown in Figure 5.2. At a magnetic field of 0.5 mT, the frequency of the memory qubit

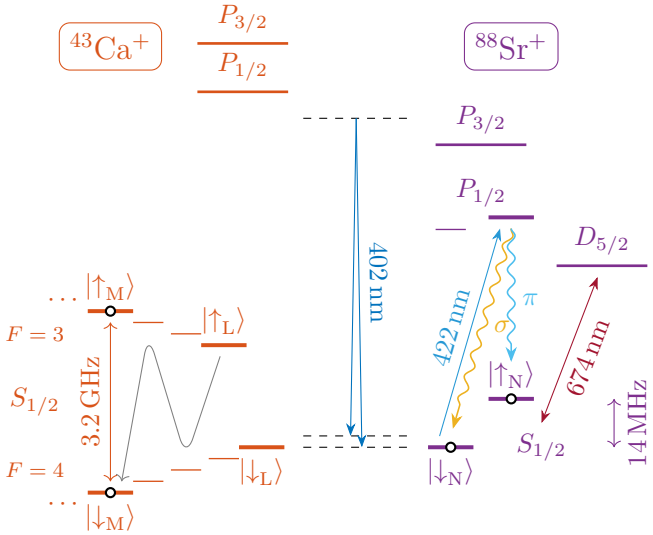

Figure 5.2: Level structure of $^{43}Ca^+$ (orange) and $^{88}Sr^+$ (violet), not to scale. The memory qubit M comprises the $m_F = 0$ states in the $^{43}Ca^+$ $S_{1/2}$ manifold. Raman lasers (blue arrows, 422 nm) are used to drive mixed-species entangling gates between the logic qubit L and the network qubit N, as well as transitions between $^{43}Ca^+$ hyperfine ground states. A σ^+-polarized laser pulse excites the $S_{1/2} \leftrightarrow P_{1/2}$ transition in $^{88}Sr^+$ to generate a single photon whose polarization (see σ and π decay channels) is entangled with the state of the ion. A narrow-linewidth laser (red arrow, 674 nm) is used to manipulate the $^{88}Sr^+$ qubit via the quadrupole transition.

transition depends weakly on the magnetic field magnitude, with a sensitivity of 122 kHz mT^{-1}. Compared to the sensitivity of the $^{88}Sr^+$ network qubit of 28 MHz mT^{-1}, the memory qubit is significantly more resilient to magnetic field noise. Furthermore, the mass ratio between $^{43}Ca^+$ and $^{88}Sr^+$ is reasonably favourable for sympathetic cooling [Kie+00] and the electronic level structure facilitates mixed-species gates [Hug+20] (see Section 4.4).

5.1.1 Ion-photon entanglement

Single photons that are entangled with the network qubit of $^{88}Sr^+$ are generated by spontaneous emission into free-space (see Section 2.1), collected by an NA = 0.6 objective into an optical fibre, and detected using APDs, which are part of the same photonic Bell state analyser used to herald remote entanglement between

two network nodes [Ste+20]. The second input port of the Bell state analyser is reserved for quantum networking experiments and is left open here (see Figure 5.1). The expected end-to-end efficiency of this photon detection system is $\sim 5\,\%$; the probability to decay on the 422 nm transition is 0.95 ($\sim 5\,\%$ decay into $D_{3/2}$); only 10 % are emitted into the solid angle subtended by the objective; the overlap of the image with the fibre mode is less than 0.74 [Nad22]; absorption in the ~ 1.5 m fibre accounts for $\sim 1\,\%$ loss; the light coupling efficiency into the detectors is $\sim 85\,\%$; the quantum efficiency of the detectors is $\sim 70\,\%$. In practice, we observe a lower end-to-end efficiency of $\sim 2\,\%$, attributing the extra loss to imperfections in the mode overlap of the image with the fibre due to aberrations. Because of these losses, the pulsed excitation sequence is repeated in a loop until a photon is detected (see Section 3.4.4.1), which triggers the execution of a preprogrammed pulse sequence (see Section 3.4.4.3). The attempt rate of 1 MHz leaves 1 µs per iteration of this loop, which includes latencies (~ 400 ns), fast state preparation by optical pumping (300 ns), pulsed excitation and photon detection (~ 50 ns) (see Section 6.2 in Reference [Ste19]).

5.1.2 Transfer of entanglement

Having generated ion-photon entanglement, we want to transfer the state of the network qubit in $^{88}Sr^+$ to the memory qubit in $^{43}Ca^+$ ($|F=4,\, m_F=0\rangle \leftrightarrow |F=3,\, m_F=0\rangle$), see Figure 5.2. The memory qubit is magnetic field-insensitive at low magnetic field, but unlike the logic qubit, $|F=4,\, m_F=4\rangle \leftrightarrow |F=3,\, m_F=3\rangle$, it cannot be prepared using optical pumping, and does not experience the light shift force required for our gate scheme. We therefore proceed in two steps. First (see Section 5.1.2.1), we swap the network qubit state from $^{88}Sr^+$ to the logic qubit in $^{43}Ca^+$ using the light-shift force (see Section 4.2). Second, a sequence of π pulses coherently transfers the superposition from the logic qubit to the memory qubit for storage (see Section 5.1.2.2).

5.1.2.1 From strontium to calcium

Transferring quantum information between two qubits is a coherent process. In its most general form, the SWAP gate is bidirectional and can be implemented by three native CZ gates (see Section 4.4.1) and single-qubit rotations. In our situation, however, the target qubit (the state of $^{43}Ca^{+}$) is known to be prepared in $|\downarrow_{\mathrm{L}}\rangle$. This enables a more efficient scheme: we use the iSWAP gate (see Section 4.4.2), which can be decomposed into two native CZ gates and global single-qubit rotations.

Error detection. We want to perform the mapping of a state $|\phi\rangle$ from the network qubit to a logic qubit: the ideal iSWAP performs the mapping $|\phi_{\mathrm{N}}\rangle \otimes |\downarrow_{\mathrm{L}}\rangle \mapsto |\downarrow_{\mathrm{N}}\rangle \otimes |\phi_{\mathrm{L}}\rangle$, leaving the network qubit in the $|\downarrow_{\mathrm{N}}\rangle$ state if no error occurred. Experimental imperfections leading to deviations from the target subspace $\mathcal{T} = |\downarrow_{\mathrm{N}}\rangle\langle\downarrow_{\mathrm{N}}| \otimes 1_{\mathrm{L}}$ can thus be detected via a mid-circuit measurement on the network qubit [Sta+22]. If it is found in $|\uparrow_{\mathrm{N}}\rangle$ instead, the current round is aborted and repeated.[1] Otherwise, the measurement projects the state into $\mathcal{T}$, which enhances the gate fidelity to 0.977(7) (from 0.913(3) of the bare iSWAP). This fidelity is inferred from the same tomography data as presented in Figure 4.17 by post-selecting data from the target subspace (see Figure 5.3(a)).

5.1.2.2 To the memory qubit in calcium

Once the network qubit state has been transferred to the logic qubit in $^{43}Ca^{+}$, it needs to be mapped to the memory qubit. This is achieved using a sequence of 9 Raman pulses. Figure 5.4 illustrates the transitions in the relevant section of the hyperfine structure of $^{43}Ca^{+}$ that are addressable using the chosen Raman beam geometry and polarisation configuration (see caption for details).

First, a sequence of four π-pulses transfers population from $|F=3, m_F=3\rangle$ into $|F=3, m_F=0\rangle$. Subsequently, population from $|F=4, m_F=4\rangle$ is transferred into $|F=3, m_F=1\rangle$. At this point, a complication arises as the $|F=4, m_F=1\rangle \leftrightarrow |F=3, m_F=0\rangle$ and the $|F=4, m_F=0\rangle \leftrightarrow |F=3, m_F=1\rangle$ transitions are only

[1] Unfortunately, the symptom does not contain enough information for correcting the error.

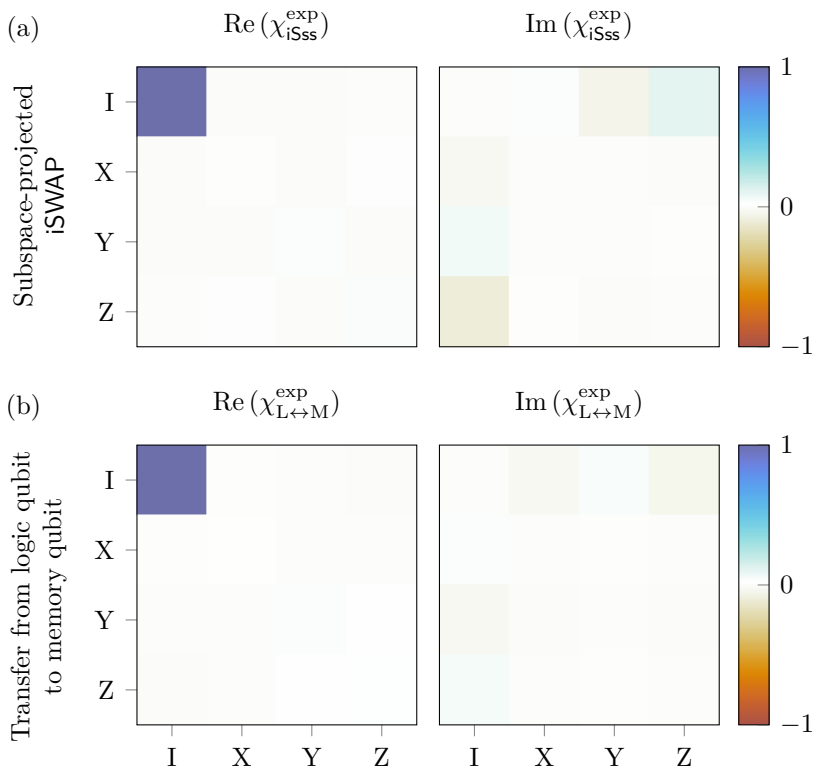

Figure 5.3: The Choi matrix reconstructed from process tomography of (a) the mixed-species iSWAP gate after error detection (i.e. after post-selecting data from the subspace $|{\downarrow_{\text{N}}}\rangle\langle{\downarrow_{\text{N}}}| \otimes 1_{\text{L}}$), and (b) the transfer pulse sequence from the logic qubit to the memory qubit in $^{43}Ca^{+}$. The fidelity of (a) the conditional process is 0.977(7), and (b) 0.980(4), both with respect to the identity operation.

separated by $\Delta f \approx 15\,\text{kHz}$ at the 0.5 mT magnetic field (see Figure 5.4). To coherently reverse the effect of off-resonant excitation on the $|F=4,\, m_F=1\rangle \leftrightarrow |F=3,\, m_F=0\rangle$ transition, we apply two $\pi/2$ pulses on the $|F=4,\, m_F=0\rangle \leftrightarrow |F=3,\, m_F=1\rangle$ transition with a delay of $157\,\mu\text{s} \sim 2/\Delta f$ in between. During this delay, the $\{|F=4,\, m_F=1\rangle, |F=3,\, m_F=0\rangle\}$ qubit acquires a relative phase of π with respect to the laser resonant with the $|F=4,\, m_F=0\rangle \leftrightarrow |F=3,\, m_F=1\rangle$ transition, thus acting like a spin-echo in a Ramsey sequence (see Section 2.4.2.1).

We characterise the transfer protocol using process tomography (see Figure 5.3(b)). Ideally, the process implements the identity mapping between the logic qubit and the memory qubit; we measure a process fidelity of 0.980(4) with respect to this ideal case.

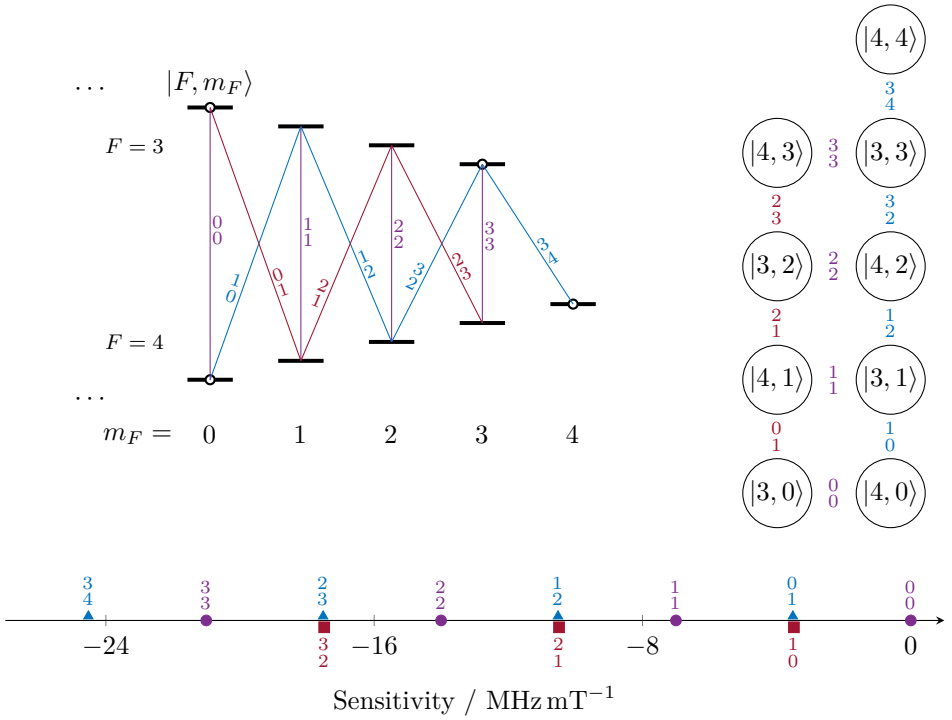

Figure 5.4: Hyperfine transitions with $m_F \geq 0$ in the ground level of $^{43}Ca^+$, $|F=4, m_F=m_4\rangle \leftrightarrow |F=3, m_F=m_3\rangle$, are labelled by $\binom{m_3}{m_4}$. The energy level diagram (not to scale) can be transformed into a topologically equivalent graph. The graph is useful for finding the shortest sequence of transfer pulses to reach a given state starting from any other state. Transferring a superposition from the logic qubit to the memory qubit requires special attention to σ^+ transitions with near-resonant σ^- transitions nearby; the sensitivity difference between $\binom{m+1}{m}$ and $\binom{m}{m+1}$ is 31 kHz mT^{-1}.

5.1.3 Tomography of ion-photon entanglement

To analyse the polarisation state of the photons, we employ motorised waveplates, PBSs and APDs. The waveplate angles determine the polarisation measurement basis and are set asynchronously before a data point ($\sim$1000 shots) is acquired. Combining points with different waveplate angles, the polarisation state (density matrix) of the photon can be reconstructed fully. For each set of waveplate angles, the ion is measured in three different bases, $\hat{\sigma}_x$, $\hat{\sigma}_y$, and $\hat{\sigma}_z$, to enable a full reconstruction of the joint ion-photon density matrix.

Even though the photonic Bell state analyser contains two branches that both contain detectors for both polarisation measurement outcomes, we do not merge the data from nominally equivalent detectors because of slight differences in the birefringent properties between the two paths.

We perform maximum likelihood estimation of the joint ion-photon density matrix, for each detector $h \in \{0 \dots 3\}$, by numerically minimising the negative logarithm of the likelihood function,

$$\mathcal{L}(\hat{\rho}) \sim \prod_i \mathrm{Tr}\left(\hat{\Pi}_{\emptyset,i}\hat{\rho}_P\right)^{n_{\emptyset,i}} \prod_{k\neq h} \mathrm{Tr}\left(\hat{\Pi}_{k,i}\hat{\rho}_P\right)^{n_{k,i}} \times \prod_j \mathrm{Tr}\left[\left(\hat{\Xi}_{j,\mathrm{bright}} \otimes \hat{\Pi}_{h,i}\right)\hat{\rho}\right]^{n_{h,i,\mathrm{bright},j}} \times \mathrm{Tr}\left[\left(\hat{\Xi}_{j,\mathrm{dark}} \otimes \hat{\Pi}_{h,i}\right)\hat{\rho}\right]^{n_{h,i,\mathrm{dark},j}} ,$$

where $\hat{\Pi}$ and $\hat{\Xi}$ denote the POVMs acting on the photonic and ionic part, respectively, n are the number of experimental occurrences, $\emptyset$ represents the no-click outcome (photon loss), and $\hat{\rho}_P = \mathrm{Tr}_I(\hat{\rho})$ is the photonic part of the joint ion-photon density matrix $\hat{\rho}$. Index i enumerates the photon polarisation measurement bases, and k enumerates the other detectors, for which only the likelihood of the photonic measurements contributes. Index j enumerates the ion qubit measurement bases, and dark/bright indicates the measurement outcome.

The unitary map $\hat{U}_P$ from the polarisation basis of an incoming photon to the four spatially separated, $\{H, V\} \ni q$-polarised output modes $|h, q\rangle$ is a function of waveplate retardances, r, waveplate rotation angles relative to the fast axis, β, transmission of the beam splitter, t_{BS}, and the polarisation extinction ratios of the PBSs, ϵ (see Table 5.1 for independently measured values).

Parameter	$r_{\lambda/4}$	$r_{\lambda/2}$	$t_{\mathrm{BS},H}$	$t_{\mathrm{BS},V}$	$\epsilon_{\mathrm{A},H}$	$\epsilon_{\mathrm{A},V}$	$\epsilon_{\mathrm{B},H}$	$\epsilon_{\mathrm{B},V}$
Values	0.217	0.449	0.5283	0.5307	1:12500	1:700	1:3000	1:1900

Table 5.1: Independently characterised parameters of optical elements in the photonic Bell state analyser (see also Reference [Ste19]). Subscripts A and B refer to the optical paths corresponding to the two output ports of the beam splitter. H and V refer to orthogonal linear polarisation states aligned with the axis of the PBS.

The POVMs for detection of a photon on a particular detector h, dropping index i for readability, are

$$\hat{\Pi}_h = \sum_{q\in\{H,V\}} \eta_h \hat{U}_P^\dagger |h, q\rangle\langle h, q| \hat{U}_P ,$$

$$\hat{\Pi}_\emptyset = \hat{1} - \sum_{k=0}^{3} \hat{\Pi}_k ,$$

where η_h is the overall detection efficiency for this detector. We model the waveplates as unitary retarders. By placing the quarter waveplate nearest to the PBS, followed by the half waveplate, a measurement along a rotated polarisation basis is implemented. For tomography, the half waveplate angle is chosen from $\{0, \pi/8\}$ and the quarter waveplate angle from $\{0, \pi/4\}$ with respect to the respective fast axis. The projector for the ion state is

$$\hat{\Xi}_s(\vartheta, \varphi) = \hat{R}(\theta, \varphi)^\dagger \, |s\rangle\langle s| \, \hat{R}(\theta, \varphi) \ ,$$

with θ, φ parametrising the rotation (Equation (2.24)). For tomography, we use the settings $\theta = \frac{\pi}{2}, \varphi \in \{0, \frac{\pi}{4}, \frac{\pi}{2}, \frac{3\pi}{4}\}$ and twice the setting $\theta = 0$ to establish an over-complete set of measurement bases. For ion-photon tomography, we exhaust all 24 measurement basis settings, collecting (typically) 1000 ion-photon measurements at every step. For simultaneous tomography on both $^{88}Sr^+$ and $^{43}Ca^+$, the same measurement basis settings are used for both ions and both photons. The collected data from the two ion-photon states are analysed separately using the MLE method described here.

5.1.4 Non-parametric bootstrapping

Each set of data can be resampled according to inherent statistical properties, in order to generate new data sets, which can be analysed in the same way as the measured data. The bootstrapped results approximate the measured result on average, but with a spread indicating how sensitive the analysis is to statistical fluctuations in the input data. For the ion-photon experiments presented here, the number of excitation attempts is exponentially distributed, photons are multinomially distributed into the four detectors, and the thresholded ion fluorescence readout follows binomial statistics. The underlying probabilities for these distributions are estimated from the measured data set in frequentist manner.

5.1.5 Entanglement fidelity

In quantifying the entanglement contained in the reconstructed ion-photon states, we allow for arbitrary *local* qubit and polarisation rotations, $\hat{U}_1$ and $\hat{U}_2$, to transform the state $\hat{\rho}$ to overlap maximally with a maximally entangled Bell state, such as $|\Psi^+\rangle = \frac{1}{\sqrt{2}}(|\uparrow\uparrow\rangle + |\downarrow\downarrow\rangle)$. We define the fidelity of $\hat{\rho}$ by

$$\mathcal{F}[\hat{\varrho}] = \max_{\hat{U}_1,\hat{U}_2} \langle\Psi^+|(\hat{U}_1 \otimes \hat{U}_2)\hat{\varrho}(\hat{U}_1 \otimes \hat{U}_2)^\dagger|\Psi^+\rangle \ . \tag{5.1}$$

In practice, we calculate Equation (5.1) using singular value decomposition of the matrix containing the Pauli expectation values of $\hat{\rho}$ [Bad+00].

5.2 Results

The iSWAP operation enables the transfer of IPE from the network qubit in $^{88}Sr^+$ to the memory qubit in $^{43}Ca^+$, so that IPE can be created a second time with the network qubit. To probe the memory properties of the integrated system of entangled photons and ions, we perform tomography on both ion-photon states in parallel after a variable storage duration. For this, we initialise $|\downarrow_L\rangle \otimes |\downarrow_N\rangle$ and execute the attempt loop until a single photon is detected (point *I* in Figure 5.5(a)). Subsequently, we swap the network qubit state to the logic qubit, and further to the memory qubit for storage (see Section 5.1.2). If the 130 µs mid-circuit measurement on the network qubit indicates a success (point *II* in Figure 5.5(a)), the attempt loop is executed until a second photon is detected (point *III* in Figure 5.5(a)). After a variable delay Δt, both the memory and the network qubit are measured. Note that no dynamical decoupling is used throughout this sequence. Figure 5.6 shows the fidelity of ion-photon states to the closest maximally entangled state [Bad+00] for different storage durations. The raw $^{88}Sr^+$-photon fidelity is 0.97(2), but dephasing of the network qubit limits the coherence time of this state to 2 ms. Swapping the ion state into the memory qubit extends the coherence time by a factor $\sim$70 with an initial fidelity of 0.93(2). The additional infidelity is due to the high heating rates limiting the iSWAP operation (see Section 4.4.2),

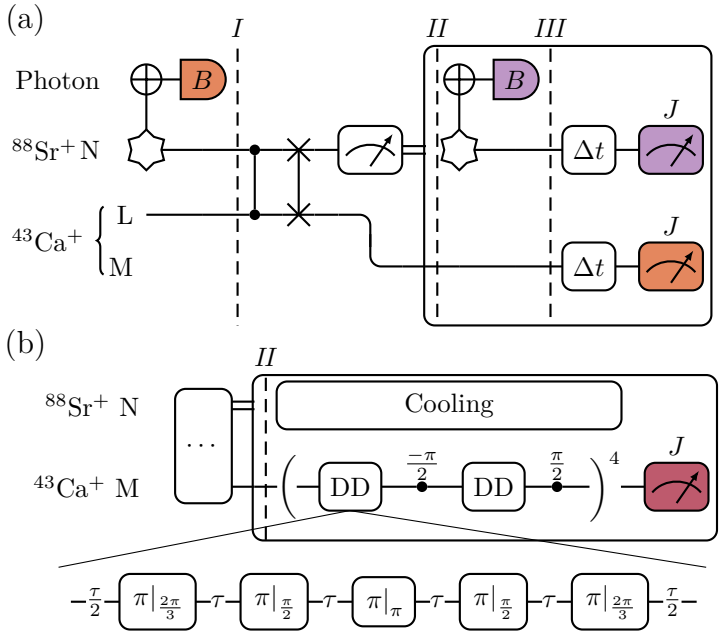

Figure 5.5: Experimental sequences to probe the memory properties of the network node. Delayed measurements from a complete set of bases $B \otimes J$ are used to tomographically reconstruct the density matrices of the ion-photon states. If the mid-circuit measurement detects errors in the iSWAP gate, the sequence is immediately restarted. (a) A second photon is generated after transferring the state entangled with the first photon to the memory qubit. (b) After transferring IPE from the network qubit to the memory qubit, ^{88}Sr$^+$ is used to sympathetically cool ^{43}Ca$^+$. Dynamical decoupling and ion transport are used to extend the memory coherence time during the storage period.

and imperfections in the L → M transfer pulse sequence. The fidelity shown in Figure 5.6 decays due to magnetic field noise and laser leakage; heating during the storage duration causes single-qubit rotation errors in ^{88}Sr$^+$, whereas the Raman beam geometry eliminates this effect in ^{43}Ca$^+$.

5.2.1 Decoupled memory qubit

In a second experiment, we demonstrate that the limitations of magnetic field noise, heating, and laser leakage can be overcome. We employ Knill dynamical decoupling [SÁS11; Wan+21] (see Section 2.4.2.3) with 40 spin flips to suppress the effect of magnetic field noise (see Figure 5.5(b)). To minimise the effect of laser leakage, we transport the ions 100 µm away from the laser interaction zone. Furthermore, sympathetic Doppler cooling on ^{88}Sr$^+$ avoids ion loss due to heating. We achieve an IPE fidelity of 0.81(4) after 10 s (squares and right panels in Figure 5.6).

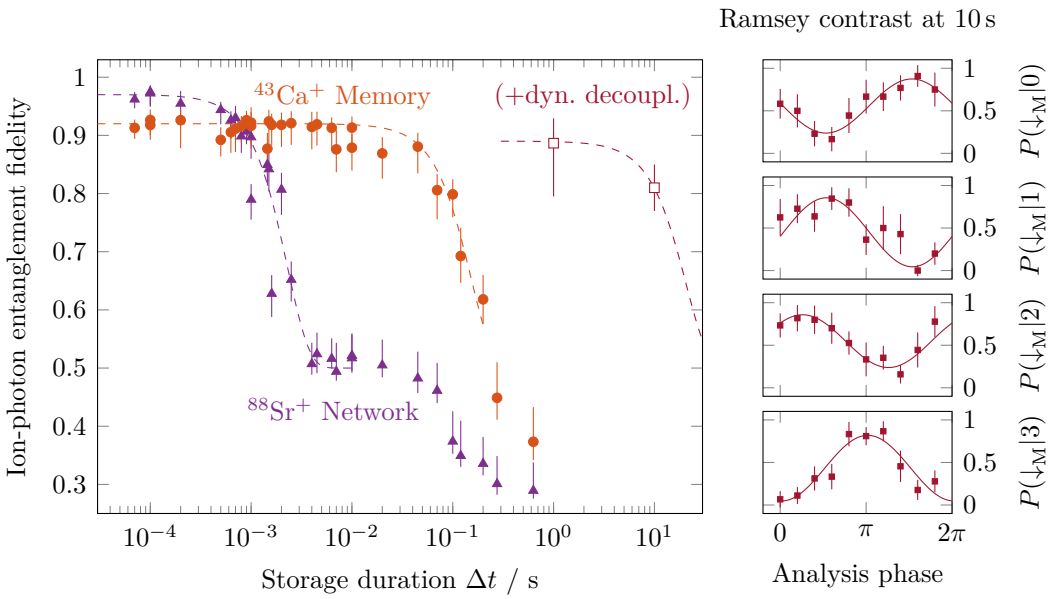

Figure 5.6: The fidelities of the ion-photon states with respect to the closest maximally entangled state (see Section 5.1.5) are calculated from the density matrix obtained from maximum likelihood estimation (see Section 5.1.3) and averaged over all four photon detectors. Error bars span the 95 % confidence interval obtained from non-parametric bootstrapping. Dashed curves show Gaussian decay models to guide the eye. Squares indicate the fidelity with dynamical decoupling, ion transport, and sympathetic cooling using ^{88}Sr$^+$ during the storage time. At 10 s, only the populations and the Ramsey contrast were measured to infer the fidelity (see right column: individual signal for APDs 0-3).

5.2.2 Robustness to network activity

Crucially, there is negligible error associated with generating a second ion-photon pair, as the lasers used during the attempt loop are far off-resonant (> THz) from transitions in ^{43}Ca$^+$. To demonstrate this, we perform Ramsey experiments on the memory qubit while the loop is ongoing in the background for up to 10^5 excitation attempts (see Figure 5.7(a) and Figure 5.7(b)), enough to herald > 1500 entangled ion-photon states. The light shift per excitation attempt is 8.8(6) µrad, and can easily be corrected in real-time by adjusting the phase reference. From the same data, we do not observe any statistically significant reduction in contrast (see Figure 5.7(b)). A secondary consequence of the loop is excess heating due to photon recoil. We measure excess heating of $9.3(9) \times 10^{-4}$ phonons per attempt (see Figure 5.7(c)) on the relevant (axial) motional mode, which is insignificant

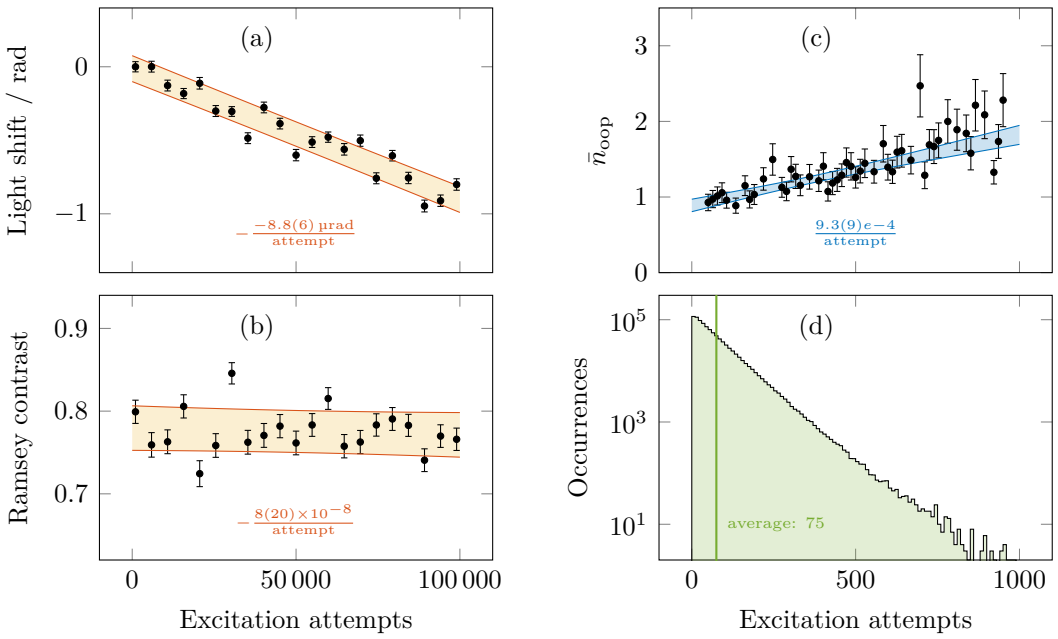

Figure 5.7: The effect of excitation attempts on (a) the phase and (b) coherence of the memory qubit, and on (c) the temperature of the OOP mode. A variable duration $0 \leq T \leq T_{\max}$ of a fixed total duration $T_{\max}$ is spent executing attempts at a rate of $1\,\mu s^{-1}$ before the state of the ion is analysed. The sensitivity of each measured quantity to the number of excitation attempts is extracted from linear least-squares fits. Error intervals span one standard deviation. (a-b) Ramsey experiments with $T_{\max} = 100\,ms$. Filled single-prediction bands guide the eye to (a) phase and (b) contrast of the Ramsey fringe. (c) Sideband-ratio thermometry with $T_{\max} = 1\,ms$. The 95 % confidence band is shown in blue. (d) Histogram of excitation attempts until detection of a photon, indicating a success probability of 0.013.

in the context of this experiment (see Figure 5.7(d)).

5.3 Summary

In summary, we have demonstrated the coherent transfer of IPE from a network qubit in $^{88}Sr^+$ to a memory qubit in $^{43}Ca^+$ within a quantum network node. We note that the measurements reveal the presence of entanglement even though the photon was destroyed before the transfer took place [Meg+13]. We extend the storage duration of this entanglement by ~ 4 orders of magnitude, to more than 10 s, while ensuring that subsequent IPE can be performed without crosstalk affecting the memory qubit. Extending the storage duration beyond the time taken to generate IPE is essential for applications that require multiple communication

photons. The ratio of decoherence rate to the node-to-node entanglement rate in a quantum network impacts the resource scaling for fault-tolerant error correction [Mon+14]. Here, this ratio is estimated to be 0.0006 and 0.08 with and without dynamical decoupling, respectively, assuming the entanglement rate of $182\,\mathrm{s}^{-1}$ previously observed in our setup [Ste+20].

For long-distance networks, communication latencies due to time-of-flight and classical signaling would limit the rate at which nodes with a single network qubit can generate entanglement. However, if the state of this network qubit is stored in an available memory qubit immediately after emission of the photon, entanglement attempts could be made without dead-time in between [Kru+23a]. A constant attempt rate could be reached independent of distance, limited only by the local swapping procedure. In that scheme, the memory qubits would be stored until the corresponding herald signals arrive to indicate which had been entangled successfully. In our system, link losses, rather than memory coherence, would set the limit on the maximum possible node separation.

To increase the photon collection efficiency, cavities can be used [Stu+13; Kru+23b; Sch+21]. To reduce the fibre losses, quantum frequency conversion to infrared wavelengths has been proven feasible [Wri+18; Kru+19; HSQ22]. Combined with these improvements, our system integrating a high-fidelity photonic interface with mixed-species quantum logic, a robust memory and ion transport capabilities, paves the way for more powerful trapped-ion quantum networks.

6 Verifiable blind quantum computing

Contents

In this chapter I present experimental results of delegating single-qubit rotations from a photonic client to a trapped-ion quantum processor (server), which are published in Reference [Drm+24]. The experimental techniques developed throughout my studies amalgamate in this demonstration; the fast polarisation analyser described in Section 3.3 is deployed together with the ion-photon entanglement memory presented in Chapter 5, which is based on the tools for mixed-species quantum operations that are described in Chapter 4.

6.1 Background

Conventionally, quantum algorithms are expressed in terms of circuits of logic gates drawn from a universal set of gates. The measurement-based quantum computing (MBQC) model, also known as one-way quantum computing [RB01], is an alternative representation of quantum logic which prescribes a sequence of measurements on a highly entangled universal resource state [Nie06; MDF17]. MBQC has been studied extensively since the realisation that it can be applied to photonic quantum computing [Nie04]. MBQC has also been demonstrated with trapped ions [Lan+13], which shows that this platform supports both computational models. A hybrid model, where the circuit model and MBQC are combined to unify their advantages [ZBD14], is therefore particularly amenable for a trapped-ion quantum processor with a photonic interface. Our implementation harnesses this hybrid approach to perform BQC.

BQC is a framework in which a client with limited quantum resources can delegate quantum computations to a universal quantum server without disclosing the data or even the algorithm – this property is called 'blindness'. Perfect blindness can be achieved, even against maliciously operating servers, if the state preparation step[1] is performed by the client [CLN05; BFK09; MF13; Fit17]. To this end, the client must ensure that the quantum information stored by the server appears maximally mixed to any adversary, including the server [Fis+14]. Additionally, the client encrypts all classical messages using a secret random key that is kept private and later used to decrypt the results received from the server. In the following sections, I introduce MBQC and extend it with blindness and verification. For a comprehensive introduction to this field, see References [Nie06; BB06; Fit17; GKK19].

6.1.1 Measurement-based paradigm

To illustrate the idea underlying this paradigm, we start by examining a gate teleportation circuit. The circuit shown in Figure 6.1 teleports a single-qubit

[1] In another version (*receive-and-measure*), the client performs the measurement step. However, the *prepare-and-send* variation allows a straight-forward implementation with our experimental apparatus.

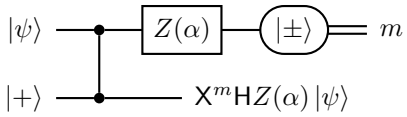

Figure 6.1: Teleportation of $Z(\alpha)$ rotation of an arbitrary state, $|\psi\rangle$, using an auxiliary qubit initialised in the state $|+\rangle$ and a measurement in the rotated $|\pm\rangle$ basis with measurement outcome m.

rotation $Z(\alpha)$ onto an arbitrary state $|\psi\rangle$ by performing an entangling CZ operation (Section 4.4.1) with an auxiliary qubit and measuring the original qubit. After the measurement m, the output qubit in Figure 6.1 obtains the state of the original qubit with the gate applied. Additional by-product Clifford terms can be corrected classically, as they merely flip the output bit at the end of the circuit depending on previous measurement outcomes m. The circuit shown in Figure 6.2 extends this idea to an arbitrary single-qubit rotation, which utilises three auxiliary qubits and three measurements. Using SWAP gates, the auxiliary qubits can be reused

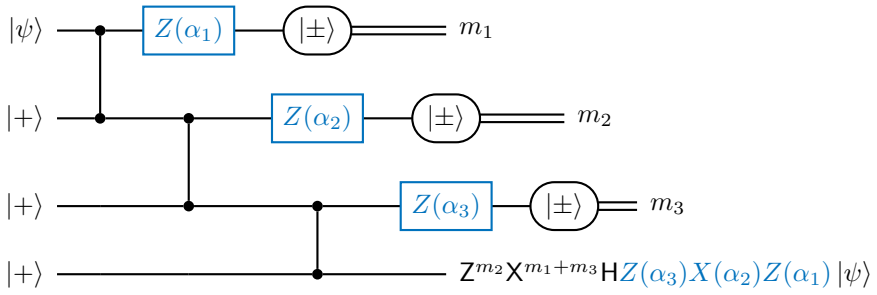

Figure 6.2: Measurement-based single-qubit rotation. Each measurement teleports a gate $\mathsf{H}Z(\alpha)$ onto the next qubit. To arrive at the final expression for the output qubit, the identities $\mathsf{H}Z(\alpha) = X(\alpha)\mathsf{H}$ and $\mathsf{HH} = \hat{1}$ were used. Up to by-product Clifford terms that can be correct classically, this measurement-based circuit implements the most general single-qubit rotation $|\psi\rangle \mapsto Z(\alpha_3)X(\alpha_2)Z(\alpha_1)\,|\psi\rangle$.

after being measured, which enables more efficient use of qubit resources (see the equivalent circuit in Figure 6.3). This measurement-based computation is more compactly expressed in terms of a graph state, 

. Graph states are specific multi-qubit states in which nodes represent qubits prepared in $|+\rangle = \frac{1}{\sqrt{2}}(|0\rangle + |1\rangle)$ and edges represent entanglement created by two-qubit CZ gates. The qubits are measured in a fixed order, using the basis $\hat{B}_{\alpha_\ell}$ at node ℓ, where α_ℓ depends on the algorithm and on previous measurement outcomes.

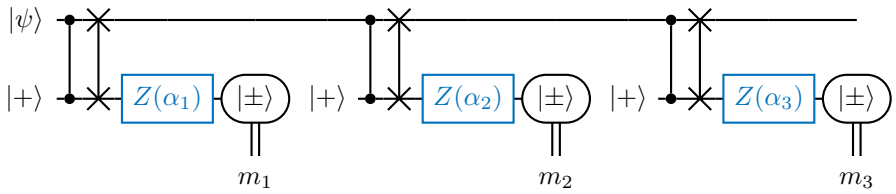

Figure 6.3: Resource-efficient measurement-based single-qubit rotation. Using an additional SWAP gate at every step enables the measured qubit to be reused in the next step.

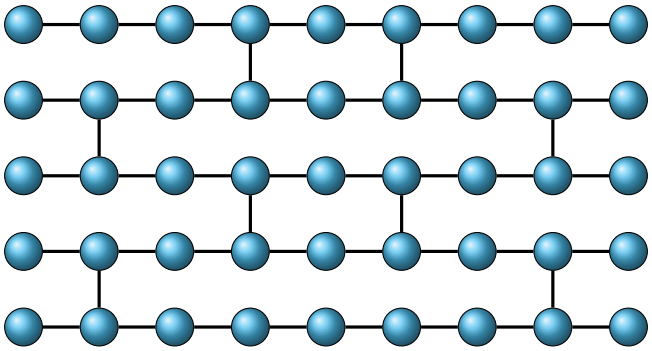

Figure 6.4: The brickwork state is a universal resource for universal quantum computing in the measurement-based model. Nodes (spheres) represent qubits initially prepared in $|+\rangle$ and edges (lines) denote entanglement created by CZ gates.

For universal quantum computation, particular graph states that are called 'brickwork states' (see Figure 6.4), and a discrete set of single-qubit measurement bases, $\{\hat{B}_\alpha = \cos(\alpha)\mathsf{X} + \sin(\alpha)\mathsf{Y}\}_{\alpha\in\Theta}$, are sufficient [MDF17], where $\Theta = \{0, \pi/4, \ldots, 7\pi/4\}$, and X, Y are Pauli operators.

The gate teleportation circuit can be generalised by introducing Z rotations of every qubit (see Figure 6.5), which adds the necessary degrees of freedom for randomising the states such that the cluster state appears to be maximally mixed. The rotations that apply the phase offsets, θ_1 and θ_2, do not change the behaviour

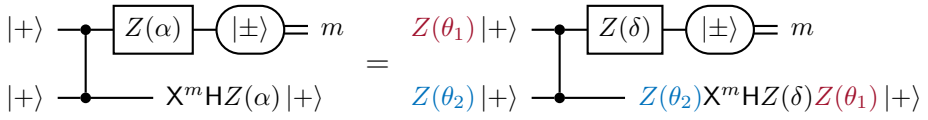

Figure 6.5: Introducing phase offsets θ on each qubit enables a client to hide the information content of the cluster state from the server.

of the circuit as they commute with the entangling CZ gate [Nie06].

In a cloud computing setting where the client has control over the initial state of the qubits in the server, the client can randomly choose secret offsets, $\theta_\ell \in \Theta$, such that the states appear maximally mixed to the server and therefore contain no useful information. The measurement angles which the client has to communicate to the server are consequently shifted by the same amount, with θ_ℓ acting as a classical encryption key such that the α_ℓ, which encode the quantum algorithm and the data, remain private to the client. The client can keep track of the individual qubit encodings classically and thereby delegate a universal quantum computation in a fashion that leaves the server blind.

6.1.2 Verifiability

In the presence of noise, even a faithfully operating server produces erroneous results that are indistinguishable from nefarious deviations from the honest protocol [Aha+17; FK17; Bro18; GKK19]. Blindness allows the client to perform tests on the quantum resources provided by the server without leaking information, and subsequently to verify the outcomes to establish confidence in the quantum operations performed by the server. Besides having implications for the client-server scenario, such verification could become a crucial tool for establishing a *provable* quantum advantage on quantum computers that might one day outperform the most powerful classical computers. The protocol implemented here incorporates verification by repeatedly interleaving 'computation' and 'test' rounds; the latter use the same quantum resources as the former and are therefore indistinguishable from them by the server. A statistical argument provides bounds for the security and robustness of this protocol for the important class of BQP decision problems [Lei+21]. Accepting incorrect results would be considered a security issue, whilst a protocol that rejects all results cannot be considered robust against noise. The client accepts the result if the observed fraction of failed test rounds, p_{fail}, is below a chosen threshold, ω, which must itself be below the theoretical maximum, ω_{max}. If this condition is met, the overhead due to repetition is low: the probability of accepting an incorrect result decreases exponentially with the number of rounds. The minimum

value for ω depends on the amount of noise in the devices. The client assumes a maximum expected test round failure rate, $p_{\max}$, and chooses $\omega > p_{\max}$ such that the probability of rejecting any result also decreases exponentially with the number of rounds, making the protocol robust to a limited amount of noise. Therefore it is important that any real apparatus has sufficiently low noise to satisfy $p_{\max} < \omega_{\max}$.

6.2 Experimental implementation

In this implementation of BQC, the client measures the photonic half of an ion-photon Bell state, which steers the ion remotely into a state only known to the client (Section 6.3). The complexity needed for universal quantum computation is contained entirely within the server, while the client is a simple photon polarisation measurement device that is independent of the size and complexity of the algorithm and supports near-perfect blindness by construction (Section 6.5). The client and the server are controlled by independent hardware and connected only by a classical signalling bus and an optical fibre.

Figure 6.6 illustrates our scheme: the server holds $m + 1$ physical qubits, one of which is the network qubit which can be prepared remotely by the client, and the remaining m memory qubits form a quantum register. To delegate a computation, the client builds up a virtual[2] $m \times d$ universal cluster state (e.g. a brickwork state) in the server by steering qubit by qubit remotely over the quantum link, and instructing the server to swap the state of this (network) qubit with the trailing memory qubit in the register. That way, the trailing qubit becomes the leading qubit and the network qubit becomes the trailing qubit, which is next in line to be measured. The measurement angles are provided by the client who follows the MBQC representation of the target computation. After this measurement, the network qubit is again available for RSP in the next iteration.

In Figure 6.7 we illustrate our implementation of blind quantum computing on linear cluster states ($m = 1$). Two physical qubits are sufficient to implement

[2]To highlight that only one layer of the cluster state is physically retained, qubits that have already been measured as part of the MBQC algorithm are shown as virtual qubits. The cluster state is continuously rebuilding and never exists in physical form at any one time.

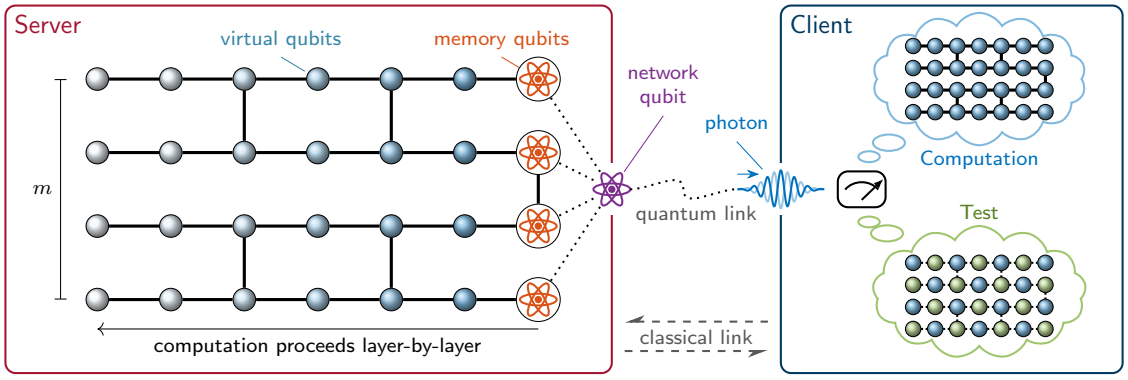

Figure 6.6: Verifiable blind quantum computing in the MBQC model. The computation is expressed as a sequence of measurements on a brickwork state (two-dimensional graph with vertices representing virtual qubits, and edges indicating CZ gates). The server (left) holds m physical memory qubits (orange atoms) and one physical network qubit (violet atom). The server can entangle these qubits deterministically with each other. The network qubit can also be entangled with a photon; by measuring this photon, the client (right) can steer the network qubit in the server remotely without the server learning about its state. This allows the client to hide the computation (inputs, outputs, and circuit) from the server. Moreover, the client can verify that the computation has not been tampered with by interleaving test rounds, which produce classically simulatable outcomes and cannot be distinguished from the actual computation by the server.

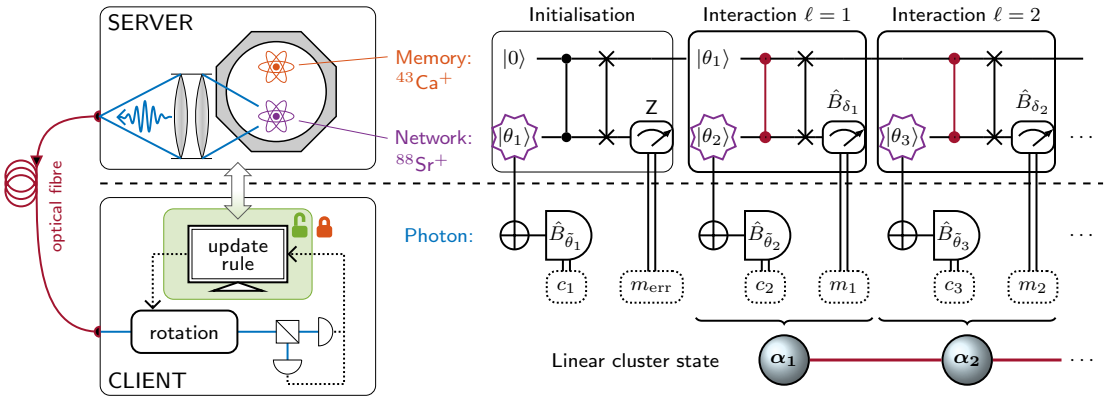

Figure 6.7: Protocol used to generate a linear cluster state using a trapped-ion quantum network node and a photonic client. As the network qubit (violet, $^{88}Sr^+$ ion) is entangled with the emitted photon, the client can steer the state of the network qubit by measuring the polarisation of the photon. The outcome $a_\ell \in \{0, 1\}$ of a polarisation measurement in the basis $\hat{B}_{\tilde{\theta}_\ell}$ steers this qubit into the state $|\tilde{\theta}_\ell + a_\ell \pi\rangle$. In the initialisation step, the server transfers this state, $|\theta_1\rangle$, onto a memory qubit (orange, $^{43}Ca^+$ ion) such that the network qubit can be steered again [Drm+23]. Every subsequent interaction step extends the size of the cluster state; the client steers the network qubit remotely into $|\theta_{\ell+1}\rangle$, the server entangles it (red CZ gates), and performs a measurement in the basis $\hat{B}_{\delta_\ell}$, where δ_ℓ is provided by the client.

linear clusters of arbitrary length, as qubits can be reinitialised after every mid-circuit measurement. The first qubit – the network qubit – can be steered into an arbitrary state by the client using RSP [Ben+01] (Section 6.3), while the second qubit – the memory qubit – carries the information encoded in the leading node of the expanding linear cluster state.

To blindly run the measurement-based protocol outlined in Section 6.1.1 with measurement angles α_ℓ, the client performs RSP into superposition states, $|\theta_\ell\rangle = Z(\theta_\ell)\,|+\rangle$, with secret random phase reference, $\theta_\ell \in \Theta$, for every qubit $\ell = 1, 2, \ldots, q$ in the cluster computation. To ensure that the measurement outcomes, $m_\ell \in \{0, 1\}$, are maximally mixed, the client hides bit flips in half of the measurement angles that are indicated by secret key bits, $r_\ell \in \{0, 1\}$ (Equation (6.1)). The client can recover the unencrypted measurement outcomes as $m_\ell \oplus r_\ell$.

We break the cluster state into discrete interaction steps between the server and the client, starting after the initialisation step (see Figure 6.7), which prepares the memory qubit in $|\theta_1\rangle$. At each interaction of a computation round, indexed by ℓ, the client performs RSP to steer the network qubit into $|\theta_{\ell+1}\rangle$ and communicates

$$\delta_\ell = (-1)^{R_{\ell-1}}\alpha_\ell + \theta_\ell + \pi r_\ell \tag{6.1}$$

to the server, where $R_\ell = \bigoplus_{1\leq j<\ell/2}(m_{\ell-2j} \oplus r_{\ell-2j})$ is the adaptive feedforward correction from decrypted previous measurements. The server applies an iSWAP gate, which is equivalent to the CZ gate followed by a SWAP, but requires only two instead of four native CZ gates. Thereafter, the server measures the network qubit in the $\hat{B}_{\delta_\ell}$ basis and returns the result, m_ℓ, to the client (interaction blocks in Figure 6.7). In computation rounds, the memory qubit state after q interactions is given by

$$|\psi_{q+1}\rangle = Z(\theta_{q+1})\mathsf{X}^{R_q}\mathsf{Z}^{R_{q-1}}\left(\mathsf{H}Z(\alpha_q)\cdots\mathsf{H}Z(\alpha_1)\right)|+\rangle \ .$$

This state is left on the memory qubit, while the network qubit is available for further RSP. To complete the cluster computation, the client needs to specify the angle δ_{q+1} for a final measurement of the memory qubit.

The client randomly assigns each round a secret label identifying them as a computation or a test, where the optimal proportion of rounds which are tests depends on the protocol parameters [Lei+21]. In test rounds, trap qubits are prepared in $|\theta_\ell\rangle$ and adjacent dummy qubits in the Z basis eigenstate $|r_\ell\rangle$. This step disentangles adjacent trap qubits, enabling the client to predict their outcomes, $m_\ell \stackrel{!}{=} r_\ell$, if they are measured with $\delta_\ell = \theta_\ell + \pi r_\ell$.

6.3 Remote state preparation

The client receives single photons from the server through an optical fibre. The quantum capability of the client is reduced to projective polarisation measurements of these photons in a basis that can be dynamically changed using a fast-switching polarisation analyser (Chapter 3.3). This polarisation analyser can be configured to perform an arbitrary polarisation rotation by changing the voltages on two EOMs. Following this rotation, a PBS and two APDs implement the polarisation measurement. This measurement remotely steers the network qubit into a state that depends only on the polarisation measurement basis and the measurement outcome obtained, information known exclusively to the client ($\tilde{\theta}_\ell$ and a_ℓ in Figure 6.7).

As the fibre connecting the server and the client is naturally exposed to changes in temperature and strain, its birefringence needs to be calibrated periodically. In order to do so, the client instructs the server to perform X-, Y- and Z-basis measurements for EOM voltages on a regular 21×21 grid, in random overall order. Ion readout results are inverted for heralds in APD s and combined with results for APD p.[3] Let $\Sigma^{\mathsf{B}}_{|y\rangle}$ denote the number of readout observations with outcome $y \in \{s, p\}$ when measured in the $\mathsf{B} \in \{\mathsf{X}, \mathsf{Y}, \mathsf{Z}\}$ basis. Direct inversion tomography is used to reconstruct the Bloch vector $\vec{b} = (b_\mathsf{X}, b_\mathsf{Y}, b_\mathsf{Z})$ with components

$$b_\mathsf{B} = \frac{\Sigma^{\mathsf{B}}_{|1\rangle} - \Sigma^{\mathsf{B}}_{|0\rangle}}{\Sigma^{\mathsf{B}}_{|1\rangle} + \Sigma^{\mathsf{B}}_{|0\rangle}} \,.$$

[3] This step leads to a reduction in RSP fidelity if the states created by different heralds are not exactly orthogonal, for example due to a systematic delay mismatch in the heralding signal chains (see Figure 6.10(a)) At the time the experiments were performed, this resulted in $\sim 5\,\%$ infidelity in each qubit in the cluster state.

The client then determines the EOM voltage settings which minimise the angular deviation of $\vec{b}$ from the axis on the Bloch sphere corresponding to each of the 5 target bases required during the verifiable blind quantum computing protocol.

To analyse the performance of RSP, we reconstruct the steered state of the network qubit using maximum likelihood tomography [Řeh+07] and evaluate the fidelity to each of the target states needed for the verifiable blind quantum computing (VBQC) protocol. The average fidelity of steering superposition states, $|\theta\rangle$, and of steering Z basis eigenstates, $|z\rangle$, where $z \in \{0, 1\}$, is shown in Figure 6.8. The

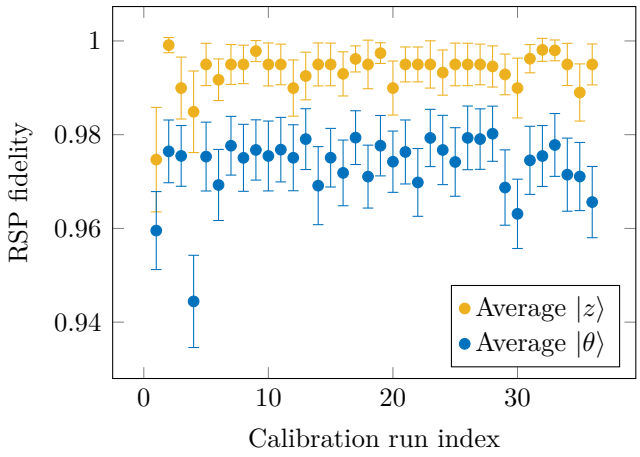

Figure 6.8: Fidelity of the remotely steered states obtained from 36 calibration runs over a period of ~ 2 weeks. The fidelity is averaged over $z \in \{0, 1\}$ and $\theta \in \Theta$ as we assume the dominant error channels are depolarising and dephasing, which are independent of polarity and phase, respectively.

RSP fidelity of superposition states, 0.973(7), is smaller compared to the 0.996(3) fidelity of Z basis eigenstates due to dephasing processes in the system. The effect of magnetic field noise is expected to contribute negligibly to this error, as independent measurements on the $^{88}Sr^{+}$ network qubit yield a coherence time of ~ 1 ms, which is orders of magnitude longer than the delay between an RSP herald and the qubit measurement. Therefore, we believe that the dephasing that we observe is rooted in the photonic part of the system.

6.4 Results

We realise different quantum computations with one and two interaction steps, see Figure 6.9(a) and Figure 6.9(b), respectively. We could use the output qubit in

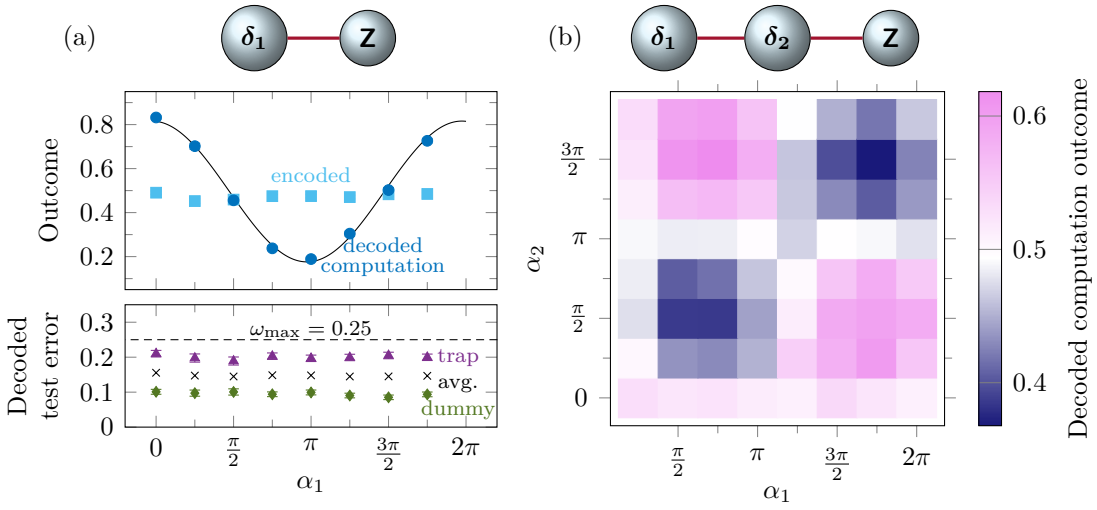

Figure 6.9: Experimental results on an expanding linear cluster state, where the leading qubit is measured in the Z basis after (a) one interaction step, and (b) two interaction steps between the client and the server. (a) While the server observes mixed outcomes (squares), the client can decode the results using the secret keys. A fit to the decoded computation outcomes (circles) is shown to guide the eye. The expected average test round error for the two-node cluster state (crosses) is below the threshold for verification (dashed line). Error bars indicate binomial standard errors. (b) The decoded computation outcome is shown as a function of blind measurement angles α_1 and α_2.

further interaction steps, or make a final measurement in the basis $\hat{B}_{\delta_{q+1}}$ to complete the $(q+1)$-node cluster computation. In this demonstration, however, the output qubit is always measured in the Z basis. Since this measurement commutes with the CZ gate preceding it, the computation result is equivalent to the result for a cluster state with one fewer node. The actions of the one- and two-step interactions are therefore given by the computations $\mathsf{H}Z(\alpha_1)\,|+\rangle$ and $X(\alpha_2)Z(\alpha_1)\,|+\rangle$, respectively, where H is the Hadamard gate, $X(\alpha) = \exp(-\mathrm{i}\frac{\alpha}{2}\mathsf{X})$ and $Z(\alpha) = \exp(-\mathrm{i}\frac{\alpha}{2}\mathsf{Z})$ are single-qubit rotations, and α_1 and α_2 are encrypted using Equation (6.1) during the protocol. From the server's perspective, the outcomes appear random (see squares in Figure 6.9(a)) as a result of the bit-flip encryption, $\delta_\ell \propto r_\ell \pi$, which is applied by the client in both the computation and test rounds. The client on the

other hand can use the round type (computation or test) and encryption key (r_ℓ) to decode the outcomes. The decoded computation outcomes indicated by the circles in Figure 6.9(a) and the colourmap in Figure 6.9(b) match the expected fringe pattern as a function of the blind measurement angles α_1 and α_2. Experimental imperfections lead to a reduction in contrast and to phase shifts. The fraction of failed tests (see bottom panel in Figure 6.9(a)) is nevertheless low enough to perform a fully verified two-node cluster computation: we observe an error rate of $p_{\text{fail}}^{\text{trap}} = 0.201(3)$ on the trap qubit. Due to the Z basis measurement performed on the final (dummy) qubit, the correctness of the dummy qubit can be verified in the same test round: we obtain $p_{\text{fail}}^{\text{dummy}} = 0.095(2)$.

For a complete two-node cluster computation, the final measurement basis would need to be changed from Z to $\hat{B}_{\delta_{q+1}}$, which would require only one additional $\pi/2$ pulse and would have no significant impact on the error budget. With this adaption, all qubits would be measured in a rotated basis, $\hat{B}_{\delta_\ell}$, and the client would choose between three distinct round types: the computation, where both qubits are prepared in a superposition state ($|\theta_\ell\rangle$), and two different test rounds, where either the first or the second qubit is prepared in a Z eigenstate (dummy). Even though the experiment presented above deviated from that protocol and was able to combine verification of both qubits in a single test round, the measured failure rates are indicative of the expected average test round failure probability for the complete two-node cluster state. We predict an average ~ 0.15 probability of failure in any given test round, which is significantly below $\omega_{\max} = 0.25$ required for secure and robust verification of the linear cluster state with two nodes. In the case of the three-node cluster computation, the observed failure rates (first qubit: 0.30(6), second qubit: 0.48(7), and third qubit: 0.13(5)) indicate that verification is not possible in this case, largely due to technical limitations on the ≈ 0.91 fidelity of the iSWAP gate (see Section 4.4.5).

Data handling. We make extensive efforts to conduct our experiments under conditions that are representative of a real deployment. The client and the server

are controlled by independent personal computers and hardware from the ARTIQ open-source control system (see Section 3.4.1). The experiment and calibration schedule is coordinated over Ethernet. For timing-critical communication, such as the interaction during the protocol, low-latency electronic signals are used. Throughout the data acquisition and analysis process, the client does not reveal any protocol secrets to the server.

Error detection. Errors during the initialisation step are detected in real time ($m_{\text{err}} = 1$ in Figure 6.7, error probability ~ 0.1) in which case the current round is aborted and restarted after a period of cooling [Drm+23]. The overhead due to repetition of this step is independent of the size of the cluster state and hence does not affect the scalability of the implemented protocol. Here, the client can keep the same random variable $\tilde{\theta}_1$ because the phase shift $a_1\pi$ depends on the photon polarisation measurement outcome, which is inherently random. The server therefore obtains a maximally mixed state on the network qubit. Information leaking through classical communication as a result of reusing $\tilde{\theta}_1$ could also be eliminated, as the client is in control of all relevant signals. The error detection probability is closely related to the iSWAP infidelity; by reducing this infidelity, error detection would become obsolete.

Photon loss. The average time taken to obtain a single-photon herald is $\approx 100\,\mu\text{s}$; hence the probability for no herald to occur within the timeout period of 1 ms is $< 10^{-4}$. If no photon is received within this period, the client instructs the server to repeat the current round starting from the initialisation step after a series of system checks. The timeout allows the server to recover from rare events that could temporarily hinder the generation of single photons, such as ion loss, misalignments in the photon collection optics, or laser failures. The information leakage due to repetition in these rounds is purely classical and could be eliminated by the client, who is in control of all relevant signals. Alternatively, the client could introduce fresh randomness at every retry to avoid this issue. The loss of determinism due to photon loss is influenced by the timeout period and could be completely eliminated if the

client continued execution of the protocol despite an unsuccessful steering attempt. In this case, the server would check for system failures after the client has completed this round of the protocol. The computational error that is incurred by this approach due to photon loss would reduce exponentially with increasing timeout period.

6.5 Quantifying blindness

Here we consider experimental imperfections that could adversely affect the blindness of the protocol. Blindness is characterised by how much information an adversarial server could learn about the client's photon measurement basis choices θ_ℓ (3 bits of information per shot). At every shot of the experiment, indexed by ℓ, we assume that the server has unrestricted access to

- the qubit measurement angle δ_ℓ (classical signal),
- the phase reference set by the photon detection time (classical signal),
- the number of attempts until a single-photon herald (classical signal),
- and the state of the memory and network qubits.

Blindness is compromised if the above observables correlate with θ_ℓ. We distinguish between information leaked via the network qubit, which is controlled by the server (see Section 6.5.2), and leakage through classical signals, which are controlled by the client (see Section 6.5.1). In our demonstration, mismatched electronic delays between heralds corresponding to different polarisation measurement outcomes are the dominant cause for information leakage in both these cases (see Table 6.1 for a quantitative summary). However, as the client is in full control of the relevant classical signals, these issues could be eliminated and information leakage to the server could be reduced to ~ 0.001 bits per interaction step. The remaining leakage would be dominated by imperfections in the polarisation optics used by the client to perform the polarisation measurement.

Channel	Source	Method	Leakage / bits	
			Observed	Optimised
classical	measurement angles	enforced	0	0
	heralding efficiency	inferred	0.00006	0.00006
	heralding delay	inferred	0.35	0.00007
quantum	measurement basis	inferred	0.035	0.0007
	imbalanced outcomes	inferred	0.00029	0.00026
	—	measured	0.031(4)	—

Table 6.1: Sources of information leakage. The optimised values assume matching heralding delay (from excitation of $^{88}Sr^{+}$ until electronic detection) and balanced polarisation measurement outcomes. We analyse the steered qubit to quantify the accessible information content and find good agreement with independent estimates inferred from known imperfections (measurement basis, imbalanced outcomes). The values are to be compared with the number of bits of information (3 bits) that specify the steered state, $|\theta_\ell\rangle$.

6.5.1 Classical information leaks

In this section, we analyse the effect of classical sources of information leakage that are present in our system. These sources do not include side-channel attacks, which are in general difficult to treat systematically. We note that, in a real deployment, the client could straightforwardly monitor and eliminate leakage on all classical channels.

Encrypted measurement angle. δ_ℓ does not leak information because it is encrypted with private randomness at every shot by the client. We note that the use of a pseudo-random number generator does not compromise blindness (against computationally-bounded adversaries) provided that its implementation is cryptographically secure.

Single-photon heralding delays. The arrival time of photons at the APDs with respect to the pulsed excitation of $^{88}Sr^{+}$, is inherently random due to the nature of spontaneous decay. As these heralding times set the phase reference for the network qubit, they must be communicated to the server. Statistical differences between the herald timing distributions could therefore be exploited by the server to learn about the polarisation measurement outcome.

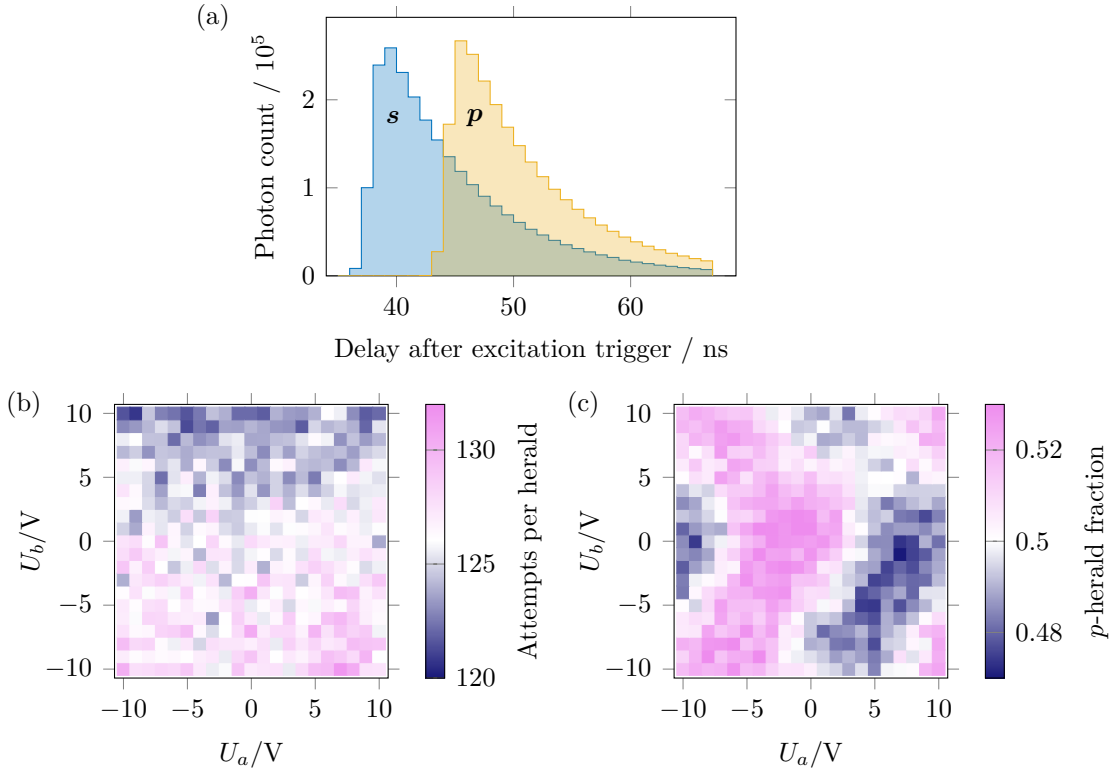

Figure 6.10: (a) Histogram of delay between pulsed excitation of $^{88}Sr^+$ and a single-photon herald from detectors s and p. (b) Average number of attempts (1 µs per attempt) until a single-photon herald is announced by the client as a function of EOM control voltages. (c) Ratio of heralds with outcome p with respect to all heralds as a function of EOM control voltages.

The server could employ a maximum-likelihood strategy to guess the photon measurement result. The detector properties may be known to the server. This includes the probability distributions $\Pr_s(x)$ and $\Pr_p(x)$ for a herald at time x in detector s and detector p, respectively. The server would assume that a photon heralded at time x was observed in detector s if $\Pr_s(x) > \Pr_p(x)$, and vice versa. This maximum-likelihood strategy succeeds with probability $\sigma(x)$. The expected information gain is given by $\mathcal{R}_{\mathrm{ML}} = \sum_x \Pr(x)\mathcal{R}(\sigma(x))$, where $\mathcal{R}(q) = 1 + q\log_2(q) + (1-q)\log_2(1-q)$ is the mutual entropy for a binary guess with success probability q, and $\Pr(x)$ is the overall probability of observing the arrival time x.

In this demonstration, no measures were taken to equalise the detector responses of the APDs. Observed differences (see Figure 6.10(a)) are mainly due to unmatched delays in the electronic signal chain, by 6.57(2) ns, leading to $\mathcal{R}_{\mathrm{ML}} \approx 0.35$ bits

information leakage. This imperfection could be minimised by adding delay to one of the signals (e.g. by extending the cable by $\approx 1.3\,\mathrm{m}$). After correcting for the delay mismatch, the information content would be reduced to $\mathcal{R}_{\mathrm{ML}} \approx 7 \times 10^{-5}$ bits, dominated by higher-order electronic distortion, such as differences in timing jitter between the electronic inputs used for timestamping. Here, a field-programmable gate array is used for timestamping; it only provides 1 ns resolution, with inconsistent jitter between input pads. We note that this is not a fundamental limitation and leakage of this kind could be eliminated by the client by appropriately conditioning the classical heralding signals.

Single-photon heralding probability. As the client publicly announces when a photon was successfully heralded, the server learns about the number of attempts taken, hence the detection efficiency, of the client apparatus. If the detection efficiency depends on the secret measurement settings chosen by the client, the server could, in principle, obtain information that would compromise the blindness of the protocol. Here we analyse the extent to which this affects our demonstration of blind quantum computing.

We observe variations in the detection efficiency depending on the EOM voltage settings of $\approx \pm 5\,\%$ (see Figure 6.10(b)). The EOM voltages are changed after every photon received by the client.[4] Therefore, the server obtains only one attempt-number sample per measurement setting. At every shot, the server's *a priori* knowledge is reset, due to this shot-by-shot randomisation, to the exponential distribution with an expectation value λ_0 estimated from the number of attempts in previous shots. The Fisher information, $\mathcal{I}(\lambda) = \lambda^{-2}$, quantifies the information each sample contributes towards an updated estimate of the underlying distribution, i.e. the exponential distribution for this shot with secret-dependent expectation value

[4] In $\lesssim 5\,\%$ of cases in the present implementation, retries (due to errors in the initialisation step, with probability ~ 0.1, and failures to produce a single-photon herald within the time-out interval, with probability $< 10^{-4}$) were performed without the client changing the measurement settings. However, this additional information does not change the conclusion of this analysis and the issue could be eliminated by introducing fresh randomness at every retry as well.

λ. This quantity needs to be compared to the relative entropy, $\mathcal{S}(\lambda_0, \lambda)$, between the exponential distributions with respective expectation values λ and λ_0.

For the observed average number of attempts, $\lambda_0 = 126$, and the maximum deviation $\Delta\lambda = |\lambda - \lambda_0| = 6$, the information gained per shot, $\mathcal{I}(\lambda) \lesssim 10^{-4}$, is negligible. Even if unlimited attempt-number samples were available for a given measurement setting, the information gain by the server could never exceed $\mathcal{S}(\lambda_0, \lambda) \sim 10^{-1}$ bits.

6.5.2 Quantum information leaks

We analyse the information which the server could gain on average from measuring the network qubit after RSP in terms of the Holevo bound χ. For perfect blindness, $\chi = 0$, whereas one qubit can maximally transmit $\chi = 1$ bit. The server receives quantum states that are generated by steering of the network qubit. For every qubit in the computation, the client chooses secretly one of 4 measurement bases[5], $\hat{B}_i$, $i \in \{1, 2, 3, 4\}$, to steer the network qubit into ρ_i^+ with probability q_i or ρ_i^- with probability $(1 - q_i)$, depending on the measurement outcome. Averaged over the outcomes[6], the server receives the states $\rho_i = q_i\rho_i^+ + (1-q_i)\rho_i^-$ with equal frequency:

$$\rho = \frac{1}{4}\sum_{i=1}^{4} \rho_i \ .$$

The Holevo information, which bounds the amount of information contained in this quantum state, is given by

$$\chi(\rho) = S(\rho) - \frac{1}{4}\sum_{i=1}^{4} S(\rho_i) \ ,$$

where $S(\rho) = -\mathrm{Tr}\left(\rho \log_2(\rho)\right)$.

In our experiment, ρ_i^+ and ρ_i^- are steered by the measurement of an entangled subsystem (a photon), which can be described using POVMs. We use the maximally-entangled Bell state $\frac{1}{\sqrt{2}}(|s\rangle|0\rangle + |p\rangle|1\rangle)$ between the photon and the environment to simulate RSP.

[5]This excludes test rounds, where the client steers the network qubit into a Z basis eigenstate, which strictly reduce the Holevo information, as no θ_ℓ is defined for these 'dummies' to correlate with.

[6]If the basis angle θ_ℓ is leaked, a simple measurement of the network qubit deterministically reveals also the client's measurement outcome.

Imbalanced and mixed outcomes. We estimate the blindness of RSP using the POVMs $\{\hat{F}\}$ describing a PBS with extinction ratios ϵ_s and ϵ_p for s- and p-polarised input, and two APDs that are placed in the (ideally) s- and p-polarised output ports of the PBS, characterised by detection efficiencies η_s and η_p, respectively:

$$\begin{aligned}\hat{F}_p &= \eta_p(1-\epsilon_s)\,|p\rangle\langle p| + \eta_s\epsilon_p\,|s\rangle\langle s| \ , \\ \hat{F}_s &= \eta_s(1-\epsilon_p)\,|s\rangle\langle s| + \eta_p\epsilon_s\,|p\rangle\langle p| \ , \\ \hat{F}_0 &= 1 - \hat{F}_p - \hat{F}_s \ ,\end{aligned}$$

where $\hat{F}_p$ and $\hat{F}_s$ correspond to photon detection in APD p and APD s, respectively, and $\hat{F}_0$ corresponds to a photon loss event. As long as PBS imperfections act as depolarising noise, such as for finite polarisation extinction, these effects have no effect on the Holevo information. We may therefore assume without loss of generality $\forall i$ that ρ_i^+ and ρ_i^- are orthogonal pure states, which occur with probability $q_i = \frac{\eta_p}{\eta_p+\eta_s} \approx \frac{1}{2}$. Choosing the more favourable configuration of measurement bases[7], the average information contained in one qubit is bounded from above by

$$\chi = \frac{(6-\sqrt{2})\left(q-\frac{1}{2}\right)^2}{4\log_2(2)} + \mathcal{O}\left(\left(q-\frac{1}{2}\right)^4\right) \ .$$

With the average imbalance $\langle|0.5-q|\rangle_{U_a,U_b}$ derived from measurements shown in Figure 6.10(c) and specified in the main text, we infer that the information leakage due to this effect is $\chi \approx 2.9\times10^{-4}$ bits. Even if static photon loss is introduced to balance the detection efficiency on both detectors, the secret-dependent variation remains the dominant source of leakage: we estimate $\chi \approx 2.6\times10^{-4}$ bits for this scenario. While the origin of the variations shown in Figure 6.10(c) has not been confirmed, we suspect that the EOMs disturb the wavefront of the photons, which affects the mode matching into the optical fibres that are used for convenience to couple the photons into the APDs. Because the quantum information is encoded in the polarisation of the photon, their spatial mode is irrelevant to our implementation,

[7]It is less favourable to let $\rho_j^+ = |j\pi/4\rangle\langle j\pi/4|$, as the error due to imbalanced rates adds constructively. However, using $\{\rho_1^+,\rho_2^-,\rho_3^+,\rho_4^+\}_j = |j\pi/4\rangle\langle j\pi/4|$ for example, part of the error cancels.

rendering this observation of voltage-dependent imbalance of heralds practically insignificant. Alternatively, this source of leakage could be eliminated fully if the client conditioned heralds on local randomness (at the cost of a 50 % reduction in the total heralding rate).

Rotated POVMs. Using the POVMs in the product space of the photon polarisation and the network qubit,

$$\begin{aligned}\hat{G}_p &= \hat{F}_p \otimes 1 \ , \\ \hat{G}_s &= \hat{F}_s \otimes \hat{Z}(\phi) \ , \\ \hat{G}_0 &= (1 \otimes 1) - \hat{G}_p - \hat{G}_s \ ,\end{aligned}$$

the Holevo information can be approximated by $\chi \approx 0.103 \times \phi^2$.

The electronic signal delay between orthogonal heralds shown in Figure 6.10(a) not only leaks information via the classical reference time signal, but also causes a relative Z rotation of the network qubit depending on the photon measurement outcome. Inserting $\phi = \Omega_Z \Delta t$, where $\Omega_Z \approx 2\pi \times 14\,\mathrm{MHz}$ is the $^{88}\mathrm{Sr}^+$ Zeeman qubit splitting and $\Delta t = 6.57(2)\,\mathrm{ns}$ is the measured delay difference between the two heralds (see Figure 6.10(a)), we obtain $\chi \approx 0.035$ bits.

Once the heralding delays are matched, imperfections in the photon polarisation measurement are expected to dominate information leakage through this channel. Using the average overlap of 0.0016 between projectors corresponding to different heralds (see Figure 3.20), we obtain $\phi \approx 0.08\,\mathrm{rad}$, resulting in $\chi \approx 7 \times 10^{-4}$ bits of potential information leakage.

Alternatively, rather than relying on the orthogonality of the polarisation measurement, the client could exploit the fact that every polarisation measurement basis can be reached by two distinct EOM voltage settings and switch randomly between them. The effectiveness of this approach would depend on the accuracy of the voltage calibration, which could be increased by acquiring calibration data with sufficient precision.

6.6 Summary

We have implemented a protocol for blindly delegating quantum computations to a trapped-ion quantum processor, using a client apparatus that requires only single-photon polarisation measurements and classical communication (Section 6.2). We have established bounds on the information that could leak to the server through both the classical and quantum channels that are present in our implementation (Section 6.5) and devised strategies to minimise all known sources of leakage. We have shown that the size of the cluster state can be increased without increasing the number of physical qubits in the server and without modifications to the client hardware (Section 6.4). If more memory qubits were added to the server [Wri+19], the computational space could be extended to higher-dimensional cluster states.

We have taken steps to include verification into the protocol, and the measured test round error indicates that the system noise is low enough to perform a fully verified computation on the two-node cluster state robustly and reliably. For a threshold $\omega = 0.18$ and $n = 20\,000$ repetitions (including 9800 test rounds), we predict that the probability of accepting an incorrect result of a BQP decision problem with small inherent algorithmic error would be 3×10^{-9}, and the probability of rejecting any result 2×10^{-9}. This approach is expected to provide both security and robustness for larger cluster states and other algorithms as long as the errors remain below the size-dependent threshold, $\omega_{\max} \approx 1 - (3/4)^{2/q}$, where q is the total number of qubits in the cluster state (see Figure 6.11). The protocol that we have implemented does not incorporate error correction; to verify larger cluster states, the error per interaction step would need to be reduced. The infidelity of the iSWAP gate is the leading error source, but we note that in other systems, CZ gates between $^{88}Sr^{+}$ and $^{43}Ca^{+}$ with fidelity 0.998 have been demonstrated [Hug+20]. The state-of-the-art ion-photon entanglement fidelity of 0.979(1) (this apparatus) is limited primarily by technical imperfections in the optical setup.

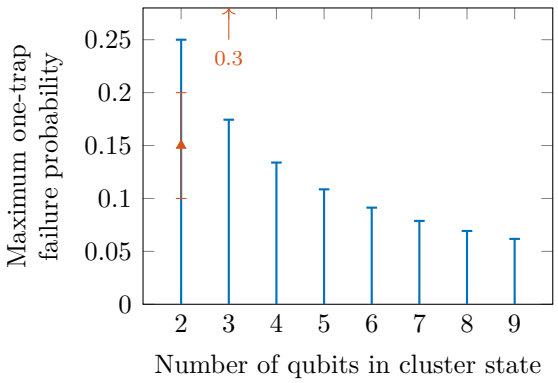

Figure 6.11: If the average trap failure rate is below the threshold of 0.25, there exist parameters that make the protocol both secure and robust [Lei+21]. We plot here the maximum one-trap failure rate such that the average test failure rate remains below this threshold, for varying size of the cluster state. Red marks indicate this work's predicted average failure probability.

The photonically-interfaced trapped-ion quantum information platform demonstrated here paves the way for secure delegation of confidential quantum computations from a client with minimal quantum resources to a fully capable, but untrusted, quantum server. In comparison with previous experimental implementations of BQC [Bar+12; Bar+13; Fis+14; Gre+16], which were based on purely photonic platforms without quantum memory, this work overcomes several major challenges associated with real-world BQC deployments. As quantum logic operations in the server are deterministic and the interaction with the client is heralded, our implementation eliminates the need for post-selection, avoiding the associated efficiency, scalability, and security issues [Bar+12; Bar+13; Gre+16]. Here, photon losses in particular do not present a security threat, and the use of a memory qubit combined with fast and adaptive hardware facilitates true shot-by-shot randomisation of all protocol parameters in real time.

7 Outlook

In this thesis I have presented work on the first trapped-ion-based quantum network node integrating a memory qubit with a photonic interface (Chapter 5), and have shown the first hybrid matter-photon implementation of BQC using this system (Chapter 6). The methods involved in these applications have been developed separately over many years. In particular, manipulation of $^{43}Ca^{+}$ with high fidelity had been perfected [Har+14; Bal+16; Sep+19] and high-fidelity mixed-species operations between $^{88}Sr^{+}$ and $^{43}Ca^{+}$ ions had been established [Sch18; Thi19; Hug+20] before I started this project. This is the first time that these tools are combined with IPE in a 'full-stack' quantum network node. With BQC, this platform has already demonstrated a practically relevant application in the field of secure cloud computing and verification [Drm+24]. However, several improvements can be made to further increase the impact of our demonstration:

- **Ion trap.** The biggest limitation to our network node is the infidelity of quantum gates, which is due to high heating rates (see Section 4.1.2) intrinsic to the ion trap used here. Our second network node has recently been upgraded by replacing the HOA2 trap by the Phoenix trap.[1] Preliminary measurements of the heating rate of the axial mode of a $^{88}Sr^{+}$ ion at 1.43 MHz

[1] Both traps are supplied by Sandia National Laboratory.

yield $\dot{\bar{n}}_z = 415(20)\,\mathrm{s}^{-1}$ in the Phoenix trap, which is ~ 8.5 times lower than in the HOA2 trap. With this improvement, we expected to significantly reduce the infidelity of two-qubit gates, thus enabling more advanced algorithms to be performed in this system.

- **State transfer.** The 2 % infidelity due to the transfer pulse sequence from the logic qubit to the memory qubit in $^{43}Ca^{+}$ constitutes the second-largest error source in our mixed-species network node. Using a 729 nm quadrupole laser, the sequence of 9 Raman laser pulses that is currently used (see Section 5.1.2.2) could be replaced by a sequence of 4 quadrupole laser pulses. This would also eliminate the complication of near-resonant transitions within the ground state hyperfine structure. Alternatively, the optical qubit could be used instead of the memory qubit, which would eliminate the need for transfer pulses (see below).

- **Protocol.** In the experiment described in Chapter 6, we performed a Z basis measurement on the final qubit in the cluster state, which commutes with the CZ gate preceding it. This effectively reduces the length of the cluster state by one, but the error due to the additional CZ gate remains. It is therefore preferable to change the final measurement basis to $\hat{B}_{\delta_q}$.

- **Blindness.** Based on the estimates presented in Chapter 6.5, our client currently leaks 0.35 bits per node in the cluster state – a significant fraction of the 3 bits of information required to completely describe the computation. With minor adjustments (matching the length of heralding cables), we expect this leakage to reduce to 0.001 bits per node in the cluster state.

- **Randomness.** The use of a pseudo-random number generator by the client to generate the private key constitutes an unnecessary security issue that can easily be resolved by using a commercial quantum random number generator instead.

- **Memory.** As linear cluster states can only implement single-qubit rotations, *universal* BQC requires at least one additional memory qubit. At least two memory qubits are required in the server to generate two-dimensional cluster states using our protocol (see Figure 6.6). Adding more $^{43}Ca^{+}$ ions to the server requires no changes to the existing apparatus; we have already demonstrated the necessary ion transport techniques (see Section 3.2) and CZ gates between two $^{43}Ca^{+}$ ions (see Section 4.3) in this system.

Future realisations of BQC could involve a complex network of servers and clients. Photons could be routed to a number of clients using optical switches, and the distance to the server increased using frequency conversion of the photons to telecommunication wavelengths [Kru+19] or using recent developments in fibre technology [Fok+23].

Calcium quadrupole laser. Our apparatus will soon have access to a 729 nm laser to address the $S_{1/2} \leftrightarrow D_{5/2}$ quadrupole transition of Ca^{+}. Using this laser has several advantages. First, Protocol 3.1.2 for shelving of $^{43}Ca^{+}$ can be replaced by a single π pulse on the 729 nm transition. As a result, the 393 nm and 850 nm lasers are no longer needed. Secondly, at magnetic field strengths of 0.338 mT and 0.496 mT, the optical qubit $|{\downarrow_O}\rangle = |S_{1/2},\, F=4,\, m_F=4\rangle \leftrightarrow |{\uparrow_O}\rangle = |D_{5/2},\, F=4,\, m_F=3\rangle$ in $^{43}Ca^{+}$ is insensitive to magnetic field fluctuations to first order [Ben+07]. As the optical qubit states lie in different manifolds, the light shift force can be non-zero despite this 'clock' qubit property.[2] This enables the direct use of the $\hat{W}_{ZZ}$ gate described in Section 4.2 and eliminates the need for transfer pulses in cases where the ~ 1 s lifetime of the $D_{5/2}$ level is sufficient.

[2]For hyperfine ground state 'clock' qubits, the light shift force is always zero. In our implementation without the 729 nm laser, we therefore need to transfer the state to an intermediate qubit for performing two-qubit gates and back for storage (see Section 5.1.2.2).

7.1 Quantum network applications

The trapped-ion 'server' used in the BQC demonstration presented in Chapter 6 is part of a quantum networking apparatus [Ste+20] that was designed to generate remote entanglement between $^{88}Sr^{+}$ ions trapped in separate systems, to swap this entanglement locally to $^{43}Ca^{+}$ ions using mixed-species quantum gates, and to carry on from there using high-fidelity quantum logic with $^{43}Ca^{+}$ [Bal+16]. This system will form a proof-of-concept for an extensible network of quantum processors working together analogously to a classical computing cluster. While the work reported in this thesis was performed on only one of our two network nodes, namely Alice, the apparatus of the second node, Bob, was maintained to match the capabilities of Alice. So far, I only mentioned the topic of remote ion-ion entanglement en passant; remote entanglement is generated by swapping of IPE from the individual nodes onto the remote ions. This is done by bringing the photons together at a central point and measuring them jointly in a Bell basis. Using only a single $^{88}Sr^{+}$ ion in each node, we have established remote entanglement [Ste+20] of 96 % fidelity at a rate of $\sim 100\,\mathrm{s}^{-1}$ and used this entanglement to demonstrate device-independent quantum key distribution [Nad+22] and a network of entangled atomic clocks [Nic+22].

In the following, I briefly outline future experiments that we could perform in our apparatus, in order of increasing complexity. First, I describe how our apparatus could be used to study 'hidden non-locality'. Further, I explore applications that involve mixed-species remote entanglement between two nodes, each equipped with the tools presented in this thesis.

Hidden non-locality. *Local* quantum states cannot violate any Bell inequality under very general assumptions, such as describing the measurement using POVMs. However, there exist local states for which a sequence of such measurements can lead to maximal violation of a Bell inequality [Hir+13]. These states are attributed with 'hidden' non-locality. For an experimental demonstration of this property, three distinct steps are necessary. First, the preparation of the state must be performed separately from any subsequent analysis. Starting with a remote Bell

state in our networking apparatus, we can apply a deterministic state preparation procedure to transform this state into the chosen target state using only local operations. Secondly, the prepared state must be analysed in order to conclusively prove that it is indeed local. Quantum state tomography can be used to characterise the prepared state and evaluate its properties. Lastly, after the allowed sequence of generalised measurements, the violation of a Bell inequality must be shown with statistical significance.

Mixed-species remote entanglement. We can generate entanglement between different atomic species that are located in spatially separate ion trap systems. To do this, no changes are required to the experimental sequence described in Chapter 5, where we map IPE generated with $^{88}Sr^{+}$ to a $^{43}Ca^{+}$ ion within one quantum network node. However, instead of analysing the single photon from this node in isolation, a photonic Bell state measurement is performed with the photon from the second node to transform IPE into remote ion-ion entanglement.

As the probability for heralding this two-photon coincidence event is the square of the single-photon detection probability, we expect the contribution of pulsed excitation attempts to the heating rate (see Figure 5.7(c)) to become a significant limitation to the mixed-species gate fidelity. The possibility of tuning the frequency and the timing of the pulsed excitation laser to counteract the heating effect has been explored, but the efficiency of this method is poor [Bli+06]. It is therefore likely that the maximum number of pulsed excitation attempts has to be limited, and frequent intermissions of ground state cooling included, in order to limit the maximum temperature of the motion after entanglement generation.

Entangled optical atomic clocks. We have previously demonstrated a network of entangled atomic clocks [Nic+22], where we performed correlation spectroscopy on the 674 nm quadrupole transition of remote entangled $^{88}Sr^{+}$ ions. The precision of these measurements was limited by the ~ 20 ms coherence time of the optical qubit, where dynamical decoupling was already used extensively. By transferring remote entanglement to a $^{43}Ca^{+}$ ion in each node, correlation spectroscopy could

be performed on the optical clock transition at 729 nm. The measurement precision could then approach the limit imposed by the $\sim 1\,\mathrm{s}$ lifetime of the $D_{5/2}$ level.

7.2 Towards distributed quantum computing

Scaling trapped ion systems to large numbers of qubits, which is a requirement for practically relevant applications, continues to pose an outstanding challenge. A single potential well can only hold a limited number of ions and the motional mode structure becomes increasingly difficult to navigate as more ions are added. The quantum charge-coupled device (QCCD) [KMW02; Lek+17] and photonic interfaces [Moe+07; MK13; Mon+14; Huc+15] have been proposed to solve this problem.

In the QCCD architecture, ions are physically rearranged between different interaction zones within a large segmented trap structure. Recently, ion transport across chip boundaries has been shown in an attempt to bypass fabrication constraints [Akh+23]. However, nearest-neighbour routing constraints impose an algorithmic overhead if all-to-all connectivity is desired [Hir+09].

With photonic interfaces on the other hand, remote entanglement can be generated on demand between arbitrary pairs of modules using reconfigurable optical cross-connect switches [Kim+03]. Heralded remote entanglement serves as a resource for many quantum logic primitives [Hor+09]. However, the fidelity of remote entanglement lags behind state-of-the-art two-qubit gates in trapped ions (0.96 [Nad+22] vs. $\gtrsim 0.999$ [Sri+21; Bal+16; Gae+16]). Recent theoretical results suggests that infidelities as high as $14\times$ the local gate infidelity can be tolerated using the surface code for quantum error correction [Ram+24].[3] In practice, this may not be sufficient for large-scale error-corrected quantum computing across modules and the fidelity of remote entanglement must still be improved.

It may not be possible to directly reduce the error of raw remote entangled states generated via the photonic interface. However, several raw entangled states

[3]The fault-tolerance threshold determines the minimum fidelity required for quantum logic operations such that the overhead due to error correction can be (more than) compensated. The numerical value varies for different error-correcting codes and error models [Ste03; Kni05; RH07; FWH12; Ste14].

can be 'distilled' into an entangled state with higher fidelity using LOCC [Ben+96]. Entanglement distillation across a quantum network link was first demonstrated with solid-state qubits [Kal+17].

The mixed-species techniques described in this thesis will enable entanglement distillation in a trapped-ion system, where the number of qubits per node can be chosen depending on the application. At a minimum, the single-stage distillation protocol shown in Figure 7.1 could be implemented using the same $^{88}Sr^{+}$-$^{43}Ca^{+}$ crystal and mixed-species gates as were used for the BQC implementation described in Chapter 6. Using more memory qubits ($^{43}Ca^{+}$ ions) and ion transport (see

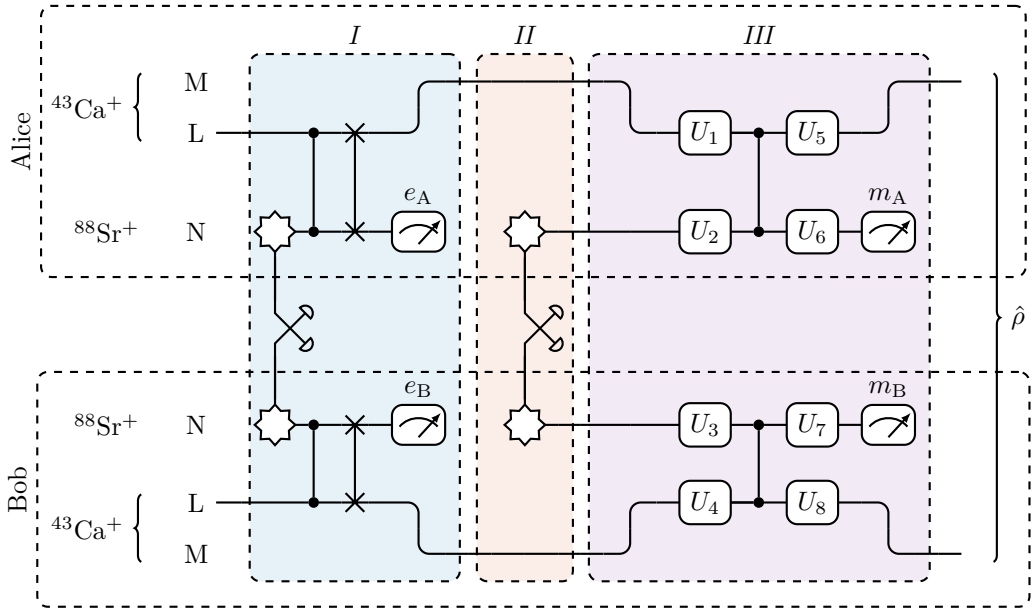

Figure 7.1: Entanglement distillation protocol (adapted from [Mai23]). Two raw Bell pairs (stars) are distilled into one Bell pair ($\hat{\rho}$) of higher fidelity using a probabilistic protocol. In step *I*, the first raw pair generated with the network qubit (N) in $^{88}Sr^{+}$ is swapped onto a memory qubit (M) via the logic qubit (L) in $^{43}Ca^{+}$, using an iSWAP gate and error detection (e_A and e_B, see Section 5.1.2). In step *II*, a second Bell pair is generated with the network qubit. In step *III*, a unitary operation entangles the two Bell pairs and a measurement of the network qubits (m_A and m_B) reveals if the distillation was successful.

Section 3.2), higher-level distillation protocols could be implemented [Nig+16], including optimised distillation circuits [KAJ19]. Improving the fidelity of remote entanglement to close the gap to the fidelity of local operations would mark an important milestone on the way to a scalable and fault-tolerant quantum computer.

We believe that our mixed-species quantum network architecture will bring this prospect one step closer to reality.

List of Abbreviations

ACK acknowledgement

ADC analogue to digital converter

AMO atomic, molecular and optical physics

AOM acousto-optic modulator

APD avalanche photodiode

ARTIQ advanced real-time infrastructure for quantum physics

BB1 broadband type 1

BPP bounded-error probabilistic polynomial time

BQC blind quantum computing

BQP bounded-error quantum polynomial time

BSB blue sideband

CHSH Clauser-Horne-Shimony-Holt

CPMG Carr-Purcell Meiboom-Gill

CPU central processing unit

CW continuous-wave

DAC digital to analogue converter

DDS direct digital synthesis

DIO digital input/output

DMA direct memory access

DRTIO distributed real-time input/output

EIT electromagnetically-induced transparency

EMCCD electron-multiplying charge-coupled device

EOM electro-optic modulator

FHE fully homomorphic encryption

FIFO first-in, first-out

FPGA field-programmable gate array

FSM finite-state machine

GPS global positioning system

IP in-phase

IPE ion-photon entanglement

KDD Knill dynamical decoupling

LDA Lamb-Dicke approximation

LOCC local operations and classical communication

MBQC measurement-based quantum computing

MCWF Monte-Carlo wavefunction

MRI magnetic resonance imaging

NMR nuclear magnetic resonance

OMG optical-frequency, metastable-state, and ground-state

OOP out-of-phase

PBS polarising beamsplitter

PECL positive emitter coupled logic

PI proportional-gain, integral-gain

PID proportional-gain, integral-gain, differential-gain

PMT photomultiplier tube

POVM positive operator-valued measurement

QCCD quantum charge-coupled device

RAM random access memory

RBM randomised benchmarking

RF radio frequency

RPC remote procedure call

RSA Rivest–Shamir–Adleman

RSB red sideband

RSP remote state preparation

RTIO real-time input/output

RWA rotating wave approximation

SBC sideband cooling

SDF spin-dependent force

SFP small form-factor pluggable

SPAM state preparation and measurement

TTL transistor-transistor logic

UDD Uhrig dynamical decoupling

UHV ultra-high vacuum

VBQC verifiable blind quantum computing

WE write-enable

References

[Aha+17] D. Aharonov, M. Ben-Or, E. Eban and U. Mahadev. 'Interactive Proofs for Quantum Computations'. Preprint (arXiv, 2017). DOI: 10.48550/arXiv.1704.04487.

[Aik+20] Y. Aikyo, G. Vrijsen, T. W. Noel, A. Kato, M. K. Ivory and J. Kim. 'Vacuum characterization of a compact room-temperature trapped ion system'. Applied Physics Letters **117**, 234002 (2020). DOI: 10.1063/5.0029236.

[Akh+23] M. Akhtar, F. Bonus, F. Lebrun-Gallagher, N. Johnson, M. Siegele-Brown, S. Hong, S. Hile, S. Kulmiya, S. Weidt and W. Hensinger. 'A high-fidelity quantum matter-link between ion-trap microchip modules'. Nature Communications **14**, 531 (2023). DOI: 10.1038/s41467-022-35285-3.

[ALP20] J. Alcazar, V. Leyton-Ortega and A. Perdomo-Ortiz. 'Classical versus quantum models in machine learning: insights from a finance application'. Machine Learning: Science and Technology **1**, 035003 (2020). DOI: 10.1088/2632-2153/ab9009.

[All+21] D. T. C. Allcock, W. C. Campbell, J. Chiaverini, I. L. Chuang, E. R. Hudson, I. D. Moore, A. Ransford, C. Roman, J. M. Sage and D. J. Wineland. 'omg blueprint for trapped ion quantum computing with metastable states'. Applied Physics Letters **119**, 214002 (2021). DOI: 10.1063/5.0069544.

[Ama+22] D. Amaro, C. Modica, M. Rosenkranz, M. Fiorentini, M. Benedetti and M. Lubasch. 'Filtering variational quantum algorithms for combinatorial optimization'. Quantum Science and Technology **7**, 015021 (2022). DOI: 10.1088/2058-9565/ac3e54.

[An+22] F. A. An, A. Ransford, A. Schaffer, L. R. Sletten, J. Gaebler, J. Hostetter and G. Vittorini. 'High Fidelity State Preparation and Measurement of Ion Hyperfine Qubits with $I > \frac{1}{2}$'. Physical Review Letters **129**, 130501 (2022). DOI: 10.1103/PhysRevLett.129.130501.

[AL12] A. Anis and A. I. Lvovsky. 'Maximum-likelihood coherent-state quantum process tomography'. New Journal of Physics **14**, 105021 (2012). DOI: 10.1088/1367-2630/14/10/105021.

[Arn+16] K. J. Arnold, R. Kaewuam, A. Roy, E. Paez, S. Wang and M. D. Barrett. 'Observation of the $^1S_0$ to $^3D_1$ clock transition in $^{175}Lu^+$'. Physical Review A **94**, 052512 (2016). DOI: 10.1103/PhysRevA.94.052512.

[Bad+00] P. Badziąg, M. Horodecki, P. Horodecki and R. Horodecki. 'Local environment can enhance fidelity of quantum teleportation'. Physical Review A **62**, 012311 (2000). DOI: 10.1103/PhysRevA.62.012311.

[Bal+16] C. J. Ballance, T. P. Harty, N. M. Linke, M. A. Sepiol and D. M. Lucas. 'High-Fidelity Quantum Logic Gates Using Trapped-Ion Hyperfine Qubits'. Physical Review Letters **117**, 060504 (2016). DOI: 10.1103/PhysRevLett.117.060504.

[Bal+15] C. J. Ballance, V. M. Schäfer, J. P. Home, D. J. Szwer, S. C. Webster, D. T. C. Allcock, N. M. Linke, T. P. Harty, D. P. L. Aude Craik, D. N. Stacey, A. M. Steane and D. M. Lucas. 'Hybrid quantum logic and a test of Bell's inequality using two different atomic isotopes'. Nature **528**, 384–386 (2015). DOI: 10.1038/nature16184.

[Bal14] C. J. Ballance. 'High-Fidelity Quantum Logic in Ca+'. DPhil thesis (University of Oxford, 2014).

[Bal+18] T. G. Ballance, J. F. Goodwin, B. Nichol, L. J. Stephenson, C. J. Ballance and D. M. Lucas. 'A short response time atomic source for trapped ion experiments'. Review of Scientific Instruments **89**, 053102 (2018). DOI: 10.1063/1.5025713.

[Ban+20] L. Banchi, M. Fingerhuth, T. Babej, C. Ing and J. M. Arrazola. 'Molecular docking with Gaussian Boson Sampling'. Science Advances **6**, eaax1950 (2020). DOI: 10.1126/sciadv.aax1950.

[Bar+03] G. P. Barwood, K. Gao, P. Gill, G. Huang and H. A. Klein. 'Observation of the hyperfine structure of the $^2S_{1/2}$−$^2D_{5/2}$ transition in $^{87}Sr^+$'. Physical Review A **67**, 013402 (2003). DOI: 10.1103/PhysRevA.67.013402.

[Bar+13] S. Barz, J. F. Fitzsimons, E. Kashefi and P. Walther. 'Experimental verification of quantum computation'. Nature Physics **9**, 727–731 (2013). DOI: 10.1038/nphys2763.

[Bar+12] S. Barz, E. Kashefi, A. Broadbent, J. F. Fitzsimons, A. Zeilinger and P. Walther. 'Demonstration of Blind Quantum Computing'. Science **335**, 303–308 (2012). DOI: 10.1126/science.1214707.

[BW83] W. Becker and G. Werth. 'Precise determination of the ground state hyperfine splitting of135Ba+'. Zeitschrift für Physik A Atoms and Nuclei **311**, 41–47 (1983). DOI: 10.1007/BF01411605.

[Ben+07] J. Benhelm, G. Kirchmair, U. Rapol, T. Körber, C. F. Roos and R. Blatt. 'Measurement of the hyperfine structure of the S_{12}−D_{52} transition in $^{43}Ca^+$'. Physical Review A **75**, 032506 (2007). DOI: 10.1103/PhysRevA.75.032506.

[BB84] C. H. Bennett and G. Brassard. 'Quantum cryptography: public key distribution and coin tossing'. Theoretical Computer Science **560**, 7–11 (1984). DOI: 10.1016/j.tcs.2014.05.025.

[Ben+93] C. H. Bennett, G. Brassard, C. Crépeau, R. Jozsa, A. Peres and W. K. Wootters. 'Teleporting an unknown quantum state via dual classical and Einstein-Podolsky-Rosen channels'. Physical Review Letters **70**, 1895–1899 (1993). DOI: 10.1103/PhysRevLett.70.1895.

[Ben+96] C. H. Bennett, G. Brassard, S. Popescu, B. Schumacher, J. A. Smolin and W. K. Wootters. 'Purification of Noisy Entanglement and Faithful Teleportation via Noisy Channels'. Physical Review Letters **76**, 722–725 (1996). DOI: 10.1103/PhysRevLett.76.722.

[Ben+01] C. H. Bennett, D. P. DiVincenzo, P. W. Shor, J. A. Smolin, B. M. Terhal and W. K. Wootters. 'Remote State Preparation'. Physical Review Letters **87**, 077902 (2001). DOI: 10.1103/PhysRevLett.87.077902.

[BIW87] J. C. Bergquist, W. M. Itano and D. J. Wineland. 'Recoilless optical absorption and Doppler sidebands of a single trapped ion'. Physical Review A **36**, 428–430 (1987). DOI: 10.1103/PhysRevA.36.428.

[Ber+03] I. Bergström, M. Björkhage, K. Blaum, H. Bluhme, T. Fritioff, S. Nagy and R. Schuch. 'High-precision mass measurements of hydrogen-like 24Mg11+ and26Mg11+ ions in a Penning trap'. The European Physical Journal D **22**, 41–45 (2003). DOI: 10.1140/epjd/e2002-00216-x.

[Bli+02] B. B. Blinov, L. Deslauriers, P. Lee, M. J. Madsen, R. Miller and C. Monroe. 'Sympathetic cooling of trapped Cd^+ isotopes'. Physical Review A **65**, 040304 (2002). DOI: 10.1103/PhysRevA.65.040304.

[Bli+04] B. B. Blinov, D. L. Moehring, L.-M. Duan and C. Monroe. 'Observation of entanglement between a single trapped atom and a single photon'. Nature **428**, 153–157 (2004). DOI: 10.1038/nature02377.

[Bli+06] B. B. Blinov, J. R. N. Kohn, M. J. Madsen, P. Maunz, D. L. Moehring and C. Monroe. 'Broadband laser cooling of trapped atoms with ultrafast pulses'. Journal of the Optical Society of America B **23**, 1170–1173 (2006). DOI: 10.1364/JOSAB.23.001170.

[Blu+22] N. S. Blunt, J. Camps, O. Crawford, R. Izsák, S. Leontica, A. Mirani, A. E. Moylett, S. A. Scivier, C. Sünderhauf, P. Schopf, J. M. Taylor and N. Holzmann. 'Perspective on the Current State-of-the-Art of Quantum Computing for Drug Discovery Applications'. Journal of Chemical Theory and Computation **18**, 7001–7023 (2022). DOI: 10.1021/acs.jctc.2c00574.

[Bog+23] M. J. Boguslawski, Z. J. Wall, S. R. Vizvary, I. D. Moore, M. Bareian, D. T. C. Allcock, D. J. Wineland, E. R. Hudson and W. C. Campbell. 'Raman Scattering Errors in Stimulated-Raman-Induced Logic Gates in $^{133}Ba^+$'. Physical Review Letters **131**, 063001 (2023). DOI: 10.1103/PhysRevLett.131.063001.

[Boh13] N. Bohr. 'I. On the constitution of atoms and molecules'. The London, Edinburgh, and Dublin Philosophical Magazine and Journal of Science **26**, 1–25 (1913). DOI: 10.1080/14786441308634955.

[Bou+21] S. Bourdeauducq et al. 'm-labs/artiq: 6.0' (2021). DOI: 10.5281/zenodo.1492176.

[Bra+07] G. Brassard, A. Broadbent, J. Fitzsimons, S. Gambs and A. Tapp. 'Anonymous Quantum Communication'. In: *Advances in Cryptology – ASIACRYPT 2007*. Vol. 4833, pp. 460–473 (Springer, Berlin, Heidelberg, 2007). DOI: 10.1007/978-3-540-76900-2_28.

[Bre+19] S. M. Brewer, J.-S. Chen, A. M. Hankin, E. R. Clements, C. W. Chou, D. J. Wineland, D. B. Hume and D. R. Leibrandt. '$^{27}Al^+$ Quantum-Logic Clock with a Systematic Uncertainty below 10^{-18}'. Physical Review Letters **123**, 033201 (2019). DOI: 10.1103/PhysRevLett.123.033201.

[Bro18] A. Broadbent. 'How to Verify a Quantum Computation'. Theory of Computing **14**, 1–37 (2018). DOI: 10.4086/toc.2018.v014a011.

[BFK09] A. Broadbent, J. Fitzsimons and E. Kashefi. 'Universal Blind Quantum Computation'. In: *2009 50th Annual IEEE Symposium on Foundations of Computer Science*, pp. 517–526 (Atlanta, GA, USA, 2009). DOI: 10.1109/FOCS.2009.36.

[BB06] D. E. Browne and H. J. Briegel. 'One-way Quantum Computation - a tutorial introduction'. arXiv:quant-ph/0603226 (arXiv, 2006). DOI: 10.48550/arXiv.quant-ph/0603226.

[Bro+15] M. Brownnutt, M. Kumph, P. Rabl and R. Blatt. 'Ion-trap measurements of electric-field noise near surfaces'. Reviews of Modern Physics **87**, 1419–1482 (2015). DOI: 10.1103/RevModPhys.87.1419.

[Bro07] M. Brownnutt. '$^{88}Sr^+$ ion trapping techniques and technologies for quantum information processing'. PhD thesis (Imperial College London, 2007).

[Bru+19] C. D. Bruzewicz, R. McConnell, J. Stuart, J. M. Sage and J. Chiaverini. 'Dual-species, multi-qubit logic primitives for Ca^+/Sr^+ trapped-ion crystals'. npj Quantum Information **5**, 102 (2019). DOI: 10.1038/s41534-019-0218-z.

[BKD08] D. Budker, D. F. Kimball and D. P. DeMille. *Atomic physics: an exploration through problems and solutions*. 2nd ed. (Oxford University Press, 2008).

[Bur10] A. H. Burrell. 'High Fidelity Readout of Trapped Ion Qubits'. DPhil thesis (University of Oxford, 2010).

[Cet+22] M. Cetina, L. Egan, C. Noel, M. Goldman, D. Biswas, A. Risinger, D. Zhu and C. Monroe. 'Control of Transverse Motion for Quantum Gates on Individually Addressed Atomic Qubits'. PRX Quantum **3**, 010334 (2022). DOI: 10.1103/PRXQuantum.3.010334.

[Chi05] A. M. Childs. 'Secure Assisted Quantum Computation'. Quantum Information Computation **5**, 456–466 (2005).

[CLN05] A. M. Childs, D. W. Leung and M. A. Nielsen. 'Unified derivations of measurement-based schemes for quantum computation'. Physical Review A **71**, 032318 (2005). DOI: 10.1103/PhysRevA.71.032318.

[Chr+20] J. E. Christensen, D. Hucul, W. C. Campbell and E. R. Hudson. 'High-fidelity manipulation of a qubit enabled by a manufactured nucleus'. npj Quantum Information **6**, 35 (2020). DOI: 10.1038/s41534-020-0265-5.

[Chw09] M. Chwalla. 'Precision Spectroscopy with $^{40}Ca^+$ Ions in a Paul Trap'. Dissertation (University of Innsbruck, 2009).

[Cla+21] C. R. Clark, H. N. Tinkey, B. C. Sawyer, A. M. Meier, K. A. Burkhardt, C. M. Seck, C. M. Shappert, N. D. Guise, C. E. Volin, S. D. Fallek, H. T. Hayden, W. G. Rellergert and K. R. Brown. 'High-Fidelity Bell-State Preparation with $^{40}Ca^+$ Optical Qubits'. Physical Review Letters **127**, 130505 (2021). DOI: 10.1103/PhysRevLett.127.130505.

[Cli+94] R. A. Cline, J. D. Miller, M. R. Matthews and D. J. Heinzen. 'Spin relaxation of optically trapped atoms by light scattering'. Optics Letters **19**, 207–209 (1994). DOI: 10.1364/OL.19.000207.

[Cro+19] C. Crocker, M. Lichtman, K. Sosnova, A. Carter, S. Scarano and C. Monroe. 'High purity single photons entangled with an atomic qubit'. Optics Express **27**, 28143–28149 (2019). DOI: 10.1364/OE.27.028143.

[Dan+09] C. Dankert, R. Cleve, J. Emerson and E. Livine. 'Exact and approximate unitary 2-designs and their application to fidelity estimation'. Physical Review A **80**, 012304 (2009). DOI: 10.1103/PhysRevA.80.012304.

[Deh69] H. G. Dehmelt. 'Radiofrequency Spectroscopy of Stored Ions II: Spectroscopy'. In: *Advances in Atomic and Molecular Physics*. Vol. 5, pp. 109–154 (Academic Press, 1969). DOI: 10.1016/S0065-2199(08)60156-6.

[Deu85] D. Deutsch. 'Quantum theory as a universal physical theory'. International Journal of Theoretical Physics **24**, 1–41 (1985). DOI: 10.1007/BF00670071.

[DiV00] D. P. DiVincenzo. 'The Physical Implementation of Quantum Computation'. Fortschritte der Physik **48**, 771–783 (2000). DOI: 10.1002/1521-3978(200009)48:9/11<771::AID-PROP771>3.0.CO;2-E.

[DD22] N. Döttling and J. Dujmovic. 'Maliciously Circuit-Private FHE from Information-Theoretic Principles'. In: *Leibniz International Proceedings in Informatics*. 3rd Conference on Information-Theoretic Cryptography (ITC 2022), 4:1–4:21 (Dagstuhl Publishing, 2022). DOI: 10.4230/LIPIcs.ITC.2022.4.

[Drm+23] P. Drmota, D. Main, D. P. Nadlinger, B. C. Nichol, M. A. Weber, E. M. Ainley, A. Agrawal, R. Srinivas, G. Araneda, C. J. Ballance and D. M. Lucas. 'Robust Quantum Memory in a Trapped-Ion Quantum Network Node'. Physical Review Letters **130**, 090803 (2023). DOI: 10.1103/PhysRevLett.130.090803.

[Drm+24] P. Drmota, D. P. Nadlinger, D. Main, B. C. Nichol, E. M. Ainley, D. Leichtle, A. Mantri, E. Kashefi, R. Srinivas, G. Araneda, C. J. Ballance and D. M. Lucas. 'Verifiable Blind Quantum Computing with Trapped Ions and Single Photons'. Physical Review Letters **132**, 150604 (2024). DOI: 10.1103/PhysRevLett.132.150604.

[DCG09] R. Dubessy, T. Coudreau and L. Guidoni. 'Electric field noise above surfaces: a model for heating rate scaling law in ion traps'. Physical Review A **80**, 031402 (2009). DOI: 10.1103/PhysRevA.80.031402.

[Ehr11] P. Ehrenfest. 'Welche Züge der Lichtquantenhypothese spielen in der Theorie der Wärmestrahlung eine wesentlich Rolle?' Annalen der Physik **36**, 91–118 (1911).

[Ein05] A. Einstein. 'Über einen die Erzeugung und Verwandlung des Lichtes betreffenden heuristischen Gesichtspunkt'. Annalen der Physik **322**, 132–148 (1905). DOI: 10.1002/andp.19053220607.

[Eke91] A. K. Ekert. 'Quantum cryptography based on Bell's theorem'. Physical Review Letters **67**, 661–663 (1991). DOI: 10.1103/PhysRevLett.67.661.

[EAŻ05] J. Emerson, R. Alicki and K. Życzkowski. 'Scalable noise estimation with random unitary operators'. Journal of Optics B: Quantum and Semiclassical Optics **7**, S347–S352 (2005). DOI: 10.1088/1464-4266/7/10/021.

[Fed+22] A. K. Fedorov, N. Gisin, S. M. Beloussov and A. I. Lvovsky. 'Quantum computing at the quantum advantage threshold: a down-to-business review'. Preprint (arXiv, 2022). DOI: 10.48550/arXiv.2203.17181.

[Fey82] R. P. Feynman. 'Simulating physics with computers'. International Journal of Theoretical Physics **21**, 467–488 (1982).

[Fis+14] K. A. G. Fisher, A. Broadbent, L. K. Shalm, Z. Yan, J. Lavoie, R. Prevedel, T. Jennewein and K. J. Resch. 'Quantum computing on encrypted data'. Nature Communications **5**, 3074 (2014). DOI: doi.org/10.1038/ncomms4074.

[Fit17] J. F. Fitzsimons. 'Private quantum computation: an introduction to blind quantum computing and related protocols'. npj Quantum Information **3**, 23 (2017). DOI: 10.1038/s41534-017-0025-3.

[FK17] J. F. Fitzsimons and E. Kashefi. 'Unconditionally verifiable blind quantum computation'. Physical Review A **96**, 012303 (2017). DOI: 10.1103/PhysRevA.96.012303.

[Fok+23] E. N. Fokoua, S. A. Mousavi, G. T. Jasion, D. J. Richardson and F. Poletti. 'Loss in hollow-core optical fibers: mechanisms, scaling rules, and limits'. Advances in Optics and Photonics **15**, 1–85 (2023). DOI: 10.1364/AOP.470592.

[FWH12] A. G. Fowler, A. C. Whiteside and L. C. L. Hollenberg. 'Towards Practical Classical Processing for the Surface Code'. Physical Review Letters **108**, 180501 (2012). DOI: 10.1103/PhysRevLett.108.180501.

[Gae+16] J. P. Gaebler, T. R. Tan, Y. Lin, Y. Wan, R. Bowler, A. C. Keith, S. Glancy, K. Coakley, E. Knill, D. Leibfried and D. J. Wineland. 'High-Fidelity Universal Gate Set for $^{9}Be^{+}$ Ion Qubits'. Physical Review Letters **117**, 060505 (2016). DOI: 10.1103/PhysRevLett.117.060505.

[Gay+08] O. Gayer, Z. Sacks, E. Galun and A. Arie. 'Temperature and wavelength dependent refractive index equations for MgO-doped congruent and stoichiometric LiNbO3'. Applied Physics B **91**, 343–348 (2008). DOI: 10.1007/s00340-008-2998-2.

[GMR09] H. Geiger, E. Marsden and E. Rutherford. 'On a diffuse reflection of the α-particles'. Proceedings of the Royal Society of London. Series A, Containing Papers of a Mathematical and Physical Character **82**, 495–500 (1909). DOI: 10.1098/rspa.1909.0054.

[Gen09] C. Gentry. 'Fully homomorphic encryption using ideal lattices'. In: *Proceedings of the forty-first annual ACM symposium on Theory of computing*. STOC '09: Symposium on Theory of Computing, pp. 169–178 (ACM, Bethesda MD USA, 2009). DOI: 10.1145/1536414.1536440.

[GKK19] A. Gheorghiu, T. Kapourniotis and E. Kashefi. 'Verification of Quantum Computation: An Overview of Existing Approaches'. Theory of Computing Systems **63**, 715–808 (2019). DOI: 10.1007/s00224-018-9872-3.

[GLM08] V. Giovannetti, S. Lloyd and L. Maccone. 'Quantum Private Queries'. Physical Review Letters **100**, 230502 (2008). DOI: 10.1103/PhysRevLett.100.230502.

[Got98] D. Gottesman. 'The Heisenberg Representation of Quantum Computers'. Preprint (arXiv, 1998). DOI: 10.48550/arXiv.quant-ph/9807006.

[GC01] D. Gottesman and I. Chuang. 'Quantum Digital Signatures'. arXiv:quant-ph/0105032 (arXiv, 2001). DOI: 10.48550/arXiv.quant-ph/0105032.

[Gre+16] C. Greganti, M.-C. Roehsner, S. Barz, T. Morimae and P. Walther. 'Demonstration of measurement-only blind quantum computing'. New Journal of Physics **18**, 013020 (2016). DOI: 10.1088/1367-2630/18/1/013020.

[Gul+01] S. Gulde, D. Rotter, P. Barton, F. Schmidt-Kaler, R. Blatt and W. Hogervorst. 'Simple and efficient photo-ionization loading of ions for precision ion-trapping experiments'. Applied Physics B **73**, 861–863 (2001). DOI: 10.1007/s003400100749.

[Hah50] E. L. Hahn. 'Spin Echoes'. Physical Review **80**, 580–594 (1950). DOI: 10.1103/PhysRev.80.580.

[HSQ22] J. Hannegan, J. D. Siverns and Q. Quraishi. 'Entanglement between a trapped-ion qubit and a 780-nm photon via quantum frequency conversion'. Physical Review A **106**, 042441 (2022). DOI: 10.1103/PhysRevA.106.042441.

[Har+14] T. P. Harty, D. T. C. Allcock, C. J. Ballance, L. Guidoni, H. A. Janacek, N. M. Linke, D. N. Stacey and D. M. Lucas. 'High-Fidelity Preparation, Gates, Memory, and Readout of a Trapped-Ion Quantum Bit'. Physical Review Letters **113**, 220501 (2014). DOI: 10.1103/PhysRevLett.113.220501.

[Hay+12] D. Hayes, S. M. Clark, S. Debnath, D. Hucul, I. V. Inlek, K. W. Lee, Q. Quraishi and C. Monroe. 'Coherent Error Suppression in Multiqubit Entangling Gates'. Physical Review Letters **109**, (2012). DOI: 10.1103/PhysRevLett.109.020503.

[Hea] 'Healthcare Cloud Computing Market (By Cloud Deployment: Private,Public, Hybrid), Service (Paas, Iaas,and Saas); By Application: Non-clinical Information System and Clinical Information System; By End-use: Healthcare Providers and Healthcare Payers) - Global Market Size, Trends Analysis, Segment Forecasts, Regional Outlook 2022 - 2030'. https://www.precedenceresearch.com/healthcare-cloud-computing-market. Accessed: 2023-07-08.

[Hen+15] B. Hensen, H. Bernien, A. E. Dréau, A. Reiserer, N. Kalb, M. S. Blok, J. Ruitenberg, R. F. L. Vermeulen, R. N. Schouten, C. Abellán, W. Amaya, V. Pruneri, M. W. Mitchell, M. Markham, D. J. Twitchen, D. Elkouss, S. Wehner, T. H. Taminiau and R. Hanson. 'Loophole-free Bell inequality violation using electron spins separated by 1.3 kilometres'. Nature **526**, 682–686 (2015). DOI: 10.1038/nature15759.

[Hir+09] Y. Hirata, M. Nakanishi, S. Yamashita and Y. Nakashima. 'An Efficient Method to Convert Arbitrary Quantum Circuits to Ones on a Linear Nearest Neighbor Architecture'. In: *2009 Third International Conference on Quantum, Nano and Micro Technologies*, pp. 26–33 (2009). DOI: 10.1109/ICQNM.2009.25.

[Hir+13] F. Hirsch, M. T. Quintino, J. Bowles and N. Brunner. 'Genuine Hidden Quantum Nonlocality'. Physical Review Letters **111**, 160402 (2013). DOI: 10.1103/PhysRevLett.111.160402.

[HP13] M. Hojsík and V. Půlpánová. 'A Fully Homomorphic Cryptosystem with Approximate Perfect Secrecy'. In: *Topics in Cryptology – CT-RSA 2013*. Lecture Notes in Computer Science, pp. 375–388 (Springer, Berlin, Heidelberg, 2013). DOI: 10.1007/978-3-642-36095-4_24.

[Hol+22] C. A. Holliman, M. Fan, A. Contractor, S. M. Brewer and A. M. Jayich. 'Radium Ion Optical Clock'. Physical Review Letters **128**, 033202 (2022). DOI: 10.1103/PhysRevLett.128.033202.

[Hom+09] J. P. Home, M. J. McDonnell, D. J. Szwer, B. C. Keitch, D. M. Lucas, D. N. Stacey and A. M. Steane. 'Memory coherence of a sympathetically cooled trapped-ion qubit'. Physical Review A **79**, 050305(R) (2009). DOI: 10.1103/PhysRevA.79.050305.

[Hom13] J. P. Home. 'Quantum science and metrology with mixed-species ion chains'. Preprint (arXiv, 2013). DOI: 10.48550/arXiv.1306.5950.

[Hor+09] R. Horodecki, P. Horodecki, M. Horodecki and K. Horodecki. 'Quantum entanglement'. Reviews of Modern Physics **81**, 865–942 (2009). DOI: 10.1103/RevModPhys.81.865.

[Huc+15] D. Hucul, I. V. Inlek, G. Vittorini, C. Crocker, S. Debnath, S. M. Clark and C. Monroe. 'Modular entanglement of atomic qubits using photons and phonons'. Nature Physics **11**, 37–42 (2015). DOI: 10.1038/nphys3150.

[Hug+20] A. C. Hughes, V. M. Schäfer, K. Thirumalai, D. P. Nadlinger, S. R. Woodrow, D. M. Lucas and C. J. Ballance. 'Benchmarking a High-Fidelity Mixed-Species Entangling Gate'. Physical Review Letters **125**, 080504 (2020). DOI: 10.1103/PhysRevLett.125.080504.

[Hug21] A. Hughes. 'Benchmarking memory and logic gates for trapped-ion quantum computing'. DPhil thesis (University of Oxford, 2021).

[Inl+17] I. V. Inlek, C. Crocker, M. Lichtman, K. Sosnova and C. Monroe. 'Multispecies Trapped-Ion Node for Quantum Networking'. Physical Review Letters **118**, 250502 (2017). DOI: 10.1103/PhysRevLett.118.250502.

[JJ07] D. F. V. James and J. Jerke. 'Effective Hamiltonian Theory and Its Applications in Quantum Information'. Canadian Journal of Physics **85**, 625–632 (2007). DOI: 10.1139/P07-060.

[Kae+19] R. Kaewuam, T. R. Tan, K. J. Arnold and M. D. Barrett. 'Spectroscopy of the $^1S_0 - ^1D_2$ clock transition in $^{176}Lu^+$'. Physical Review A **99**, 022514 (2019). DOI: 10.1103/PhysRevA.99.022514.

[Kal+17] N. Kalb, A. A. Reiserer, P. C. Humphreys, J. J. W. Bakermans, S. J. Kamerling, N. H. Nickerson, S. C. Benjamin, D. J. Twitchen, M. Markham and R. Hanson. 'Entanglement distillation between solid-state quantum network nodes'. Science **356**, 928–932 (2017). DOI: 10.1126/science.aan0070.

[Kas+20] G. Kasprowicz, P. Kulik, M. Gaska, T. Przywozki, K. Pozniak, J. Jarosinski, J. W. Britton, T. Harty, C. Balance, W. Zhang, D. Nadlinger, D. Slichter, D. Allcock, S. Bourdeauducq, R. Jördens and K. Pozniak. 'ARTIQ and Sinara: Open Software and Hardware Stacks for Quantum Physics'. In: *OSA Quantum 2.0 Conference*. (Optica Publishing Group, 2020). DOI: 10.1364/QUANTUM.2020.QTu8B.14.

[Kel+15] J. Keller, H. L. Partner, T. Burgermeister and T. E. Mehlstäubler. 'Precise Determination of Micromotion for Trapped-Ion Optical Clocks'. Journal of Applied Physics **118**, 104501 (2015). DOI: 10.1063/1.4930037.

[Kel15] J. Keller. 'Spectroscopic characterization of ion motion for an optical clock based on Coulomb crystals'. PhD thesis (Gottfried Wilhelm Leibniz Universität Hannover, 2015).

[Kie+00] D. Kielpinski, B. E. King, C. J. Myatt, C. A. Sackett, Q. A. Turchette, W. M. Itano, C. Monroe, D. J. Wineland and W. H. Zurek. 'Sympathetic cooling of trapped ions for quantum logic'. Physical Review A **61**, 032310 (2000). DOI: 10.1103/PhysRevA.61.032310.

[KMW02] D. Kielpinski, C. Monroe and D. J. Wineland. 'Architecture for a large-scale ion-trap quantum computer'. Nature **417**, 709–711 (2002). DOI: 10.1038/nature00784.

[Kim+03] J. Kim, C. Nuzman, B. Kumar, D. Lieuwen, J. Kraus, A. Weiss, C. Lichtenwalner, A. Papazian, R. Frahm, N. Basavanhally, D. Ramsey, V. Aksyuk, F. Pardo, M. Simon, V. Lifton, H. Chan, M. Haueis, A. Gasparyan, H. Shea, S. Arney, C. Bolle, P. Kolodner, R. Ryf, D. Neilson and J. Gates. '1100 x 1100 port MEMS-based optical crossconnect with 4-dB maximum loss'. IEEE Photonics Technology Letters **15**, 1537–1539 (2003). DOI: 10.1109/LPT.2003.818653.

[Kim08] H. J. Kimble. 'The quantum internet'. Nature **453**, 1023–1030 (2008). DOI: 10.1038/nature07127.

[Kir+22] J. J. M. Kirsopp, C. Di Paola, D. Z. Manrique, M. Krompiec, G. Greene-Diniz, W. Guba, A. Meyder, D. Wolf, M. Strahm and D. Muñoz Ramo. 'Quantum computational quantification of protein–ligand interactions'. International Journal of Quantum Chemistry **122**, e26975 (2022). DOI: 10.1002/qua.26975.

[Kni05] E. Knill. 'Quantum computing with realistically noisy devices'. Nature **434**, 39–44 (2005). DOI: 10.1038/nature03350.

[Kni+08] E. Knill, D. Leibfried, R. Reichle, J. Britton, R. B. Blakestad, J. D. Jost, C. Langer, R. Ozeri, S. Seidelin and D. J. Wineland. 'Randomized benchmarking of quantum gates'. Physical Review A **77**, 012307 (2008). DOI: 10.1103/PhysRevA.77.012307.

[Kóm+14] P. Kómár, E. M. Kessler, M. Bishof, L. Jiang, A. S. Sørensen, J. Ye and M. D. Lukin. 'A quantum network of clocks'. Nature Physics **10**, 582–587 (2014). DOI: 10.1038/nphys3000.

[KAJ19] S. Krastanov, V. V. Albert and L. Jiang. 'Optimized Entanglement Purification'. Quantum **3**, 123 (2019). DOI: 10.22331/q-2019-02-18-123.

[Kru+23a] V. Krutyanskiy, M. Canteri, M. Meraner, J. Bate, V. Krcmarsky, J. Schupp, N. Sangouard and B. P. Lanyon. 'Telecom-Wavelength Quantum Repeater Node Based on a Trapped-Ion Processor'. Physical Review Letters **130**, 213601 (2023). DOI: 10.1103/PhysRevLett.130.213601.

[Kru+23b] V. Krutyanskiy, M. Galli, V. Krcmarsky, S. Baier, D. A. Fioretto, Y. Pu, A. Mazloom, P. Sekatski, M. Canteri, M. Teller, J. Schupp, J. Bate, M. Meraner, N. Sangouard, B. P. Lanyon and T. E. Northup. 'Entanglement of Trapped-Ion Qubits Separated by 230 Meters'. Physical Review Letters **130**, 050803 (2023). DOI: 10.1103/PhysRevLett.130.050803.

[Kru+19] V. Krutyanskiy, M. Meraner, J. Schupp, V. Krcmarsky, H. Hainzer and B. P. Lanyon. 'Light-matter entanglement over 50 km of optical fibre'. npj Quantum Information **5**, 72 (2019). DOI: 10.1038/s41534-019-0186-3.

[Lan+22] R. Lange, N. Huntemann, A. A. Peshkov, A. Surzhykov and E. Peik. 'Excitation of an Electric Octupole Transition by Twisted Light'. Physical Review Letters **129**, 253901 (2022). DOI: 10.1103/PhysRevLett.129.253901.

[Lan+13] B. P. Lanyon, P. Jurcevic, M. Zwerger, C. Hempel, E. A. Martinez, W. Dür, H. J. Briegel, R. Blatt and C. F. Roos. 'Measurement-Based Quantum Computation with Trapped Ions'. Physical Review Letters **111**, 210501 (2013). DOI: 10.1103/PhysRevLett.111.210501.

[Lan+07] B. P. Lanyon, T. J. Weinhold, N. K. Langford, M. Barbieri, D. F. V. James, A. Gilchrist and A. G. White. 'Experimental Demonstration of a Compiled Version of Shor's Algorithm with Quantum Entanglement'. Physical Review Letters **99**, 250505 (2007). DOI: 10.1103/PhysRevLett.99.250505.

[Lan+10] B. P. Lanyon, J. D. Whitfield, G. G. Gillett, M. E. Goggin, M. P. Almeida, I. Kassal, J. D. Biamonte, M. Mohseni, B. J. Powell, M. Barbieri, A. Aspuru-Guzik and A. G. White. 'Towards quantum chemistry on a quantum computer'. Nature Chemistry **2**, 106–111 (2010). DOI: 10.1038/nchem.483.

[Lec+16] R. Lechner, C. Maier, C. Hempel, P. Jurcevic, B. P. Lanyon, T. Monz, M. Brownnutt, R. Blatt and C. F. Roos. 'Electromagnetically-induced-transparency ground-state cooling of long ion strings'. Physical Review A **93**, 053401 (2016). DOI: 10.1103/PhysRevA.93.053401.

[Lei+03] D. Leibfried, R. Blatt, C. Monroe and D. Wineland. 'Quantum dynamics of single trapped ions'. Reviews of Modern Physics **75**, 281–324 (2003). DOI: 10.1103/RevModPhys.75.281.

[Lei+21] D. Leichtle, L. Music, E. Kashefi and H. Ollivier. 'Verifying BQP Computations on Noisy Devices with Minimal Overhead'. PRX Quantum **2**, 040302 (2021). DOI: 10.1103/PRXQuantum.2.040302.

[Lek+17] B. Lekitsch, S. Weidt, A. G. Fowler, K. Mølmer, S. J. Devitt, C. Wunderlich and W. K. Hensinger. 'Blueprint for a microwave trapped ion quantum computer'. Science Advances **3**, e1601540 (2017). DOI: 10.1126/sciadv.1601540.

[Li+15] Y. Li, P. C. Humphreys, G. J. Mendoza and S. C. Benjamin. 'Resource Costs for Fault-Tolerant Linear Optical Quantum Computing'. Physical Review X **5**, 041007 (2015). DOI: 10.1103/PhysRevX.5.041007.

[Luc+07] D. M. Lucas, B. C. Keitch, J. P. Home, G. Imreh, M. J. McDonnell, D. N. Stacey, D. J. Szwer and A. M. Steane. 'A long-lived memory qubit on a low-decoherence quantum bus'. Preprint (arXiv, 2007). DOI: 10.48550/arXiv.0710.4421.

[Luc+04a] D. M. Lucas, A. Ramos, J. P. Home, M. J. McDonnell, S. Nakayama, J.-P. Stacey, S. C. Webster, D. N. Stacey and A. M. Steane. 'Isotope-selective photoionization for calcium ion trapping'. Physical Review A **69**, 012711 (2004). DOI: 10.1103/PhysRevA.69.012711.

[Luc+04b] D. M. Lucas, A. Ramos, J. P. Home, M. J. McDonnell, S. Nakayama, J.-P. Stacey, S. C. Webster, D. N. Stacey and A. M. Steane. 'Isotope-selective photoionization for calcium ion trapping'. Physical Review A **69**, 012711 (2004). DOI: 10.1103/PhysRevA.69.012711.

[LBC11] W. E. Lybarger, J. C. Berengut and J. Chiaverini. 'Precision measurement of the $5\ ^2S_{1/2} - 4\ ^2D_{5/2}$ quadrupole transition isotope shift between $^{88}Sr^+$ and $^{86}Sr^+$'. Physical Review A **83**, 052509 (2011). DOI: 10.1103/PhysRevA.83.052509.

[MGE12] E. Magesan, J. M. Gambetta and J. Emerson. 'Characterizing quantum gates via randomized benchmarking'. Physical Review A **85**, 042311 (2012). DOI: 10.1103/PhysRevA.85.042311.

[Mai20] D. Main. 'Magnetic Field Stabilisation in Ion Traps'. MSc thesis (University of Oxford, 2020).

[Mai23] D. Main. 'Local Entangling Operations in a Mixed-Species Trapped-Ion Network Node'. Confirmation of status report (University of Oxford, 2023).

[MDF17] A. Mantri, T. F. Demarie and J. F. Fitzsimons. 'Universality of quantum computation with cluster states and (X, Y)-plane measurements'. Scientific Reports **7**, 42861 (2017). DOI: 10.1038/srep42861.

[Mar+18] I. Marinković, A. Wallucks, R. Riedinger, S. Hong, M. Aspelmeyer and S. Gröblacher. 'Optomechanical Bell Test'. Physical Review Letters **121**, 220404 (2018). DOI: 10.1103/PhysRevLett.121.220404.

[Mat+03] K. Matsubara, U. Tanaka, H. Imajo, S. Urabe and M. Watanabe. 'Laser cooling and isotope-shift measurement of Zn+ with 202-nm ultraviolet coherent light'. Applied Physics B **76**, 209–213 (2003). DOI: 10.1007/s00340-002-1081-7.

[Mat+08] D. N. Matsukevich, P. Maunz, D. L. Moehring, S. Olmschenk and C. Monroe. 'Bell Inequality Violation with Two Remote Atomic Qubits'. Physical Review Letters **100**, 150404 (2008). DOI: 10.1103/PhysRevLett.100.150404.

[Mau16] P. L. W. Maunz. *High Optical Access Trap 2.0.* Tech. rep. (Sandia National Lab. (SNL-NM), Albuquerque, NM, USA, 2016). DOI: 10.2172/1237003.

[Mee+96] D. M. Meekhof, C. Monroe, B. E. King, W. M. Itano and D. J. Wineland. 'Generation of Nonclassical Motional States of a Trapped Atom'. Physical Review Letters **76**, 1796–1799 (1996). DOI: 10.1103/PhysRevLett.76.1796.

[Meg+13] E. Megidish, A. Halevy, T. Shacham, T. Dvir, L. Dovrat and H. S. Eisenberg. 'Entanglement Swapping between Photons that have Never Coexisted'. Physical Review Letters **110**, 210403 (2013). DOI: 10.1103/PhysRevLett.110.210403.

[MM87] A. A. Michelson and E. W. Morley. 'On the Relative Motion of the Earth and the Luminiferous Ether'. American Journal of Science **34**, 333–345 (1887). DOI: 10.2475/ajs.s3-34.203.333.

[MW01] F. Mintert and C. Wunderlich. 'Ion-trap quantum logic using long-wavelength radiation'. Physical Review Letters **87**, 257904 (2001). DOI: 10.1103/PhysRevLett.87.257904.

[Moe+07] D. L. Moehring, M. J. Madsen, K. C. Younge, J. R. N. Kohn, P. Maunz, L.-M. Duan, C. Monroe and B. B. Blinov. 'Quantum networking with photons and trapped atoms'. Journal of the Optical Society of America B **24**, 300–315 (2007). DOI: 10.1364/JOSAB.24.000300.

[MCD93] K. Mølmer, Y. Castin and J. Dalibard. 'Monte Carlo wave-function method in quantum optics'. Journal of the Optical Society of America B **10**, 524–538 (1993). DOI: 10.1364/JOSAB.10.000524.

[MK13] C. Monroe and J. Kim. 'Scaling the Ion Trap Quantum Processor'. Science **339**, 1164–1169 (2013). DOI: 10.1126/science.1231298.

[Mon+14] C. Monroe, R. Raussendorf, A. Ruthven, K. R. Brown, P. Maunz, L.-M. Duan and J. Kim. 'Large-scale modular quantum-computer architecture with atomic memory and photonic interconnects'. Physical Review A **89**, 022317 (2014). DOI: 10.1103/PhysRevA.89.022317.

[Moo98] G. E. Moore. 'Cramming more components onto integrated circuits'. Proceedings of the IEEE **86**, 82–85 (1998). DOI: 10.1109/N-SSC.2006.4785860.

[Moo+23] I. D. Moore, W. C. Campbell, E. R. Hudson, M. J. Boguslawski, D. J. Wineland and D. T. C. Allcock. 'Photon scattering errors during stimulated Raman transitions in trapped-ion qubits'. Physical Review A **107**, 032413 (2023). DOI: 10.1103/PhysRevA.107.032413.

[MF13] T. Morimae and K. Fujii. 'Blind quantum computation protocol in which Alice only makes measurements'. Physical Review A **87**, 050301 (2013). DOI: 10.1103/PhysRevA.87.050301.

[Mos+23] S. A. Moses, C. H. Baldwin, M. S. Allman, R. Ancona, L. Ascarrunz, C. Barnes, J. Bartolotta, B. Bjork, P. Blanchard, M. Bohn, J. G. Bohnet, N. C. Brown, N. Q. Burdick, W. C. Burton, S. L. Campbell, J. P. Campora, C. Carron, J. Chambers, J. W. Chan, Y. H. Chen, A. Chernoguzov, E. Chertkov, J. Colina, J. P. Curtis, R. Daniel, M. DeCross, D. Deen, C. Delaney, J. M. Dreiling, C. T. Ertsgaard, J. Esposito, B. Estey, M. Fabrikant, C. Figgatt, C. Foltz, M. Foss-Feig, D. Francois, J. P. Gaebler, T. M. Gatterman, C. N. Gilbreth, J. Giles, E. Glynn, A. Hall, A. M. Hankin, A. Hansen, D. Hayes, B. Higashi, I. M. Hoffman, B. Horning, J. J. Hout, R. Jacobs, J. Johansen, L. Jones, J. Karcz, T. Klein, P. Lauria, P. Lee, D. Liefer, S. T. Lu, D. Lucchetti, C. Lytle, A. Malm, M. Matheny, B. Mathewson, K. Mayer, D. B. Miller, M. Mills, B. Neyenhuis, L. Nugent, S. Olson, J. Parks, G. N. Price, Z. Price, M. Pugh, A. Ransford, A. P. Reed, C. Roman, M. Rowe, C. Ryan-Anderson, S. Sanders, J. Sedlacek, P. Shevchuk, P. Siegfried, T. Skripka, B. Spaun, R. T. Sprenkle, R. P. Stutz, M. Swallows, R. I. Tobey, A. Tran, T. Tran, E. Vogt, C. Volin, J. Walker, A. M. Zolot and J. M. Pino. 'A Race-Track Trapped-Ion Quantum Processor'. Physical Review X **13**, 041052 (2023). DOI: 10.1103/PhysRevX.13.041052.

[Mye+08] A. H. Myerson, D. J. Szwer, S. C. Webster, D. T. C. Allcock, M. J. Curtis, G. Imreh, J. A. Sherman, D. N. Stacey, A. M. Steane and D. M. Lucas. 'High-Fidelity Readout of Trapped-Ion Qubits'. Physical Review Letters **100**, 200502 (2008). DOI: 10.1103/PhysRevLett.100.200502.

[Nad+21] D. P. Nadlinger, P. Drmota, D. Main, B. C. Nichol, G. Araneda, R. Srinivas, L. J. Stephenson, C. J. Ballance and D. M. Lucas. 'Micromotion minimisation by synchronous detection of parametrically excited motion'. Preprint6 (arXiv, 2021). DOI: 10.48550/arXiv.2107.00056.

[Nad+22] D. P. Nadlinger, P. Drmota, B. C. Nichol, G. Araneda, D. Main, R. Srinivas, D. M. Lucas, C. J. Ballance, K. Ivanov, E. Y.-Z. Tan, P. Sekatski, R. L. Urbanke, R. Renner, N. Sangouard and J.-D. Bancal. 'Experimental quantum key distribution certified by Bell's theorem'. Nature **607**, 682–686 (2022). DOI: 10.1038/s41586-022-04941-5.

[Nad22] D. Nadlinger. 'Device-Independent Key Distribution between Trapped-Ion Quantum Network Nodes'. DPhil thesis (University of Oxford, 2022).

[Nad16] D. P. Nadlinger. 'Entanglement between trapped strontium ions and photons'. MSc thesis (ETH Zürich, 2016).

[Nat22] National Institute of Standards and Technology. *Experimental Polarizabilites*. (2022). URL: https://cccbdb.nist.gov/pollistx.asp (visited on 21/04/2023).

[Nee19] B. de Neeve. 'Calibrating an Ion-Trap Quantum Computer'. MSc thesis (ETH Zürich, 2019).

[Neg+18] V. Negnevitsky, M. Marinelli, K. K. Mehta, H.-Y. Lo, C. Flühmann and J. P. Home. 'Repeated multi-qubit readout and feedback with a mixed-species trapped-ion register'. Nature **563**, 527–531 (2018). DOI: 10.1038/s41586-018-0668-z.

[Neg18] V. Negnevitsky. 'Feedback-stabilised quantum states in a mixed-species ion system'. Dissertation (ETH Zürich, 2018).

[Nic+22] B. C. Nichol, R. Srinivas, D. P. Nadlinger, P. Drmota, D. Main, G. Araneda, C. J. Ballance and D. M. Lucas. 'An elementary quantum network of entangled optical atomic clocks'. Nature **609**, 689–694 (2022). DOI: 10.1038/s41586-022-05088-z.

[Nic22] B. C. Nichol. 'An elementary quantum network of entangled optical atomic clocks'. DPhil thesis (University of Oxford, 2022).

[Nie04] M. A. Nielsen. 'Optical Quantum Computation Using Cluster States'. Physical Review Letters **93**, 040503 (2004). DOI: 10.1103/PhysRevLett.93.040503.

[Nie06] M. A. Nielsen. 'Cluster-state quantum computation'. Reports on Mathematical Physics **57**, 147–161 (2006). DOI: 10.1016/S0034-4877(06)80014-5.

[Nig+16] R. Nigmatullin, C. J. Ballance, N. d. Beaudrap and S. C. Benjamin. 'Minimally complex ion traps as modules for quantum communication and computing'. New Journal of Physics **18**, 103028 (2016). DOI: 10.1088/1367-2630/18/10/103028.

[Osp+11] C. Ospelkaus, U. Warring, Y. Colombe, K. R. Brown, J. M. Amini, D. Leibfried and D. J. Wineland. 'Microwave quantum logic gates for trapped ions'. Nature **476**, 181–184 (2011). DOI: 10.1038/nature10290.

[Oze+07] R. Ozeri, W. M. Itano, R. B. Blakestad, J. Britton, J. Chiaverini, J. D. Jost, C. Langer, D. Leibfried, R. Reichle, S. Seidelin, J. H. Wesenberg and D. J. Wineland. 'Errors in trapped-ion quantum gates due to spontaneous photon scattering'. Physical Review A **75**, 042329 (2007). DOI: 10.1103/PhysRevA.75.042329.

[Oze+05] R. Ozeri, C. Langer, J. D. Jost, B. DeMarco, A. Ben-Kish, B. R. Blakestad, J. Britton, J. Chiaverini, W. M. Itano, D. B. Hume, D. Leibfried, T. Rosenband, P. O. Schmidt and D. J. Wineland. 'Hyperfine Coherence in the Presence of Spontaneous Photon Scattering'. Physical Review Letters **95**, 030403 (2005). DOI: 10.1103/PhysRevLett.95.030403.

[PHW94] E. Peik, G. Hollemann and H. Walther. 'Laser cooling and quantum jumps of a single indium ion'. Physical Review A **49**, 402–408 (1994). DOI: 10.1103/PhysRevA.49.402.

[Pfa+14] W. Pfaff, B. J. Hensen, H. Bernien, S. B. van Dam, M. S. Blok, T. H. Taminiau, M. J. Tiggelman, R. N. Schouten, M. Markham, D. J. Twitchen and R. Hanson. 'Unconditional quantum teleportation between distant solid-state quantum bits'. Science **345**, 532–535 (2014). DOI: 10.1126/science.1253512.

[Pir+10] S. Pironio, A. Acín, S. Massar, A. B. de la Giroday, D. N. Matsukevich, P. Maunz, S. Olmschenk, D. Hayes, L. Luo, T. A. Manning and C. Monroe. 'Random numbers certified by Bell's theorem'. Nature **464**, 1021–1024 (2010). DOI: 10.1038/nature09008.

[Pla00] M. Planck. 'Entropie und Temperatur strahlender Wärme'. Annalen der Physik **306**, 719–737 (1900). DOI: 10.1002/andp.19003060410.

[Pla44] M. Planck. *Wege zur physikalischen Erkenntnis: Reden und Vorträge*. Vol. 1. (Hirzel, 1944).

[Poi+96] M. E. Poitzsch, J. C. Bergquist, W. M. Itano and D. J. Wineland. 'Cryogenic linear ion trap for accurate spectroscopy'. Review of Scientific Instruments **67**, 129–134 (1996). DOI: 10.1063/1.1146560.

[Pre06] J. Preskill. *Notes on noise*. (2006). URL: https://www.preskill.caltech.edu/papers/decoherence_notes.pdf (visited on 26/01/2025).

[Pro+22] T. Proctor, K. Rudinger, K. Young, E. Nielsen and R. Blume-Kohout. 'Measuring the capabilities of quantum computers'. Nature Physics **18**, 75–79 (2022). DOI: 10.1038/s41567-021-01409-7.

[Ram+24] J. Ramette, J. Sinclair, N. P. Breuckmann and V. Vuletić. 'Fault-tolerant connection of error-corrected qubits with noisy links'. npj Quantum Information **10**, 58 (2024). DOI: 10.1038/s41534-024-00855-4.

[RB01] R. Raussendorf and H. J. Briegel. 'A One-Way Quantum Computer'. Physical Review Letters **86**, 5188–5191 (2001). DOI: 10.1103/PhysRevLett.86.5188.

[RH07] R. Raussendorf and J. Harrington. 'Fault-Tolerant Quantum Computation with High Threshold in Two Dimensions'. Physical Review Letters **98**, 190504 (2007). DOI: 10.1103/PhysRevLett.98.190504.

[Řeh+07] J. Řeháček, Z. Hradil, E. Knill and A. I. Lvovsky. 'Diluted maximum-likelihood algorithm for quantum tomography'. Physical Review A **75**, 042108 (2007). DOI: 10.1103/PhysRevA.75.042108.

[RAD+78] R. L. Rivest, L. Adleman, M. L. Dertouzos et al. 'On data banks and privacy homomorphisms'. Foundations of secure computation **4**, 169–180 (1978).

[Roo+08] C. F. Roos, T. Monz, K. Kim, M. Riebe, H. Häffner, D. F. V. James and R. Blatt. 'Nonlinear coupling of continuous variables at the single quantum level'. Physical Review A **77**, 040302 (2008). DOI: 10.1103/PhysRevA.77.040302.

[SWM10] M. Saffman, T. G. Walker and K. Mølmer. 'Quantum information with Rydberg atoms'. Reviews of Modern Physics **82**, 2313–2363 (2010). DOI: 10.1103/RevModPhys.82.2313.

[Sar+19] A. Sarma, R. Chatterjee, K. Gili and T. Yu. 'Quantum unsupervised and supervised learning on superconducting processors'. Quantum Information Computation **20**, 541–552 (2019).

[Sch+18] V. M. Schäfer, C. J. Ballance, K. Thirumalai, L. J. Stephenson, T. G. Ballance, A. M. Steane and D. M. Lucas. 'Fast quantum logic gates with trapped-ion qubits'. Nature **555**, 75–78 (2018). DOI: 10.1038/nature25737.

[Sch18] V. M. Schäfer. 'Fast gates and mixed-species entanglement with trapped ions'. DPhil thesis (University of Oxord, 2018).

[Sch+21] J. Schupp, V. Krcmarsky, V. Krutyanskiy, M. Meraner, T. Northup and B. Lanyon. 'Interface between Trapped-Ion Qubits and Traveling Photons with Close-to-Optimal Efficiency'. PRX Quantum **2**, 020331 (2021). DOI: 10.1103/PRXQuantum.2.020331.

[Sep+19] M. A. Sepiol, A. C. Hughes, J. E. Tarlton, D. P. Nadlinger, T. G. Ballance, C. J. Ballance, T. P. Harty, A. M. Steane, J. F. Goodwin and D. M. Lucas. 'Probing Qubit Memory Errors at the Part-per-Million Level'. Physical Review Letters **123**, 110503 (2019). DOI: 10.1103/PhysRevLett.123.110503.

[She+92] H. Y. Shen, H. Xu, Z. D. Zeng, W. X. Lin, R. F. Wu and G. F. Xu. 'Measurement of refractive indices and thermal refractive-index coefficients of $LiNbO_3$ crystal doped with 5 mol % MgO'. Applied Optics **31**, 6695 (1992). DOI: 10.1364/AO.31.006695.

[Sho99] P. W. Shor. 'Polynomial-time algorithms for prime factorization and discrete logarithms on a quantum computer'. SIAM Review **41**, 303–332 (1999). DOI: 10.1137/S0097539795293172.

[SCS12] B. N. Simon, C. M. Chandrashekar and S. Simon. 'Hamilton's turns as a visual tool kit for designing single-qubit unitary gates'. Physical Review A **85**, 022323 (2012). DOI: 10.1103/PhysRevA.85.022323.

[SÁS11] A. M. Souza, G. A. Álvarez and D. Suter. 'Robust Dynamical Decoupling for Quantum Computing and Quantum Memory'. Physical Review Letters **106**, 240501 (2011). DOI: 10.1103/PhysRevLett.106.240501.

[Sri+21] R. Srinivas, S. C. Burd, H. M. Knaack, R. T. Sutherland, A. Kwiatkowski, S. Glancy, E. Knill, D. J. Wineland, D. Leibfried, A. C. Wilson, D. T. C. Allcock and D. H. Slichter. 'High-fidelity laser-free universal control of trapped ion qubits'. Nature **597**, 209–213 (2021). DOI: 10.1038/s41586-021-03809-4.

[Sta+22] P.-J. Stas, Y. Q. Huan, B. Machielse, E. N. Knall, A. Suleymanzade, B. Pingault, M. Sutula, S. W. Ding, C. M. Knaut, D. R. Assumpcao, Y.-C. Wei, M. K. Bhaskar, R. Riedinger, D. D. Sukachev, H. Park, M. Lončar, D. S. Levonian and M. D. Lukin. 'Robust multi-qubit quantum network node with integrated error detection'. Science **378**, 557–560 (2022). DOI: 10.1126/science.add9771.

[Ste97] A. Steane. 'The ion trap quantum information processor'. Applied Physics B **64**, 623–643 (1997). DOI: 10.1007/s003400050225.

[Ste03] A. M. Steane. 'Overhead and noise threshold of fault-tolerant quantum error correction'. Physical Review A **68**, 042322 (2003). DOI: 10.1103/PhysRevA.68.042322.

[Ste14] A. M. Stephens. 'Fault-tolerant thresholds for quantum error correction with the surface code'. Physical Review A **89**, 022321 (2014). DOI: 10.1103/PhysRevA.89.022321.

[Ste+20] L. J. Stephenson, D. P. Nadlinger, B. C. Nichol, S. An, P. Drmota, T. G. Ballance, K. Thirumalai, J. F. Goodwin, D. M. Lucas and C. J. Ballance. 'High-Rate, High-Fidelity Entanglement of Qubits Across an Elementary Quantum Network'. Physical Review Letters **124**, 110501 (2020). DOI: 10.1103/PhysRevLett.124.110501.

[Ste19] L. Stephenson. 'Entanglement between Nodes of a Quantum Network'. DPhil thesis (University of Oxford, 2019).

[Stu+13] A. Stute, B. Casabone, B. Brandstätter, K. Friebe, T. E. Northup and R. Blatt. 'Quantum-state transfer from an ion to a photon'. Nature Photonics **7**, 219–222 (2013). DOI: 10.1038/nphoton.2012.358.

[Szw+11] D. J. Szwer, S. C. Webster, A. M. Steane and D. M. Lucas. 'Keeping a single qubit alive by experimental dynamic decoupling'. Journal of Physics B **44**, 025501 (2011). DOI: 10.1088/0953-4075/44/2/025501.

[Szw09] D. J. Szwer. 'High Fidelity Readout and Protection of a $^{40}Ca^{+}$ Trapped Ion Qubit.' DPhil thesis (University of Oxford, 2009).

[Thi19] K. Thirumalai. 'High-fidelity mixed species entanglement of trapped ions'. DPhil thesis (University of Oxford, 2019).

[Tom19] T.-M. Tomescu. 'Qubit Encryption by Rotation of Polarization States'. MSc thesis (University of Oxford, 2019).

[Tur+00] Q. A. Turchette, D. Kielpinski, B. E. King, D. Leibfried, D. M. Meekhof, C. J. Myatt, M. A. Rowe, C. A. Sackett, C. S. Wood, W. M. Itano, C. Monroe and D. J. Wineland. 'Heating of trapped ions from the quantum ground state'. Physical Review A **61**, 063418 (2000). DOI: 10.1103/PhysRevA.61.063418.

[Tur+98] Q. A. Turchette, C. S. Wood, B. E. King, C. J. Myatt, D. Leibfried, W. M. Itano, C. Monroe and D. J. Wineland. 'Deterministic Entanglement of Two Trapped Ions'. Physical Review Letters **81**, 3631–3634 (1998). DOI: 10.1103/PhysRevLett.81.3631.

[Uys+10] H. Uys, M. J. Biercuk, A. P. VanDevender, C. Ospelkaus, D. Meiser, R. Ozeri and J. J. Bollinger. 'Decoherence due to Elastic Rayleigh Scattering'. Physical Review Letters **105**, 200401 (2010). DOI: 10.1103/PhysRevLett.105.200401.

[Van+06] K. Vant, J. Chiaverini, W. Lybarger and D. J. Berkeland. 'Photoionization of strontium for trapped-ion quantum information processing'. arXiv:quant-ph/0607055 (arXiv, 2006). DOI: 10.48550/arXiv.quant-ph/0607055.

[Vri+19] G. Vrijsen, Y. Aikyo, R. F. Spivey, I. V. Inlek and J. Kim. 'Efficient isotope-selective pulsed laser ablation loading of 174Yb+ ions in a surface electrode trap'. Optics Express **27**, 33907–33914 (2019). DOI: 10.1364/OE.27.033907.

[Wan+21] P. Wang, C.-Y. Luan, M. Qiao, M. Um, J. Zhang, Y. Wang, X. Yuan, M. Gu, J. Zhang and K. Kim. 'Single ion qubit with estimated coherence time exceeding one hour'. Nature Communications **12**, 233 (2021). DOI: 10.1038/s41467-020-20330-w.

[Web22] M. Weber. 'High-Fidelity, Near-Field Microwave Gates in a Cryogenic Surface Trap'. DPhil thesis (University of Oxford, 2022).

[WW30] V. Weisskopf and E. Wigner. 'Berechnung der natürlichen Linienbreite auf Grund der Diracschen Lichttheorie'. Zeitschrift für Physik **63**, 54–73 (1930). DOI: 10.1007/BF01336768.

[Wen17] G. Wendin. 'Quantum information processing with superconducting circuits: a review'. Reports on Progress in Physics **80**, 106001 (2017). DOI: 10.1088/1361-6633/aa7e1a.

[Wim94] S. Wimperis. 'Broadband, Narrowband, and Passband Composite Pulses for Use in Advanced NMR Experiments'. Journal of Magnetic Resonance, Series A **109**, 221–231 (1994). DOI: 10.1006/jmra.1994.1159.

[Win+03] D. J. Wineland, M. Barrett, J. Britton, J. Chiaverini, B. DeMarco, W. M. Itano, B. Jelenković, C. Langer, D. Leibfried, V. Meyer, T. Rosenband and T. Schätz. 'Quantum information processing with trapped ions'. Philosophical Transactions of the Royal Society of London. Series A: Mathematical, Physical and Engineering Sciences **361**, 1349–1361 (2003). DOI: 10.1098/rsta.2003.1205.

[Win+98] D. Wineland, C. Monroe, W. Itano, D. Leibfried, B. King and D. Meekhof. 'Experimental issues in coherent quantum-state manipulation of trapped atomic ions'. Journal of Research of the National Institute of Standards and Technology **103**, 259 (1998). DOI: 10.6028/jres.103.019.

[Wri+19] K. Wright, K. M. Beck, S. Debnath, J. M. Amini, Y. Nam, N. Grzesiak, J.-S. Chen, N. C. Pisenti, M. Chmielewski, C. Collins, K. M. Hudek, J. Mizrahi, J. D. Wong-Campos, S. Allen, J. Apisdorf, P. Solomon, M. Williams, A. M. Ducore, A. Blinov, S. M. Kreikemeier, V. Chaplin, M. Keesan, C. Monroe and J. Kim. 'Benchmarking an 11-qubit quantum computer'. Nature Communications **10**, 5464 (2019). DOI: 10.1038/s41467-019-13534-2.

[Wri+18] T. A. Wright, R. J. A. Francis-Jones, C. B. E. Gawith, J. N. Becker, P. M. Ledingham, P. G. R. Smith, J. Nunn, P. J. Mosley, B. Brecht and I. A. Walmsley. 'Two-Way Photonic Interface for Linking the Sr^+ Transition at 422 nm to the Telecommunication C Band'. Physical Review Applied **10**, 044012 (2018). DOI: 10.1103/PhysRevApplied.10.044012.

[Yan+22] H.-X. Yang, J.-Y. Ma, Y.-K. Wu, Y. Wang, M.-M. Cao, W.-X. Guo, Y.-Y. Huang, L. Feng, Z.-C. Zhou and L.-M. Duan. 'Realizing coherently convertible dual-type qubits with the same ion species'. Nature Physics **18**, 1058–1061 (2022). DOI: 10.1038/s41567-022-01661-5.

[YY03] A. Yariv and P. Yeh. *Optical waves in crystals: propagation and control of laser radiation*. Wiley Classics Library ed. (Wiley-Interscience, Hoboken, NJ, 2003).

[YJT07] K. Yonekura, L. Jin and K. Takizawa. 'Measurement of Wavelength Dependence of Electro-Optic Coefficients r_{22} of Non-doped and 5% MgO-doped Congruent LiNbO3 Crystals and 1.8% MgO-doped Quasi-stoichiometric LiNbO3 Crystal by Multiple Reflection Interference Method'. Optical Review **14**, 194–200 (2007). DOI: 10.1007/s10043-007-0194-y.

[YJT08] K. Yonekura, L. Jin and K. Takizawa. 'Measurement of Dispersion of Effective Electro-Optic Coefficients r_{13}^{E} and r_{33}^{E} of Non-Doped Congruent $LiNbO_3$ Crystal'. Japanese Journal of Applied Physics **47**, 5503–5508 (2008). DOI: 10.1143/JJAP.47.5503.

[YPF14] L. Yu, C. A. Pérez-Delgado and J. F. Fitzsimons. 'Limitations on information-theoretically-secure quantum homomorphic encryption'. Physical Review A **90**, 050303 (2014). DOI: 10.1103/PhysRevA.90.050303.

[ZN42] J. G. Ziegler and N. B. Nichols. 'Optimum Settings for Automatic Controllers'. Transactions of the American Society of Mechanical Engineers **64**, 759–765 (1942).

[ZBD14] M. Zwerger, H. J. Briegel and W. Dür. 'Hybrid architecture for encoded measurement-based quantum computation'. Scientific Reports **4**, 5364 (2014). DOI: 10.1038/srep05364.